



MA... Instrument and a Methodology for... eous and... al Measurements of... nal Electron... mperature and the... Wind Velocity on the Solar Corona

11 August 1999 in Elazig, Turkey



N... ics and
S... tion
G... Flight Center
G... and 20771

The NASA STI Program Office ... in Profile

Since its founding, NASA has been dedicated to the advancement of aeronautics and space science. The NASA Scientific and Technical Information (STI) Program Office plays a key part in helping NASA maintain this important role.

The NASA STI Program Office is operated by Langley Research Center, the lead center for NASA's scientific and technical information. The NASA STI Program Office provides access to the NASA STI Database, the largest collection of aeronautical and space science STI in the world. The Program Office is also NASA's institutional mechanism for disseminating the results of its research and development activities. These results are published by NASA in the NASA STI Report Series, which includes the following report types:

- **TECHNICAL PUBLICATION.** Reports of completed research or a major significant phase of research that present the results of NASA programs and include extensive data or theoretical analysis. Includes compilations of significant scientific and technical data and information deemed to be of continuing reference value. NASA's counterpart of peer-reviewed formal professional papers but has less stringent limitations on manuscript length and extent of graphic presentations.
- **TECHNICAL MEMORANDUM.** Scientific and technical findings that are preliminary or of specialized interest, e.g., quick release reports, working papers, and bibliographies that contain minimal annotation. Does not contain extensive analysis.
- **CONTRACTOR REPORT.** Scientific and technical findings by NASA-sponsored contractors and grantees.
- **CONFERENCE PUBLICATION.** Collected papers from scientific and technical conferences, symposia, seminars, or other meetings sponsored or cosponsored by NASA.
- **SPECIAL PUBLICATION.** Scientific, technical, or historical information from NASA programs, projects, and mission, often concerned with subjects having substantial public interest.
- **TECHNICAL TRANSLATION.** English-language translations of foreign scientific and technical material pertinent to NASA's mission.

Specialized services that complement the STI Program Office's diverse offerings include creating custom thesauri, building customized databases, organizing and publishing research results . . . even providing videos.

For more information about the NASA STI Program Office, see the following:

- Access the NASA STI Program Home Page at <http://www.sti.nasa.gov/STI-homepage.html>
- E-mail your question via the Internet to help@sti.nasa.gov
- Fax your question to the NASA Access Help Desk at (301) 621-0134
- Telephone the NASA Access Help Desk at (301) 621-0390
- Write to:
NASA Access Help Desk
NASA Center for AeroSpace Information
7121 Standard Drive
Hanover, MD 21076-1320

NASA/TM—2000—209973



**MACS, An Instrument and a Methodology
for Simultaneous and Global Measurements
of the Coronal Electron Temperature and
the Solar Wind Velocity on the Solar Corona**

*Nelson Leslie Reginald
University of Delaware, Newark*

National Aeronautics and
Space Administration

Goddard Space Flight Center
Greenbelt, Maryland 20771

December 2000

Available from:

NASA Center for AeroSpace Information
7121 Standard Drive
Hanover, MD 21076-1320
Price Code: A17

National Technical Information Service
5285 Port Royal Road
Springfield, VA 22161
Price Code: A10

**MACS, AN INSTRUMENT, AND A METHODOLOGY FOR
SIMULTANEOUS AND GLOBAL MEASUREMENTS OF THE CORONAL
ELECTRON TEMPERATURE AND THE SOLAR WIND VELOCITY
ON THE SOLAR CORONA**

by

Nelson Leslie Reginald

A dissertation submitted to the Faculty of the University of Delaware in partial fulfillment of the requirements for the degree of Doctor of Philosophy with a major in Physics

Fall 2000

© 2000 Nelson Leslie Reginald

All Rights Reserved

**MACS, AN INSTRUMENT, AND A METHODOLOGY FOR
SIMULTANEOUS AND GLOBAL MEASUREMENTS OF THE CORONAL
ELECTRON TEMPERATURE AND THE SOLAR WIND VELOCITY
ON THE SOLAR CORONA**

by

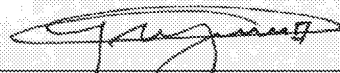
Nelson Leslie Reginald

Approved: _____



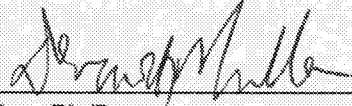
Henry R. Glyde, Ph.D.
Chairman, Department of Physics and Astronomy

Approved: _____

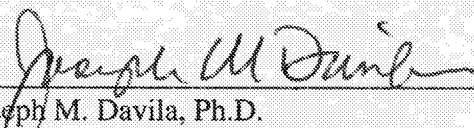


Conrad M. Gempesaw II, Ph.D.
Vice Provost for Academic Programs and Planning

I certify that I have read this dissertation and that in my opinion it meets the academic and professional standard required by the University as a dissertation for the degree of Doctor of Philosophy.

Signed: 
Dermott J. Mullan, Ph.D.
Professor in charge of dissertation

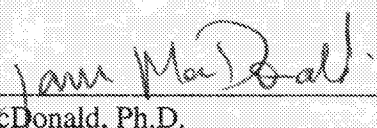
I certify that I have read this dissertation and that in my opinion it meets the academic and professional standard required by the University as a dissertation for the degree of Doctor of Philosophy.

Signed: 
Joseph M. Davila, Ph.D.
Member of dissertation committee

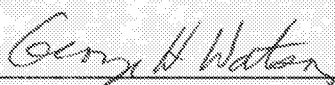
I certify that I have read this dissertation and that in my opinion it meets the academic and professional standard required by the University as a dissertation for the degree of Doctor of Philosophy.

Signed: 
Stanley P. Owocki, Ph.D.
Member of dissertation committee

I certify that I have read this dissertation and that in my opinion it meets the academic and professional standard required by the University as a dissertation for the degree of Doctor of Philosophy.

Signed: 
James MacDonald, Ph.D.
Member of dissertation committee

I certify that I have read this dissertation and that in my opinion it meets the academic and professional standard required by the University as a dissertation for the degree of Doctor of Philosophy.

Signed: 
George H. Watson, Ph.D.
Member of dissertation committee

Acknowledgements

I am greatly proud for the opportunity afforded to conduct my Ph.D. dissertation research at the Solar Physics Division of the NASA's Goddard Space Flight Center in Greenbelt, Maryland, USA under the able guidance of Dr. Joseph M. Davila. I am also thankful for the opportunity provided to participate in the assembly of the SERTS (Solar Extreme Ultraviolet Rocket Telescope) payload and its launch on the 26 July 2000 from the White Sands Missile Range, New Mexico.

In this regard I wish to convey my hearty thanks to Dr. Dermott J. Mullan for the trust and faith in recommending me for the graduate research position offered by Dr. Davila, for providing the funds to attend the International Summer School on "The Sun As Seen From Space" in L'Aquila, Italy (1997) and for serving as the chairman of the Ph.D. thesis committee.

This research that spanned over the years 1998 to 2000 involved in the theoretical modeling, the design and construction of an instrument, an eclipse expedition to Turkey (1999), the analyses and travel to the AAS meetings in Chicago (1999) & Nevada (2000), the TRACE workshop in California (1999), the AGU conference in Washington D.C

(2000) and the IAP “Eclipses and the Solar Corona” conference in France (2000), thus molding me for a successful scientific career.

My sincere thanks are also extended to Mr. Chuck Condor for helping with all the encouragement and logistics for the eclipse expedition to Turkey, and to Mr. Larry White for the long hours spent on the engineering drawings and fabrication of MACS.

I also wish to convey my regards to the staff of my high school at S. Thomas’ College, Mount Lavinia, Sri Lanka and my undergraduate institute at the University of Peradeniya in Sri Lanka, my MS thesis advisor and chairman Prof. James MacDonald at the University of Delaware and for the full tuition scholarship and teaching assistantship awarded by the University of Delaware, which enabled me to travel to the USA in 1994 in pursuance with my graduate studies.

My sincere thanks is also extended to Miss. Elizabeth (Sugar Bug) Chapman for her help in preparing the text.

Dedicated to my loving parents
Gnaniah J. Reginald & Beryl A. Reginald

TABLE OF CONTENTS

LIST OF TABLES.....	xii
LIST OF FIGURES.....	xv
ABSTRACT.....	xxxviii
Chapter	
1 INTRODUCTION.....	1
1.1 Introduction to the solar corona.....	1
1.2 Other methods to measure the solar wind velocity and the coronal temperature.....	12
2 FORMATION OF THE K-CORONA AND THE FOCUS OF THIS RESEARCH.....	18
2.1 K-corona.....	18
2.2 The photospheric spectrum.....	18
2.3 The scattering source.....	20
2.4 The effects on the incident radiation by the scattering source.....	21
2.5 The K-coronal spectrum.....	22
2.6 Further explanation for the formation of the temperature sensitive anti- nodes.....	29

2.7	The influence of the solar wind on the K-coronal spectrum.....	38
2.8	Simultaneous determination of the coronal temperature and the solar wind velocity.....	44
2.9	Global determination of the coronal temperature and the solar wind velocity.....	47
2.10	The essence of this dissertation.....	48
3	THE INSTRUMENT.....	49
3.1	Overview of the instrument.....	49
3.2	Description of the optical elements in detail	58
3.2.1	The telescope.....	58
3.2.2	The fibers.....	61
3.2.3	The lenses.....	65
3.2.4	The grating.....	67
3.2.5	The camera.....	68
3.3	Analytical expressions for the integration time, the spectral resolution and the spatial resolution.....	69
3.4	Cost of the instrument	87
4	OBSERVATIONAL RESULTS AND ANALYSES.....	88
4.1	Observational site.....	88
4.2	Spectra observed by MACS.....	90
4.3	Identifying the individual fiber location on the corona.....	93

4.4	The telescope-spectrometer sensitivity curve	108
4.5	Application of the intensity correction factor	115
4.6	Determination of the Thermal electron temperature and the Solar wind velocity for each fiber location	116
4.7	Sources of error and error bars.....	132
4.8	Summary.....	135
5	MODIFIED CRAM'S THEORY AND ITS DEPENDENCE ON VARIOUS PARAMETERS.....	136
5.1	Modified Cram's theory.....	136
5.2	Dependence on the electron density distribution function.....	140
5.3	Dependence on the temperature profile.....	155
5.4	Dependence on the wind profile.....	158
5.5	Dependence on the numerical method.....	162
6	COMPARISON BETWEEN AND OBSERVATION AND THEORY.....	167
6.1	An unexpected phenomenon noticed in the observations.....	167
6.2	Comparison between theory and observation.....	169
6.3	Remedial measures.....	179
7	CONCLUSION.....	185
7.1	Summary of this thesis.....	185
7.2	Using a space platform.....	188

Appendix

A	THE THEORY OF FORMATION OF THE K-CORONA.....	197
A.1	The general theory of scattering of radiation by free electrons.....	197
A.2	The total power radiated per unit solid angle for the cases where the electric vector is aligned parallel and perpendicular to the scattering plane	206
A.3	Contribution due to Compton scattering.....	216
A.4	Expression for the total K-coronal scattered intensity.....	218
A.5	Expressions for the dependent variables in equation (A.78) in terms of the independent variables.....	226
A.6	Expression for the incident solar intensity on the coronal electrons....	230
A.7	Final expression for the observed intensity.....	233
B	CODE.....	235
B.1	The basic equation to be solved.....	235
B.2	Approximations to the $\int d\lambda'$ integral.....	237
B.3	$b, Q_{//}^{Ra}$ and Q_{\perp}^{Ra} in terms of the independent variables ω, φ and x	239
B.4	Rewriting the basic equation with all parameters expressed in terms of the independent variables (ω, φ, x, y)	241
B.5	Changing the independent variable $\cos\omega$ to $\cos\theta$	243
B.6	Expression for the extraterrestrial solar irradiance $f(\xi)$	247
B.7	Expressions for the limb-darkening coefficient $u_1(\xi)$	248

B.8	Expression for the coronal electron density model $N_e(\sqrt{x^2 + \rho^2} R_{\text{solar}})$	250
B.9	Expressions for the coronal temperature model $T(\sqrt{x^2 + \rho^2} R_{\text{solar}})$ and the solar wind model $W(\sqrt{x^2 + \rho^2} R_{\text{solar}})$	251
B.10	Evaluation of the integrals.....	252
B.11	The symbols used in the code.....	264
B.12	The IDL code.....	267
C	A STREAMER MODEL	276
C.1	The effects due to streamers.....	276
	REFERENCES	285

LIST OF TABLES

- 3.1 A table showing the values for the angle of diffraction, the linear dispersion, the line width and the resolvable theoretical wavelength range for three different wavelengths using the physical parameters of the optical components used in MACS. In column 3 the reciprocal linear dispersion is calculated per pixel, which is the dimension of a pixel in the CCD camera used in MACS.....**79**
- 3.2 The transmission efficiencies of the fibers, the lenses and the grating for three different wavelengths. This information is from figure (3.9), figure (3.11) and figure (3.12)..... **83**
- 3.3 The list of lenses and the associated number of surfaces through which the incident light had to pass before entering the detector..... **83**
- 3.4 The effective transmission efficiency ($\tau_{\lambda}^{\text{eff}}$) of MACS for the wavelengths 3600.0, 4000.0 and 4500.0 angstroms. The values are based on the information from tables (3.2) and (3.3)..... **84**

3.5	The K-coronal brightness at 1.1 and 1.6 solar radii for three different wavelengths during the solar maximum. The values were obtained from Allen (1973) from pages 172 and 176. The units are in ergs/sec/cm ² /angs/steradians. (1 Joule=10 ⁷ ergs).....	84
3.6	Lower limit of the integration time for the K-coronal spectrum for MACS based on equation (3.36).....	85
3.7	Cost associated with the construction of MACS.....	87
4.1	List of the emission lines reported by Athay and Orrall (1957) of a prominence from the total solar eclipse of 1952. In this paper the Sr II line at 4077.7 has been erroneously recorded as 3077.7 angstrom. In the following table only the emission lines that could lie within the wavelength range of MACS is enumerated.....	96
4.2	List of the emission lines reported by Jefferies, Smith and Smith (1959) from the flare of 18 September 1957. This table only includes those emission lines categorized as very strong and strong. Also in this following table only the emission lines that could lie within the wavelength range of MACS is enumerated.....	100
6.1	Comparison of the wind and the temperature sensitive intensity ratios between the observational and the theoretical K-coronal spectrum, for fiber #04. These values are based on figure (6.5).....	177

B.1	The dependence of the extraterrestrial solar irradiance and the limb-darkening functions with the wavelength.. The columns 1 and 4 are from section (B.6) and columns 2 and 3 are from section (B.7).....	259
B.2	Cumulative values of the columns 2,3 and 4 of table (B.1).....	260
B.3	Multiplying column 4 of table (B.2) with column 2 and 3 of table (B.2). This is the format of the table used by the code.....	260
B.4	The format of the input information on the wind velocity in km/sec, isothermal temperature in MK and the distance to the line of sight in SR.....	275

LIST OF FIGURES

1.1	The solar corona as seen during the solar eclipse of February 26, 1998. Picture: NASA eclipse library.....	1
1.2	This plot shows the variation of the E, K and F components of the solar coronal brightness with height above the solar limb.....	7
1.3	A cross section of the sun to highlight the prominent parts of it and the temperature scales between the core, photosphere and the corona. Picture: SOHO pictures library.....	9
2.1	This is a plot of the extraterrestrial solar irradiance spectrum. This was obtained by starting with the ground-based Fourier Transform Spectrometer at the McMath/Pierce Solar Telescope at Kitt Peak, Arizona, and then correcting for wavelength-dependent absorption in the Earth's atmosphere.....	19
2.2	The photospheric radiation is emitted from a point S on the surface of the sun. The electrons at point P in the corona scatter some of the incident radiation towards a terrestrial observer at E, which is known as K-coronal radiation.....	23

2.3	This plot shows the modeled K-coronal intensity spectra against wavelength. The composite plots are for different isothermal temperatures assumed for the solar corona for a given line of sight at 1.1 solar radii.....	24
2.4	Modeled K-coronal intensity spectrum against wavelength for different isothermal coronal temperatures for a given line of sight at 1.3 solar radii.....	25
2.5	Modeled K-coronal intensity spectrum against wavelength for different isothermal coronal temperatures for a given line of sight at 1.5 solar radii.....	26
2.6	This is a plot of the K-coronal intensity ratios at 3850.0 to 4100.0 angstroms against the assumed isothermal coronal temperatures. The ratios were calculated from the modeled K-coronal spectra for different temperatures shown in figure (2.3). These values pertain to a line of sight at 1.1 solar radii.....	27
2.7	An input intensity spectrum containing an absorption line centered at 4000.0 angstrom with a FWHM of 40.0 angstrom in an otherwise uniform continuum.....	29
2.8	The theoretical scattered intensity spectrum by the coronal electrons for an input spectrum given by figure (2.7). The theory assumes an isothermal corona. The plots show that the smearing of the absorption line in the scattered increases with increasing temperatures.....	30

2.9	An input intensity spectrum containing two absorption lines centered at 4000.0 and 4500.0 angstroms with a FWHM of 40.0 angstrom in an otherwise uniform continuum.....	31
2.10	The theoretical scattered intensity spectrum by the coronal electrons for an input spectrum given by figure (2.9). The theory assumes an isothermal corona. The difference in the depths of the absorption lines in the scattered spectrum is due to the wavelength dependent limb-darkening coefficient.....	32
2.11	An input intensity spectrum consisting of two absorption lines centered at 4000.0 and 4500.0 angstroms while an emission line centered at 4250.0 angstrom and with a FWHM of 40.0 angstrom for the absorption and emission lines in an otherwise uniform continuum.....	33
2.12	The theoretical scattered intensity spectrum by the coronal electrons for an input spectrum given by figure (2.11). The theory assumes an isothermal corona. The difference in the depths of the absorption lines in the scattered spectrum is due to the wavelength dependent limb-darkening coefficient.....	34

2.13	This figure shows the theoretical K-coronal intensity spectra for four isothermal coronal temperatures whose electron density is given by equation (5.8). The absolute intensity of the disk center photospheric spectrum is also shown. The vertical bars at the bottom of the figure indicate the relative strengths of the three coronal lines “c”, and nine flash spectrum lines “f”. Reproduced from Cram (1976).....	37
2.14	This is a schematic drawing to illustrate the redshifting of the photospheric radiation scattered off the coronal electrons, which are radially flowing away from the sun at a uniform velocity (w). Electron 2 is located at the closest point on the line of sight to the center of the sun. Electrons 1 and 3 are located symmetrically on either sides of electron 2.....	39
2.15	This figure shows the scale of the thermal Doppler broadening and the redshift associated with the solar wind velocity in the wavelength scale in comparison to the features of the photospheric spectrum. The scale of the redshift is shown by a red dot, which is highlighted by a circle. This comparison is made for an incident wavelength of 4000.0 angstrom on the coronal electrons, which are radially outflowing at a velocity of 300.0 km/sec in a million degree Kelvin corona.....	40
2.16	Modeled K-coronal intensity against wavelength for different isothermal coronal temperatures, for line of sight at 1.1 solar radii and a wind velocity of 400.0 km/sec.....	41

2.17	Modeled K-coronal intensity against wavelength for different isothermal coronal temperatures, for line of sight at 1.1 solar radii and a wind velocity of 800.0 km/sec.....	42
2.18	Modeled K-coronal intensity against wavelength for solar wind velocities of 0.0 km/sec to 900.0 km/sec in intervals of 100.0 km/sec, for line of sight at 1.1 solar radii and an isothermal coronal temperature of 1.0 MK.....	43
2.19	The intensity ratio at 3850.0 to 4100.0 angstroms against isothermal coronal temperatures for a range of solar wind velocities with the line of sight at 1.1 solar radii. The horizontal spread in the low end of the temperature scale is ~0.02 MK over the velocity range of 0.0 km/sec to 900.0 km/sec.....	45
2.20	The intensity ratio at 3987.0 to 4233.0 angstroms against solar wind velocities for a range of isothermal coronal temperatures with the line of sight at 1.1 solar radii. To determine the wind velocity, first the temperature has to be determined from figure (2.19). Then the K-coronal models need to be created for a range of wind velocities at this temperature and plotted in figure (2.20).....	46
3.1	Meade 12-inch, F/10.0 Schmidt-Cassegrain telescope with auto tracking capabilities.....	51
3.2	F/6.3 focal reducer reduces the focal length by a factor of 0.63. The device shown in figure (3.4) was placed at the focal plane behind the F/6.3 focal reducer.....	52

3.3	A drawing depicting the location of the fiber tips on the image plane of the telescope. The inner and outer rings are at 1.1 and 1.5 solar radii, respectively. During the eclipse the lunar shadow replaces the sun.....	53
3.4	The glass plate imbedded with twenty-one fibers. The inner and the outer circles are located at 1.1 and 1.5 solar radii, respectively, on the image plane of the sun. The fiber at the center was to record the background signal during the eclipse.....	54
3.5	This is a picture of the spectrograph. The coronal light was fed into the spectrograph by twenty-one fibers that were vertically arranged at a regular spacing. Its location in the spectrograph was at the focal point of the collimating lens.....	55
3.6	This is a picture of the inside of the spectrograph between the grating and the camera lens. Baffling were used to prevent all orders but the first order from entering into the camera lens.....	56
3.7	This is a picture of the thermoelectrically cooled CCD camera used in the experiment. The front end housed the camera lens that focused the dispersed light from the grating on to the camera.....	57
3.8	Schematic drawing on the image formation by the primary mirror of the telescope.....	59
3.9	Transmission efficiency of the fibers used in MACS and marked as UV/VIS. The region of wavelength interest in MACS was from 3500.0 –4500.0 angstroms.....	62

3.10	Schematic diagram depicting the light ray path at the focal plane of the telescope into a fiber optic cable.....	63
3.11	Reflection properties for the anti UV-reflective coating on the collimating and the camera lenses used in the spectrograph.....	66
3.12	Transmission properties at normal incidence for the anti UV-reflection coating on the transmission grating. Here the back surface reflection is not considered. The substrate material is fused silica. The black squares pertain to the grating used in MACS.....	67
3.13	Quantum efficiency (QE) curve for the back thinned SITE 512.0×512.0, 24.0μm square chip used in MACS. This chip also featured a full well depth in excess of 300,000.0 electrons, a dynamic range of ~ 90.0 dB and a readout time of ~ 5.0 seconds with an ISA card.....	68
3.14	Schematic diagrams of the optical components that make up MACS and the parameters that determine the spatial and the spectral resolutions.....	69
3.15	Schematic diagram showing the projected width and height of a single fiber on the camera plane.....	71
3.16	Schematic diagram of the dispersing element showing the angular and the linear dispersions.....	72
3.17	Schematic layout of the slit spectrometer. In this diagram collimated light is incident on the grating.....	73
3.18	Schematic diagrams showing the diffraction limited spectral resolution and the resolving power.....	76

4.1	A photograph of the August 1999 eclipse from the Black Sea area. The photograph also reveals a detached prominence eruption above the southwest limb.....	89
4.2	A map showing the path of the eclipse over Turkey. Courtesy: NASA Reference Publication 1398.....	89
4.3	A picture showing the layout of MACS and the telescope. The telescope is on a polar mount and MACS is laid out on the metal box.....	90
4.4	The spectra from twenty-one fibers exposed to the sky while four other fibers exposed to the mercury calibration lamp in Elazig, Turkey.....	91
4.5	The coronal spectra recorded by MACS for the exposure times 4.0, 8.0 and 83.0 seconds, respectively. Each vertical line corresponds to a spectrum from a single fiber. It is also clear that five of the fibers show emission lines...	93
4.6	This picture shows the envisaged location of the twenty-one fibers in the focal plane during the eclipse. The inner and the outer rings correspond to 1.1 and 1.5 solar radii, respectively. The picture is not the actual eclipse on 11 August 1999. The fiber in the center was expected to record the background signal.....	94
4.7	The spectrum recorded by the fiber #19 in the 4.0 seconds exposure. The emission lines and their corresponding wavelengths and pixel positions are identified.....	97
4.8	The regression fit between the emission line peaks and the peak positions of the fiber #19 in the 4.0 seconds exposure. The table incorporated shows the wavelength scale between any two-emission lines.....	98

4.9	The spectrum recorded by the fiber #20 in the 4.0 seconds exposure. This too matches with all the emission lines recorded by the fiber #19 as shown in figure (4.7).....	99
4.10	The spectrum recorded by the fiber #22 in the 4.0 seconds exposure. The emission lines and their corresponding wavelengths and pixel positions are identified.....	101
4.11	The regression fit between the emission line peaks and the peak positions of the fiber #19 in the 4.0 seconds exposure. The table incorporated shows the wavelength scale between any two-emission lines.....	102
4.12	This is a comparison between solar image by SOHO in 304.0 angstrom at 11:14 UT and an eclipse photograph taken from the Black Sea at ~ 11:16UT. The orientation was made by matching the prominence eruption ~ 68 ⁰ southwest in the SOHO image. The orientation of the polar axis of the sun with respect to the polar axis of the earth was obtained from the p-angle data given in, ‘The Astronomical Almanac 1999’ for 11 August 1999.....	104
4.13	Images of the sun taken by the LASCO instrument on SOHO on the 11 August 1999. The numbers denote the time in UT. C2 and C3 are coronal images of the sun from 2.0 – 6.0 solar radii and 3.7 – 32.0 solar radii, respectively, using an externally occulted disk.....	105
4.14	Images of the sun taken by the EIT instrument on SOHO on the 11 August 1999. The numbers denote the time in UT.....	106

4.15	Images of the sun taken by the radiograph in Nancy, France and the x-ray telescope on Yohkoh on the 11 August 1999.....	107
4.16	Plots of the sky spectrum recorded by fiber #06 in Elazig, Turkey before and after correcting for Rayleigh scattering. The plots have been normalized at 3968.5 Angstrom.....	109
4.17	Plots of the extraterrestrial photospheric intensity spectrum and the terrestrial photospheric intensity spectrum recorded by fiber #06. The extraterrestrial photospheric spectrum is a smoothed version of the extraterrestrial photospheric spectrum shown in figure (2.1).....	110
4.18	Plots of the smoothed extraterrestrial photospheric intensity spectrum and the terrestrial photospheric intensity spectrum recorded by fiber #06.....	111
4.19	Plots of the smoothed extraterrestrial photospheric intensity spectrum, terrestrial photospheric intensity spectrum recorded by fiber #06 and the ratio between these two against wavelength.....	112
4.20	Polynomial fit made to the ratio between the extraterrestrial photospheric spectrum and the terrestrial photospheric intensity spectrum. The numbers on the plot are the coefficients of the polynomial fit.....	113
4.21	Application of the polynomial fit shown in figure (4.20) to the terrestrial photospheric intensity spectrum to obtain the extraterrestrial photospheric intensity. Also plotted for comparison purpose is the smoothed extraterrestrial photospheric intensity spectrum as shown in figure (4.18).....	114

4.22	These plots show the coronal spectra recorded by the twenty-one fibers located at various latitudes and heights on the corona as depicted in figure (4.12). Fiber #23 was centered on the moon. The above spectra were recorded in the 18.0 seconds exposure. The x-coordinate is in pixel units.....	117
4.23	The coronal spectrum recorded by fiber #06.....	119
4.24	The terrestrial K-coronal spectrum reduced from the coronal spectrum recorded by fiber #06.....	120
4.25	This plot shows the extraterrestrial K-coronal spectrum derived for fiber #06. The wind and the temperature sensitive intensity ratios are 1.245 and 1.488, respectively.....	121
4.26	The temperature sensitive plot. This assigns a thermal electron temperature of ~1.73 MK for fiber #06.....	122
4.27	The wind sensitive plot. This assigns a solar wind velocity of ~467.0 km/sec for fiber #06.....	122
4.28	The temperature sensitive plot. This assigns a thermal electron temperature of ~1.29 MK for fiber #04.....	123
4.29	The wind sensitive plot. This assigns a solar wind velocity of ~300.0 km/sec for fiber #04.....	123
4.30	This plot shows the extraterrestrial K-coronal spectrum for fiber #10. The wind and the temperature sensitive intensity ratios are 1.248 and 1.524, respectively.....	124

4.31	The temperature sensitive plot. This assigns a thermal electron temperature of ~1.34 MK for fiber #10.....	125
4.32	The wind sensitive plot. This assigns a solar wind velocity of ~571.0 km/sec for fiber #10.....	125
4.33	This plot shows the terrestrial coronal spectrum recorded by fiber #14. The continuum is a measure of the terrestrial F+K corona. The E-corona is removed by making Gaussian fits of the form given in equation (4.1) to the individual emission lines and fitting the background given by equation (4.2) to the continuum.....	126
4.34	This plot shows the extraterrestrial K-coronal spectrum for fiber #14. This is following the elimination of the E-corona from figure (4.33).....	127
4.35	The temperature sensitive plot. This assigns a thermal electron temperature of ~0.73 MK for fiber #14.....	128
4.36	The wind sensitive plot. This assigns a solar wind velocity of ~819.0 km/sec for fiber #14.....	128
4.37	Plot showing the variation in the temperature-sensitive intensity ratio, from the theoretical models without streamers, for a streamer of geometry described in Appendix-C and density enhanced by a factor of 50.0 together with various streamer inclinations in front and behind the solar limb.....	129

4.38	<p>The thermal electron temperature and the solar wind velocity determined for solar coronal locations observed by fibers #04, 06, 08, 10, 12, 14 & 22 that are located at 1.1 solar radii and fiber #15 & 17 located at 1.5 solar radii. These values are based on the theoretical models. The temperature and the wind velocity are measured in MK and km/sec, respectively. However the wind measurements seem too far high. In this regard it is acknowledged that the experiment was not successful in measuring the wind velocities and the absolute values should be disregarded.....</p>	131
4.39	<p>The spectrum recorded by fiber #23, which was centered on the lunar shadow during the eclipse. Its purpose was to measure the background counts.....</p>	132
5.1	<p>This is a schematic diagram showing the mathematical description of the scattering phenomenon where the photospheric radiation from the sun is scattered by the free electrons lying along the line of sight of an observer. The line of sight is at a distance (ρ) from the center of the sun.....</p>	137
5.2	<p>A plot showing the solar radial log-intensity variation as a function of solar radii (r) from the center of the sun. The solid curve represents the measurements by November and Koutchmy (1996) while the dashed curve represents the measurements by Baumbach (1937) based on several eclipses observations.....</p>	142

5.3	A plot showing the log of the electron density variation as a function of the solar radii (r) from the center of the sun. The solid curve represents the calculations by November and Koutchmy (1996) while the dashed curve represents the calculations by Baumbach (1937) based on several eclipses observations.....	143
5.4	A photograph of the solar corona during the total solar eclipse of 11 August 1999 where the sun was approaching the maximum phase. Here the corona is uniformly bright and circular in shape.....	144
5.5	A photograph of the solar corona during the total solar eclipse of 4 November 1994 where the sun was approaching the minimum phase. Here the corona is elongated in the equatorial regions and brighter than the polar regions.....	144
5.6	A series of plots showing the radial dependence of the mean electron density in coronal holes computed from various sets of polarization brightness data. This plot was obtained from Cranmer et al. (1999).....	148
5.7	A plot showing the electron densities for the north (solid line) and south polar coronal holes (dashed line) and the north (dotted line) and south (dot-dashed line) polar coronal rays as a function of height. Reproduced from Fisher and Guhathakurta (1995).....	151

5.8	A comparison of the electron number density functions based on the models by Baumbach (1937, equation (5.7)), Ichimoto et al. (1996, equation (5.8)), Newkirk (1961, equation (5.9)), Cranmer et al. (1999, equation (5.10)) and Guhathakurta and Holzer (1994, equation (5.12)).....	152
5.9	Plots of the theoretical K-coronal intensity spectra based on the electron number density functions given by Baumbach (1937, equation (5.7)), Ichimoto et al. (1996, equation (5.8)), Newkirk (1961, equation (5.9)), Cranmer et al. (1999, equation (5.10)) and Guhathakurta and Holzer (1994, equation (5.12)) and the line of sight at 2.0 solar radii from the center of the sun. The curves have been normalized at 4000.0 angstrom.....	153
5.10	Plots of the theoretical K-coronal intensity spectra based on the electron number density functions given by Baumbach (1937, equation (5.7)), Ichimoto et al. (1996, equation (5.8)), Newkirk (1961, equation (5.9)), Cranmer et al. (1999, equation (5.10)) and Guhathakurta and Holzer (1994, equation (5.12)) and the line of sight at 1.1 solar radii from the center of the sun. The curves have been normalized at 4000.0 angstrom....	154
5.11	This is a plot of the temperature profile along the line of sight at 1.3 solar radii based on the assumption of a conductive corona Chapman (1957). The temperature at the point of intersection of the line of sight and the plane of the solar limb is 1.0 MK.....	156

5.12	<p>This is a plot of the modeled K-coronal intensity spectra for an isothermal corona of 1.0 MK and a model with the temperature profiles given by $T(r) = 1.0 \times (1.3/r)^{2/7}$ and $T(r) = 1.0 + (1.0 + 9.0 * (r - 1.75)^2)^{-1}$. Here (r) is the distance between the center and points along the line of sight 1.3 solar radii. The temperature at the point of intersection of the line of sight and the plane of the solar limb is 1.0 MK.....</p>	157
5.13	<p>Coronal wind profile based on the Parker model for an isothermal corona. In the ideal solution the velocity is equal to the isothermal sound speed at the critical radius and starts with subsonic velocities at the lower boundary and reaches supersonic velocities at large distances.....</p>	159
5.14	<p>Comparison of the theoretical K-coronal intensity spectrum for an isothermal corona at 1.0 MK, zero wind velocity and line of sight at 1.5 solar radii with the intensity spectrum due to the bulk flow velocity that naturally arises with the Parker wind model for an isothermal corona as given in equation (5.14).....</p>	160
5.15	<p>Comparison between two theoretical K-coronal intensity spectra due to isothermal coronal temperatures of 1.0 and 1.5 MK and with the inclusion of the Parker wind model for an isothermal corona.....</p>	161

5.16	<p>Plot of the polarization from theoretical modeling for the formation of the K-corona, at a given isothermal coronal temperature of 1.0 MK, for lines of sight at 1.1, 1.3 and 1.5 solar radii. The behavior of the polarization conforms to the observations. That is, the polarization is almost wavelength independent and increases with coronal heights.....</p>	163
6.1	<p>The spectrum recorded by the fiber located in the center of the lunar shadow during the eclipse. The x-coordinate corresponds to wavelength scale. The two prominent peaks are associated with the Calcium K & H lines corresponding to 3933.7 and 3968.5 angstroms, respectively.....</p>	168
6.2	<p>Theoretical isothermal K-coronal models fitted to the observed K-coronal intensity spectrum to determine the temperature by Ichimoto et al. (1996). The lower curves show the differences between the observational spectrum and the theoretical models. The model that showed the least difference determined the temperature.....</p>	169

- 6.3 This plot shows the comparison between experimentally obtained K-coronal spectrum for fiber # 04 with theoretical models for various isothermal temperatures. From the intensity ratio method the wind velocity and the temperature deduced for fiber # 04 are, 300.0 km/sec and 1.29 MK, respectively. The theoretical K-coronal models plotted in figure (6.3) correspond to a wind velocity of 300.0 km/sec and isothermal coronal temperatures of 0.5MK, 1.0 MK, 1.5 MK and 2.0 MK. In such a scenario the experimentally obtained K-coronal spectrum may be expected to take a position between the theoretical models for 1.0 MK and 1.5 MK. (Expt: = Experimental, Theo: Theoretical)..... **172**
- 6.4 A plot of the superposition of figure (6.1) and figure (6.3). The shape of the spectrum recorded by the fiber located in the center of the lunar shadow corresponds with the shape of the observed K-coronal spectrum by fiber #04. The expected location of the observed spectrum is between the theoretical isothermal K-coronal spectra for 1.0 MK and 1.5 MK..... **174**
- 6.5 A plot showing the observed K-coronal spectrum for fiber #04 along with the theoretical K-coronal spectrum for the wind velocity and temperature derived from fiber #04. The plot also includes the difference between the observational and the theoretical plots along with the scattered light spectrum observed by the fiber in the center of the lunar shadow..... **175**

6.6	Plots showing the effect on the shape of the observed K-coronal spectrum of fiber # 04, as shown in figure (6.5), in comparison with the shape of the theoretical K-coronal spectrum by subtracting various fractions of the scattered spectrum from the observed K-coronal spectrum. A, B, C, D, E and F correspond to a subtraction of 0.0%, 15.0%, 10.0%, 8.0 %, 5.0% and 3.0%, respectively, of the scattered light spectrum recorded by the fiber that was located in the center of the lunar shadow from the spectrum recorded by fiber #04. These plots show that the observed spectrum closely follows the shape of the theoretical spectrum with various fractional subtraction of the scattered spectrum.....	178
6.7	The extra fibers placed in the shadow of the moon and outside the field of view in order to record the instrumental stray light distribution.....	181
6.8	A schematic diagram showing the introduction of a very thin high transmission glass surface (AB) inclined at 45° to the optical axis with a semi-reflecting coating on the side facing the fiber optic plate along with the fibers embedded on an optical flat. This alteration will enable the simultaneous imaging of the image formed on the fiber optic plate.....	184

7.1	The path envisaged for the unmanned Solar Probe Spacecraft. At the perihelion (C) and the poles the spacecraft will be four and eight solar radii, respectively, from the center of the sun. The position of the spacecraft (P) is given by (r, θ) with respect to the center of the sun. In this picture the parabolic path, the detector plane and the center of the sun are in the same plane.....	188
7.2	The theoretical K-coronal intensity variation for various detector elevations for 0.0 km/sec wind velocity and the spacecraft positioned at the pole (P).....	192
7.3	The theoretical K-coronal intensity variation for various detector elevations for 400.0 km/sec wind velocity and the spacecraft positioned at the pole (P)...	192
7.4	The variation of the wind-sensitive intensity ratio against γ for various wind velocities at T=1.0 MK and the spacecraft positioned at the pole.....	193
7.5	The variation of the temperature-sensitive intensity ratio against γ for various temperatures at W=400.0 km/sec and the spacecraft positioned at the pole.....	193
7.6	Temperature-sensitive intensity ratio VS Temperature for various wind velocities at $\gamma = 0.0$ degrees and the spacecraft positioned at the pole.....	194
7.7	Wind-sensitive intensity ratio VS Wind velocity for various temperatures at $\gamma = 0.0$ degrees and the spacecraft positioned at the pole.....	194
7.8	Temperature-sensitive intensity ratio VS Temperature for various wind velocities with intensities measured through filters of fifty angstrom bandpass centered at those wavelengths for line of sight at 1.1 solar radii.....	195

7.9	Wind-sensitive intensity ratio VS Wind velocities for various temperatures with intensities measured through filters of fifty angstrom bandpass centered at those wavelengths for line of sight at 1.1 solar radii.....	196
A.1	The general coordinates where $\underline{\mathbf{r}}$ is a field point and $\underline{\mathbf{r}}'$ is a source point.....	197
A.2	The general coordinates of the incident and scattered radiation and the orientations of the parallel and the perpendicular components of the electric vectors with respect to the scattering plane.....	206
A.3	Propagation of a monochromatic plane EM waves.....	210
A.4	Coordinates for the rotational transformation of the scattering plane through an angle α about the line of sight.....	212
A.5	Geometrical configuration for the scattering of photospheric radiation by coronal electrons.....	214
A.6	Geometrical configuration for the formation of the K- Corona. Photospheric radiation emitted from a point S on the Sun is scattered from an electron E towards an observer O. The solar wind on the electron is radial and blows in the direction CE.....	215
A.7	Scattering of radiation off an electron also known as Compton scattering.....	216
A.8	Construction to obtain an expression for the scattered intensity in the rest frame of the observer. Consider a coronal electron with velocity $\underline{\mathbf{u}}$ subjected to radial solar wind velocity $\underline{\mathbf{w}}$ in a coordinate system where the x-axis bisects the supplement of the scattering angle.....	219
A.9	Highlighted map of the radial and the scattering planes of figure (A.6).....	226

A.10	Highlight of the spherical triangle formed by EDJI in figure (A.6).....	228
A.11	Highlight of the triangle ESC of figure (A.6).....	229
B.1	The plot of extraterrestrial solar irradiance VS wavelength obtained with a Fourier Transform Spectrometer at the McMath/Pierce Solar Telescope on Kitt Peak, Arizona.....	247
B.2	The plot of limb-darkening coefficient versus wavelength with linear approximation super imposed.....	248
B.3	The plot of electron number density versus the radial distance from the solar surface for the two models given by equation (B.31) and equation (B.32).....	251
B.4	Illustrating the integration procedure of the first integral in equation (B.44)...	261
B.5	Plot of the cumulative y-axis values of figure (B.4) against the wavelength η'	262
C.1	Model streamer of thickness d in front of the solar limb with an electron density enhancement by a factor f_s and thermal electron temperature T_s	277
C.2	Plot to show the effect of streamers on the K-coronal spectrum with d=0.5 SR, $f_s=4.0$, $T_s=T=1.0$ MK and at angles $\epsilon=-45.0$ and $+45.0$ degrees.....	280
C.3	Model streamers of similar dimensions at -45.0 and $+45.0$ degrees above and below the plane of the solar limb, respectively.....	281
C.4	Plot to show the effect of streamers on the K-coronal spectrum with d=0.5 SR, $f_s=4.0$, $T_s=T=1.0$ MK and spread over various angles ϵ	282

C.5	Effects by streamers on the ratio $I(4233)/I(3987)$ for $W=400$ km/sec and $\rho=1.1$ SR. The horizontal lines show the intensity ratio for a given solar wind velocity of 400.0 km/sec and line of sight at 1.1 solar radii, and for different isothermal coronal temperature in the absence of streamers.....	283
C.6	Effects by streamers on the ratio $I(4100)/I(3850)$ for $W=400$ km/sec and $\rho=1.1$ SR. The horizontal lines show the intensity ratio for a given solar wind velocity of 400.0 km/sec and line of sight at 1.1 solar radii, and for different isothermal coronal temperature in the absence of streamers.....	284

Abstract

The determination of the radial and latitudinal temperature and wind profiles of the solar corona is of great importance in understanding the coronal heating mechanism and the dynamics of coronal expansion. Cram (1976) presented the theory for the formation of the K-coronal spectrum and identified two important observations. He observed the existence of temperature sensitive anti-nodes at certain wavelengths in the theoretical K-coronal spectra. The anti-nodes are separated by temperature-insensitive nodes. Remarkably, Cram showed that the wavelengths of the nodes and anti-nodes are almost independent of altitude above the solar limb. Because of these features, Cram suggested that the intensity ratios at two anti-nodes could be used as a diagnostic of the electron temperature in the K-corona. Based on this temperature diagnostic technique prescribed by Cram a slit-based spectroscopic study was performed by Ichimoto et.al (1996) on the solar corona in conjunction with the total solar eclipse of 3 November 1994 in Putre, Chile to determine the temperature profile of the solar corona. In this thesis Cram's theory has been extended to incorporate the role of the solar wind in the formation of the K-corona, and we have identified both temperature and wind sensitive intensity ratios. The instrument, MACS, for Multi Aperture Coronal Spectrometer, a fiber optic based spectrograph, was designed for global and simultaneous measurement of the

thermal electron temperature and the solar wind velocity in the solar corona. The first ever experiment of this nature was conducted in conjunction with the total solar eclipse of 11 August 1999 in Elazig, Turkey. In this instrument one end of each of twenty fiber optic tips were positioned in the focal plane of the telescope in such a way that we could observe conditions simultaneously at many different latitudes and two different radial distances in the solar corona. The other ends of the fibers were vertically aligned and placed at the primary focus of the collimating lens of the spectrograph to obtain simultaneous and global spectra on the solar corona. By isolating the K-coronal spectrum from the spectrum recorded by each fiber the temperature and the wind sensitive intensity ratios were calculated to obtain simultaneous and global measurements of the thermal electron temperature and the solar wind velocity. We were successful in obtaining reliable estimates of the coronal temperature at many positions in the corona. This is the first time that simultaneous measurements of coronal temperatures have been obtained at so many points. However due to instrumental scattering encountered during observations, reliable estimates of the wind velocity turned out to be impossible to obtain. Although remedial measures were taken prior to observation, this task proved to be difficult owing to the inability to replicate the conditions expected during an eclipse in the laboratory. The full extent of the instrumental scattering was apparent only when we analyzed the observational sequence. Nevertheless the experience obtained from this very first attempt to simultaneously and globally measure both the wind velocity and the temperature on the solar corona have provided valuable information to conduct any future observations successfully.

Chapter 1

INTRODUCTION

1.1 Introduction to the solar corona

The solar corona is the region which begins at an altitude of ~2000 km above the solar photosphere, and then extends out to many solar radii. This region becomes visible to the naked eye during a solar eclipse as seen in figure (1.1).

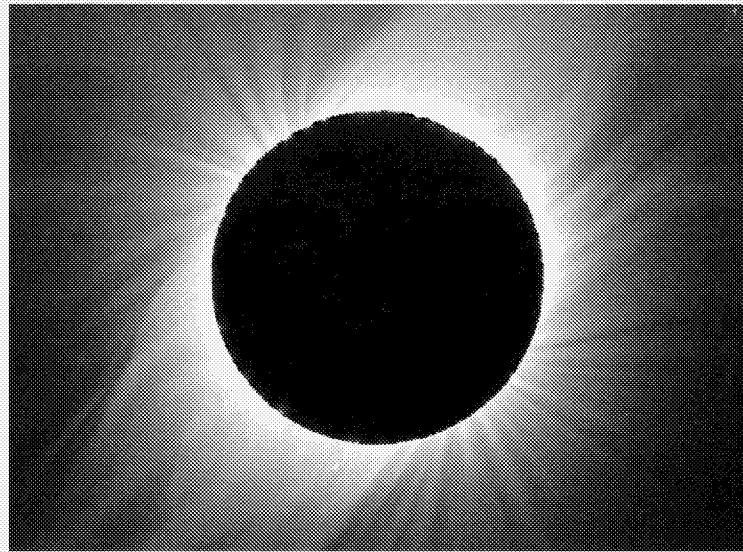


Figure (1.1). The solar corona as seen during the solar eclipse of February 26, 1998. Picture: NASA eclipse library

Accounts of solar eclipses date back to at least the fourteenth century BC. However it is not clear that the solar corona was ever mentioned. The first clear mention of the corona was from Kepler in his *Astronomiae pars Optica*, although he seemed to have attributed the corona to be a property of the moon. With the advent of photographic methods and spectroscopy in the nineteenth century experimental studies were initiated on the nature of the sun during eclipses. By then eclipse path predictions were also possible. Edmond Halley was the first to predict the path of an eclipse in 1715 using the Newton's law of gravity.

At the 1860 solar eclipse, comparisons of photographs by De la Rue and Secchi from different locations confirmed that prominences were solar in nature. Prominences are cloud-like features with a reddish color, often seen during solar eclipses off the sun's limb. This confirmation also added weight to the fact the corona too was solar in nature.

Further discoveries followed with each subsequent solar eclipse. In the solar eclipse of 1871, Janssen discovered and identified absorption features in the solar spectrum. In 1814, Fraunhofer had been the first to label certain absorption features in the spectrum of the sun, and Janssen was able to identify some of Fraunhofer's lines in the coronal spectrum. Most of the Fraunhofer features in the solar spectrum are atomic lines that are formed in the solar photosphere, although some are caused by molecules in the earth's atmosphere. Janssen's discovery of the solar absorption lines in the coronal spectrum confirmed that the corona was also solar in nature.

At the same eclipse of 1871, through spectroscopic observations Lockyer showed that the coronal gases extended $\sim 500,000$ km above the solar limb. This observation provided the first clue that the corona was also very hot. Later observations have showed that the corona extended to over thirty solar radii above the solar limb. Because of this great spatial extent, it can be inferred that the coronal gas is very hot. As to how hot the gas actually is, we look to the coronal spectrum for an answer: this is a major aim of the present work. However it was already known in 1957 (from work of E.N. Parker) that the coronal temperature is so high that it has important dynamical effects. To see this, we note that the extended nature of the solar corona is a result of a competition between gravity and gas pressure: the radial gradient of gas pressure tends to force material away from the sun, whereas gravity tends to hold the material back. In the inner corona, within one or two solar radii of the surface, these opposing tendencies balance each other almost exactly. However, beyond a few solar radii, Parker (1965) showed that gravity loses the competition, and the corona accelerates away from the sun to form the solar wind. Spacecraft measurements of the wind flux show that if the corona were not continually re-supplied with material, the wind would empty the corona in a time-scale of a few days.

With the dawn of the spectroscopic age it was now possible to identify the elements present in hot gases through spectrum analyses. Hot gases emit photons at wavelengths, which are precisely characteristic of the elements present in the gases. However the coronal spectrum posed a great problem because most of the wavelengths could not be identified with known elements on Earth. Edlen (1937) identified some of

the emission lines as originating in **forbidden transitions** of the element iron in highly stripped stages of ionization, FeX and FeXIV. Forbidden transitions are those which are not allowed by electric dipole selection rules: the transitions must be induced by magnetic dipole or electric quadrupole interactions. For iron to be in the ionization stages FeX or FeXIV requires that the electron temperature in the coronal gas be at least 1.0 MK. For the forbidden transitions to occur, the ambient gas must have densities that are lower than a certain value. The upper limit of the density depends on the details of the transition. Golub and Pasachoff (1997) give a very detailed account of the history that led to the discovery of the solar corona and its properties.

Figure (1.1) shows the solar corona during an eclipse. It is also evident from this picture that the coronal intensity peaks around the solar equator and gradually diminishes as it approaches the solar poles. Due to the reduced coronal intensity around the solar poles, these regions are called **coronal holes**. Although the coronal light intensity is small in these holes compared to the equatorial region, the holes are also the region for the **fast solar wind**. Figure (1.1) also shows solar plumes that radiate out from the north pole and south pole of the sun tracing its magnetic field.

In the solar wind, material consisting of protons, electrons and a mixture of heavy elements flow out from the sun into interplanetary space. This ionized flow is so highly conducting that it drags along the magnetic field from the sun. The spatial extent of the solar wind is unknown: eventually, the wind runs into the interstellar medium and is

terminated at a shock. Spacecraft has not yet located the termination shock of the solar wind, but estimates put it at a distance of order 100 AU from the sun.

In essence the solar corona is an extremely hot ($>$ million Kelvin), highly ionized gas surrounding the sun. This is visible only during a total solar eclipse as a white light region extending to several solar radii, displaying streamers, plumes and loops. Its appearance changes during the solar cycle. At solar maximum it consists of many structures around the disk, but at the solar minimum it is dominated by large coronal holes at each pole and sheet-like structure near the equator.

The brightness of the solar corona surrounding the solar disk is composed of three main components, namely;

a. K- (*Kontinuierlich*) corona: The K-corona is due to the scattering of the photospheric light incident on the rapidly moving free electrons in the solar corona. The free electrons are a result of the electrons stripped off the coronal gas elements due to extremely hot temperature in the corona. Due to the high thermal velocity of these electrons they tend to broaden the photospheric spectrum, which consists of narrow lines, giving rise to a continuous spectrum. This scattering process is commonly known as Thomson scattering.

- b. E- (*Emission*) corona:** The E-corona is due to the emission from coronal ions, especially in highly ionized states. These emission lines are in many cases forbidden transitions resulting from atomic transitions from the highly ionized ions in the corona. Although these transitions are difficult to replicate in laboratories, however, they are not over ruled by selection rules for atomic transitions.
- c. F- (*Fraunhofer*) corona:** The F-corona is due to photospheric light being scattered by dust particles in interplanetary space. Dust particles which are refractory enough to be able to survive at radial distances of a few solar radii also emit radiation in the near and mid-infrared wavelength regimes. The F-corona dominates the visible coronal brightness from about three solar radii distance from the center of the sun and has an increasing contribution to the total coronal brightness at longer wavelength.

Figure (1.2) shows the radial brightness distribution of the F-corona, the K-corona and the E-corona. From figure (1.2) it is evident that the K-corona dominates in the coronal brightness to a height of ~ 2.0 solar radii above the limb and the F-corona begins to dominate beyond that height.

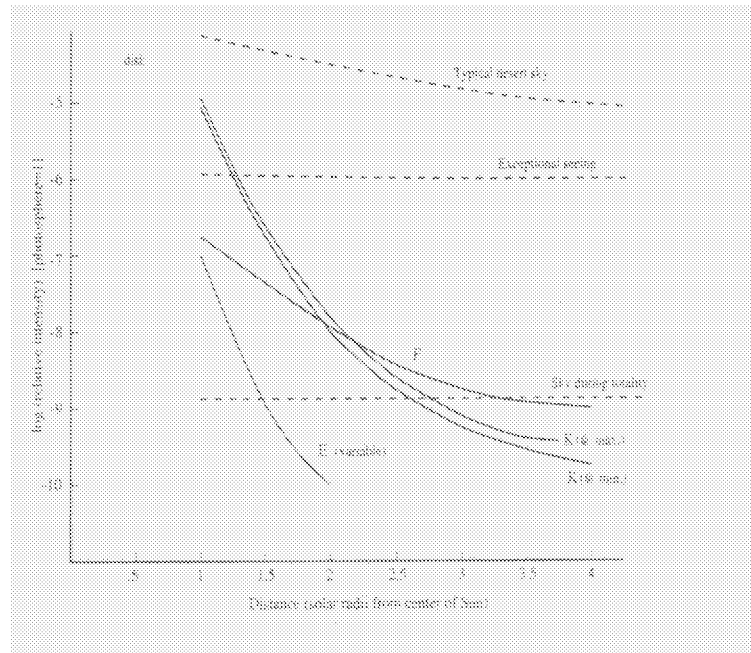


Figure (1.2). This plot shows the variation of the E, K and F components of the solar coronal brightness with height above the solar limb.

As for the reason for the existence of the solar corona there does not exist a firm answer. Observations of other stars have revealed that many stars have coronae and many others do not. Empirically, the solar corona is densest and hottest in regions of closed magnetic fields (“loops”), and is coolest and fastest moving in regions of open fields (“coronal holes”). These results indicate that magnetic fields play an important role in the coronal heating process.

Figure (1.3) shows a cross section of the sun with some of its prominent features and the temperature scales between the core, photosphere and the corona. The **core** is the innermost part of the sun where energy is generated by nuclear reactions and its temperature is $\sim 15,000,000$ K. The **photosphere** is the visible surface of the sun and also the layer which emits the light the human eye sees. Its temperature is $\sim 6,000$ K. The **corona** is the outer most layer in the solar atmosphere and consists of highly rarefied gas. This layer begins at altitudes of about ~ 2000 km above the photosphere and its temperature is $\sim 1,000,000$ K. The corona is visible to the naked eye only during a solar eclipse. The region between the photosphere and the corona is the **chromosphere**. The region demarcating the chromosphere and the corona is the **transition region** that features a sharp temperature rise from $\sim 10^4$ K to $\sim 10^6$ K within a range of ~ 500 km. The coronal **streamers** are large-scale magnetic structures in the corona.

From the point of view of physics, the most interesting aspect of the corona is the huge increase in temperature that occurs as we move from the photosphere (~ 6000 K) up into the corona (~ 1.0 MK). Now, coronal material must be replenished every few days (due to the solar wind): the only source of this material is the photospheric gas. Therefore, the creation of the corona is a continual process that involves heating the 6000 K gas to several million K. It is impossible for a thermal process, i.e. one based on solely on exchange of internal energy, to do this. Therefore, a variety of non-thermal processes have been considered in the literature (Narain and Ulmschneider, 1996). The energy

budget of the corona is not very demanding. Of the total energy flow through the solar surface, one part in 10^5 suffices to heat the corona (Tsuneta, 1996).

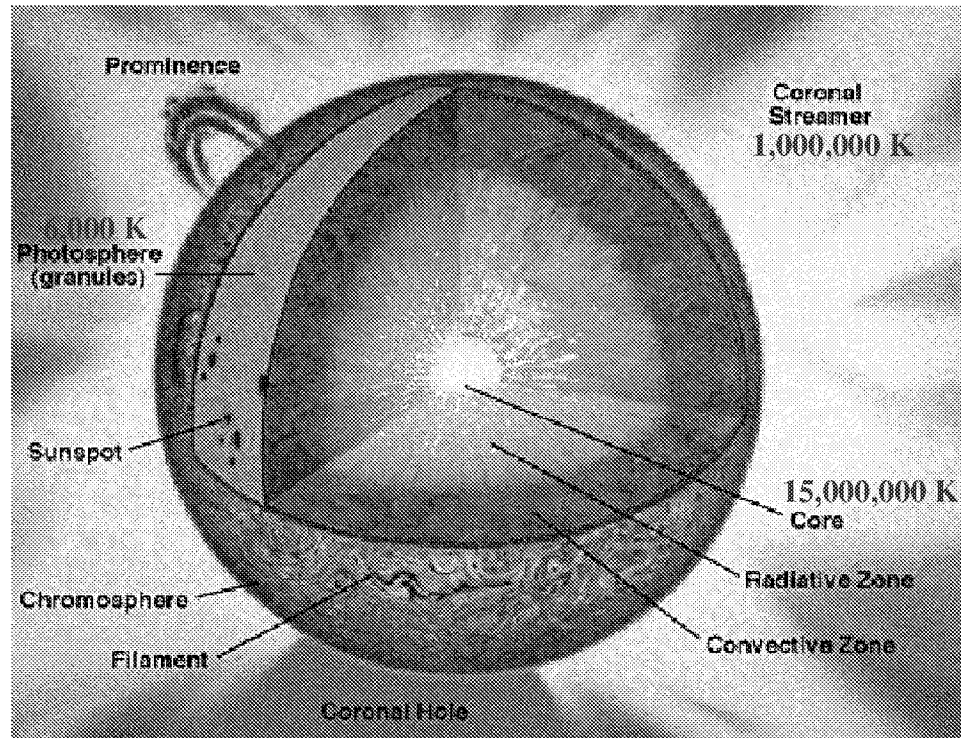


**Figure (1.3). A cross section of the sun to highlight the prominent parts of it and the temperature scales between the core, photosphere and the corona.
Picture: SOHO pictures library**

The most likely source of non-thermal energy input to the solar corona is associated with disturbances generated in the solar convective layers, as shown in figure (1.3). These disturbances in the solar interior are manifested as supergranulations, granulations, magnetic flux tubes, and wave motions on the solar photosphere and acoustic energy above the photosphere. Now the question is to determine, which of these

energy forms can propagate upwards and then dissipate in the solar corona. However this process is further compounded by the need for the widely differing power requirements for the different coronal structures. The following are some of the popular method of non-thermal energy deposition in the solar corona.

The most favored candidates are the Ohmic dissipation of the coronal electric currents and the viscous dissipation of magnetohydrodynamic (MHD) waves and turbulence (Narain and Ulmschneider 1990). The coronal electric currents are believed to be generated by the twisting of the magnetic flux tubes and, depending on the resistivity of the coronal plasma, dissipate through Joule heating in the coronal plasma. The MHD disturbances are believed to propagate along the magnetic fields protruding from the solar surface into the solar corona and dissipate their energy. These MHD waves can be visualized as a combination of the longitudinal sound waves and the transverse Alfvén waves. Alfvén waves are waves generated by the disturbance of the magnetic field lines and the sound waves could be produced by pressure perturbation. See Zirker (1993) for a survey of coronal heating theories, and conditions a successful theory must satisfy.

The sun is also occasionally the site of transient releases of energy in the form of flares. These events emit high-energy particles and shock waves that may create aurorae on the earth. Although the reason for the solar wind is well understood to be driven by gas pressure due to the high temperature of the gas, however, the driving mechanism that

causes the solar wind flow velocity to change from subsonic velocities to supersonic velocities during its flow in the solar corona is yet to be established. The first analytical treatment of the solar wind model is due to Parker (1965). It was based on a thermally driven wind model. However the large velocities predicted at 1.0 AU do not seem to match the physical parameters at the coronal base. Here again the treatment of the solar wind as a purely thermally driven wind cannot produce the experimentally observed high velocities for the solar wind and some form of other non-thermal energy deposition mechanisms are needed to describe its transformation into supersonic velocities. Solar Wind Nine (1998) and the references therein give a summary of the present situation.

Since the corona itself does not contain any heat sources that could possibly heat the corona to above million degrees or drive the solar wind flow to supersonic velocities the possibilities need to be linked to various phenomena on the solar surface itself. And, as a natural consequence to link various solar surface phenomena with the properties of the solar corona it is important to measure the coronal properties as accurately as possible. In this regard two of the most important physical parameters on the solar corona are the temperature and the solar wind velocity at different latitudes and radii in the solar corona. Therefore measurement of the coronal temperature and the solar wind velocity, simultaneously and globally on the solar corona, would help in gaining further insight into the state of the matter and its dynamics in the solar corona and its association with the solar surface phenomena.

The focus of this research is on the measurement of the coronal temperature and the solar wind velocity, simultaneously and globally, on the solar corona from the measurement of a single observable quantity. In section (1.2) some of the methods used by other researchers for the determination of the coronal temperature and the solar wind velocity are discussed.

1.2 Other methods to measure the solar wind velocity and the coronal temperature

The following are some of the techniques adopted in the measurement of the coronal temperature and the solar wind velocity.

- (a) Measurements of the radial intensity distribution of the white light corona (Saito 1965, Koutchmy 1971, Guhathakurta et al. 1992) allow one to derive the scale-height of electron density. This can be converted to an equivalent electron temperature if one assumes hydrostatic equilibrium.

- (b) Emission line intensities of various lines have been used to determine the temperature of coronal electrons (Gabriel 1971, Nakada et al. 1975, Tsubaki 1975, Guhathakurta et al. 1992). These emission line theories rely on the ionization balances, various excitation mechanisms and atomic constants. Some of these quantities are subject to major changes owing to new discoveries in atomic physics. Ionization balance occurs when the rate at which an ion loses electrons per second (as

a result of collisional ionization by free electrons) is balanced by the rate at which the ion gains electrons per second (as a result of recombination). The excitation mechanism that is assumed to be predominant is collisional excitation. This model is a simple two-level atom consisting of the ground level m and an excited state n . The population of the upper state is set by a balance between collisional excitation from m to n due to electron-atom collisions, and by spontaneous radiative decay from n to m via an allowed atomic transition. For the coronal conditions the induced emission from n to m , the photoexcitation from m to n and the collisional de-excitation from impacts with electrons are considered negligible. The atomic constants that are inherent in this model are the Einstein coefficients for spontaneous emission, statistical weights of the various atomic levels, collisional excitation coefficient and the collision strength factor. The latter is a slowly varying function of the incident electron energy and involves difficult quantum mechanical calculations. In this regard we have preliminary evidence to suggest that Thomson scattering could be partly responsible for the emission lines in the EUV region using the Thomson scattering code developed as part of this dissertation work.

- (c) Hara et al. (1994) used the ratio of the soft X-ray intensities in different energy bands to determine the coronal ‘color temperature’. They used the X-ray analysis filters onboard Yohkoh to formulate a filter ratio method to determine the temperature of the quiet corona and have reported a value of 2.7 MK (Hara et al. 1992). Here photon energy ratios are determined for different filters. These are again functions of

the wavelength and temperature dependent emissivities and the response characteristics of the filters. Hara et al. (1994) and Withbroe (1988) contains reviews of coronal temperature measurements by various other groups.

(d) Withbroe et al. (1985) measured the temperature of coronal ions using the Doppler widths of emission lines. The Doppler width measures the wavelength shift due to motion of the gas responsible for the observed emission line, which could be determined by comparison with a calibration lamp for the same emission line. Here the motion is attributed to the kinetic temperature, which includes both thermal and non-thermal motions. However to isolate the thermal effect on the motion the non-thermal effects on the motion, such as motions due to turbulence and waves, have to be eliminated.

(e) Radio observational techniques have also been used to infer the temperature of coronal electrons (Zirin 1966). This method involves the radio observation of the quiet sun in determining the coronal temperature. From each level of the solar atmosphere only emission at frequencies higher than the plasma frequency may escape. Therefore, by tuning on to different frequencies the radio emission down to the region where the plasma frequency matches to the tuned frequency could be measured. This will include levels on the solar atmosphere with different temperatures too. If these temperatures are irregular the hotter regions are heavily weighted. For low optical depth the radio emission intensity is a product of the source

function and the optical depth where optical depth is a measure of how far the radiation will travel before being absorbed or scattered, which is also a function of the frequency. The radiation in the radio region is assumed to be due to free-free emission neglecting other non-thermal processes where the free-free emission is due to deceleration of an unbound electron during its passage close to an ionized atom. In addition the Planck function is assumed to represent the source function. Here again these are beset with uncertainties associated with the optical depth effects, refraction and the emission mechanisms. Furthermore, the presence of magnetic fields could produce other cut-off-frequencies associated with gyroresonance, which complicates the propagation. This reversal of the above procedure is also possible where radar signals are directed at the corona and are bounced off the layer where the plasma frequency is greater than the frequency of the incoming signal.

- (f) Doppler dimming technique has been used to measure solar wind velocity. In this technique (Strachan et al. 1993) the aim is to measure the intensity of a chromospheric line which has been resonantly scattered off coronal material. If the coronal material were to be at rest relative to the chromosphere, then the resonant scattering would be optimized, and the intensity of the scattered line would be maximized. However in the event that the coronal material has a non-zero velocity relative to the chromosphere, there is more or less significant reduction in the overlap of the line profiles in the chromosphere and corona. As a result of this mis-match between chromospheric and coronal line profiles, the efficiency of the resonant

scattering is reduced. The scattered line becomes dimmer, the larger the velocity difference between corona and chromosphere. Quantitative interpretation of an observed dimming in terms of wind velocity is subject to a number of uncertainties: among these are the emission mechanism of the line, and the associated atomic constants.

- (g) Solar wind velocities have also been measured using remote sensing techniques. Here a known radio signal is made to propagate through the solar corona and through the detection of fluctuations in various properties of the radio signal is utilized to determine the motions of density inhomogeneities in the solar corona. For these remote sensing techniques, a variety of methods are available, depending on whether the distant source is a natural source (broadband) or artificial (narrow-band). The fluctuations which the solar corona creates in intensity or in phase or in frequency or in line-width contain information on coronal density inhomogeneities on a broad variety of length scales, from a few kilometers up to tens of thousands of kilometers (Yakovlev and Mullan 1996). Observations can also be made from widely spaced ground stations or from single stations (Coles et al. 1986, Watanabe & Schwenn 1989, Efimov 1994). Here the results are acknowledged to be substantially lower than the Doppler dimming techniques (Strachan et al. 1993). These too could be beset with problems owing to solar radio interference, carrier signal broadening and the sensitivity to variations in the density of the ionosphere. In addition they also detect the motions of density inhomogeneities that include not only the bulk outflow of the

solar wind, but may also include wave motions if the latter have a compressive component. A review on this subject is found in Bird (1982).

In all of the techniques summarized above, the aim is to measure the temperature of the coronal electrons or ions, or the solar wind speed. The techniques depend in different ways on a number of parameters, each of which is subject to uncertainty. However the theoretical idea utilized in this dissertation work is based on an well-understood simple physical principle, which is based on Thomson scattering of the photospheric radiation by the coronal free electrons, which is responsible for the formation of the K-corona. Here the quantity measured, which is the intensity, is dispersed over a wavelength region. The scattered intensity over this wavelength region is dependent on both the coronal temperature and the solar wind velocity with certain regions in the wavelength spread being sensitive to either the temperature or the wind velocity. This feature of selective sensitivity is exploited to formulate temperature and velocity diagnostics. In chapter-2 the physical overview for the formation of the K-corona is explained, together with a methodology to derive the thermal electron temperature and the solar wind velocity from the K-coronal spectrum.

Chapter 2

FORMATION OF THE K-CORONA AND THE FOCUS OF THIS RESERACH

2.1 The K-corona

The K-coronal spectrum, as described in chapter-1, is the coronal brightness attributed to the photospheric spectrum scattered off the free electrons in the solar corona. The existence of the free electrons is due to the high temperatures prevalent in the solar corona. This scattering phenomenon is commonly known as Thomson scattering. This brightness is only revealed during a total solar eclipse.

2.2 The photospheric spectrum

Figure (2.1) shows the solar spectrum in the visible region, as it would appear above the earth's atmosphere. The shape of the photospheric spectrum is similar in nature, however, with a much greater flux. As evident from the solar spectrum the visible region is replete with absorption lines. Among the deep and conspicuous absorption lines, which were labeled by Fraunhofer, are the calcium H and K lines at 3968.5 angstrom and 3933.7 angstrom, respectively. The dark Fraunhofer lines observed in the

solar spectrum are caused by selective process of line scattering or line absorption, accompanied by continuum absorption.

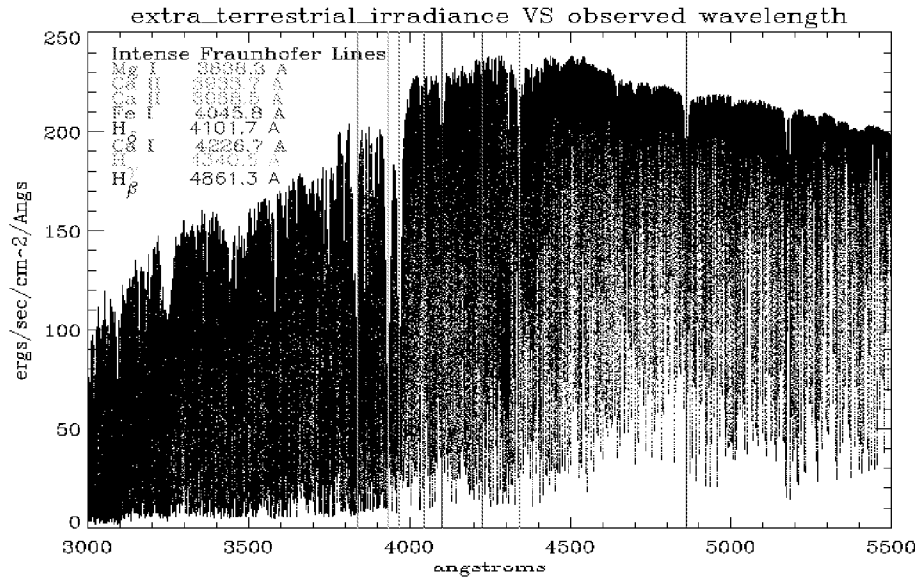


Figure (2.1). This is a plot of the extraterrestrial solar irradiance spectrum. This was obtained by starting with the ground-based Fourier Transform Spectrometer at the McMath/Pierce Solar Telescope at Kitt Peak, Arizona, and then correcting for wavelength-dependent absorption in the Earth's atmosphere

2.3 The scattering source

The scattering source for the formation of the K-corona is the free electrons in the solar corona. For a corona of one million Kelvin these free electrons have a mean thermal velocity of ~ 5500 km/sec and given by equation (2.1).

$$v = \sqrt{\frac{2kT}{m}} \text{ where} \tag{2.1}$$

k = Boltzmann constant = 1.38×10^{-23} J/K
m = Electron mass = 9.11×10^{-31} kg
T = Coronal temperature $\sim 10^6$ K

In an equilibrium state the electron velocity distribution can be described as Maxwellian in the solar corona where the electron number density in the vicinity of the solar limb is $\sim 10^8 \text{ cm}^{-3}$. This means that due to frequent collisions the velocity distribution is the same in all coordinates. However cataclysmic phenomena such as flares or coronal mass ejection can cause a deviation from a Maxwellian distribution locally. Furthermore, in the case of dilute plasma where collisions are infrequent the velocities may differ in different directions. This may be more pronounced in the interplanetary space where the particles stream from the sun in one direction.

2.4 The effects on the incident radiation by the scattering source

In section (2.3) it was shown that a free coronal electrons move with an average thermal velocity of ~5500.0 km/sec in a corona of million degree Kelvin. Such motions are called **Thermal Motions**. This also means that a photon of wavelength (λ) incident in an electron will be Doppler broadened by equation (2.2).

$\Delta\lambda = \lambda \times \frac{v}{c} \text{ where}$ $v \sim 5500 \text{ km/sec for } T = 1.0 \text{ MK}$ $c = 3 \times 10^5 \text{ km/sec}$	(2.2)
----------------------------------------------------------------------------------------------------------------------------------------------------	-------

From equation (2.2) for an incident wavelength at 4000.0 angstrom the broadening is ~70.0 angstroms. This phenomenon is called **Thermal Doppler Broadening**. This broadening increases with increasing thermal velocities for the electrons, which in turn depend on the coronal temperature. This phenomenon could be expected to cause all the narrow absorption lines, as evident in figure (2.1), to smooth into a continuum upon incidence with the coronal electrons. However weak depressions are still expected in the vicinity of the deep Fraunhofer lines thus smoothing the small-scale depressions while preserving the large-scale depressions. This near-total obliteration of the deep Fraunhofer lines by the thermal Doppler broadening served as one of the first clues for a hot corona. From equation (2.1) and equation (2.2) it is evident that the extent of smoothing ($\Delta\lambda$) is related to the coronal temperature (T) by equation (2.3).

$$\Delta\lambda \sim \sqrt{T} \tag{2.3}$$

Once the radiation is incident on the electrons the scattering process is independent of wavelength and equal numbers of photons are scattered forwards and backwards. That is the scattering is coherent in the rest frame of the electrons. Since the scattering source itself is in thermal motion the radiation reaching the observer is **Doppler shifted**. In addition to the thermal velocity the coronal electrons may also acquire velocity due to turbulence.

2.5 The K-coronal spectrum

The photospheric radiation scattered off the free coronal electrons is known as the K-coronal radiation. Cram (1976) presented a physical model for the formation of the K-corona based on the Thomson scattering of the photospheric radiation by the free electrons in the solar corona. In figure (2.2) a schematic drawing of Cram's model is shown. Here a known electron density distribution, determined by other independent means, is assumed for all positions along the line of sight. The normal to the line of sight from the center of the sun is at a distance (ρ).

Each point on the line of sight has certain number of electrons and is subject to collisions with photons that make up the photospheric spectrum. The electrons at a particular point on the line of sight are exposed to the same photospheric spectrum from all the points on the solar surface that they see and are subjected to Thomson scattering. However the photospheric radiation incident on these electrons are also subjected to the **limb-darkening effect**. That is the brightness of the incident radiation is decreased as the

Figure (2.3) shows a modeled spectrum for the scattered wavelength for an independently measured electron number density, given by equation (5.7), along the line of sight at 1.1 solar radii from the center of the sun. Here an isothermal corona was assumed and the plot shows models for different isothermal coronal temperatures.

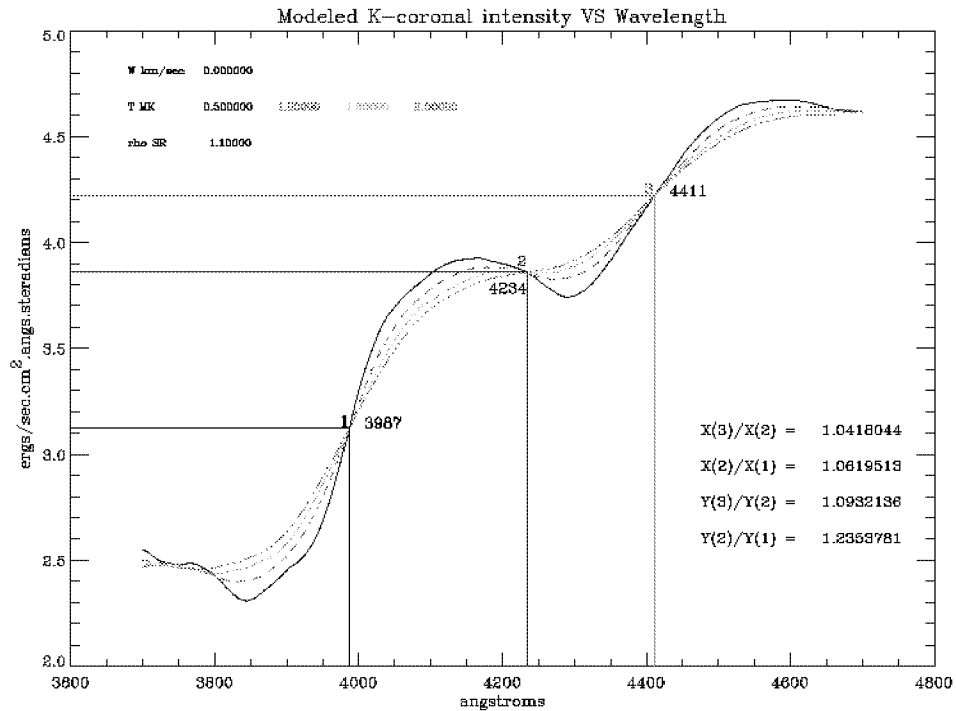


Figure (2.3). This plot shows the modeled K-coronal intensity spectra against wavelength. The composite plots are for different isothermal temperatures assumed for the solar corona for a given line of sight at 1.1 solar radii.

As predicted in section (2.3) the modeled K-coronal intensity spectrum, as depicted in figure (2.3) for a line of sight at 1.1 solar radii, is very much smoother than the shape of the radiation incident on the coronal electrons. From the shape of the incident radiation spectrum, as is shown in figure (2.1), the vertical spread in the intensity

reflects the existence of millions of narrow absorption lines together with wide absorption lines. These millions of narrow lines in the incident radiation have been completely washed away, as revealed in figure (2.3), giving rise to a continuous spectrum. However the large-scale depressions are preserved.

Figure (2.4) and figure (2.5) show the modeled K-coronal intensity spectra for lines of sight at 1.3 and 1.5 solar radii, respectively.

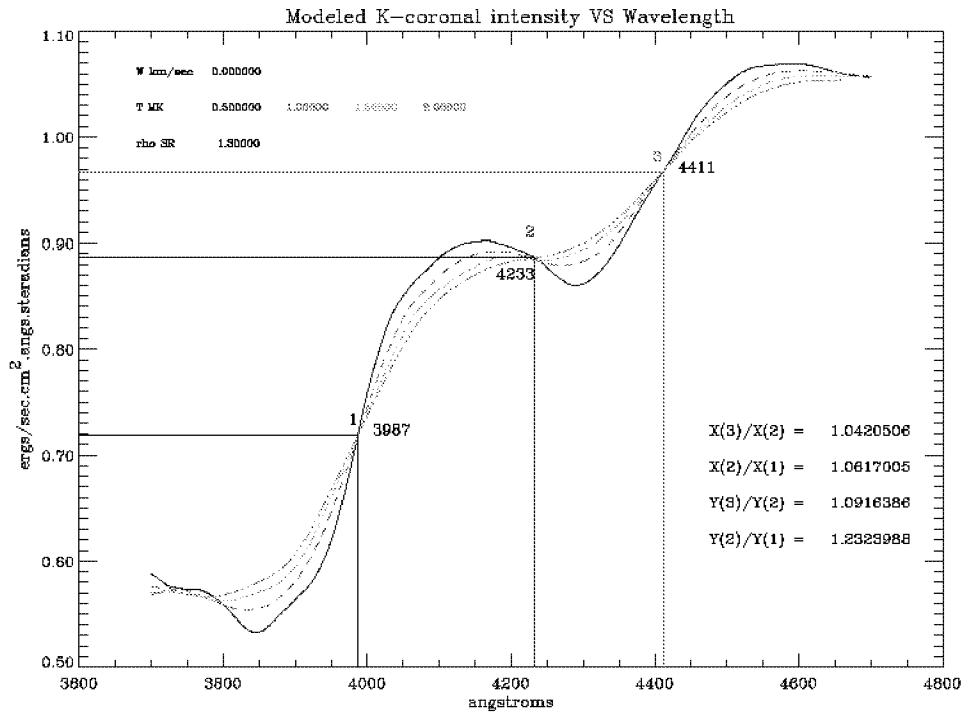


Figure (2.4). Modeled K-coronal intensity spectrum against wavelength for different isothermal coronal temperatures for a given line of sight at 1.3 solar radii.

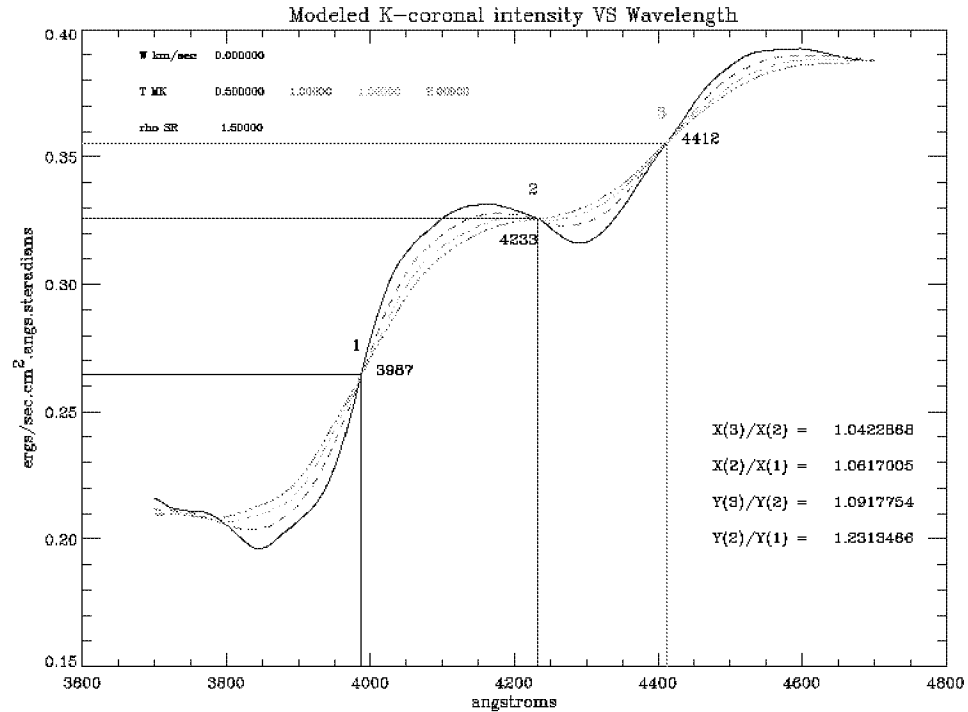


Figure (2.5). Modeled K-coronal intensity spectrum against wavelength for different isothermal coronal temperatures for a given line of sight at 1.5 solar radii.

From these modeled K-coronal intensity spectra for lines of sight at different heights off the solar limb, as depicted in figure (2.3), figure (2.4) and figure (2.5), Cram (1976) made two very important observations.

- (a) The existence of temperature insensitive nodes in the K-coronal intensity spectra for various isothermal coronal temperatures.
- (b) The remarkable independence of the positions of these nodes on the wavelength scale for lines of sight at various heights above the solar limb.

From the above two properties for the K-coronal spectrum it is now possible to implement a temperature diagnostic scheme for the measurement of the coronal temperature by means of measuring the K-coronal intensity spectrum. For this purpose suitable intensity ratios have to be determined at wavelength positions where sufficient temperature dependent parameterization of the shape could be considered. In this regard, from figure (2.3)-(2.5), it is evident that the suitable wavelength positions occur at 3850.0 angstrom and 4100.0 angstroms, respectively, which are also anti-nodes. Figure (2.6) is a plot of the K-coronal intensity ratios at 3850.0 angstrom to 4100.0 angstrom, from the K-coronal models for different isothermal coronal temperatures, against the temperatures.

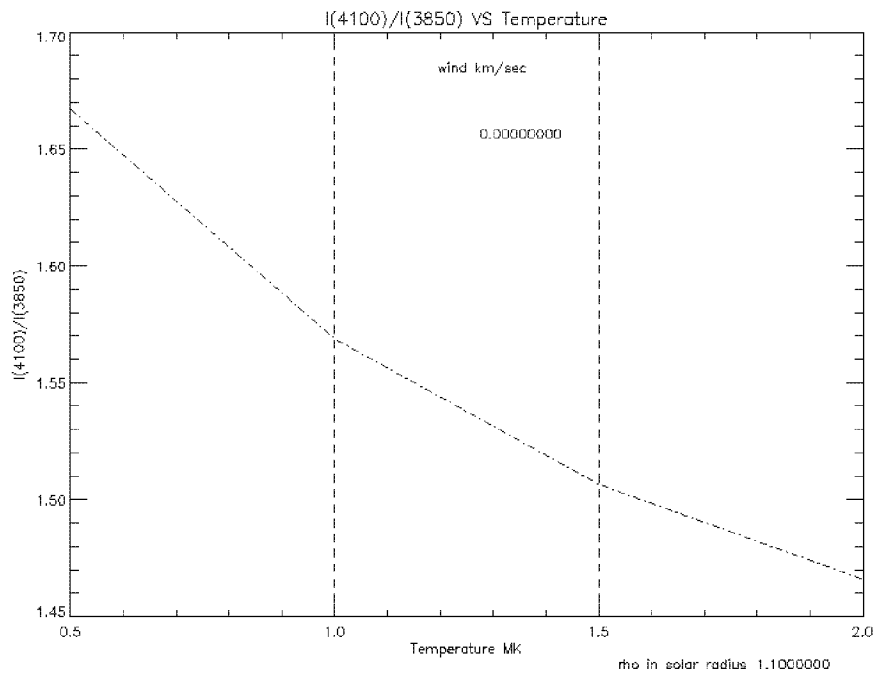


Figure (2.6). This is a plot of the K-coronal intensity ratios at 3850 .0 to 4100.0 angstroms against the assumed isothermal coronal temperatures. The ratios were calculated from the modeled K-coronal spectra for different temperatures shown in figure (2.3). These values pertain to a line of sight at 1.1 solar radii.

It is apparent from figure (2.6) that the coronal temperature could be determined by measuring the K-coronal intensity ratio at 4100.0 to 3850.0 angstroms from an observed K-coronal spectrum. Also from figure (2.6) it can be shown that if the above K-coronal intensity ratio could be determined within uncertainty of $\pm 1.0\%$ then the coronal temperature could be inferred within an uncertainty of ± 0.2 MK. However it is unfortunate that the intensity measurement at 3850.0 angstrom lies in the blue end of the spectrum, which is subject to atmospheric absorption. This requires special chemical coated optics for signal enhancement. Below 3700.0 angstrom difficulties arise from the wavelength dependent atmospheric extinction while above 4700.0 angstrom the spectrum becomes relatively temperature insensitive.

The feasibility of this method for the determination of the electron temperature in the solar corona, as first suggested by Cram (1976), was demonstrated by Ichimoto et al. (1996). Ichimoto et al. (1996) used a slit spectrograph for spectroscopic observation on the solar corona during the total solar eclipse of 3 November 1994 in Putre, Chile. By isolating the K-coronal spectra from the observed total coronal spectra temperatures of 1.07 MK and 1.71 MK were determined for the base of a coronal hole and a streamer, respectively. They also reported cirrus covering of the sky during the totality, which had caused some difficulties in the analyses.

2.6 Further explanation for the formation of the temperature sensitive anti-nodes

To adequately answer the reason for the formation of the temperature sensitive anti-nodes three simple intensity profiles are considered as input intensity spectra in order to understand the scattered intensity spectra produced by the theory. Figure (2.7) shows an absorption line centered at 4000.0 angstrom with a FWHM (Full width at half maximum) of 40.0 angstrom on an otherwise uniform continuum. In this example the intensity spectrum shown by figure (2.7) is assumed to be the sun spectrum as observed from earth.

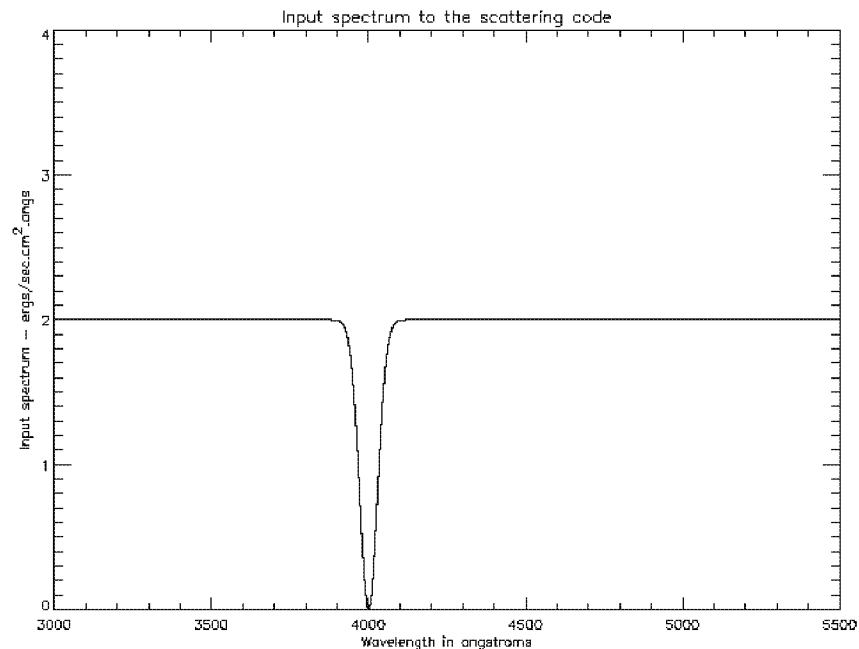


Figure (2.7). An input intensity spectrum containing an absorption line centered at 4000.0 angstrom with a FWHM of 40.0 angstrom in an otherwise uniform continuum.

Figure (2.8) shows the theoretical scattered K-coronal intensity spectrum for an input spectrum given by figure (2.7). This intensity spectrum was obtained by allowing to be scattered off the coronal electrons. The theory assumes an isothermal corona of temperatures 0.5 MK, 1.0 MK, 1.5 MK and 2.0 MK. The essential feature observed in the scattered intensity spectrum is that the smearing of photons by coronal electrons fills in the deepest absorption thus making the absorption at the line center shallower. This smearing process increases with increasing temperatures, which in essence increases the Thermal Doppler Broadening as given by equation (2.2). The essential point is that the intensity of radiation at line center increases as the temperature of the scattering electrons increases.

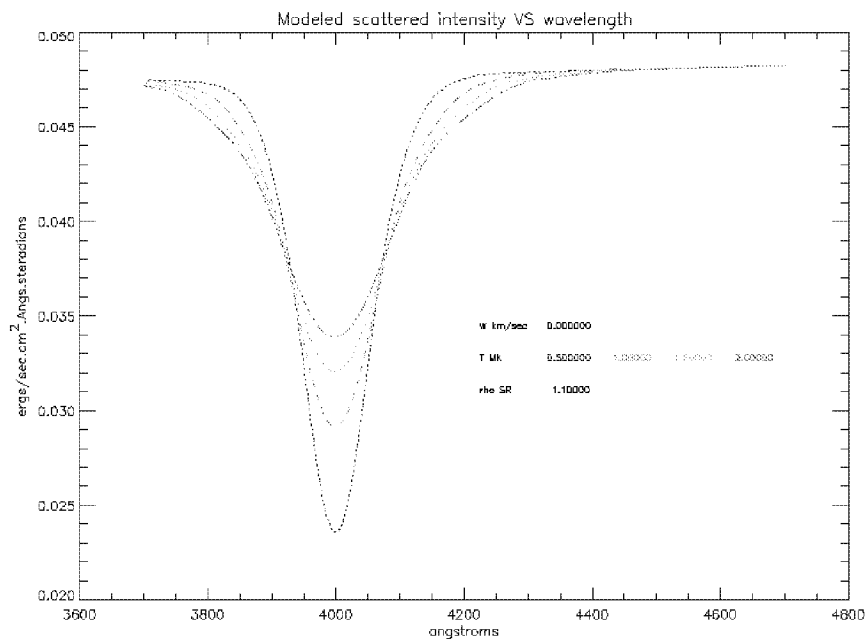


Figure (2.8). The theoretical scattered intensity spectrum by the coronal electrons for an input spectrum given by figure (2.7). The theory assumes an isothermal corona. The plots show that the smearing of the absorption line in the scattered increases with increasing temperatures.

In figure (2.8), the gradient $d(\text{Intensity})/d(\text{Temperature})$ is positive at line center. In order to ascertain the behavior for an input intensity spectrum with two identical absorption features consider figure (2.9) where two strong absorption lines are centered at 4000.0 and 4500.0 angstroms in an otherwise uniform continuum.

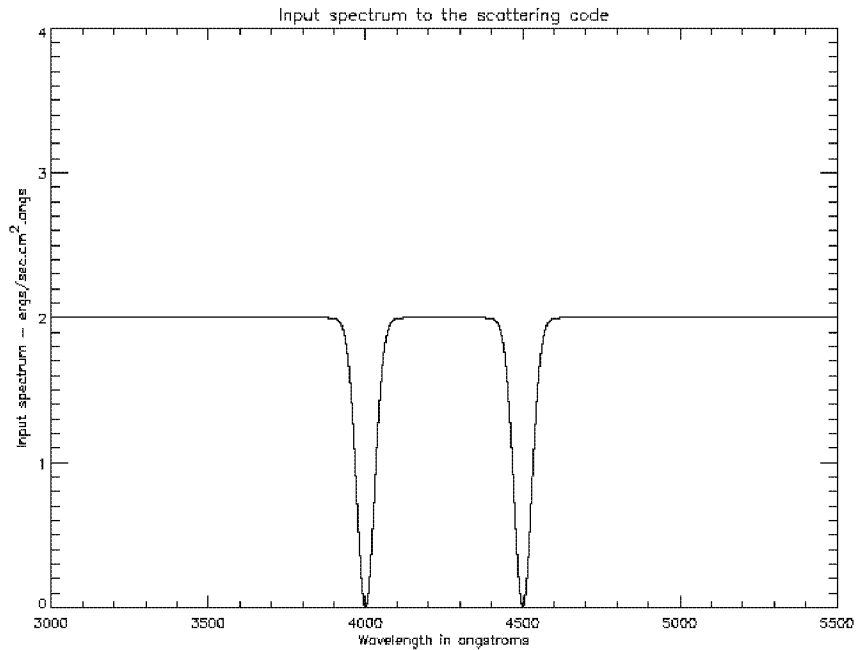


Figure (2.9). An input intensity spectrum containing two absorption lines centered at 4000.0 and 4500.0 angstroms with a FWHM of 40.0 angstrom in an otherwise uniform continuum.

Figure (2.10) shows the theoretical scattered K-coronal intensity spectrum for an input spectrum given by figure (2.9). Here we see that whereas the centers of absorption lines are filled in more and more as the temperature increases, the continuum between the line centers become progressively fainter as temperature increases. Therefore, at wavelength between the two lines (4100 – 4400 angstroms), the intensity of the continuum has a gradient $d(\text{Intensity})/d(\text{Temperature})$ which is negative. This is in

striking contrast to the positive gradient $d(\text{Intensity})/d(\text{Temperature})$ at line centers. It is this different behavior between line and non-line intensities that gives rise to anti-nodes, and provides the basis for Cram's method. The reason for the difference in the depths of the absorption lines is due to the effect of the temperature dependent limb-darkening coefficient.

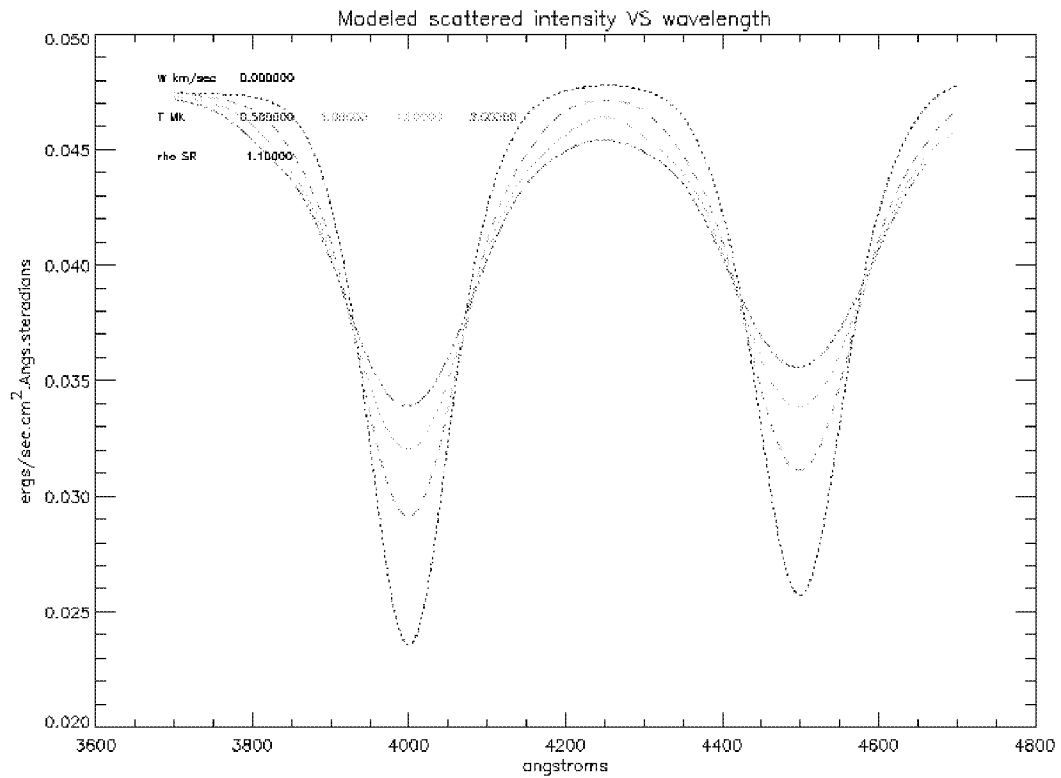


Figure (2.10). The theoretical scattered intensity spectrum by the coronal electrons for an input spectrum given by figure (2.9). The theory assumes an isothermal corona. The difference in the depths of the absorption lines in the scattered spectrum is due to the wavelength dependent limb-darkening coefficient.

Now consider the implications of introducing an emission line between the two absorption lines in an otherwise uniform continuum as shown in figure (2.11). Here the absorption lines are centered at 4000.0 and 4500.0 angstroms while the emission line is centered at 4250.0 angstrom with both the absorption and the emission lines with a FWHM of 40.0 angstrom. Figure (2.12) shows the theoretical scattered K-coronal spectrum for an input spectrum given by figure (2.11).

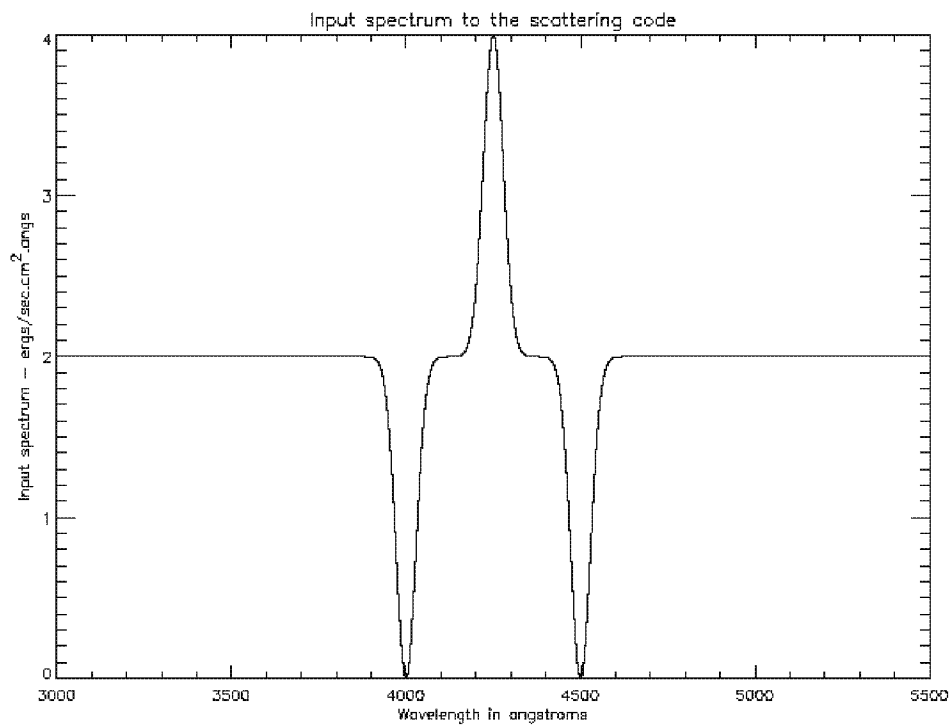


Figure (2.11). An input intensity spectrum consisting of two absorption lines centered at 4000.0 and 4500.0 angstroms while an emission line centered at 4250.0 angstrom and with a FWHM of 40.0 angstrom for the absorption and emission lines in an otherwise uniform continuum.

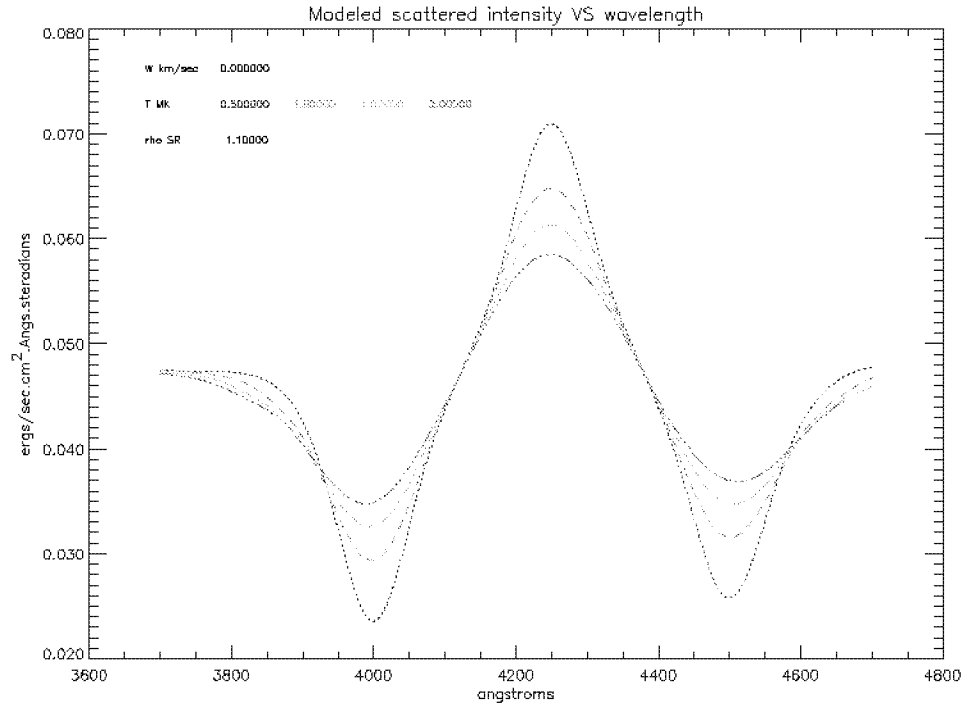


Figure (2.12). The theoretical scattered intensity spectrum by the coronal electrons for an input spectrum given by figure (2.11). The theory assumes an isothermal corona. The difference in the depths of the absorption lines in the scattered spectrum is due to the wavelength dependent limb-darkening coefficient.

With the introduction of the emission line it is evident that in the scattered K-coronal intensity spectrum, as shown in figure (2.12), the absorption lines become shallower while the emission line peak becomes reduced in strength. This again gives rise to the intensity on one side of the node to decrease while the intensity on the other side increase. In analogy, when the input spectra of the examples shown in figure (2.7), figure (2.9) and figure (2.11) are substituted by the photospheric spectrum the dips in the photospheric spectrum are progressively filled in while the higher points are progressively reduced, giving rise to anti-nodes. This is true of an integral over

wavelength of the product of the photospheric spectrum and a Gaussian kernel whose half-width lies in the range of 50 – 200 angstroms.

In the solar spectrum, the anti-nodes in the wavelength region 3900 – 4500 angstroms owe their existence mainly to two wide and strong absorption features: (1) a pair of lines labeled H and K by Fraunhofer at 3968.5 and 3933.7 angstrom, respectively; (2) the combined effects of the Fraunhofer G band at 4300 - 4320 angstroms and the Fraunhofer feature H_γ at 4340.5 angstrom. The G-band is a collection of closely spaced absorption lines predominantly due to the diatomic radical CH and iron.

In essence, the uniqueness of the spectral region around 4000 angstrom for the formation of the anti-nodes arises from the following coincidences. On the one hand, the H and K lines happen to provide essentially a single absorption feature with a width of tens of angstroms. On the other hand, the only molecular band that contributes significantly to the visible solar spectrum (the G-band: almost 100 detectable lines within a range of 60 angstroms) happen to lie within a few tens of angstroms of a strong atomic line H_γ . Both of these strong absorption features are readily identifiable in the low-resolution solar spectrum shown in figure (2.13): the figure is taken from Cram (1976) with his theoretical K-coronal spectra superposed. Note that in low-resolution, the solar photospheric spectrum between 4000 and 4300 angstroms has corrugations that give the impression of “quasi-emission lines”. For this reason, when we were modeling the

scattering of synthetic solar spectra above, as shown in figure (2.11), we included an emission feature between the two absorption lines.

Are there any other parts of the solar spectrum that might be useful to test Cram's idea? It seems unlikely. If we go shortward in wavelength from 3800 angstrom, the solar flux becomes rapidly so low that it is difficult to obtain adequate signal to noise ratio. And if we go to longer wavelengths we do not find pairs of strong absorption features that are wide enough to remain detectable when we smooth them by many tens of angstroms.

The difference in the intensity of the photospheric spectra given by figure (2.1) and figure (2.13) is due to the units of measurement. In figure (2.1) the photospheric intensity is given in units of $\text{ergs/sec.cm}^2.\text{angstrom}$ while in figure (2.13) the intensity is given in units of $\text{ergs/sec.cm}^2.\text{angstrom.steradians}$. To reconcile the photospheric intensities between figure (2.13) and figure (2.1) the latter needs to be divided by the solid angle of the sun's disk, which is 6.8×10^{-5} . The differences in the intensities of the K-coronal spectra, given by figure (2.3) and (2.13), owe to the different electron number density profiles and the line of sight chosen for the analyses.

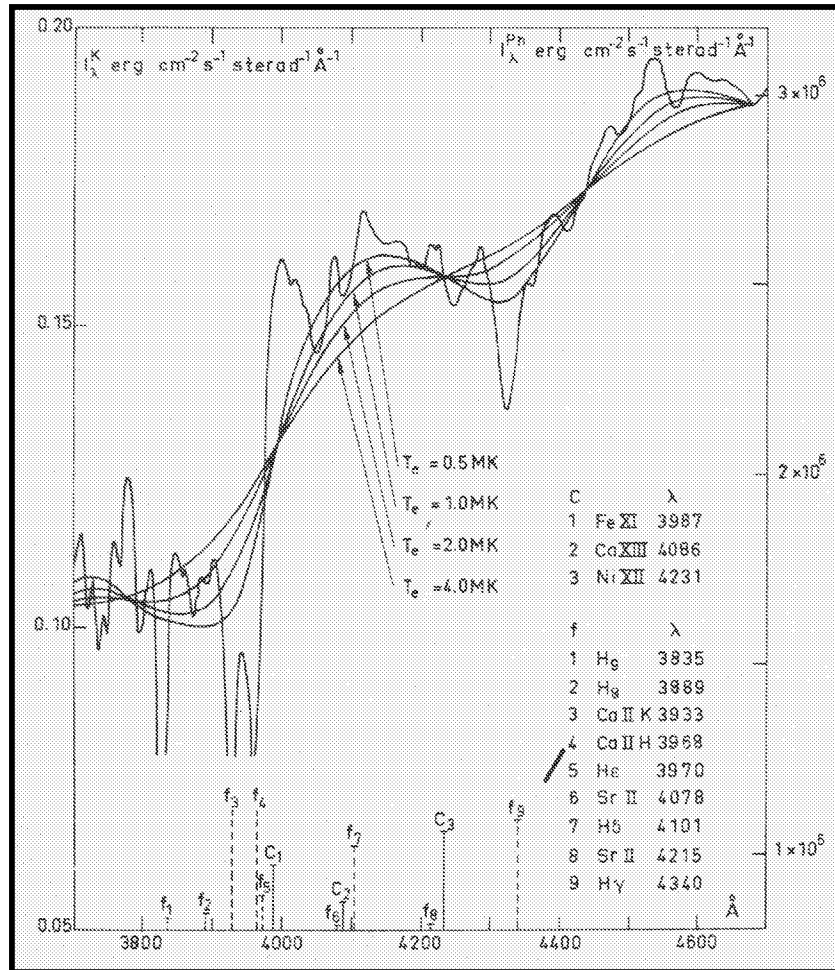


Figure (2.13). This figure shows the theoretical K-coronal intensity spectra for four isothermal coronal temperatures whose electron density is given by equation (5.8). The absolute intensity of the disk center photospheric spectrum is also shown. The vertical bars at the bottom of the figure indicate the relative strengths of the three coronal lines "c", and nine flash spectrum lines "f".

Reproduced from Cram (1976).

2.7 The influence of the solar wind on the K-coronal spectrum

The solar wind is an inherent property of the hot solar corona, a constant outflow of gas into interplanetary space. There the coronal electrons in the vicinity of the solar limb can be assumed to have a bulk outflow velocity equivalent to the solar wind velocity. In the vicinity of the sun this flow is radial and begins to take a spiral pattern at large distances, which is attributed to the rotation of the sun. However these flow velocities are latitude dependent with the fastest outflows occurring in the coronal holes.

Figure (2.14) is a schematic diagram to explain the redshift induced on the K-coronal spectrum by the radially outflowing coronal electrons due to the solar wind. For the illustration of the above consider three electrons located at positions 1,2 and 3 on the line of sight. All three electrons are embedded in a radially directed out flow: the magnitude of the outflow velocity is the same at three electrons, but the velocity vectors point in different directions. Electrons 1 and 3 are symmetrically located on either sides of electron 2 while electron 2 is located at the closest point on the line of sight to the center of the sun. Since they are all moving away from the sun the photospheric radiation incident on these electrons are redshifted in the frame of reference of the electrons. Furthermore, for Thomson scattering, the photospheric radiation scattered off these electrons is wavelength independent in the reference frame of the electrons and they scatter a fraction of this incident radiation along the line of sight of the observer. In figure (2.14), the electrons 1 and 3 have common line of sight velocity magnitudes, away and towards the observer, respectively. This allows for the scattered radiation off

electrons 1 and 3 to be red and blue shifted, respectively, in the frame of reference of the observer, thus rendering a canceling effect on the observed radiation from these two electrons. However the line of sight velocity of electron 2 is zero, which simply scatters the redshifted radiation incident on it without causing anymore wavelength shifts. Thus the Doppler shifting of the radiation scattered by these three electrons is dominated by the effect due to electron 2, which is an overall redshifting of the scattered radiation along the line of sight.

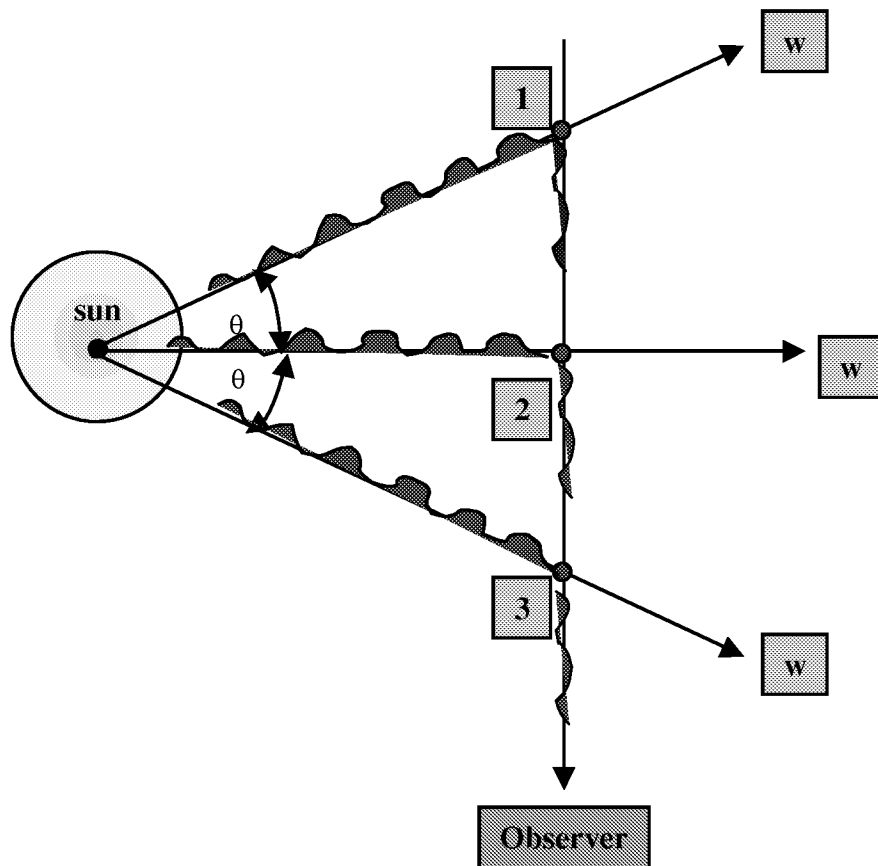


Figure (2.14). This is a schematic drawing to illustrate the redshifting of the photospheric radiation scattered off the coronal electrons, which are radially flowing away from the sun at a uniform velocity (w). Electron 2 is located at the closest point on the line of sight to the center of the sun. Electrons 1 and 3 are located symmetrically on either sides of electron 2.

The magnitude of this redshift on the K-coronal spectrum for an incident radiation of 4000.0 angstrom on the coronal electrons with an outflow velocity of 300.0 km/sec in a million degree Kelvin Corona is, from equation (2.2), ~4.0 angstrom. Figure (2.15) is a reproduction of figure (2.1) with horizontal bars to emphasize the magnitude of the thermal Doppler broadening and the redshift associated with the solar wind velocity. For this illustration these quantities are calculated for an incident wavelength of 4000.0 angstrom on the coronal electrons, which are radially outflowing at a velocity of 300.0 km/sec in a million degree Kelvin corona.

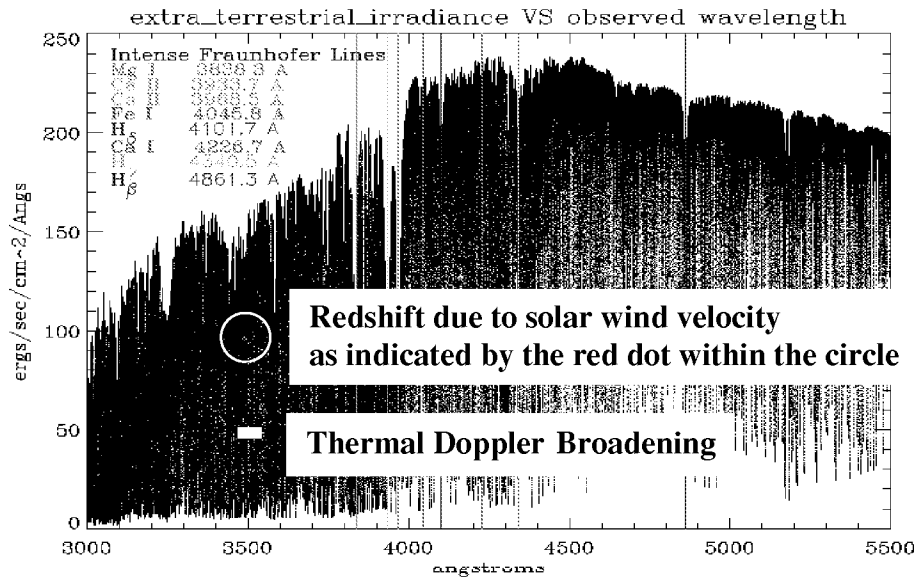


Figure (2.15). This figure shows the scale of the thermal Doppler broadening and the redshift associated with the solar wind velocity in the wavelength scale in comparison to the features of the photospheric spectrum. The scale of the redshift is shown by a red dot, which is highlighted by a circle. This comparison is made for an incident wavelength of 4000.0 angstrom on the coronal electrons, which are radially outflowing at a velocity of 300.0 km/sec in a million degree Kelvin corona.

The effect of the solar wind velocity in the model for the formation of the K-corona was considered to be negligible by Cram (1976). However an interesting additional property was revealed by the inclusion of a constant radial solar wind velocity to Cram's model. That is the temperature insensitive nodes, which were observed by Cram (1976), were now observed to shift in wavelength positions with increasing solar wind velocity while maintaining the remarkable independence of the nodal positions with height above the solar limb. Figure (2.16) and figure (2.17) are K-coronal intensity models for different isothermal coronal temperatures at a line of sight at 1.1 solar radii with assumed radial solar wind velocities of 400.0 km/sec and 800.0 km/sec, respectively.

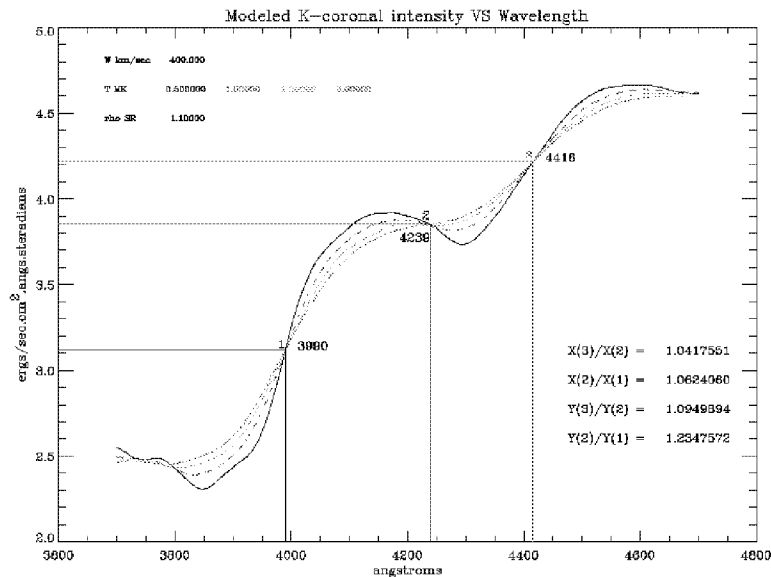


Figure (2.16). Modeled K-coronal intensity against wavelength for different isothermal coronal temperatures, for line of sight at 1.1 solar radii and a wind velocity of 400.0 km/sec.

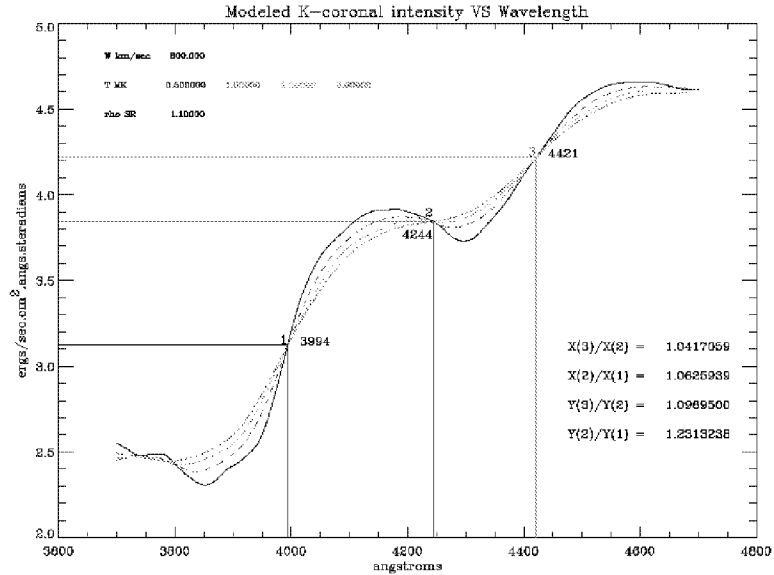


Figure (2.17). Modeled K-coronal intensity against wavelength for different isothermal coronal temperatures, for line of sight at 1.1 solar radii and a wind velocity of 800.0 km/sec.

Comparing figure (2.16) and figure (2.17) with figure (2.3), which is a K-coronal model for zero wind velocity, it is evident that the temperature insensitive nodes shift in wavelength positions with increasing solar wind velocities. This newfound physical property pertaining to the shifting in the wavelength positions of the temperature insensitive nodes with increasing solar wind velocities can be utilized to construct wind sensitive diagnostics.

Figure (2.18) is a plot of the K-coronal intensity model for different wind velocities ranging from 0.0 km/sec to 900.0 km/sec in intervals of 100.0 km/sec for an isothermal coronal temperature of 1.0 MK with the line of sight at 1.1 solar radii. It is evident from figure (2.18) on the existence of a wind insensitive node at 4233.0 angstrom with the maximum spread in intensity (anti-node) at 3987.0 angstrom. This property holds for other isothermal coronal temperatures and heights above the solar limb too.

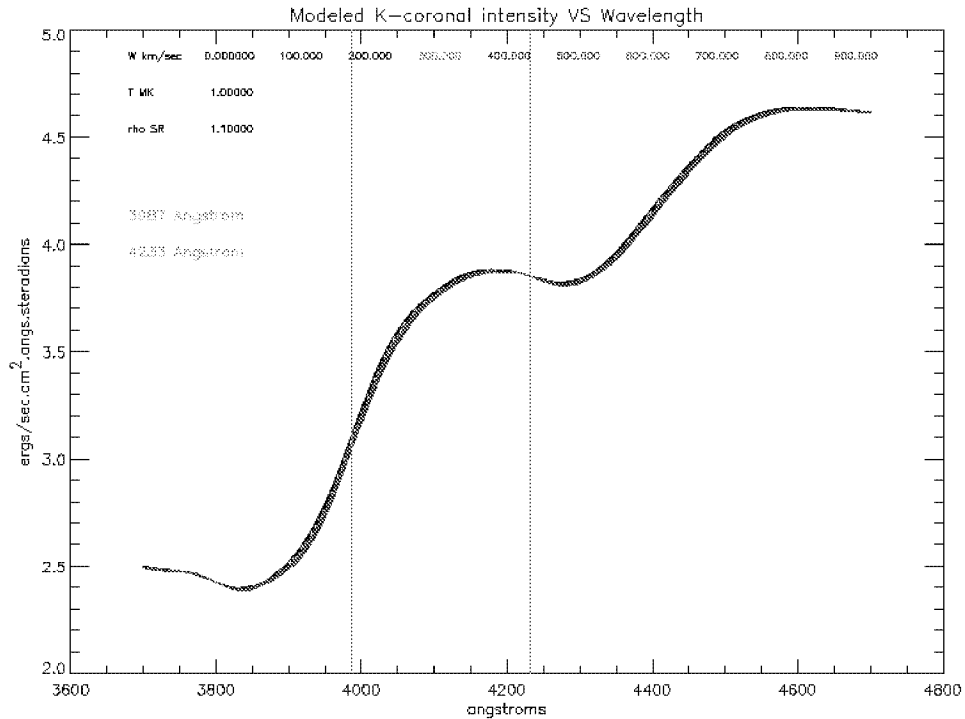


Figure (2.18). Modeled K-coronal intensity against wavelength for solar wind velocities of 0.0 km/sec to 900.0 km/sec in intervals of 100.0 km/sec, for line of sight at 1.1 solar radii and an isothermal coronal temperature of 1.0 MK.

Thus the summary of the theoretical observations on the modified version of the Cram's model, with the inclusion of the solar wind velocity is,

- (a) The existence of temperature sensitive anti-nodes at certain wavelengths in the K-coronal intensity spectrum provides a meaningful temperature diagnostics.
- (b) The wavelengths of the anti-nodes are remarkably independent of heights above the solar limb.
- (c) The simultaneous existence of nodes in the spectrum, where temperature effects are negligible, enables us to develop a diagnostic of wind speed that is more or less independent of temperature.

2.8 Simultaneous determination of the coronal temperature and the solar wind velocity

From the theoretical properties observed from the modified Cram's model it is evident on the existence of both temperature and wind diagnostics. Figure (2.19) is a plot of the intensity ratios at the anti-nodes 3850.0 to 4100.0 angstroms against isothermal coronal temperatures for a range of solar wind velocities from 0.0 km/sec to 900.0 km/sec and with the line of sight at 1.1 solar radii. It too reveals the feasibility of the coronal temperature measurement within an uncertainty of ± 0.2 MK if the above intensity ratio at the anti-nodes 3850.0 to 4100.0 angstroms could be experimentally determined within

an uncertainty of $\pm 1.0\%$. The width at the low end of the temperature range is ~ 0.02 MK over a wind velocity range of 0.0 km/sec to 900.0 km/sec.

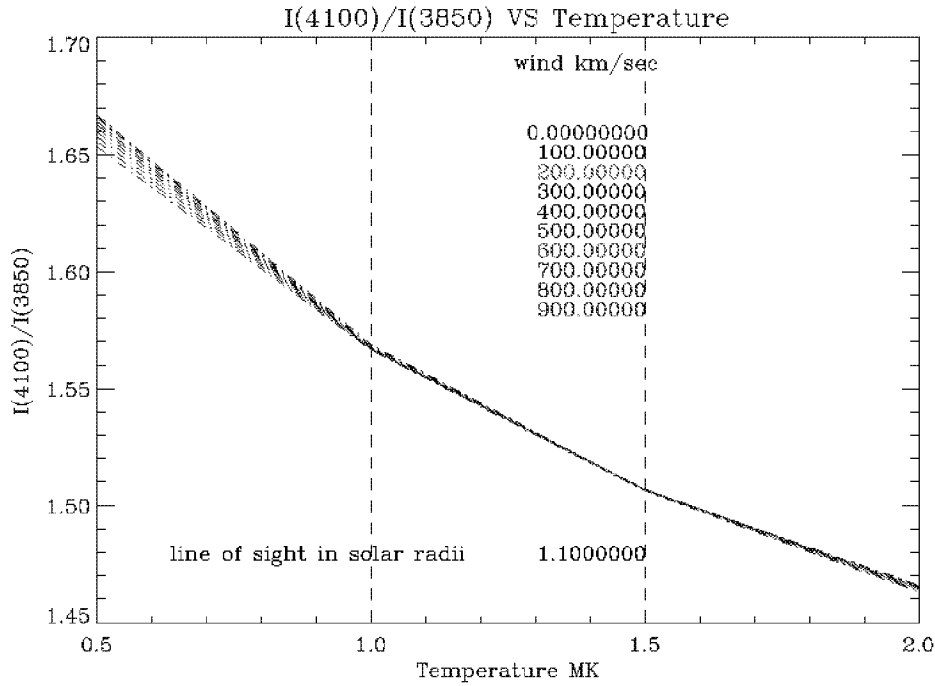


Figure (2.19). The intensity ratio at 3850.0 to 4100.0 angstroms against isothermal coronal temperatures for a range of solar wind velocities with the line of sight at 1.1 solar radii. The horizontal spread in the low end of the temperature scale is ~ 0.02 MK over the velocity range of 0.0 km/sec to 900.0 km/sec.

Figure (2.20) is a plot of the intensity ratios of the wind sensitive anti-node at 3987.0 to the wind insensitive node at 4233.0 angstroms against solar wind velocities for a range of isothermal coronal temperatures with the line of sight at 1.1 solar radii. The solar wind velocity can be determined by first determining the temperature from figure (2.19) and then by plotting in figure (2.20) the intensity ratios of the wind sensitive anti-

node at 3987.0 to the wind insensitive node at 4233.0 angstroms against the wind velocities at this temperature. Here the solar wind velocity measurements are highly sensitive to the wind-sensitive intensity ratio measurements. An uncertainty of $\pm 1.0\%$ in the wind-sensitive intensity ratio measurements can cause an uncertainty of ± 200.0 km/sec at 0.50 MK. This uncertainty increases with increasing coronal temperatures.

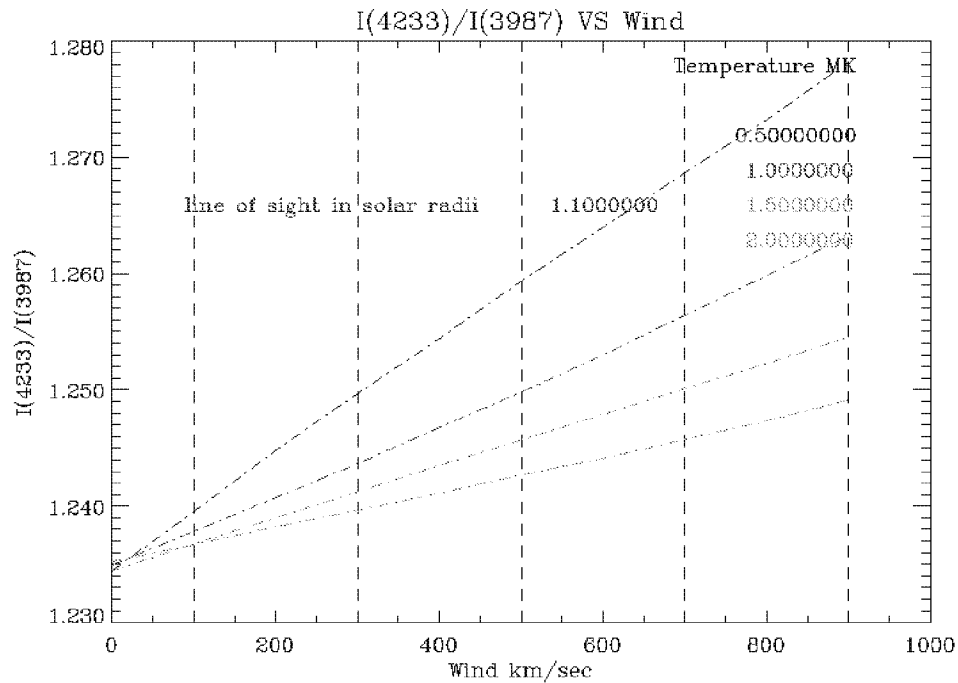


Figure (2.20). The intensity ratio at 3987.0 to 4233.0 angstroms against solar wind velocities for a range of isothermal coronal temperatures with the line of sight at 1.1 solar radii. To determine the wind velocity, first the temperature has to be determined from figure (2.19). Then the K-coronal models need to be created for a range of wind velocities at this temperature and plotted in figure (2.20).

2.9 Global determination of the coronal temperature and the solar wind velocity

In section (2.7) a methodology was developed to simultaneously determine both the coronal temperature and the solar wind velocity from the same wavelength dispersed K-coronal intensity spectrum. That is, by measuring the intensity ratios at 3850.0 angstrom to 4100.0 angstrom and 3987.0 angstrom to 4233.0 angstrom, from the observed K-coronal spectrum. The former is termed the, ‘**temperature-sensitive**’ intensity ratio, which allows for the temperature measurements from figure (2.19). The latter is termed the, ‘**wind-sensitive**’ intensity ratio, which allows for the wind measurements from figure (2.20). However for the wind measurement, further theoretical K-coronal models need to be created for various wind velocities using the measured temperature as the isothermal coronal temperature. From these models the wind-sensitive intensity ratios are plotted against the wind velocities assumed for those models in figure (2.20). Now by calculating the wind-sensitive intensity ratio from the observed K-coronal spectrum its corresponding wind velocity can be obtained.

In order to extend this measurement globally on the solar corona the wavelength dispersed K-coronal intensities need to be measured simultaneously and globally on the solar corona. Chapter-3 explains an instrument designed for simultaneous and global measurement of the wavelength dispersed coronal intensity spectra from multiple locations on the solar corona. Chapter-4 discusses the results from the very first attempt to measure both the coronal temperature and the solar wind velocity, simultaneously and

globally, on the solar corona. This experiment was performed during the total solar eclipse of 11 August 1999 in Elazig, Turkey.

2.10 The essence of this dissertation

In this dissertation the influence of the solar wind velocity was added to the Cram's model to search for both coronal temperature and solar wind velocity diagnostics. Based on the feasibility for the measurement of the **coronal temperature** and **solar wind velocity** diagnostics, from a single spectroscopic observation of the solar corona, an instrument was designed that would **globally** and **simultaneously** measures both these quantities at twenty different locations on the solar corona (Reginald & Davila, Paper I, 2000). The very first experimental effort was carried out in conjunction with the total solar eclipse of 11 August 1999 in Elazig, Turkey and the results were analyzed to obtain both the coronal temperatures and the solar wind velocities at multiple locations (Reginald & Davila, Paper II, 2000).

Chapter 3

THE INSTRUMENT

3.1 Overview of the instrument

Basically, the instrument designed was a spectrograph to obtain coronal spectra of the solar corona during the total solar eclipse of August 11, 1999.

However this design incorporated a new feature in the way the light was collected and fed to the spectrograph in obtaining spectra. The exception from the usual slit-based spectrograph was that light was collected at the focal plane of the telescope via fiber optics. The fiber optic tips at the focal plane of the telescope were positioned at various latitudes and radii on the image of the sun formed on the focal plane of the telescope during the solar eclipse. This method served two very important purposes.

1. This way the instrument was able to obtain **simultaneous coronal spectra from different latitudes and radii on the solar corona.**

2. Also as a complimentary the telescope was spared the task of carrying the weight of the spectrograph. This was because they were detached systems connected via fiber optic cables.

In essence the instrument was composed of three vital components.

1. The telescope imaged the sun during the eclipse on the focal plane of the telescope.
2. The fiber optic tips, positioned at various latitudes and radii on the sun's image on the focal plane of the telescope, carried the coronal light to the spectrograph.
3. The spectrograph produced simultaneous spectra from the light received by the individual fibers.

The telescope used in this experiment was a Schmidt-Cassegrain telescope with a primary mirror diameter of 12-inches and a focal ratio of 10.0. A focal reducer was attached to reduce the focal ratio to 6.3. Schmidt-Cassegrain telescopes by design are free from coma, spherical aberration and astigmatism. The telescope also contained auto-tracking capability. Figure (3.1) is a picture of the telescope used in this experiment and produced by the Meade Corporation. Figure (3.2) is a picture of the focal reducer attached to the back end of the telescope that increased the field of view by 56.0 % at the expense of lowering the magnifying power by 36.0 %.

At the focal plane of the telescope was a glass plate embedded with twenty-one fiber optic tips with ten each spread in equal angles in a circular loop corresponding to 1.1 and 1.5 solar radii on the sun's image and one at the center of the frame. The one in the center of the frame was used to record the background signal using the lunar shadow during the eclipse. Another four fibers were attached to a mercury calibration lamp.



Figure (3.1). Meade 12-inch, F/10.0 Schmidt-Cassegrain telescope with auto tracking capabilities.

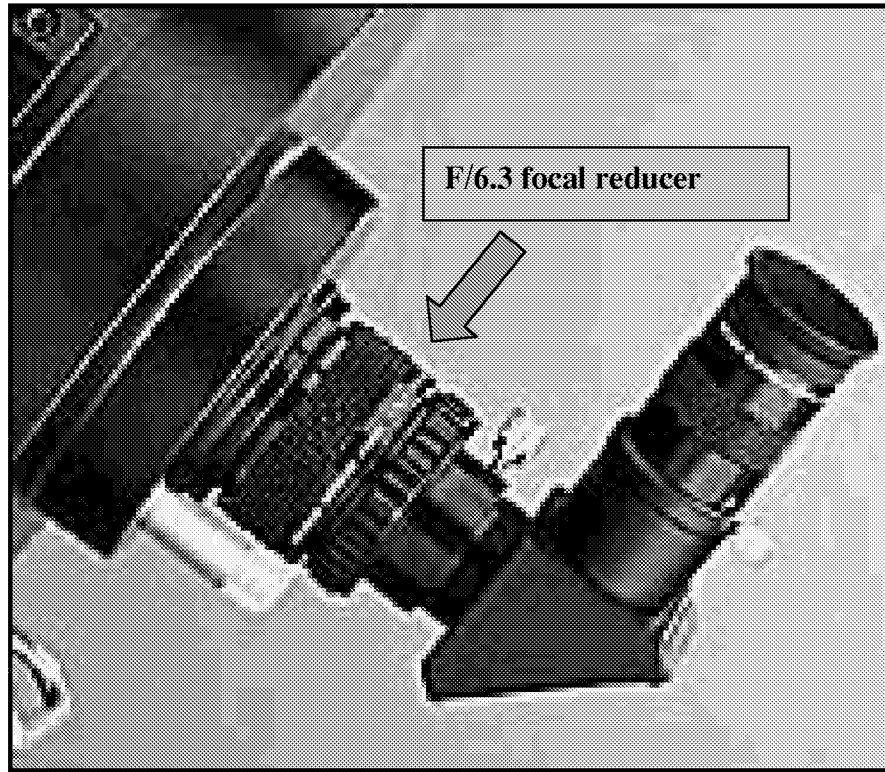


Figure (3.2). F/6.3 focal reducer reduces the focal length by a factor of 0.63. The device shown in figure (3.4) was placed at the focal plane behind the F/6.3 focal reducer.

Figure (3.3) shows a schematic of the glass plate, as it would appear when the sun is in focus. Figure (3.4) shows the picture of the fiber optic tips embedded on the glass plate. The front end of the glass plate, where the fiber ends were exposed to the coronal light, was roughened with the back end smoothed. This allowed for the focusing of the sun prior to the eclipse on the front end of the glass while observing the image going in and out of focus from the back end. The fiber in the center was to record the background signal during the eclipse.

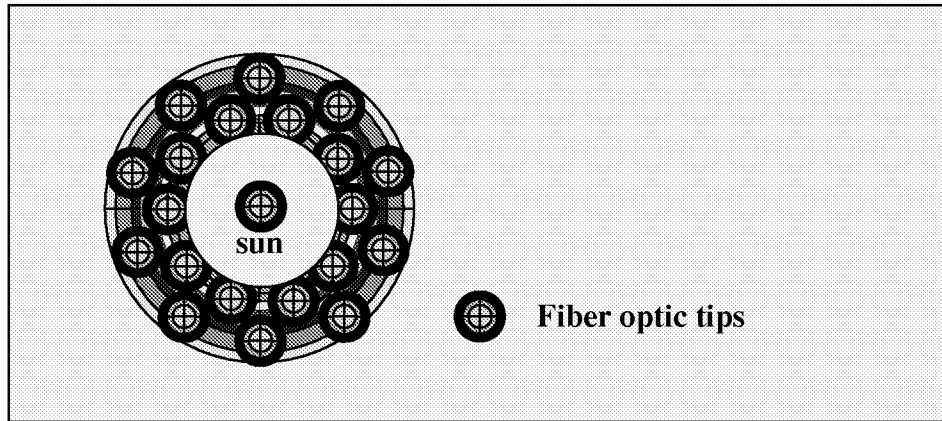


Figure (3.3) A drawing depicting the location of the fiber tips on the image plane of the telescope. The inner and outer rings are at 1.1 and 1.5 solar radii, respectively. During the eclipse the lunar shadow replaces the sun.

In figure (3.4) is the glass plate imbedded with twenty-one fibers that was placed at the focal plane of the telescope. The coronal light entering the fibers, which were located at the focal plane of the telescope and shown in figure (3.4), were all vertically aligned at the other end. The other end substitutes the position of the slit in a slit-based spectrograph. This slit, made up of multiple fibers at regular spacing between neighbors, was placed at the prime focus of the collimating lens of the spectrograph. In figures (3.5) and (3.6) are images of the spectrograph.

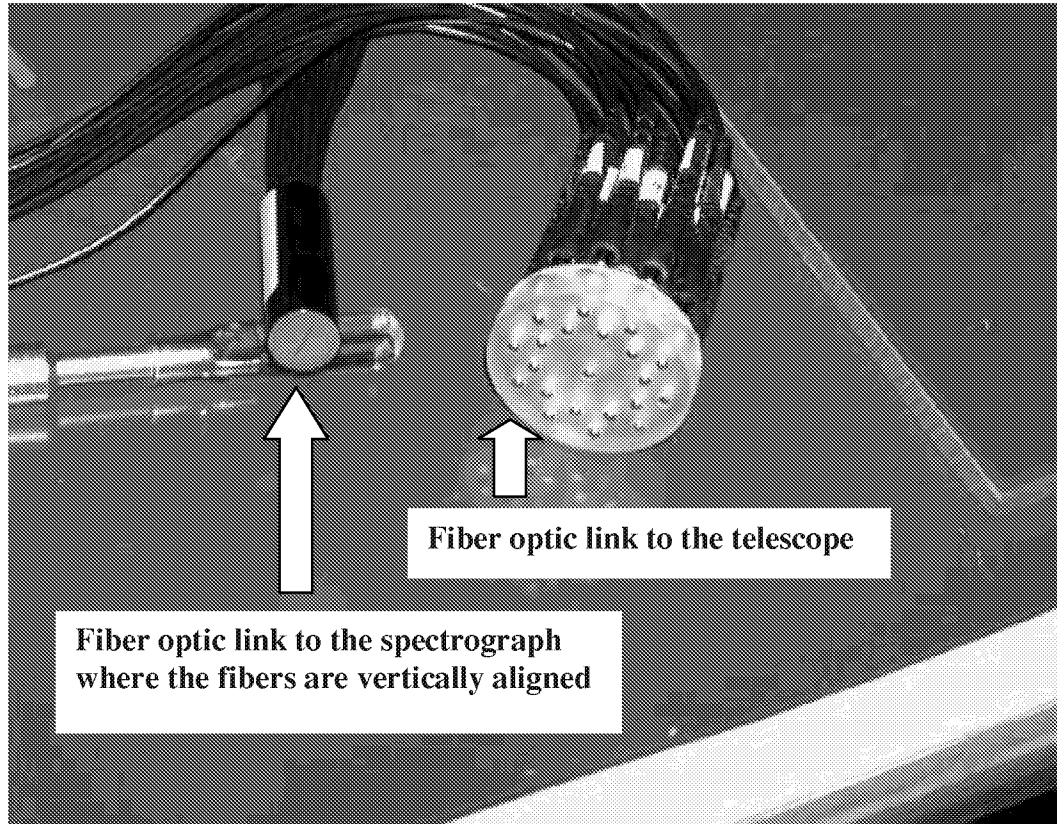


Figure (3.4). The glass plate imbedded with twenty-one fibers. The inner and the outer circles are located at 1.1 and 1.5 solar radii, respectively, on the image plane of the sun. The fiber at the center was to record the background signal during the eclipse.

From figure (3.5) it is apparent that, apart from the capability of this setup to simultaneously produce spectra, this methodology also allowed for the telescope and the spectrograph to be two independent units connected via light fiber optic cables. This is not possible in a slit-based spectrograph. In such a case the spectrograph needs to be attached to the back end of the telescope with the slit at the focal points of both the telescope and the collimating lens of the spectrograph. The purpose of the collimating lens is to transmit collimated light to the diffraction grating for dispersion.

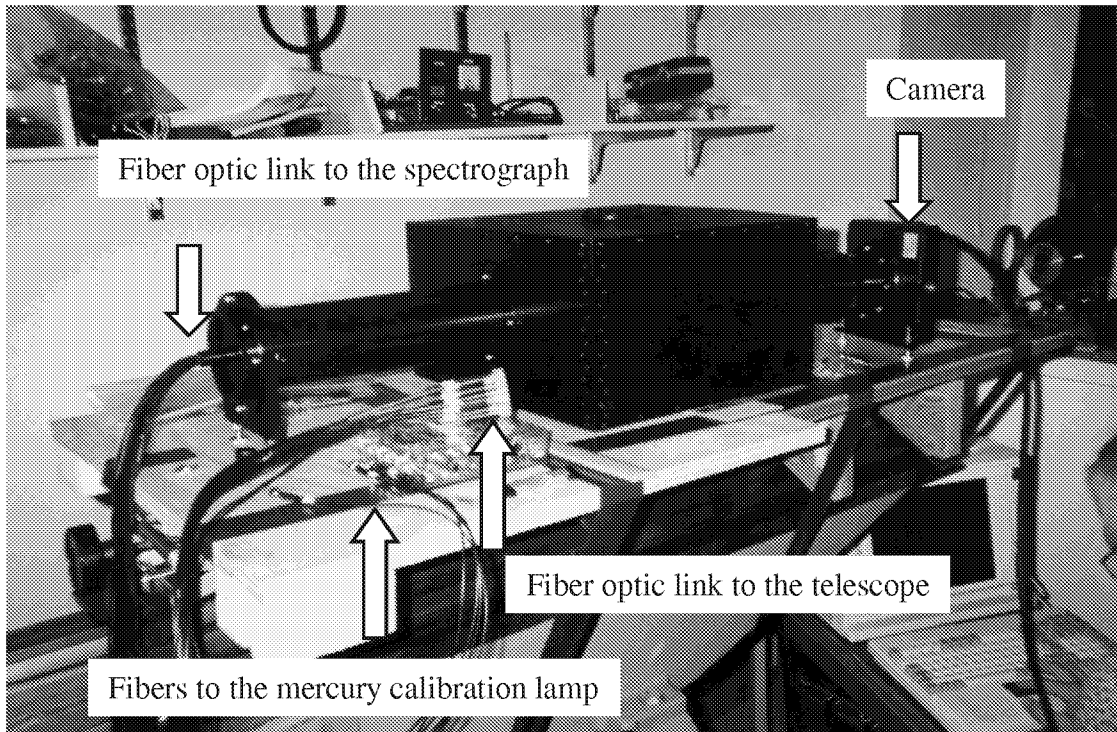


Figure (3.5). This is a picture of the spectrograph. The coronal light was fed into the spectrograph by twenty-one fibers that were vertically arranged at a regular spacing. Its location in the spectrograph was at the focal point of the collimating lens.

Figure (3.6) shows the inside of the spectrograph between the grating and the camera lens that focuses the dispersed light to the camera in the backend. The spectrograph body contained many features that made it light tight from stray light that could have found its way into the spectrograph. Also the setscrews ensured that the many parts of the spectrograph fitted in place during assembly as a single unit.

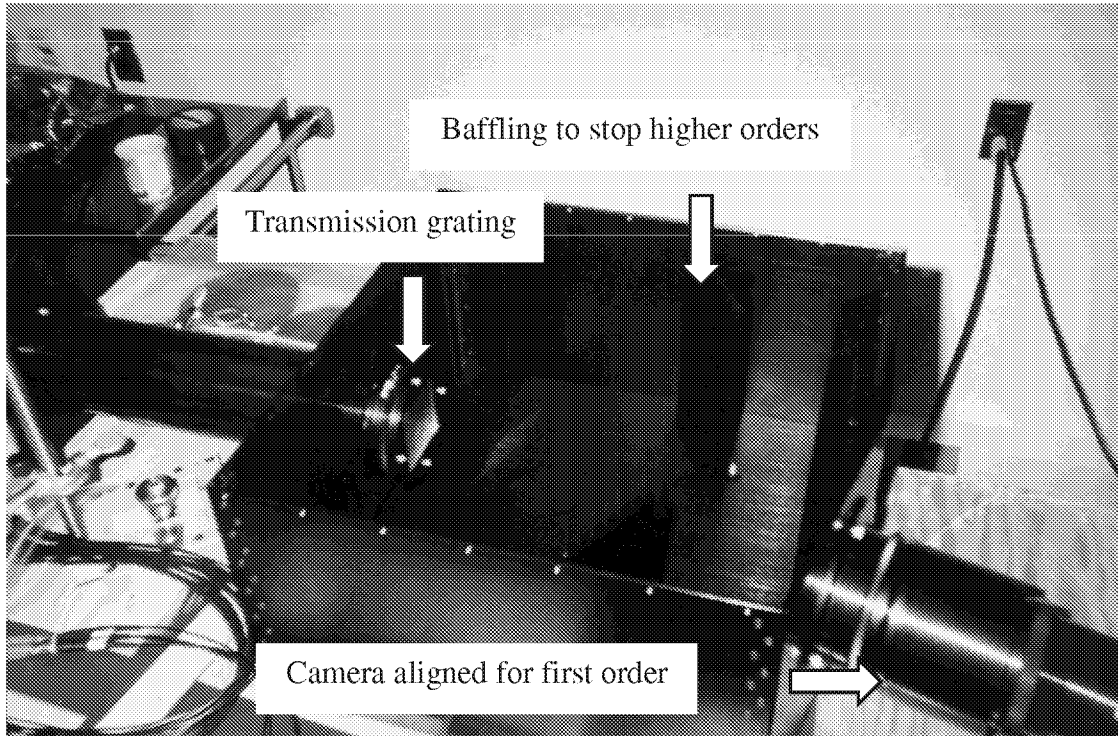


Figure (3.6). This is a picture of the inside of the spectrograph between the grating and the camera lens. Baffling were used to prevent all orders but the first order from entering into the camera lens.

In figure (3.7) is a picture of the CCD camera that was used in this experiment to record the light dispersed in the first order in the wavelength region of 3500.0 to 4500.0 angstroms. A thermoelectric cooler cooled the CCD device. Baffling were placed to restrict only the dispersed light in the first order from entering the camera. All the other orders were subjected to multiple reflections within the saw-tooth shaped grooves in the baffles for absorption by the black-coated baffling material.

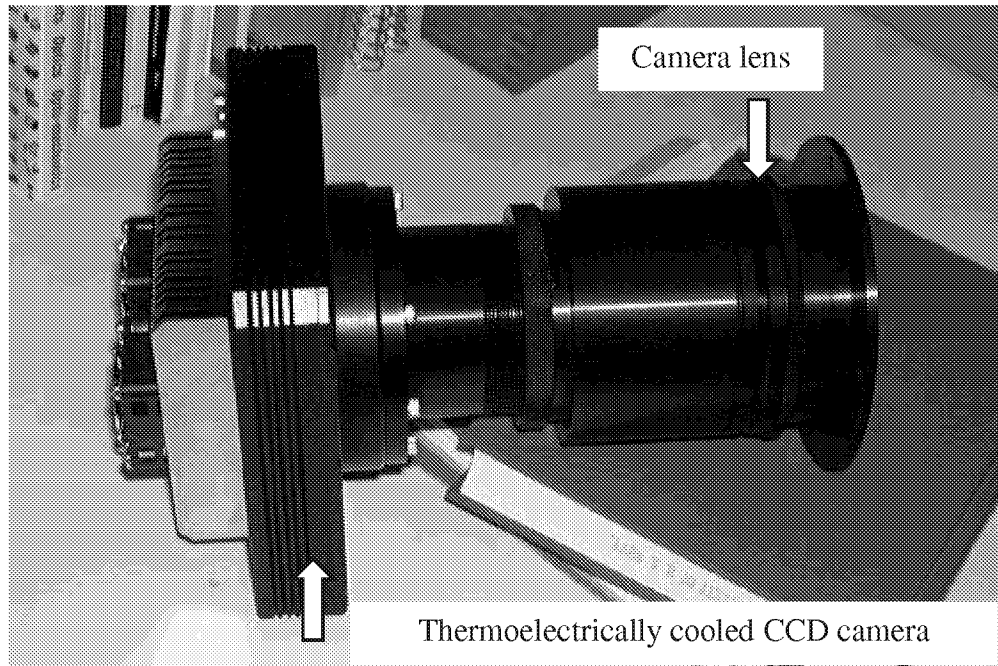


Figure (3.7). This is a picture of the thermoelectrically cooled CCD camera used in the experiment. The front end housed the camera lens that focused the dispersed light from the grating on to the camera.

As a general overview of the instrument the following could be said. The telescope imaged the eclipsed sun on to a glass plate containing twenty-one fibers, which was located at the focal plane of the telescope. The fibers picked up the light from various locations on the sun's corona and the moon's center. This light was fed to a spectrograph via the fiber optic cables. Then the grating simultaneously dispersed lights from all the fibers. The camera located at the backend of the spectrograph recorded the dispersed light in the first order in the wavelength region of 3500.0 to 4500.0 angstroms. In view of this instruments ability to record simultaneous spectra it was deemed appropriate to name this system the **Multi Aperture Coronal Spectrometer** with the acronym (**MACS**).

3.2 Description of the optical elements in detail

In the following subsections all the optical elements of MACS will be discussed in details.

3.2.1 The telescope

The telescope used in MACS was a 12-inch F/10.0 Schmidt-Cassegrain manufactured by the Meade Corporation. The f-number was reduced to F/6.3 using a focal reducer in order to increase the plate scale. The LX200 model used in MACS also featured auto tracking and a super wedge for polar alignment. By design the Schmidt-Cassegrain type telescopes eliminate image distortion due to coma, spherical aberration and astigmatism, which are explained below. These optical systems are also called *anastigmats* and consist of at least three optical elements. A Schmidt-Cassegrain telescope consists of a concave and convex mirrors as the primary and the secondary, respectively, and a thin aspheric corrector plate in the front.

Spherical aberration: Parallel rays are not brought to a focus at a point, but along a line. Therefore off-axis rays are brought to a focus closer to the lens than are on-axis rays.

Coma: Off-axis rays do not quite converge at the focal plane, thus rendering off-axis points with tails, reminiscent of comets, hence the name.

Astigmatism: Rays of different orientations having different focal lengths resulting in the distortion of the image. Rays of light from horizontal and vertical lines in a plane on the object are not focused to the same plane on the edges of the image. Off-axis points are blurred in their radial or tangential direction, and focusing can reduce one at the expense of the other.

The plate scale (**P**) of the telescope is defined as the spatial area seen in the sky, which is measured in arcseconds, corresponding to the spatial scale in the focal plane of the telescope, which is measured in micrometers and shown in figure (3.8).

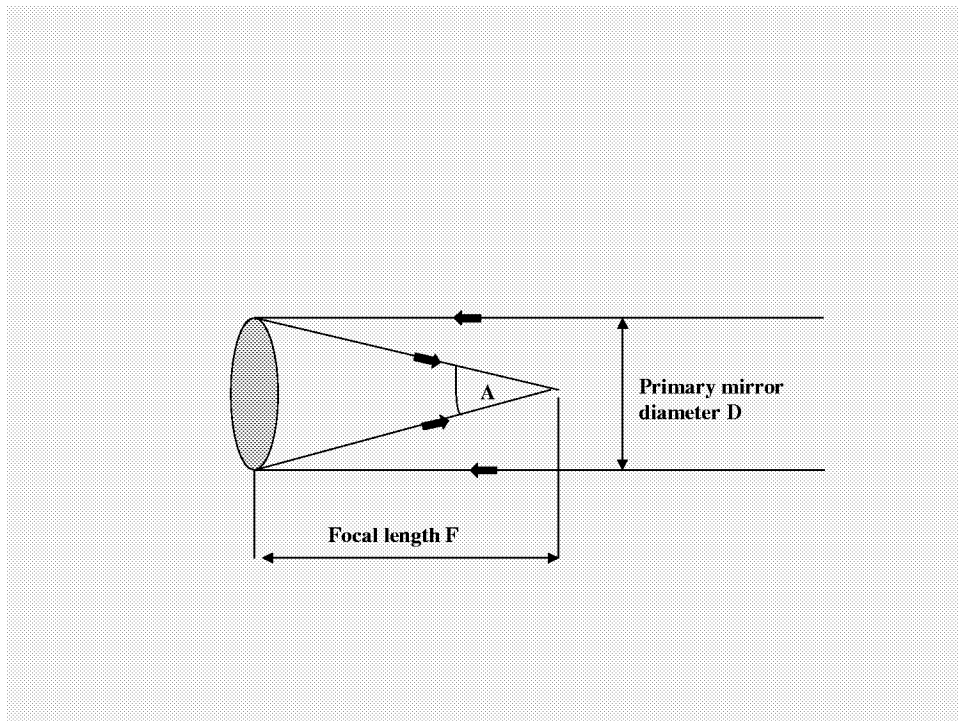


Figure (3.8). Schematic drawing on the image formation by the primary mirror of the telescope.

From figure (3.8) the expression for angle **A** is given by equation (3.1).

$$\mathbf{Tan(A) = \frac{D}{F}} \quad (3.1)$$

Since (**A**) is a small angle, expressing (**A**) in radians, where (**Tan (A) ≈ A**), and then converting radians into arcseconds, where (**1 radian = 206265**) arcseconds, gives the following expression for (**A**), as shown in equation (3.2).

$$\mathbf{A = \frac{206265 \times D}{F}} \quad (3.2)$$

From the definition of the plate scale (**P**) it could be written as shown in equation (3.3).

$$\mathbf{P = \frac{A}{D}} \quad (3.3)$$

$$= \frac{206265 \times D / F}{D}$$

$$= \frac{206265}{F}$$

$$= \frac{206265}{D \times F / \#} \text{ arcseconds}/\mu\text{m}$$

Substituting for the diameter of the primary **D** in μm ($12\text{-inch} = 12 \times 2.54 \text{ cm} = 12 \times 2.54 \times 10^4 \mu\text{m}$) and the f-number of the telescope ($F/\# = 6.3$) in equation (3.3) gives the following value for the plate scale (**P**) as shown in equation (3.4).

$$\boxed{\mathbf{P = 0.107 \text{ arcseconds}/\mu\text{m}}} \quad (3.4)$$

3.2.2 The fibers

The fibers linking the focal plane of the telescope and the spectrograph were twenty-one fibers with four more connected to a mercury calibration lamp. Each of these fibers was 1.0 m in length with a core diameter of $200.0 \mu\text{m}$. Figure (3.9) shows the transmission efficiency of the fibers, marked as UV/VIS, for the region of wavelength interest which was from 3500.0 – 4500.0 angstroms. These fibers were purchased from Oriel Corporation.

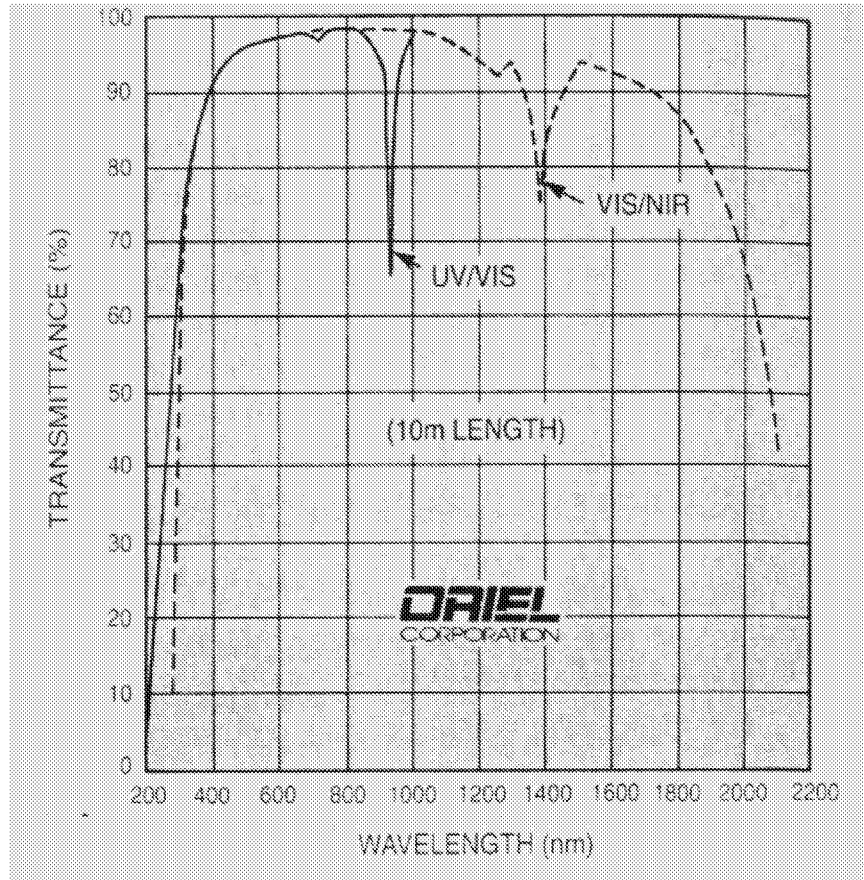


Figure (3.9) Transmission efficiency of the fibers used in MACS and marked as UV/VIS. The region of wavelength interest in MACS was from 3500.0 –4500.0 angstroms.

All optical fibers transmit light signals by total internal reflection. That is, if a ray of light in a medium of refractive index n_1 strikes the interface with another medium of refractive index n_2 ($n_2 < n_1$) at an angle θ , and if θ is greater than θ_c , the ray is totally reflected back in to the first medium where θ_c is given by equation (3.5).

$$\theta_c = \sin^{-1}\left(\frac{n_2}{n_1}\right) \tag{3.5}$$

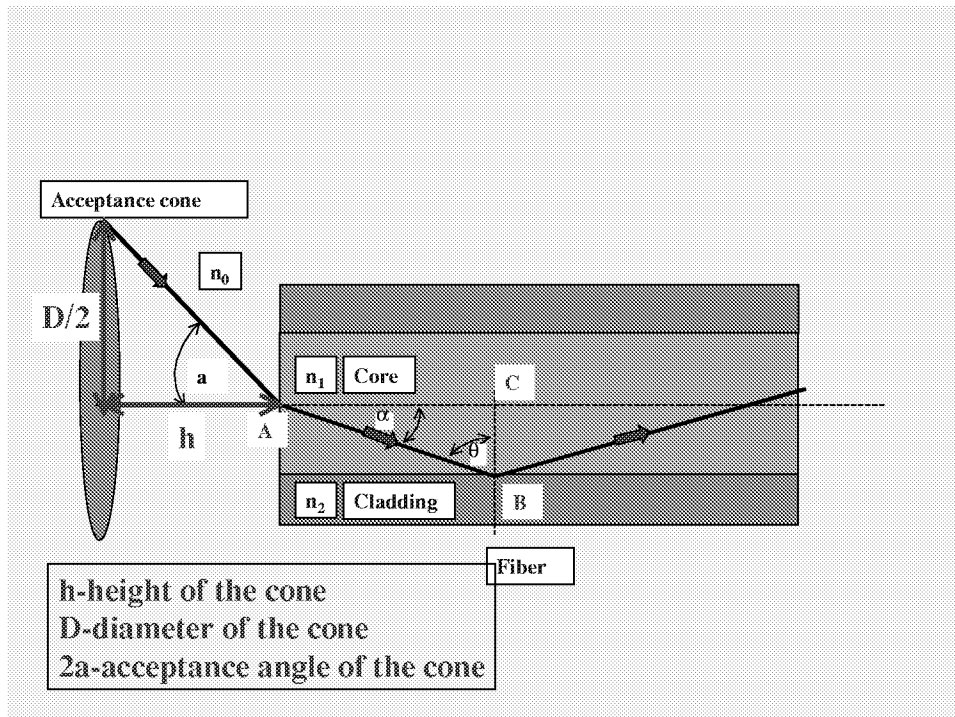


Figure (3.10). Schematic diagram depicting the light ray path at the focal plane of the telescope into a fiber optic cable.

Figure (3.10) is a schematic drawing depicting the light ray path at the focal plane of the telescope into a fiber optic cable. At point (A) applying the Snell's law gives the relationship between angles (a and α) and refractive indices (n_0 and n_1) by equation (3.6).

$$\sin(a) \times n_0 = \sin(\alpha) \times n_1 \quad (3.6)$$

Now from triangle ABC the expression for angle θ is given by equation (3.7).

$$\begin{aligned} \theta &= 90 - \alpha \\ \therefore \sin(\theta) &= \cos(\alpha) \\ &= \sqrt{1 - \sin^2(\alpha)} \end{aligned} \quad (3.7)$$

At the critical angle ($\theta = \theta_c$) using equations (3.5), (3.6) and (3.7) the expression for the acceptance angle (**a**) in terms of the refractive indices is given by equation (3.8).

$$\sin(\mathbf{a}) = \frac{\sqrt{n_1^2 - n_2^2}}{n_0} \text{ and } n_0 \sim 1 \quad (3.8)$$

The sine of the acceptance angle (**a**) is defined as the numerical aperture (**NA**). Also from figure (3.10), the expression for $\sin(\mathbf{a})$ is given by equation (3.9).

$$\boxed{\begin{aligned} \sin(\mathbf{a}) &= \frac{D/2}{h} \\ &= \frac{1}{2 \frac{h}{D}} \\ &= \frac{1}{2(\mathbf{F/\#})} \end{aligned}} \quad (3.9)$$

The fibers used in MACS have a high purity UV grade silica core and silica glass cladding with a numerical aperture of 0.27. This corresponds to an acceptance cone angle (**2a**) of 31.0 degrees and an f-number (**F/#**) of 1.9.

All the light rays entering the fiber within the acceptance cone is totally reflected at the core-cladding boundary inside the fiber and the signal is transmitted to the other end. That is, all light rays within the acceptance cone entering the fiber at an angle less than the acceptance angle (**a**) strike the core-cladding interface at an angle greater than the critical angle θ_c . This fulfils the requirement for total internal reflection at the core-cladding boundary.

The f-number of the telescope used in MACS was F/6.3, which corresponds to an acceptance cone of 9.1 degrees. However this value was much less than the acceptance cone of 31.0 degrees for the fibers. Therefore all the light that was focused onto each of the fibers at the focal plane of the telescope was expected to be transmitted.

The emergent cone from the other end of the fiber is dependent upon the input illumination, the fiber properties and the layout of the fiber bundle. For long fibers, the fiber properties dominate, while for short fibers (< 1.0 to 2.0 m) the input conditions dominate. Since the fibers in MACS were 1.0 m in length the emergent cone was expected to closely resemble the input conditions.

3.2.3 The lenses

The spectrograph contained two lenses of diameter 8.0 cm each with f-numbers F/3.9 and F/2.0. The former functioned as a collimator to collimate the light given out by the fibers. This enabled the grating to receive collimated light for dispersion. The latter acted as a focusing lens to focus the dispersed light on to the camera. Spindler & Hoyer manufactured these achromatic lenses. An anti UV-reflective coating was applied on the lens surfaces in order to enhance the transmission below 4000.0 angstrom. Figure (3.11) shows the reflection properties for the anti UV-reflective coating. Very low reflection ensures greater transmission. This was achieved with ARB2 UV chemical coating.

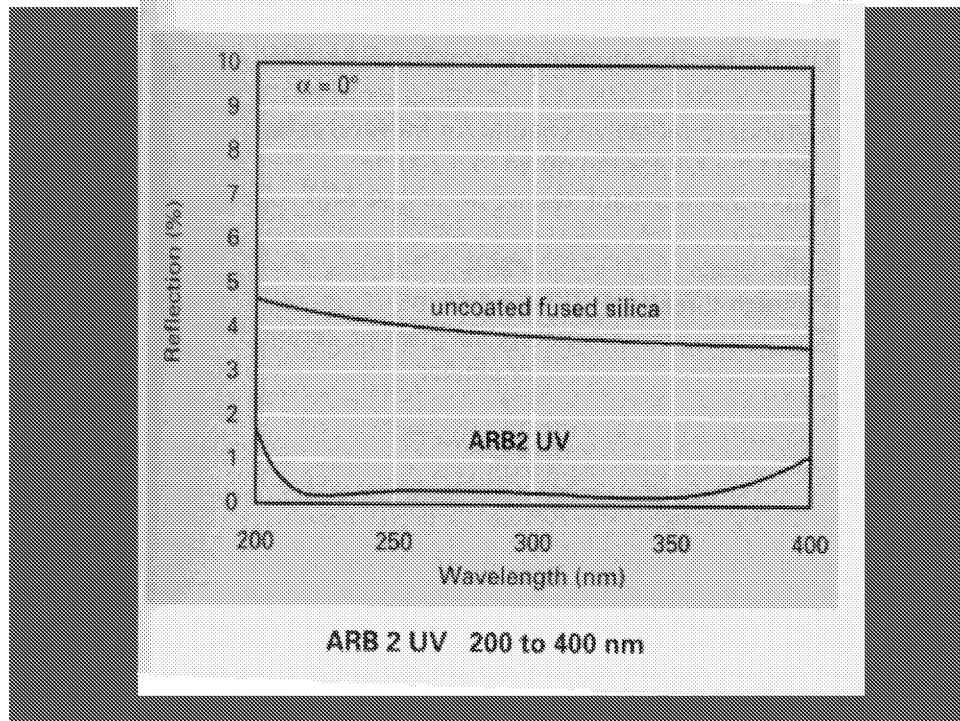


Figure (3.11). Reflection properties for the anti UV-reflective coating on the collimating and the camera lenses used in the spectrograph.

3.2.4 The grating

The dispersing element used in MACS was a square transmission grating of dimensions $6.0 \times 6.0 \text{ cm}^2$ with 6000.0 lines per cm and anti UV-reflective coating for enhanced transmission. Figure (3.12) shows the transmission properties for the anti UV-reflective coating. This grating was manufactured by American Holographic.

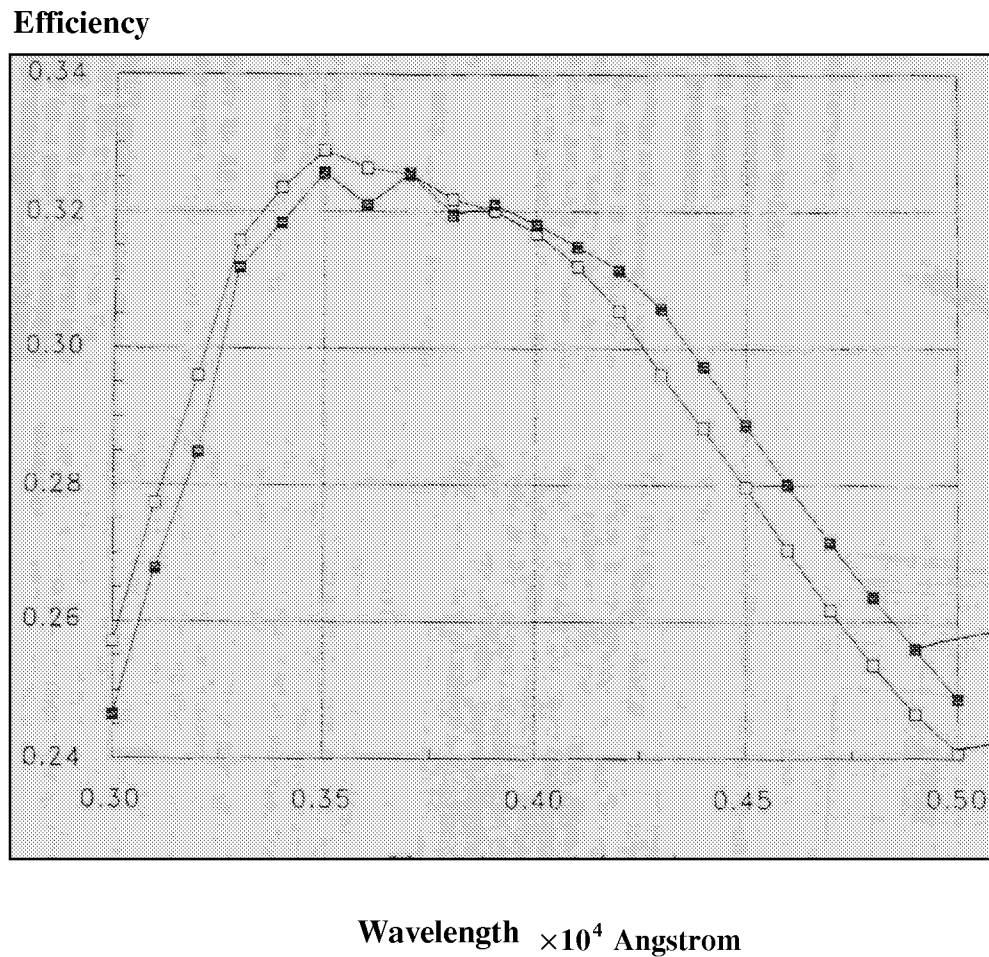


Figure (3.12). Transmission properties at normal incidence for the anti UV-reflection coating on the transmission grating. Here the back surface reflection is not considered. The substrate material is fused silica. The black squares pertain to the grating used in MACS.

3.2.5 The camera

The camera used in MACS was a CCD camera with a back thinned SITE 512.0×512.0, 24.0μm square chip and controlled with *PMIS* camera-control software. *PMIS* contains a powerful command interpreter designed for automating repetitive or complex actions. The camera can also be thermoelectrically cooled from 50.0° – 60.0° C below ambient and was manufactured by Apogee Instruments, Inc. Figure (3.13) is a plot of the quantum efficiency (QE) curve for the for the CCD chip in the camera.

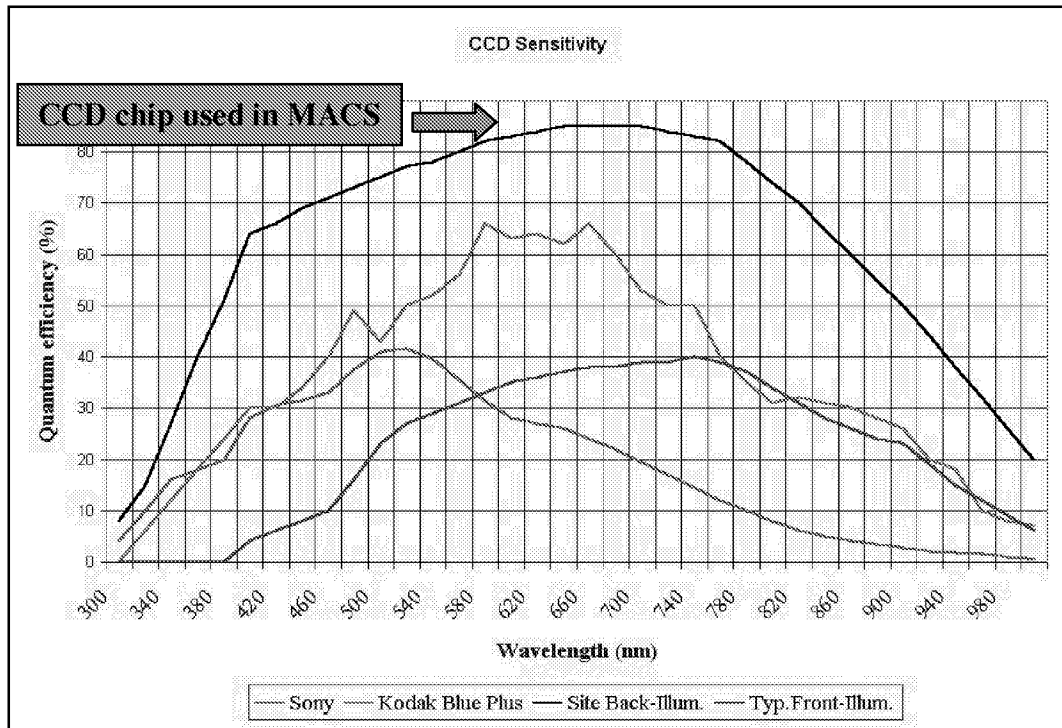


Figure (3.13). Quantum efficiency (QE) curve for the back thinned SITE 512.0×512.0, 24.0μm square chip used in MACS. This chip also featured a full well depth in excess of 300,000.0 electrons, a dynamic range of ~ 90.0 dB and a readout time of ~ 5.0 seconds with an ISA card.

3.3 Analytical expressions for the integration time, the spectral resolution and the spatial resolution

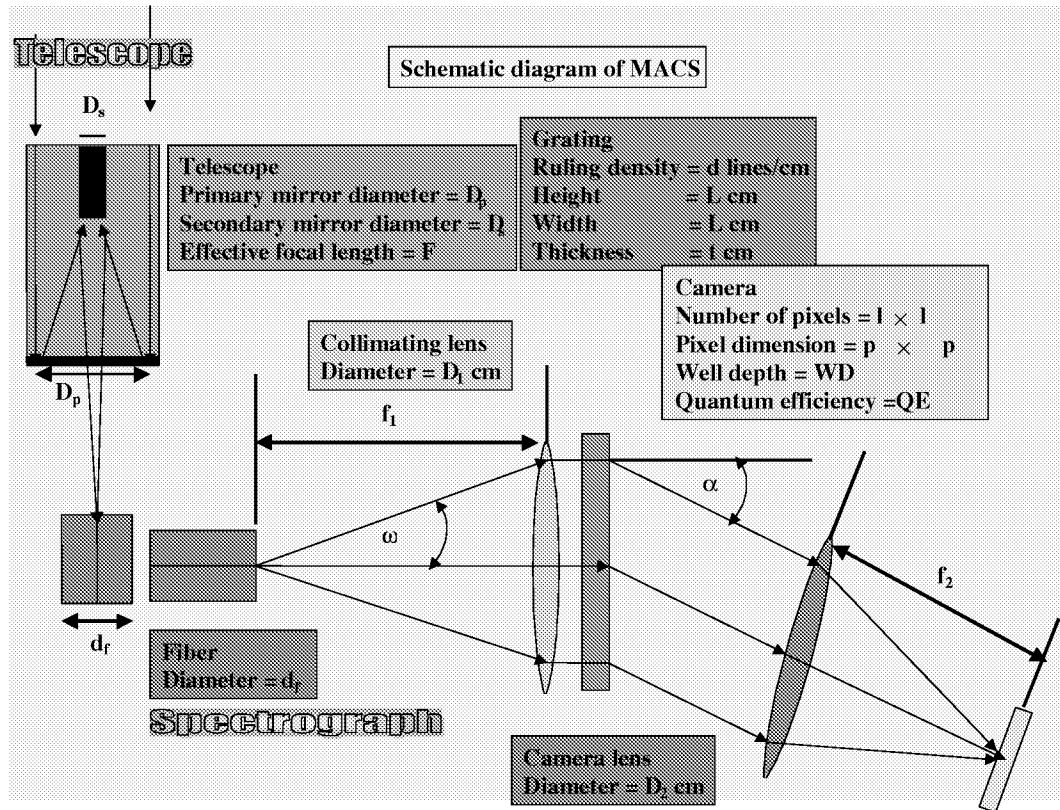


Figure (3.14). Schematic diagrams of the optical components that make up MACS and the parameters that determine the spatial and the spectral resolutions.

Figure (3.14) is a schematic diagram of the optical components that contributed to the operation of MACS and the physical parameters of the different components that determined the spectral and the spatial resolutions. In MACS the fibers substituted for a slit in a slit based spectrograph.

Consider a single fiber of diameter ($\mathbf{d_f}$) and approximate the circular end of the fiber to a square of side ($\mathbf{d_f}$). The projected fiber width (\mathbf{w}) and height (\mathbf{h}) on the camera focal plane are, respectively, given by equation (3.10) and equation (3.11).

$$\mathbf{w} = \mathbf{d_f} \left(\frac{\mathbf{f_2}}{\mathbf{f_1}} \right) \frac{\cos(\beta)}{\cos(\alpha)} \quad (3.10)$$

$$\mathbf{h} = \mathbf{d_f} \left(\frac{\mathbf{f_2}}{\mathbf{f_1}} \right) \quad (3.11)$$

In equation (3.10) (β) is the angle of incidence on the grating and is zero for normal incidence, which is the case for MACS. The direction of the dispersion is along (\mathbf{w}).

For normal incidence the grating equation is given by equation (3.12).

$$\mathbf{d} \sin(\alpha) = \mathbf{m} \lambda \quad (3.12)$$

In equation (3.12) (\mathbf{d}) is the ruling density, (α) the diffraction angle, (\mathbf{m}) the diffraction order and (λ) the wavelength.

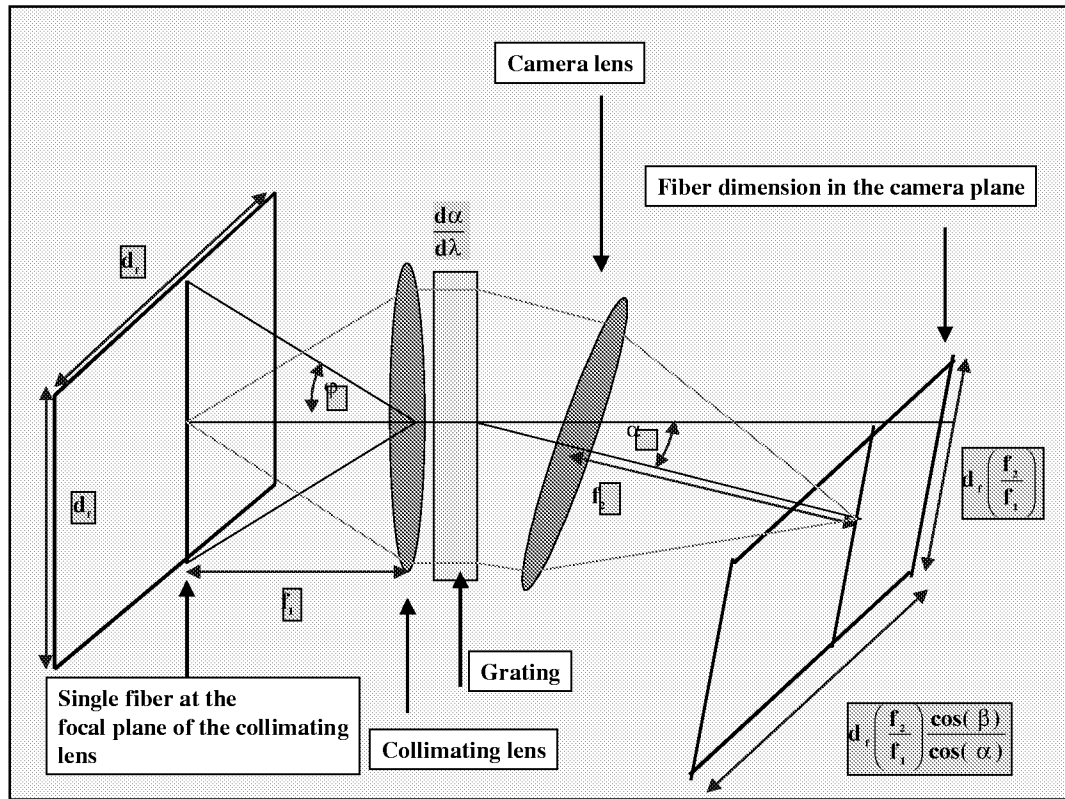


Figure (3.15). Schematic diagram showing the projected width and height of a single fiber on the camera plane.

Figure (3.15) is a schematic diagram showing the projected width and height of a single fiber on the camera plane.

For collimated light incident on the grating the angular dispersion is given by $(d\alpha/d\lambda)$, with the dispersion parallel to the rulings on the grating. Then the linear dispersion is given by $(f_2 \times (d\alpha/d\lambda))$ where (f_2) is the focal length of the camera lens.

Using equation (3.12) the angular dispersion (**AD**) and the linear dispersion (**LD**) are given, respectively, by equation (3.13) and equation (3.14).

$$\begin{aligned} \mathbf{AD} &= \frac{d\alpha}{d\lambda} \\ &= \frac{m}{d \cos(\alpha)} \end{aligned} \tag{3.13}$$

$$\begin{aligned} \mathbf{LD} &\equiv \frac{dl}{d\lambda} \\ &= f_2 \frac{d\alpha}{d\lambda} \\ &= \frac{f_2 m}{d \cos(\alpha)} \end{aligned} \tag{3.14}$$

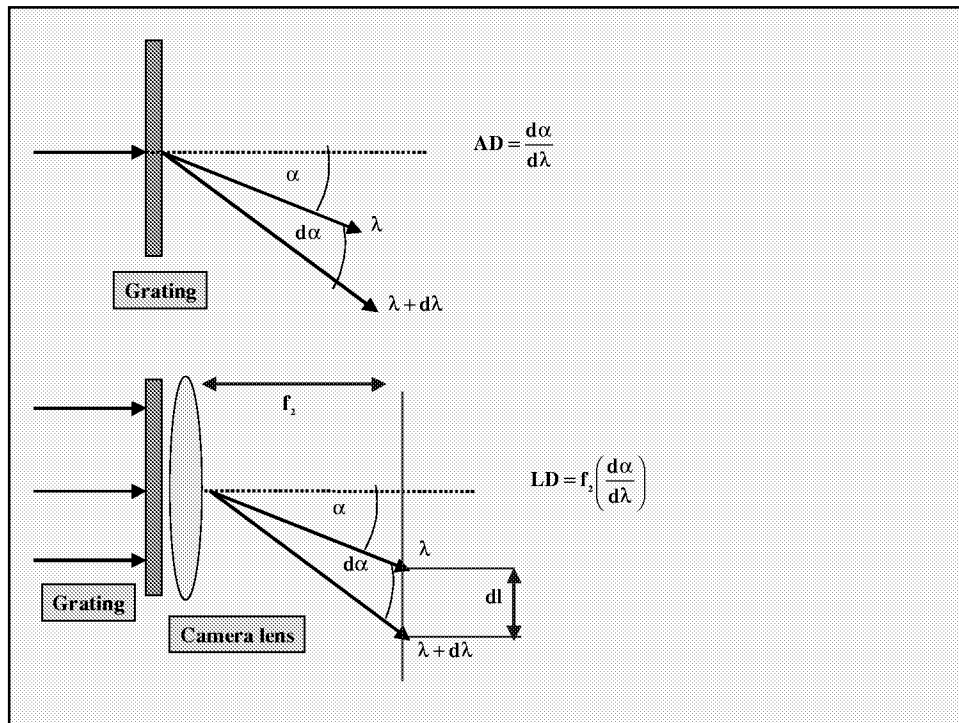


Figure (3.16). Schematic diagram of the dispersing element showing the angular and the linear dispersions.

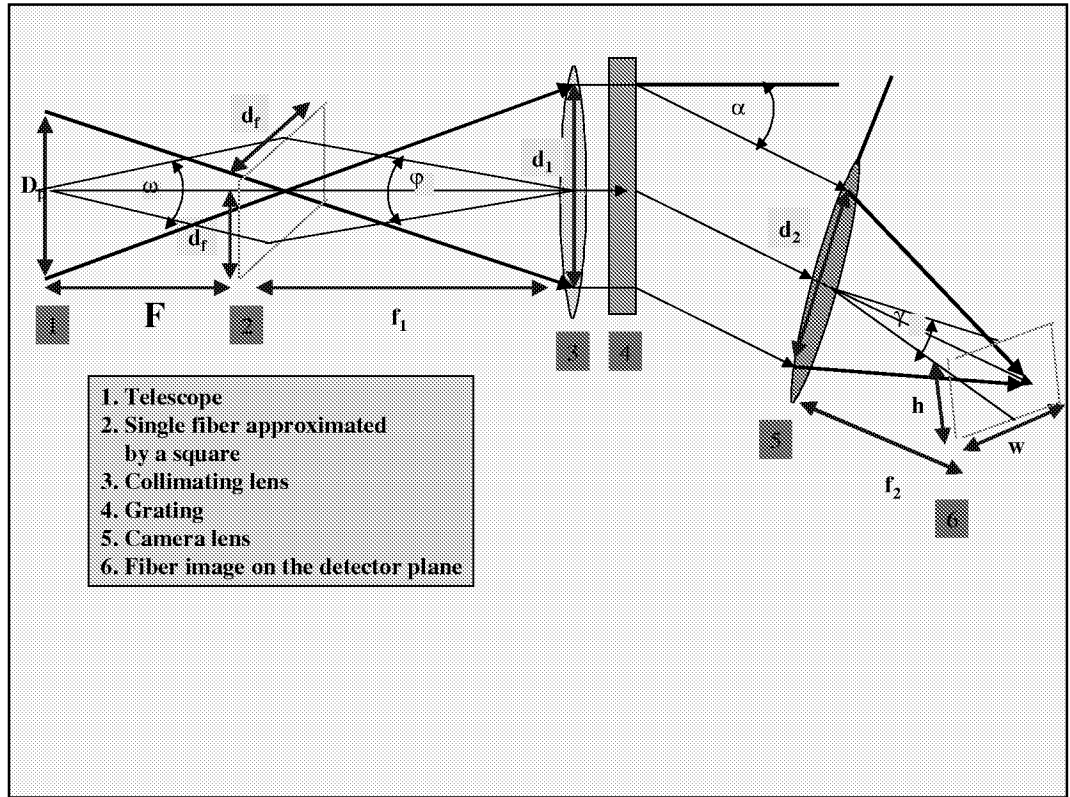


Figure (3.17). Schematic layout of the slit spectrometer. In this diagram collimated light is incident on the grating.

From figure (3.17) the height and width of the entrance slit (single fiber) subtend angles ω and ϕ on the sky and the collimating lens, respectively, and are given by equation (3.15) and equation (3.16).

$$\omega = \frac{D_p}{F} \tag{3.15}$$

$$\phi = \frac{d_f}{f_1} \tag{3.16}$$

If for the CCD detector the pixel width is (\mathbf{p}) then it needs to be decided on how many pixels are to be allowed to match the image width (\mathbf{w}). The usual convention is to consider a proper match to be one where two pixels cover the width (\mathbf{w}). However in situations constrained by, time, amount of light expected from the object to be studied, transmission efficiency of the optics and resources available in obtaining the desired optical components, the decision rests on the compromise between resolution and allowing for sufficient transmission of light to the detector.

In the absence of such constraints, say (\mathbf{n}) number of pixels are to be matched to the image width (\mathbf{w}), then from equations (3.10), (3.11) and (3.15) the expression for the pixel width (\mathbf{w}) is given by equation (3.17).

$$\begin{aligned}
 \mathbf{np} &= \mathbf{w} \\
 &= \mathbf{d}_f \left(\frac{\mathbf{f}_2}{\mathbf{f}_1} \right) \frac{\cos(\beta)}{\cos(\alpha)} \\
 &= \omega \mathbf{F} \left(\frac{\mathbf{f}_2}{\mathbf{f}_1} \right) \frac{\cos(\beta)}{\cos(\alpha)} \\
 &= \omega \left(\mathbf{D}_p \frac{\mathbf{f}_1}{\mathbf{d}_1} \right) \left(\frac{\mathbf{f}_2}{\mathbf{f}_1} \right) \frac{\cos(\beta)}{\cos(\alpha)} \\
 &= \omega \mathbf{D}_p \frac{\mathbf{f}_2}{\mathbf{d}_1} \frac{\cos(\beta)}{\cos(\alpha)}
 \end{aligned}
 \tag{3.17}$$

In equation (3.17) the relationship ($\mathbf{f}_1/\mathbf{d}_1 = \mathbf{F}/\mathbf{D}_p$) is used together with the physical parameter for the beamwidth (\mathbf{d}_1) at the collimating lens, as shown in figure (3.17). Here it is assumed that the grating diameter is at least (\mathbf{d}_1).

Consider the spectrometer slit of width (d_f) illuminated with light of wavelengths (λ) and ($\lambda + d\lambda$). The slit image in each of these wavelengths will have a width (w) on the detector. From equation (3.14) the separation between the centers of these two images is given by equation (3.18).

$$dI = \frac{f_2 m}{d \cos(\alpha)} d\lambda \quad (3.18)$$

Now defining **spectral purity** ($\delta\lambda$) as the wavelength difference for which ($\Delta I = w$), ensuring the images are just resolved. Substituting this condition in equation (3.18) and also using equation (3.10) the spectral purity is given by equation (3.19).

$$\delta\lambda = \frac{w}{d \cos(\alpha)} \frac{f_2 m}{d_f d \cos(\beta)} = \frac{d_f d \cos(\beta)}{m f_1} \quad (3.19)$$

where ($\beta = 0$) for collimated light incident on the grating. However it needs to be noted that the expression for the spectral purity given by equation (3.19) cannot be smaller than the spectral purity limit ($\delta\lambda_0$) set by diffraction. The resolving power (R) of a grating is the ratio between the smallest change of wavelength that the grating can resolve and the wavelength at which it is operating. The resolving power is given by equation (3.20).

$$R = \frac{\lambda}{\delta\lambda} \quad (3.20)$$

From figure (3.18) the path difference (**DO**) between contributions from the center and the edge of the grating is given by equation (3.21).

$$\mathbf{DO} = \frac{\mathbf{L}'}{2} \sin(\delta\alpha) \quad (3.21)$$

Then the associated phase difference (ξ) is given by equation (3.22).

$$\begin{aligned} \xi &= \frac{2\pi}{\lambda} \times \mathbf{DO} \\ &= \frac{2\pi}{\lambda} \times \frac{\mathbf{L}'}{2} \sin(\delta\alpha) \\ &= \frac{2\pi}{\lambda} \times \frac{\mathbf{L}'\mathbf{Z}_0}{2\mathbf{f}_2} \end{aligned} \quad (3.22)$$

The intensity distribution (\mathbf{I}_z) at the focal plane, due to diffraction, is given by equation (3.23).

$$\mathbf{I}_z = \mathbf{I}_0 \frac{\sin^2(\xi)}{\xi^2} \quad (3.23)$$

The first minimum of equation (3.23) is for (ξ) given by equation (3.24).

$$\begin{aligned} \xi &= \frac{2\pi}{\lambda} \times \frac{\mathbf{L}'\mathbf{Z}_0}{2\mathbf{f}_2} \\ &= \pi \end{aligned} \quad (3.24)$$

From equation (3.14) two wavelengths that are differing by ($\delta\lambda_0$), with each producing a diffraction pattern at the focal plane, as shown in figure (3.18), will be displaced by ($\delta\mathbf{l}_0$) and given by equation (3.25).

$$\delta\mathbf{l}_0 = \frac{\mathbf{f}_2 \mathbf{m}}{\mathbf{d} \cos(\alpha)} \delta\lambda_0 \quad (3.25)$$

The closest the two wavelength patterns could be without merging into each other is given by the Rayleigh's criterion. As depicted in figure (3.18) the two wavelength patterns differing by $(\delta\lambda_0)$ could just be resolved if the maximum of one pattern coincides with the first minimum of the other. In this case $(\delta l_0 = Z_0)$. Substituting (Z_0) from equation (3.24) in equation (3.25) and from figure (3.18) using $(L' = L \cos(\alpha))$ gives the following expression for $(\delta\lambda_0)$ given by equation (3.26).

$$\delta\lambda_0 = \frac{d}{Lm} \lambda \tag{3.26}$$

$$= \frac{Nm}{\lambda}$$

$$= \frac{R_0}{\lambda}$$

where (N) is the total number of grooves in the grating.

The theoretical resolving power R is then given by equation (3.27).

$$R_0 = Nm \tag{3.27}$$

The values for the physical parameters of the optical components in MACS are given in equation (3.28) and table (3.1).

$m = 1.0$ $\beta = 0^\circ$ $N = 3.6 \times 10^4$ $f_1 = 31.0 \text{ cm}$ $f_2 = 16.0 \text{ cm}$ $d = 1.67 \times 10^{-3} \text{ mm}$ $d_f = 200.0 \text{ } \mu\text{m}$ $\text{pixel} = 24.0 \text{ } \mu\text{m}$ $R_0 = 3.6 \times 10^4$	(3.28)
----------------------------------------------------------------------------------------------------------------------------------------------------------------------------------------------------------------------------------------------------------------------	--------

Table (3.1). A table showing the values for the angle of diffraction, the linear dispersion, the line width and the resolvable theoretical wavelength range for three different wavelengths using the physical parameters of the optical components used in MACS. In column 3 the reciprocal linear dispersion is calculated per pixel, which is the dimension of a pixel in the CCD camera used in MACS.

wavelength \AA	diffraction angle α degree	reciprocal linear dispersion $\frac{1}{LD} \text{\AA}/\text{pixel}$	spectral purity $\delta\lambda \text{\AA}$	resolvable theoretical wavelength range $\delta\lambda_o \text{\AA}$
3600.0	12.47	2.44	10.77	10.00
4000.0	13.86	2.43	10.77	9.00
4500.0	15.63	2.41	10.77	8.00

The exposure time allowed to record the spectra is dependent on the source brightness, the light collecting area, the transmission efficiency of the telescope-spectrograph system, the slit dimension and the sensitivity of the detector. Consider a source of brightness given by equation (3.29).

$$f_{\lambda} \text{ Joules/sec/cm}^{-2}\text{/angs/steradians} \quad (3.29)$$

The flux received by the Schmidt-Cassegrain telescope is then given by equation (3.30).

$$f_{\lambda} \times \pi \left(\frac{D_p^2 - D_s^2}{4} \right) \text{ Joules/sec/angs/steradians} \quad (3.30)$$

where (D_p) and (D_s) are, respectively, the diameters of the primary and the secondary mirrors of the telescope.

The flux through a single fiber at the focal plane of the telescope is then given by equation (3.31).

$$f_{\lambda} \times \pi \left(\frac{D_p^2 - D_s^2}{4} \right) \frac{d_f}{F} \frac{d_f}{F} \text{ Joules/sec/angs} \quad (3.31)$$

In equation (3.31), (d_f / F) is the angle subtended by the height and width of a single fiber on the sky and F the effective focal length of the telescope.

Let (τ_λ) be the wavelength dependent transmission efficiency of the telescope-spectrometer combination.

The spectral flux received by a single pixel (E) is then given by equation (3.32).

$$E_\lambda = f_\lambda \times \pi \left(\frac{D_p^2 - D_s^2}{4} \right) \frac{d_f}{F} \frac{d_f}{F} \delta\lambda \frac{p^2}{wh} \times \tau_\lambda \text{ Joules/sec} \quad (3.32)$$

In equation (3.32) (w) and (h) are the projected fiber width and height on the detector and given by equations (3.10) and (3.11), respectively, ($\delta\lambda$) the spectral purity and (p) the dimensions of a square pixel. From equation (3.32) the number photons of wavelength (λ) and energy ($h_p c/\lambda$) incident on a pixel per unit time (N_{photons}) is then given by equation (3.33) where (h_p) and (c) are the Planck constant and the speed of light, respectively.

$$N_{\text{photons}} = \frac{E_\lambda}{h_p c/\lambda} \text{ sec}^{-1} \quad (3.33)$$

The basic detection mechanism of a CCD is related to the photoelectric effect where the light incident on the semiconductor produces electron-hole pairs. These electrons are then trapped in potential wells produced by numerous small electrodes. The maximum number of electrons that could be contained in each a pixel is called the well depth (WD). The quantum efficiency (QE) is the ratio of the actual number of photons detected to the number of photons incident at a given wavelength (λ). If the time taken

for a pixel to reach the well depth (**WD**) is (**T**) then the wavelength dependent integration time (**T**) is given by equation (3.34).

$$T = \frac{h \cdot c / \lambda}{E_{\lambda} \times (QE)_{\lambda}} \times (WD) \text{ seconds} \quad (3.34)$$

The physical parameters that are used in determining the integration time (**T**) are given in equation (3.35).

$D_p = 30.5 \text{ cm},$	$D_s = 10.2 \text{ cm}$	(3.35)
$d_f = 200.0 \text{ } \mu\text{m},$	$F = 192.0 \text{ cm}$	
$p = 24.0 \text{ } \mu\text{m},$	$f_1 = 31.0 \text{ cm}$	
$f_2 = 16.0 \text{ cm},$	$m = 1.0$	
$d = 1.67 \times 10^{-3} \text{ mm},$	$\alpha = \sin^{-1} \left(\frac{m\lambda}{d} \right)$	
$\beta = 0^{\circ},$	$\delta\lambda = 10.77 \text{ } \overset{0}{\text{A}}$	
$w = d_f \left(\frac{f_2}{f_1} \right) \frac{\cos(\beta)}{\cos(\alpha)},$	$h = d_f \left(\frac{f_2}{f_1} \right)$	
$c = 3.0 \times 10^8 \text{ ms}^{-1}$		
$h_p = 6.63 \times 10^{-34} \text{ Joules/sec}$		
$WD = 300,000$		
$QE(\lambda = 3600 \text{ } \overset{0}{\text{A}}) = 0.32$		
$QE(\lambda = 4000 \text{ } \overset{0}{\text{A}}) = 0.60$		
$QE(\lambda = 4500 \text{ } \overset{0}{\text{A}}) = 0.70$		

The transmission efficiency (τ_{λ}) is a wavelength dependent parameter that depends on the transmission efficiency of the collimating lens, the fibers, the camera lens and the grating used in MACS and its wavelength dependent values are listed in table

(3.2). The number of optical surfaces that contribute to the transmission efficiency are listed in table (3.3). Table (3.4) gives effective transmission efficiency at different wavelength by considering the wavelength dependent transmission efficiencies given in table (3.2) and the number of optical surfaces through which the the light has to pass before entering the detector and given in table (3.3). Table (3.5) gives the K-coronal brightness at 1.1 and 1.6 solar radii at different wavelengths.

Table (3.2), The transmission efficiencies of the fibers, the lenses and the grating for three different wavelengths. This information is from figure (3.9), figure (3.11) and figure (3.12).

Wavelength Angstrom	Fibers	Lenses	Grating
3600.0	0.70	1.0	0.33
4000.0	0.90	0.99	0.32
4500.0	0.92	0.98	0.29

Table (3.3). The list of lenses and the associated number of surfaces through which the incident light had to pass before entering the detector.

Optical element	Number of surfaces
Corrector plate	2
Focal reducer	4
Collimating lens	4
Camera lens	4
CCD glass protector	2

Table (3.4) The effective transmission efficiency ($\tau_{\lambda}^{\text{eff}}$) of MACS for the wavelengths 3600.0, 4000.0 and 4500.0 angstroms. The values are based on the information from tables (3.2) and (3.3).

Wavelength in angstrom	Effective transmission efficiency $\tau_{\lambda}^{\text{eff}} = \tau_{\text{fiber}} \times \tau_{\text{lenses}}^{\text{\#NS}} \times \tau_{\text{grating}}$ (NS=number of surfaces)
3600.0	0.23
4000.0	0.25
4500.0	0.19

Table (3.5) The K-coronal brightness at 1.1 and 1.6 solar radii for three different wavelengths during the solar maximum. The values were obtained from Allen (1973) from pages 172 and 176. The units are in ergs/sec/cm²/angs/steradians. (1 Joule=10⁷ ergs)

Wavelength Angstrom	$f_{\lambda} \times 10^{-4}$ at 1.1 solar radii	$f_{\lambda} \times 10^{-4}$ at 1.6 solar radii
3600.0	6.21	4.26
4000.0	8.71	5.99
4500.0	12.33	8.47

Substituting equation (3.32) in equation (3.34) the expression for the integration time (T) is given by equation (3.36).

$$T = \frac{(h \ c/\lambda) \times (WD)_p}{f_\lambda \times \pi \left(\frac{D_p^2 - D_s^2}{4} \right) \frac{d_f}{F} \frac{d_f}{F} \delta\lambda \frac{p^2}{wh} \times \tau_\lambda^{\text{eff}} \times (QE)_\lambda} \text{ seconds} \quad (3.36)$$

Using the values for the physical parameters from equation (3.35) and tables (3.4) and (3.5) gives the following chart, as shown in table (3.6), for the lower limit of the integration time (T) for the K-corona at 1.1 and 1.6 solar radii.

Table (3.6). Lower limit of the integration time for the K-coronal spectrum for MACS based on equation (3.36).

Wavelength angstrom	T in seconds at 1.1 solar radii	T in seconds at 1.6 solar radii
3600.0	122.0	177.0
4000.0	38.0	55.0
4500.0	27.0	39.0

However the actual integration time will depend on the amount of light absorbed by the various optical elements, the amount of light escaping the light collecting area of the optical elements and further contributions from the F-corona.

As for the spatial resolution of MACS the width of a single fiber of $200.0 \mu\text{m}$ and a plate scale of $0.107 \text{ arcseconds}/\mu\text{m}$ corresponds to a spatial scale of $21.4''$ (0.022 solar radii). Taking the height of a single fiber as $200.0 \mu\text{m}$ and from equation (3.11) the projected height of the fiber on the spatial direction of the detector is given by equation (3.37).

$$\begin{aligned} h &= 200\mu\text{m} \times \frac{16.0 \text{ cm}}{31.0 \text{ cm}} \\ &= 103.23\mu\text{m} \end{aligned} \tag{3.37}$$

This corresponds to $(103.23\mu\text{m} / 24.0\mu\text{m})$ 4.30 pixels in the spatial direction. Therefore from the spatial scale per fiber and the projected height of the fiber given in equation (3.37) the spatial resolution is given by equation (3.38).

$$\begin{aligned} \text{Spatial resolution} &= \frac{21.4''}{4.30 \text{ pixels}} \\ &= 4.98'' / \text{pixel} \\ &\sim 5.19 \times 10^{-3} \text{ solar radii} / \text{pixel} \end{aligned} \tag{3.38}$$

3.4 Cost of the instrument

Table (3.7). Cost associated with the construction of MACS.

Item	\$ 000	Manufacturer
Telescope	6.79	Meade Corporation
Solar filters	1.02	Thousand Oak Optical
Fibers	4.05	Oriel Instruments
Collimating lens	1.39	Spindler & Hoyer
Camera lens	1.58	Spindler & Hoyer
Grating	2.35	American Holographic
CCD camera	10.5	Apogee Instruments
Camera software	0.60	PMIS
Computer	2.90	DPS 9000
GPS	0.41	Eagle Map Guide Pro
Glass base	0.45	United Glass Company
Spectrograph body	7.25	Lorr Company
Generator	0.77	Honda
Total	40.31	

Chapter 4

OBSERVATIONAL RESULTS AND ANALYSES

4.1 Observational site

The coronal intensity measurements on the total solar eclipse of 11 August 1999 were conducted by Lake Hazar in Elazig, Turkey. The totality at this location ($38^{\circ}41' \text{ N}, 039^{\circ}14' \text{ E}$) lasted for 124 seconds. The second contact was at ~ 11.36 GMT. Also no clouds could be reported for the entire duration of the totality.

Figure (4.1) is a photograph of the total solar eclipse of 11 August 1999 taken from the Black Sea area. From figure (4.1) it is evident that the coronal brightness was almost uniformly distributed all around the sun. This was expected of the sun that was approaching maximum phase in 2000. This photograph also reveals a detached prominence in the southwest limb during the totality. Figure (4.2) depicts the path of the eclipse where the maximum duration of the totality occurred in Romania. Figure (4.3) shows the layout of MACS. The spectrograph lies on the metal box. The telescope, CCD-camera, and the computer were powered from a portable generator.

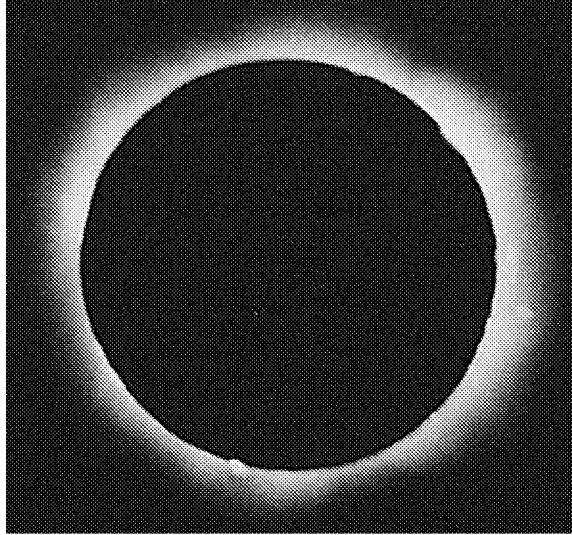


Figure (4.1). A photograph of the August 1999 eclipse from the Black Sea area. The photograph also reveals a detached prominence eruption above the southwest limb.

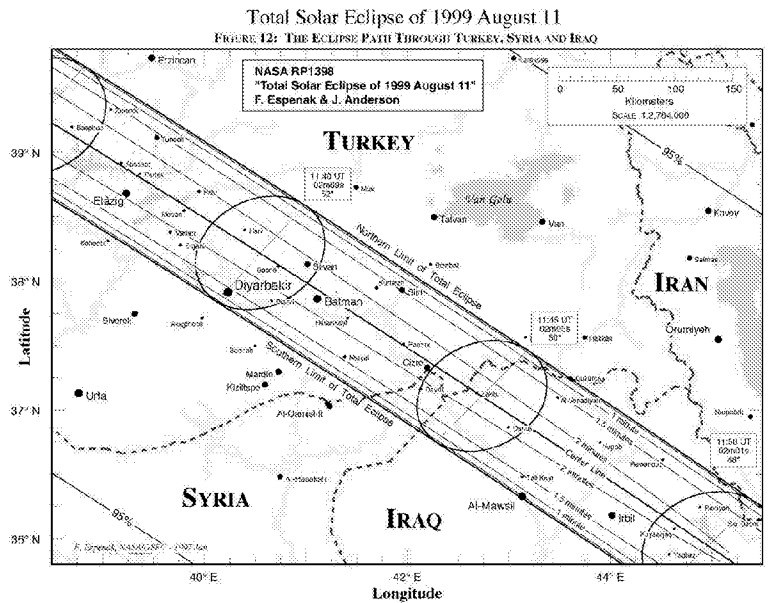


Figure (4.2). A map showing the path of the eclipse over Turkey.
 Courtesy: NASA Reference Publication 1398



Figure (4.3). A picture showing the layout of MACS and the telescope. The telescope is on a polar mount and MACS is laid out on the metal box.

4.2 Spectra observed by MACS

Figure (4.4) shows the spectra due to the twenty-one fibers being exposed to the sky and the remaining four fibers being exposed to the mercury calibration lamp in Elazig, Turkey. The horizontal lines indicate the prominent absorption lines in the sky spectrum and the four bright dots on the two ends correspond to the emission line at 4046.7 angstrom in the mercury calibration lamp. This information was used to determine the wavelength scale and was determined to have a linear dispersion of 2.39 angstrom/pixel. The positions numbered from 1 to 4 are the locations corresponding to

the temperature and the wind sensitive wavelength positions, which is explained in chapter-2.

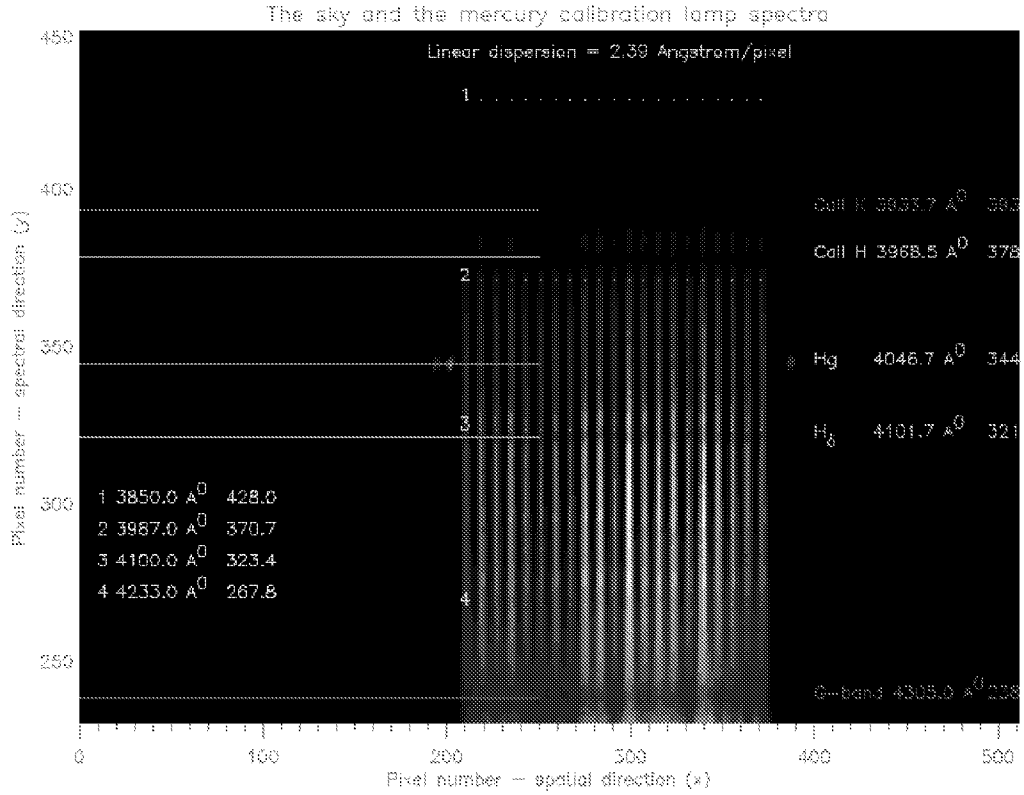
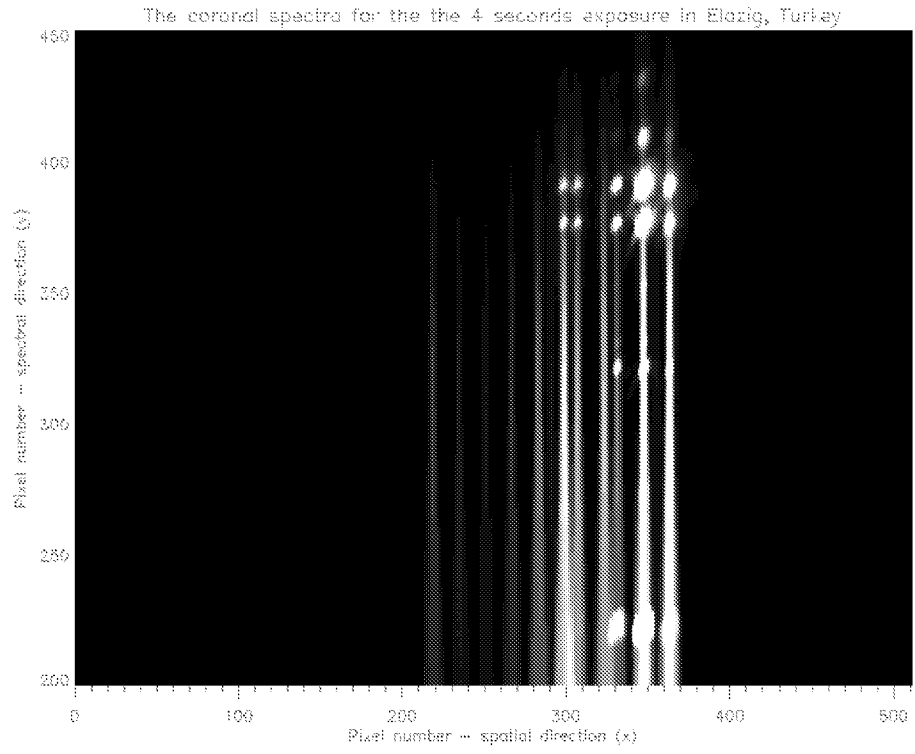


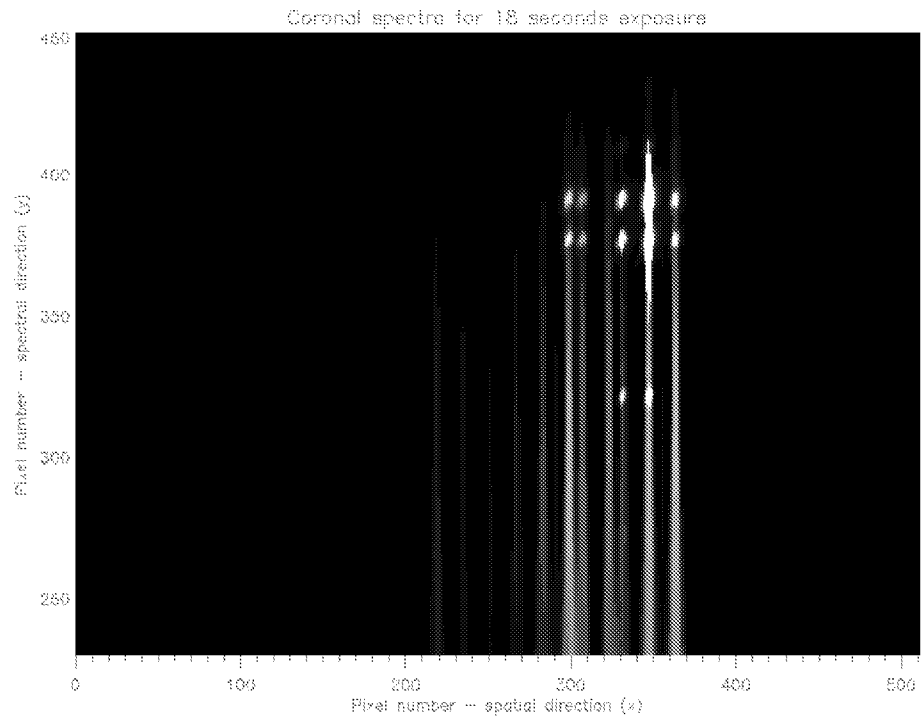
Figure (4.4). The spectra from twenty-one fibers exposed to the sky while four other fibers exposed to the mercury calibration lamp in Elazig, Turkey.

MACS was exposed to the coronal light during totality for duration of 4.0, 18.0 and 83.0-seconds. Figures (4.5 a), (4.5 b) and (4.5 c) show the spectra recorded by MACS for the above duration, respectively. Each vertical line corresponds to the spectrum from a single fiber with a total of twenty-one vertical lines corresponding to the twenty-one fibers located in the focal plane of the telescope.

(a)



(b)



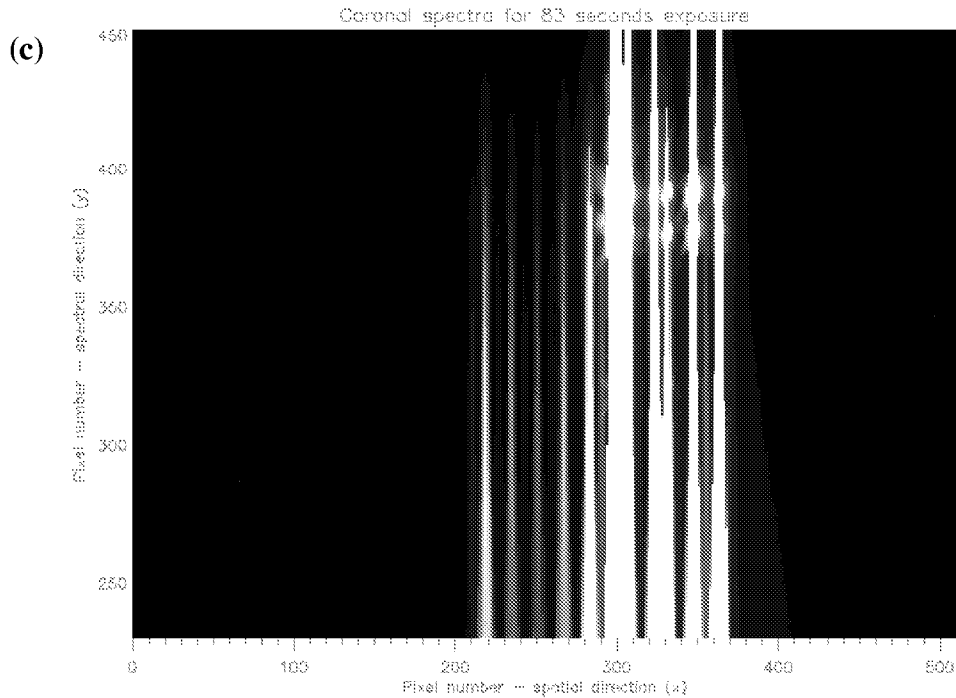


Figure (4.5 a, b, and c). The coronal spectra recorded by MACS for the exposure times 4.0, 8.0 and 83.0 seconds, respectively. Each vertical line corresponds to a spectrum from a single fiber. It is also clear that five of the fibers show emission lines.

4.3 Identifying the individual fiber location on the corona

Prior to the eclipse the sun was focused to the position identified by the moon during eclipse, as shown in figure (4.6). A solar filter attached at the front end of the telescope facilitated this process. The telescope was then allowed to track. Watching the direction of movement of the sun's image upon slewing the telescope due north and south with the auto controls the fiber #19 was oriented at the position perceived to be the earth's South Pole. Its relation to the heliographic coordinates was determined from the value listed for the P-angle for that day in, 'The Astronomical Almanac 1999'.

Figure (4.6) shows the envisaged location of the twenty-one fibers in the focal plane of the telescope during the eclipse. However the envisaged location could have drifted due to imperfect tracking or minute movements of the whole telescope structure for not being anchored on hard ground. Time constraints and the remoteness of the location compounded these problems. The term “envisaged” is emphasized because of the incapability of MACS at the present state to simultaneously record the image. This capability would have verified the exact location of the fiber rings during the eclipse.

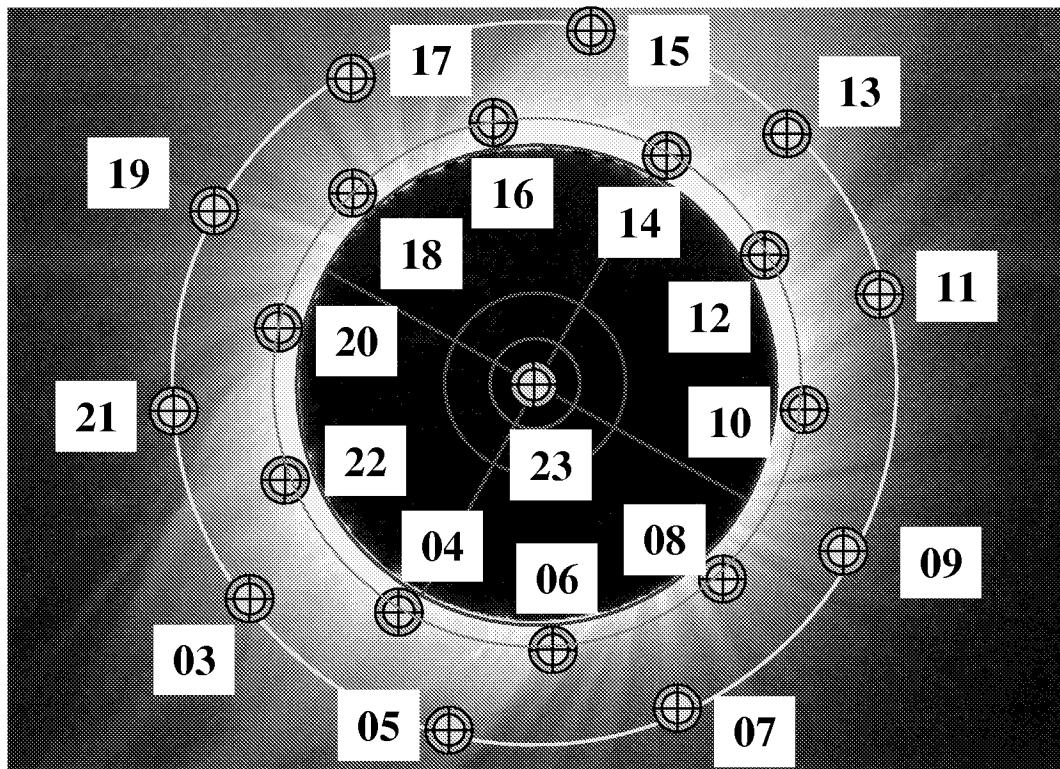


Figure (4.6). This picture shows the envisaged location of the twenty-one fibers in the focal plane during the eclipse. The inner and the outer rings correspond to 1.1 and 1.5 solar radii, respectively. The picture is not the actual eclipse on 11 August 1999. The fiber in the center was expected to record the background signal.

In order to identify the fiber orientation to a reasonable accuracy, some other information shown in the coronal spectra was utilized. This task was further aided by the very distinctive emission lines recorded in the spectra of five of the fibers as revealed in figure (4.5 a), figure (4.5 b), and figure (4.5 c). These emission lines are most pertinent to be from fibers exposed to prominence eruptions. Using imaging data at totality from other space and ground based solar instruments that are dedicated to observe specific solar features, it was now possible to infer the solar features that would have contributed to the emission lines in those fibers and accordingly orient the fibers.

The fibers that show emission lines, going from left to right in figure (4.5 a), figure (4.5 b), and figure (4.5 c), are the fibers numbered 22, 20, 19, 15 and 14 in figure (4.6). All the emission lines of fiber #19 correspond to the signatures of a prominence. Table (4.1) gives a list of prominence lines reported by Athay and Orrall (1957) from a prominence in the west limb of the total solar eclipse of 1952. Figure (4.7) shows the spectrum recorded by fiber #19. In this paper an emission line of Sr II listed at 3077.7 angstrom needs to be corrected as 4077.7angstrom. Comparison between table (4.1) and figure (4.7) reveals that the fiber #19 had recorded all the prominence emission lines reported by Athay and Orrall (1957), that falls within the wavelength range of the detector in MACS.

Table (4.1) List of the emission lines reported by Athay and Orrall (1957) of a prominence from the total solar eclipse of 1952. In this paper the Sr II line at 4077.7 has been erroneously recorded as 3077.7 angstrom. In the following table only the emission lines that could lie within the wavelength range of MACS is enumerated.

Emission line	Wavelength (angstrom)
Sr II	4215.5
H ₆ (2-6)	4101.7
Sr II	4077.7
He I	4026.3
Ca II H	3968.5
Ca II K	3933.7
H ₈ (2-8)	3889.1
H ₉ (2-9)	3835.4

Figure (4.7) shows the spectrum recorded by the fiber #19 in the 4.0 seconds exposure. This is after averaging over three pixels about its center and subtracting the dark signal. However the spectrum is not yet corrected for the wavelength sensitivity of the telescope-spectrometer system.

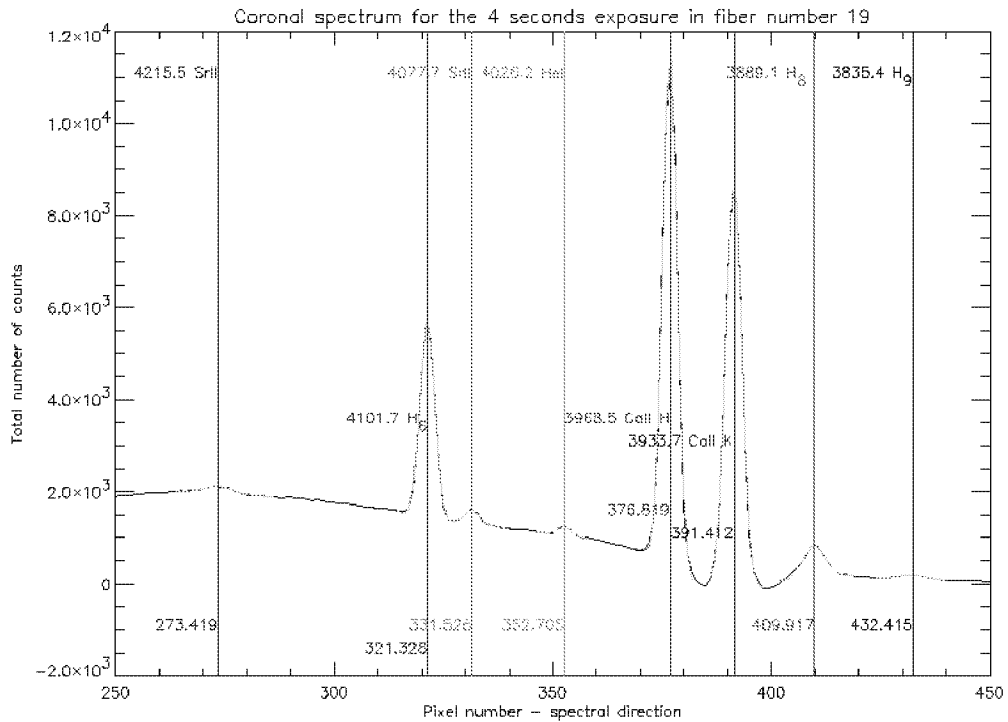


Figure (4.7). The spectrum recorded by the fiber #19 in the 4.0 seconds exposure. The emission lines and their corresponding wavelengths and pixel positions are identified.

From figure (4.7) and table (4.1) it is apparent that the fiber #19 had recorded all the prominence lines that fall within the wavelength range of the detector. The yellow curves superimposed on the spectrum are the gaussian curve fits. The wavelengths correspond to the peaks of the gaussian curves. However it needs to be yet ascertained whether the emission lines were correctly identified. This was verified by constructing a regression fit between the emission peaks and the peak positions. Figure (4.8) shows the result of the regression fit and the wavelength scale between different emission lines. These values give an average linear dispersion per pixel of 2.39 angstrom and matches with the linear dispersion per pixel calculated from the optical parameters of MACS.

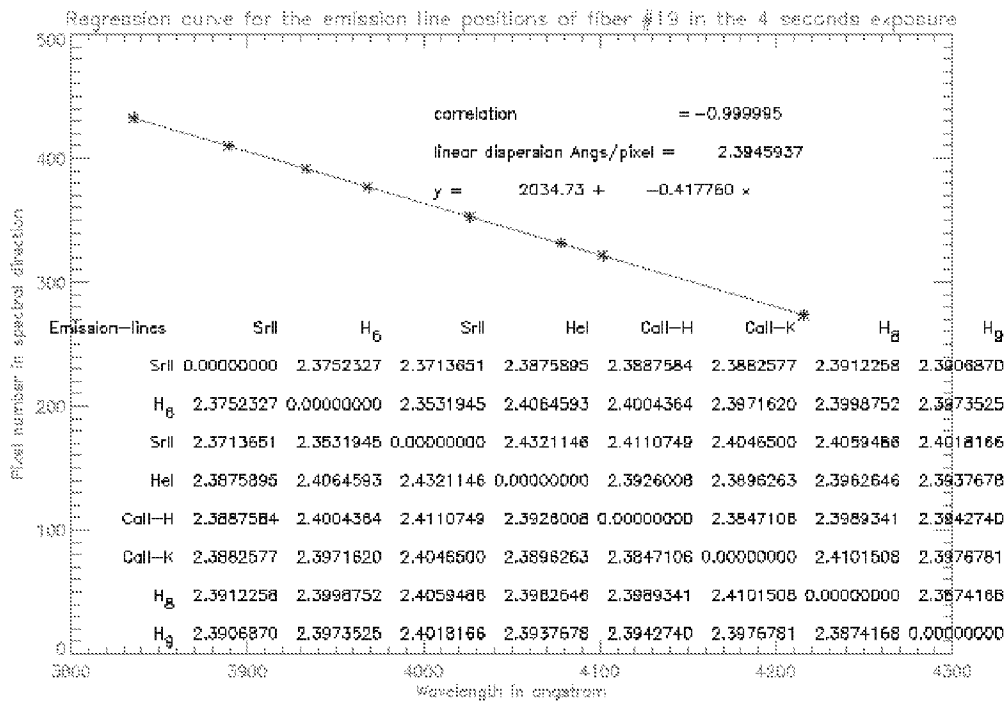


Figure (4.8). The regression fit between the emission line peaks and the peak positions of the fiber #19 in the 4.0 seconds exposure. The table incorporated shows the wavelength scale between any two-emission lines.

Furthermore, the spectrum recorded by the fiber #20 also shows all the emission lines from a prominence as listed in table (4.1). Figure (4.9) is the spectrum recorded by the fiber #20.

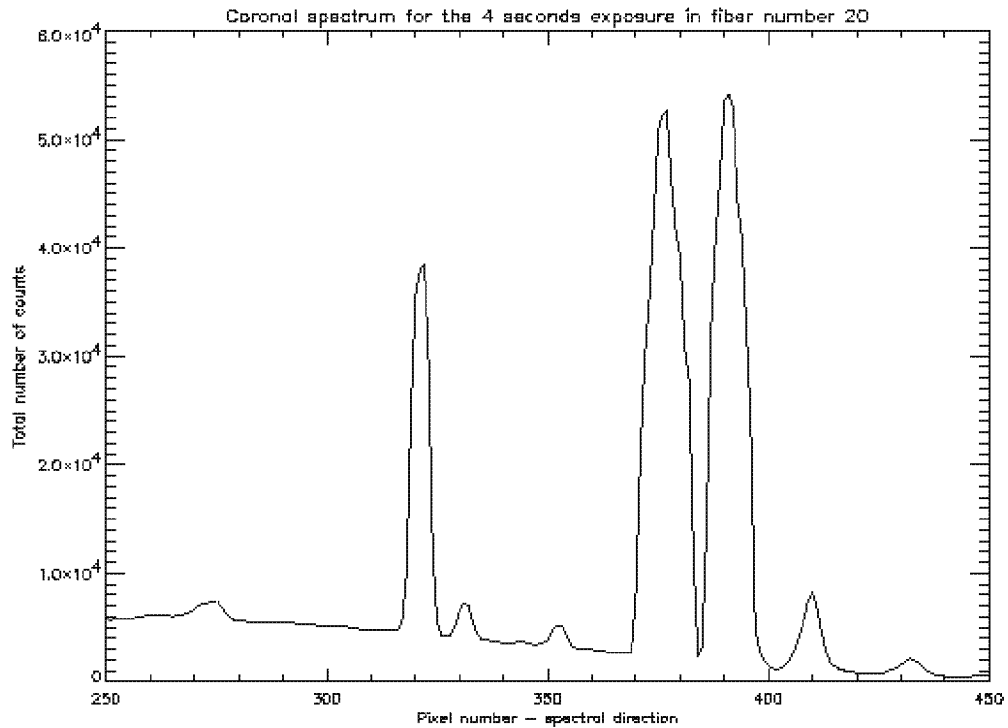


Figure (4.9). The spectrum recorded by the fiber #20 in the 4.0 seconds exposure. This too matches with all the emission lines recorded by the fiber #19 as shown in figure (4.7).

In table (4.2) is a list of emission lines, categorized as very strong and strong, from the flare of 18 September 1957 and reported by Jefferies, Smith and Smith (1959). Figure (4.10) shows the spectrum recorded by the fiber #22 in the 4.0 seconds exposure. This is after averaging over three pixels about its center and subtracting the dark signal. However the spectrum is not yet corrected for the wavelength sensitivity of the telescope-spectrometer system.

Table (4.2). List of the emission lines reported by Jefferies, Smith and Smith (1959) from the flare of 18 September 1957. This table only includes those emission lines categorized as very strong and strong. Also in this following table only the emission lines that could lie within the wavelength range of MACS is enumerated.

Emission line	Wavelength angstrom	Category
H₈	3889.1	strong
Ca II- K	3933.7	very strong
Ca II-H	3968.5	very strong
H_ε	3970.1	strong
H_δ	4101.7	very strong
H_γ	4340.5	very strong
HeI	4471.7	strong

Figure (4.10) showing the spectrum recorded by the fiber #20 does indicate that all but the **H_ε** line at 3970.1 angstrom listed in table (4.1) to be present. Since the linear dispersion is ~2.40 angstrom/pixel and, with the **H_ε** line at 3970.1 angstrom being only 2.0 angstrom away from the very strong Ca II-H line at 3968.5 angstrom, this may have caused this line to blend with the stronger line.

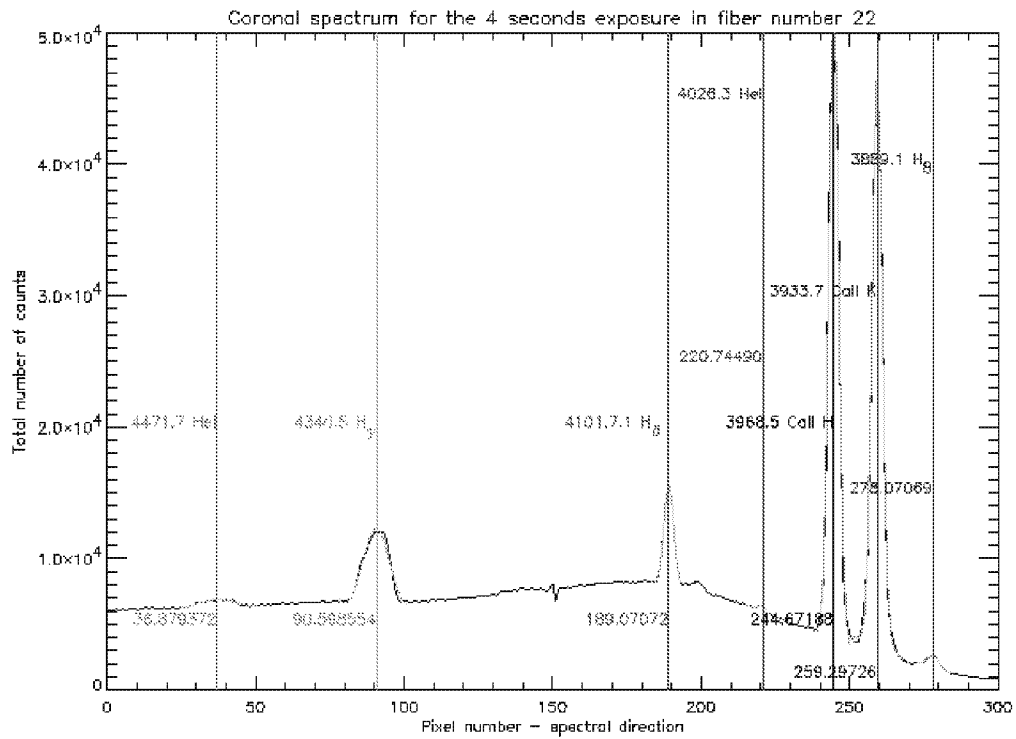


Figure (4.10). The spectrum recorded by the fiber #22 in the 4.0 seconds exposure. The emission lines and their corresponding wavelengths and pixel positions are identified.

Figure (4.11) shows the result of the regression fit and the wavelength scale between different emission lines of figure (4.10). These values give an average linear dispersion per pixel of 2.40 and matches with the linear dispersion per pixel calculated from the optical parameters for MACS, as listed in table (3.1).

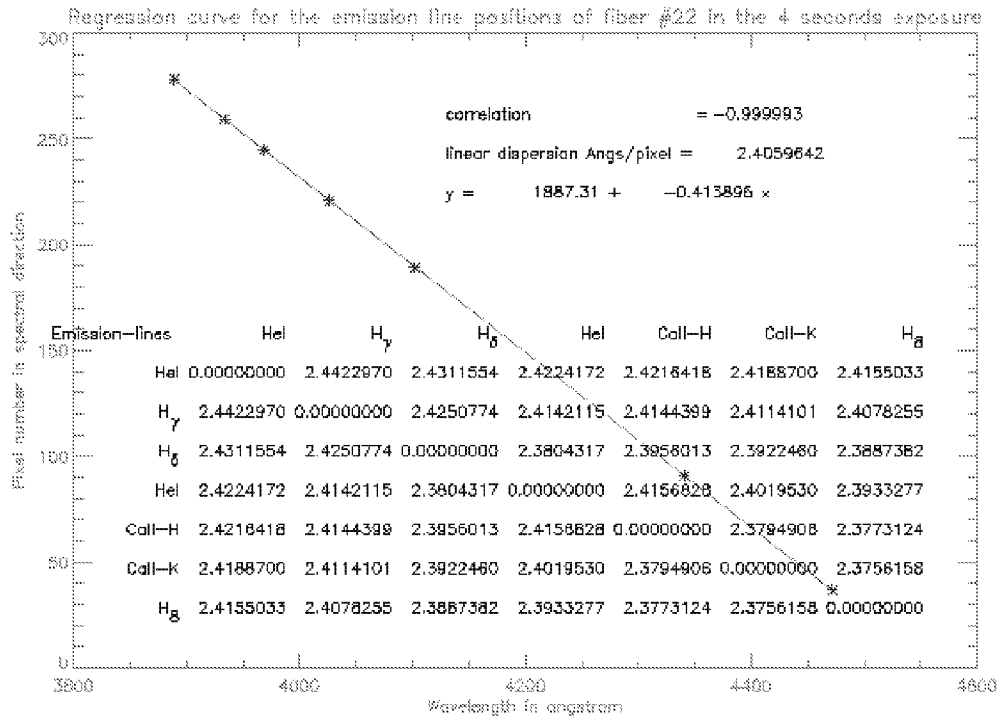


Figure (4.11). The regression fit between the emission line peaks and the peak positions of the fiber #19 in the 4.0 seconds exposure. The table incorporated shows the wavelength scale between any two-emission lines.

Based on the comparison on the spectra recorded by the fiber#19, fiber#20 and fiber #22 and the prominent emission lines expected of a prominence or a flare as listed in tables (4.1) and (4.2), respectively, it is reasonable to assume that these fibers were exposed to a prominence or a flare or to both of these features.

In order to identify the individual fiber location on the corona as accurately as possible the following analyses were performed.

1. Identifying the fibers exposed to prominence spectrum. The fibers #19, 20 and 22 were positively identified to have recorded the typical emission lines due to a prominence.
2. Orienting an eclipse photograph showing prominent eruptions with EIT images from SOHO on the day of the eclipse and matching these features. This matching was performed using the conspicuous prominence eruption identified at $\sim 68^{\circ}$ southwest in the EIT picture in 304 angstrom by SOHO at 11:26 UT with an eclipse photograph taken at $\sim 11:16$ UT from the Black Sea.
3. Drawing the polar axis of the earth, which is p-angle from the polar axis of the sun. The p-angle, which is the orientation of the polar axis of the sun with respect to the polar axis of the earth, was obtained from, 'The Astronomical Almanac 1999'.
4. Placing fiber #19 at the intersection point of the South Pole with the orbital circle at 1.5 solar radii. Prior to the eclipse the sun was focused to the position identified by the moon during eclipse, as shown in figure (4.6). A solar filter attached at the front end of the telescope facilitated this process. The telescope was then allowed to track. Watching the direction of movement of the sun's image upon slewing the telescope

due north and south with the auto controls the fiber #19 was oriented at the position perceived to be the earth's South Pole. The locations of the other fibers could be then determined based on their positions with respect to fiber #19.

Figure (4.12) shows the envisaged positions of the fibers on the corona based upon the above procedure.

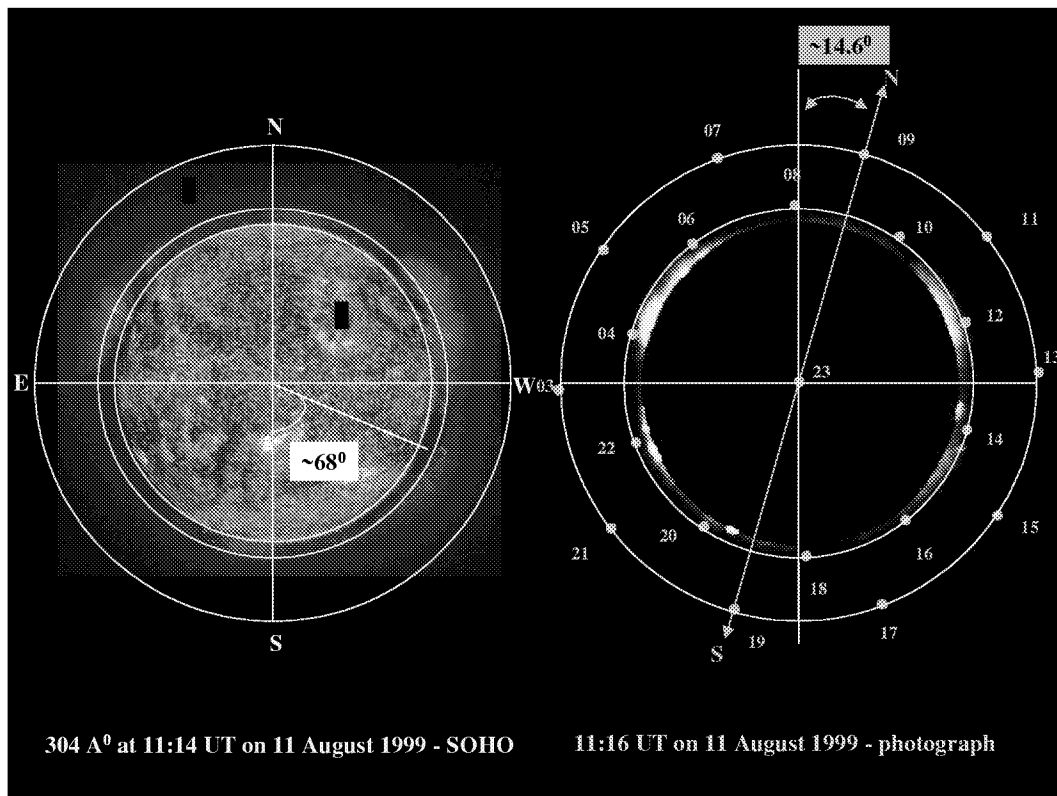


Figure (4.12). This is a comparison between solar image by SOHO in 304.0 angstrom at 11:14 UT and an eclipse photograph taken from the Black Sea at ~ 11:16UT. The orientation was made by matching the prominence eruption ~ 68° southwest in the SOHO image. The orientation of the polar axis of the sun with respect to the polar axis of the earth was obtained from the p-angle data given in, 'The Astronomical Almanac 1999' for 11 August 1999.

Figure (4.13), figure (4.14) and figure (4.15) are pictures of the sun taken by LASCO instrument on SOHO, EIT instrument on SOHO and radio image from Nancy and x-ray image by Yohkoh, respectively, on 11 August 1999.

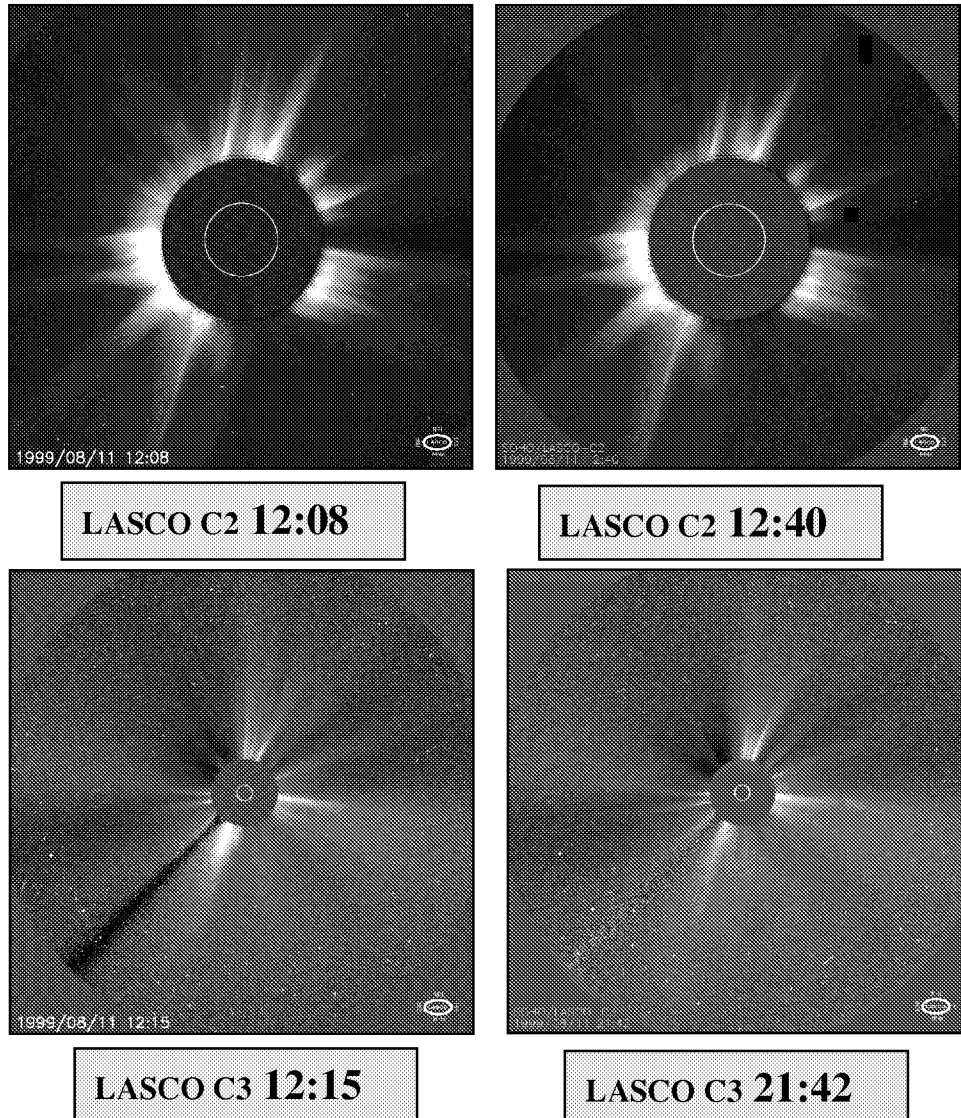


Figure (4.13). Images of the sun taken by the LASCO instrument on SOHO on the 11 August 1999. The numbers denote the time in UT. C2 and C3 are coronal images of the sun from 2.0 – 6.0 solar radii and 3.7 – 32.0 solar radii, respectively, using an externally occulted disk.

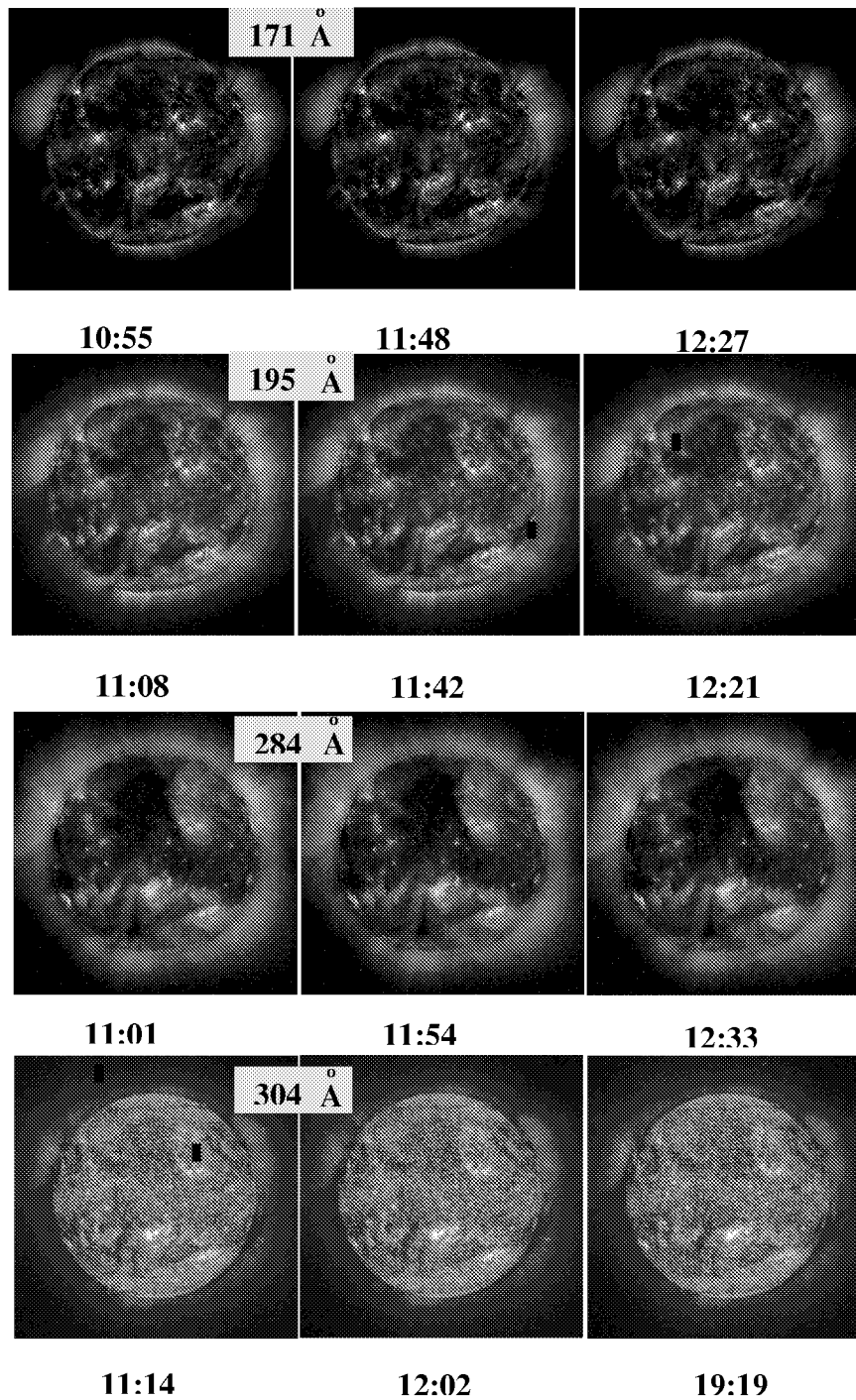
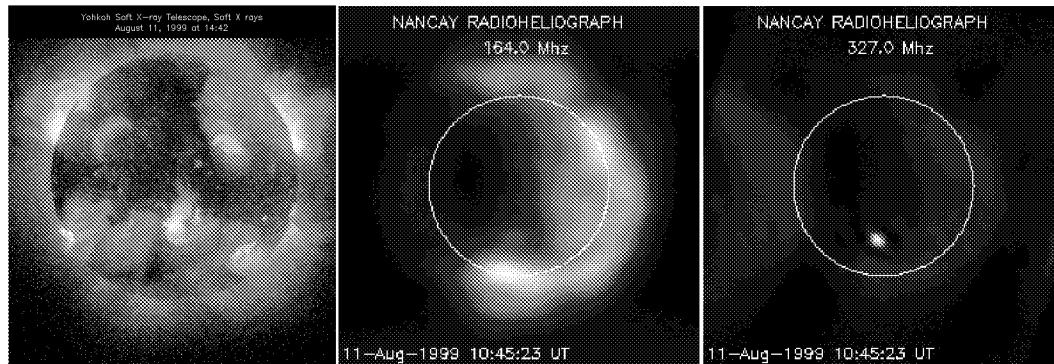


Figure (4.14). Images of the sun taken by the EIT instrument on SOHO on the 11 August 1999. The numbers denote the time in UT.



YOHKOH 14:42 UT 164 MHz 10:45 UT 327 MHz 10:45 UT

Figure (4.15). Images of the sun taken by the radiograph in Nancy, France and the x-ray telescope on Yohkoh on the 11 August 1999.

In figure (4.13) the coronal images of the sun were obtained from the C2 and C3 coronagraphs, of the LASCO (Large Angle and Spectrometric Coronagraph) instrument on SOHO, providing coronal images of the sun from 2.0 – 6.0 solar radii and 3.7 – 32.0 solar radii, respectively. These pictures reveal large-scale activities in the form of streamers in the southeast limb as compared to the rest of the limb. From figure (4.12) the fibers #19, 20, 21 and 22 were located in this region of high streamer activity.

In figure (4.14) are EIT (Extreme ultraviolet Imaging Telescope) on SOHO are images of the sun through various filters centered at different wavelengths as indicated on the images. These are images, through selected bandpasses in Fe IX/X at 171.0 \AA , Fe XII at 195.0 \AA , Fe XV at 284.0 \AA and He II at 304.0 \AA , reflect temperatures of $\sim 1.0 \text{ MK}$, $\sim 2.0 \text{ MK}$, $\sim 3.0 \text{ MK}$ and $\sim 4.0 \text{ MK}$, respectively.

In figure (4.15) are radio images from Nancy, France and a x-ray image from Yohkoh. The radio image in the center reveals that the east limb was either hotter or lesser in electron number density than the west limb. The bright spot on the image on the right shows the subflare #8662 reported at south14 east04 on 11 August 1999.

4.4 The telescope-spectrometer sensitivity curve

In section 4.4 the wavelength correction factor to convert terrestrial intensity observation to extraterrestrial intensity is discussed. The intensity recorded by MACS differs from the extraterrestrial intensity primarily due to the following two reasons.

1. The wavelength dependency of the physical parameters such as transmission efficiency, focal length, dispersion and quantum efficiency, etc of the optical components of MACS.
2. The wavelength dependency of the measured coronal intensity on the transmission efficiency and the scattering in the earth's atmosphere.

In order to find a correction term to convert terrestrial intensity observation to extraterrestrial intensity for each of the fibers the following steps were followed. This follows the procedure adopted by Ichimoto et al. (1996).

1. The dark-current subtracted terrestrial sky spectrum observed by each fiber was corrected for Rayleigh scattering (λ^{-4}). The sky represents the F-component of the solar spectrum and also closely resembles the solar spectrum itself. However the Rayleigh scattering affects the overall distribution of the sky spectrum. Thus the Rayleigh corrected sky spectrum was assumed to closely represent the terrestrial solar spectrum at the observation site. Figure (4.16) shows the sky spectrum recorded by fiber #06 before and after correcting for Rayleigh scattering.

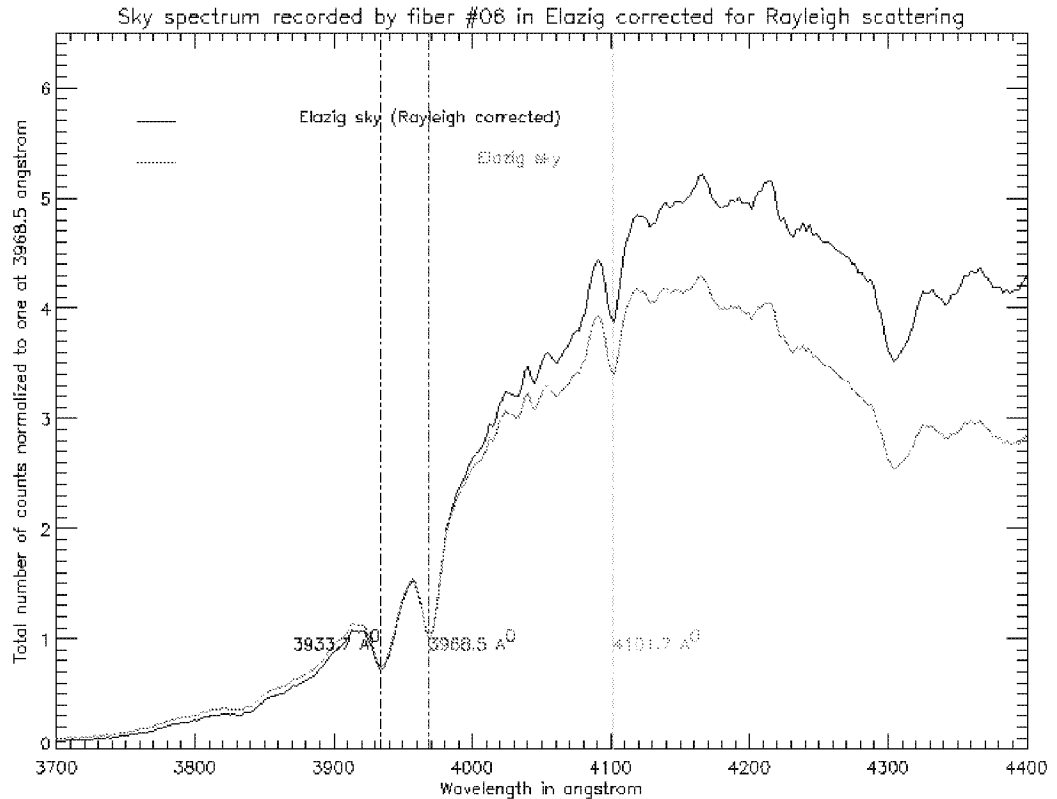


Figure (4.16). Plots of the sky spectrum recorded by fiber #06 in Elazig, Turkey before and after correcting for Rayleigh scattering. The plots have been normalized at 3968.5 Angstrom.

2. The terrestrial photospheric spectrum (Rayleigh corrected sky spectrum) recorded by MACS was calibrated with a wavelength scale using prominent absorption lines Ca II K & H at 3933.7 & 3968.5 angstrom, respectively and H_{δ} at 4101.7 angstrom. The positions of these absorption lines were matched with the corresponding positions of the same absorption lines in the extraterrestrial photospheric spectrum. These intensities were then divided by their respective intensities at 3968.5 angstrom. Figure (4.17) shows the terrestrial photospheric spectrum (Rayleigh corrected sky spectrum) recorded by fiber #06 and the extraterrestrial photospheric spectrum.

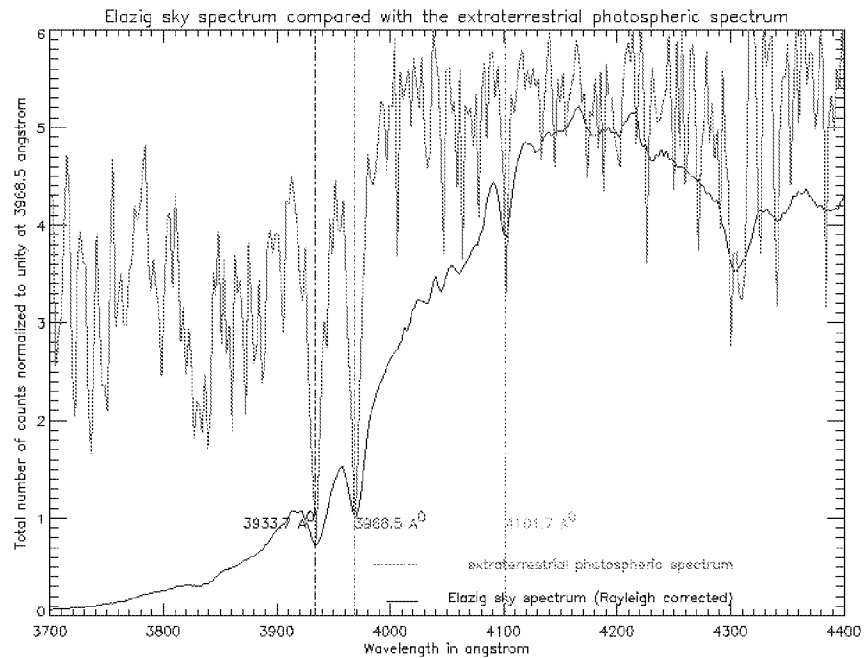


Figure (4.17). Plots of the extraterrestrial photospheric intensity spectrum and the terrestrial photospheric intensity spectrum recorded by fiber #06. The extraterrestrial photospheric spectrum is a smoothed version of the extraterrestrial photospheric spectrum shown in figure (2.1).

3. The extraterrestrial photospheric spectrum was smoothed until it matched the resolution of the terrestrial photospheric spectrum recorded by MACS. Figure (4.18) shows the terrestrial photospheric spectrum recorded by fiber #06 and the extraterrestrial photospheric spectrum smoothed in resolution to match the resolution of the terrestrial photospheric spectrum.

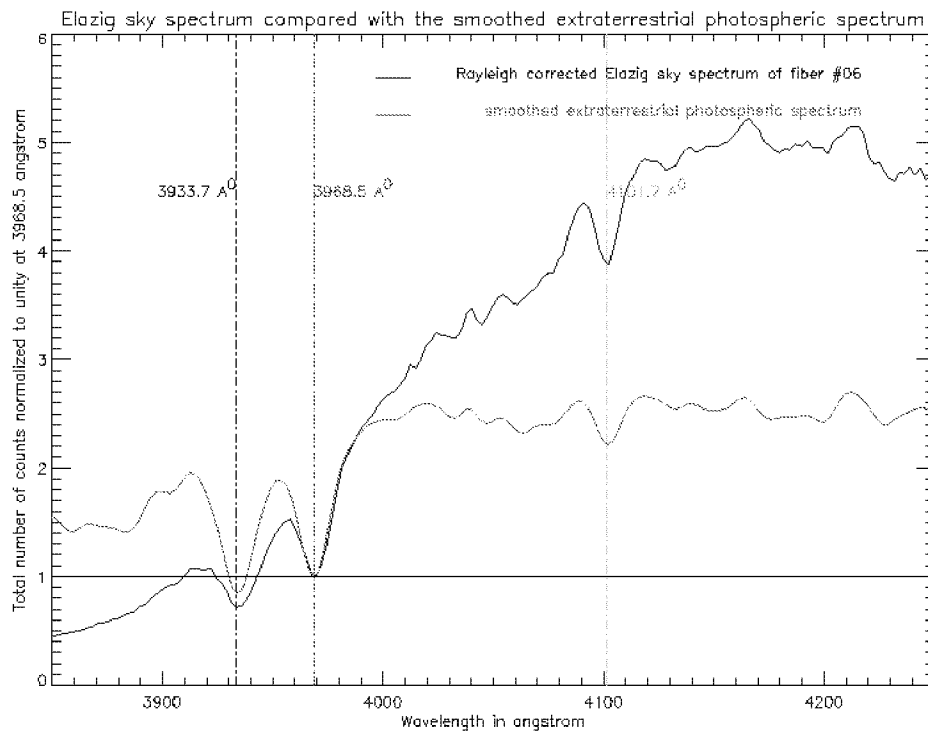


Figure (4.18). Plots of the smoothed extraterrestrial photospheric intensity spectrum and the terrestrial photospheric intensity spectrum recorded by fiber #06.

4. The ratios between the extraterrestrial and the terrestrial photospheric spectra were calculated against wavelength. Figure (4.19) shows plots of the smoothed extraterrestrial photospheric intensity spectrum, terrestrial photospheric intensity spectrum recorded by fiber #06 and the ratio between them.

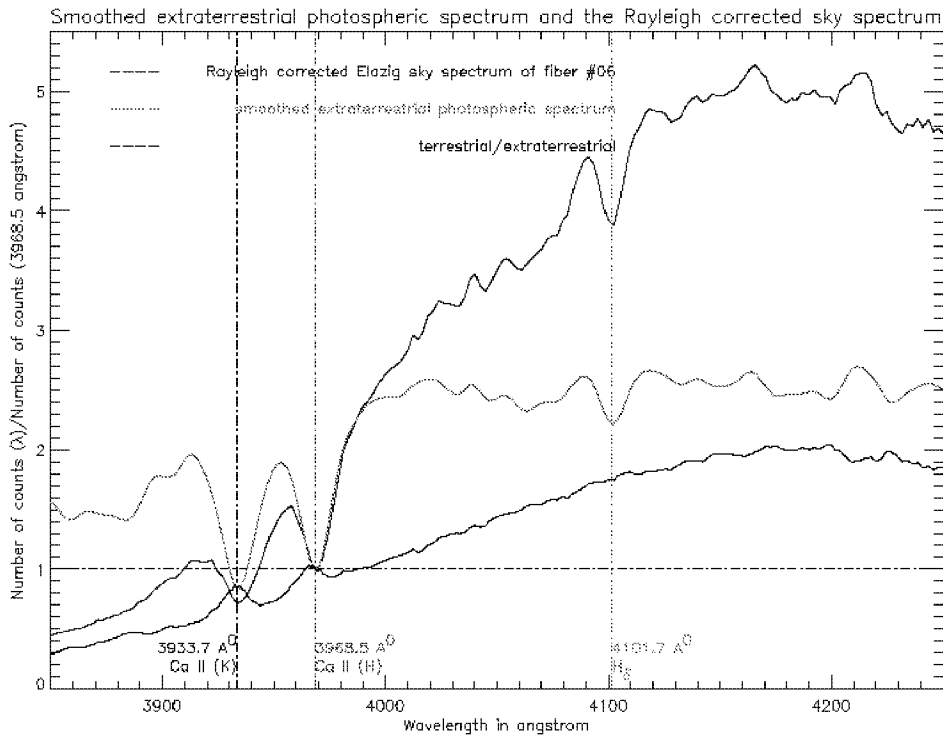


Figure (4.19). Plots of the smoothed extraterrestrial photospheric intensity spectrum, terrestrial photospheric intensity spectrum recorded by fiber #06 and the ratio between these two against wavelength.

5. A polynomial fit was made to the ratios between the extraterrestrial and the terrestrial photospheric spectra that were calculated against wavelength. Figure (4.20) shows the polynomial fit made to the ratio between the smoothed extraterrestrial photospheric intensity spectrum, and the terrestrial photospheric intensity spectrum recorded by fiber #06.

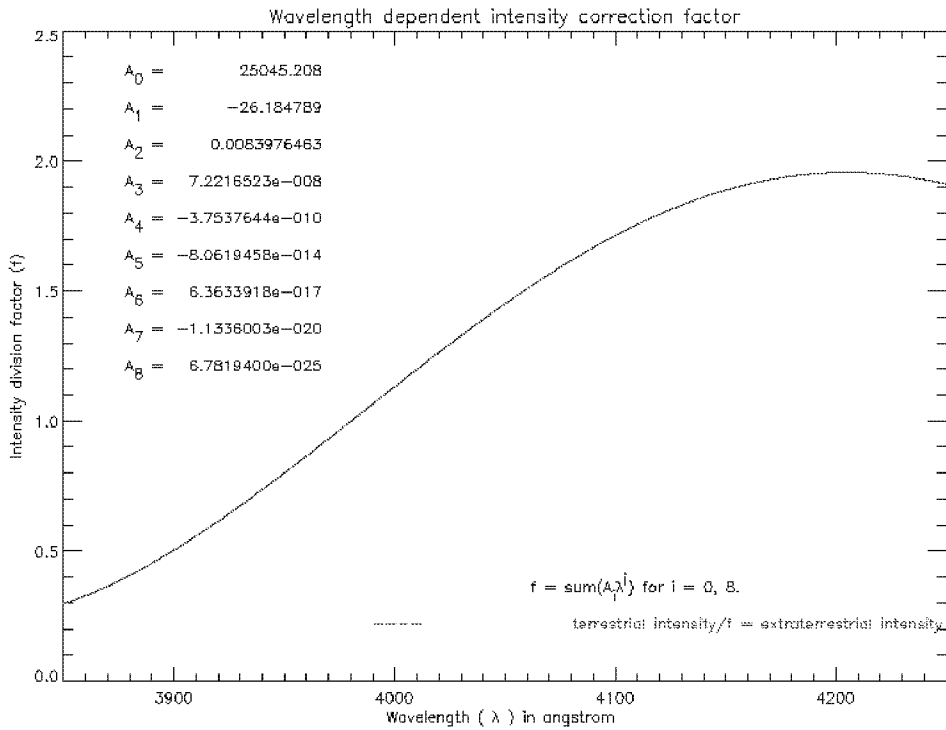


Figure (4.20). Polynomial fit made to the ratio between the extraterrestrial photospheric spectrum and the terrestrial photospheric intensity spectrum. The numbers on the plot are the coefficients of the polynomial fit.

Figure (4.21) shows the application of the polynomial fit to the terrestrial photospheric intensity spectrum to obtain the extraterrestrial photospheric intensity. This indicates a reasonably good fit. Also plotted in figure (4.12), for comparison purpose, is the smoothed extraterrestrial photospheric intensity spectrum as shown in figure (4.18).

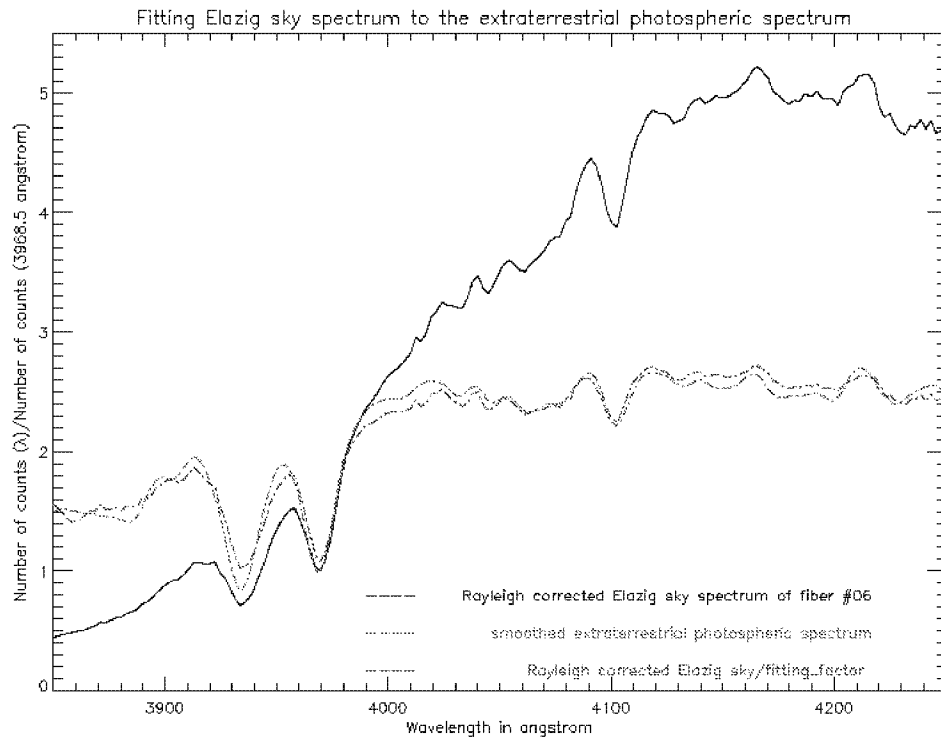


Figure (4.21). Application of the polynomial fit shown in figure (4.20) to the terrestrial photospheric intensity spectrum to obtain the extraterrestrial photospheric intensity. Also plotted for comparison purpose is the smoothed extraterrestrial photospheric intensity spectrum as shown in figure (4.18).

4.5 Application of the intensity correction factor

The extraterrestrial photospheric intensity spectrum differs from the terrestrial photospheric intensity spectrum measured by MACS primarily due to the atmosphere and the optical elements in MACS. Therefore the ratio between the extraterrestrial and the terrestrial photospheric intensity at a given wavelength could be written as shown in equation (4.1).

$$\frac{\mathbf{I}_{PT}(\lambda)/\mathbf{I}_{PT}(\lambda_0)}{\mathbf{I}_{EX}(\lambda)/\mathbf{I}_{EX}(\lambda_0)} = \mathbf{f}(\mathbf{A}, \tau) \equiv \mathbf{f}(\lambda)$$

$\tau(\lambda) = \mathbf{transmission\ efficiency\ of\ MACS}$

$\mathbf{A}(\lambda) = \mathbf{atmospheric\ attenuation}$

(4.1)

where \mathbf{I}_{PT} and \mathbf{I}_{EX} are the photospheric intensity measured by MACS from ground and the extraterrestrial photospheric intensity, respectively. Here both the extraterrestrial and the terrestrial intensities are divided by their respective intensities at a reference wavelength λ_0 . In producing figure (4.18) the reference wavelength λ_0 was selected to be the Ca-II H line at 3968.5 angstrom. The same is true for the measurement of any other extraterrestrial intensity spectrum including the measurement of the solar coronal intensity measurement during an eclipse.

Using equation (4.1) the terrestrial coronal intensity at a given wavelength λ measured by MACS during the eclipse would correspond to the extraterrestrial coronal intensity given by equation (4.2).

$$\boxed{\begin{aligned} \mathbf{I}_{\text{EX}}^{\text{C}}(\lambda) &= \frac{\mathbf{1}}{\mathbf{f}(\lambda)} \times \frac{\mathbf{I}_{\text{EX}}^{\text{C}}(\lambda_0)}{\mathbf{I}_{\text{G}}^{\text{C}}(\lambda_0)} \times \mathbf{I}_{\text{G}}^{\text{C}}(\lambda) \\ \mathbf{I}_{\text{G}}^{\text{C}}(\lambda) &= \text{terrestrial coronal intensity} \\ \mathbf{I}_{\text{EX}}^{\text{C}}(\lambda) &= \text{extraterrestrial coronal intensity} \end{aligned}} \quad (4.2)$$

From equation (4.2) the extraterrestrial coronal intensity ratio at wavelengths λ_1 and λ_2 is given by equation (4.3).

$$\boxed{\frac{\mathbf{I}_{\text{EX}}^{\text{C}}(\lambda_1)}{\mathbf{I}_{\text{EX}}^{\text{C}}(\lambda_2)} = \frac{\mathbf{f}(\lambda_2)}{\mathbf{f}(\lambda_1)} \times \frac{\mathbf{I}_{\text{G}}^{\text{C}}(\lambda_1)}{\mathbf{I}_{\text{G}}^{\text{C}}(\lambda_2)}} \quad (4.3)$$

4.6 Determination of the Thermal electron temperature and the Solar wind velocity for each fiber location

The coronal spectrum recorded by each fiber contains the K, F and E coronal spectra. In order to determine the thermal electron temperature and the solar wind velocity, as per the methodology discussed in chapter-2, the K-coronal spectrum has to be isolated. Figure (4.22) shows the coronal spectrum recorded by the twenty-one fibers in the 18.0 seconds exposure.

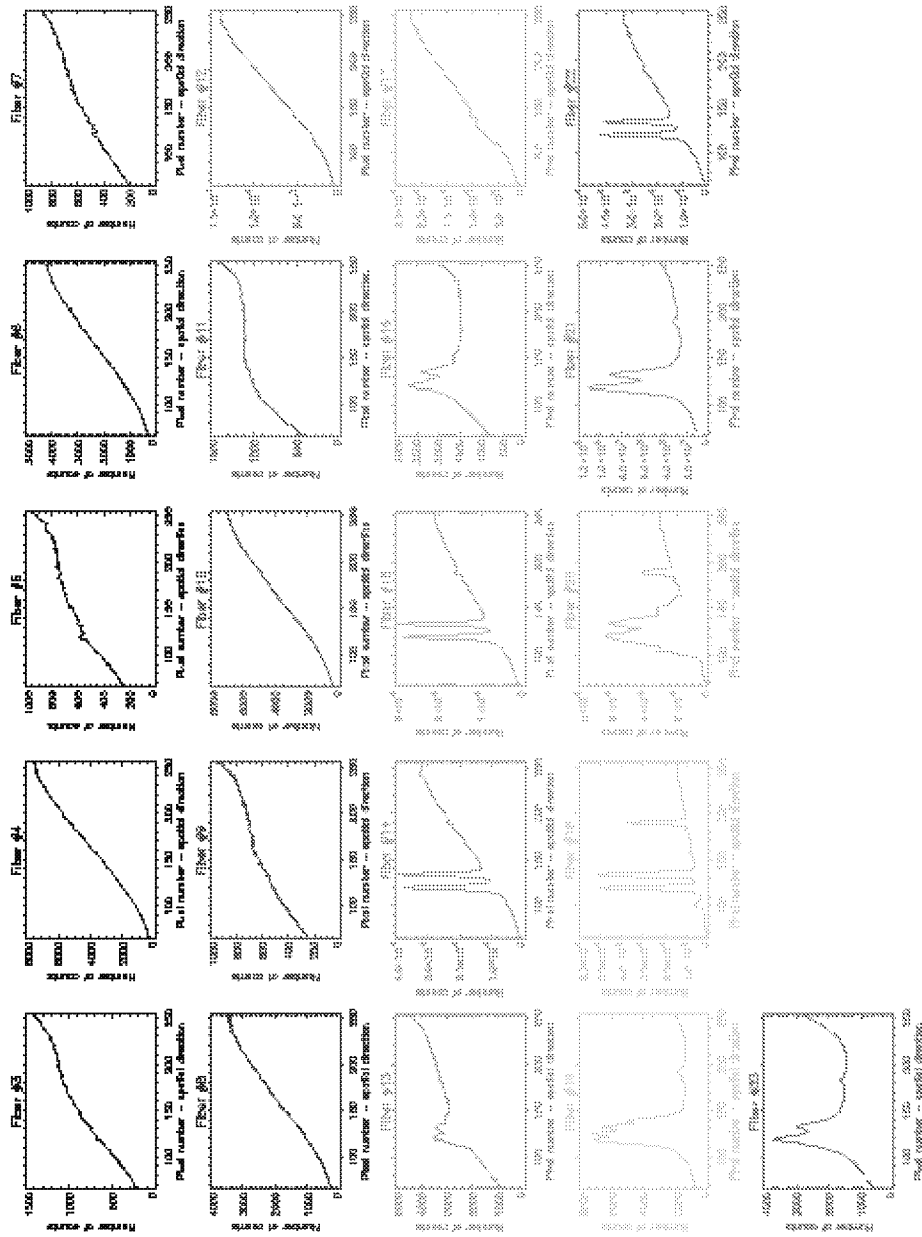


Figure (4.22). These plots show the coronal spectra recorded by the twenty-one fibers located at various latitudes and heights on the corona as depicted in figure (4.12). Fiber #23 was centered on the moon. The above spectra were recorded in the 18.0 seconds exposure. The x-coordinate is in pixel units.

Comparison between figure (4.22) and (4.12) it is evident that the fibers below the equator prominently display emission lines. From fiber #23, which was located at the center of the moon, was expected to record the background counts in addition to the coronal light reflected off the clouds and re-reflected off the moon. However the observational site in Elazig, Turkey reportedly being free of clouds the spectrum from fiber #23 only reveals the extent of the instrumental stray light. This stray light is believed, largely, to have originated in the telescope and could pose a significant error in the wind measurement. This is because the scattering is significantly large in the bright end of the spectrum in MACS. This in turn could give a larger count number for the intensity at 4233.0 angstrom, which is used in determining the wind sensitive intensity ratio. This is evident in the spectrum of fiber #23. In this regard it is prudent to eliminate at least 1-% of the counts in the bright end of the spectrum. The fibers recording emission lines can be attributed to exposure to prominence spectrum as discussed in section (4.3).

Figure (4.23) is the coronal spectrum recorded by fiber #06. As per figure (4.12) this fiber was located midway between the solar equator and the solar North Pole at 1.1 solar radii. Also LASCO images in figure (4.13) confirm this region free of streamer activities. The following steps were carried out in order to isolate the K-coronal spectrum in fiber #06 and closely resemble the methodology described by Ichimoto et.al (1996).

1. It was assumed that the Rayleigh corrected sky spectrum to closely resemble the F-component of the solar spectrum. On this basis a fraction of the sky component corresponding to about 1-% of the counts at 4250.0 angstrom in the coronal spectrum was subtracted.

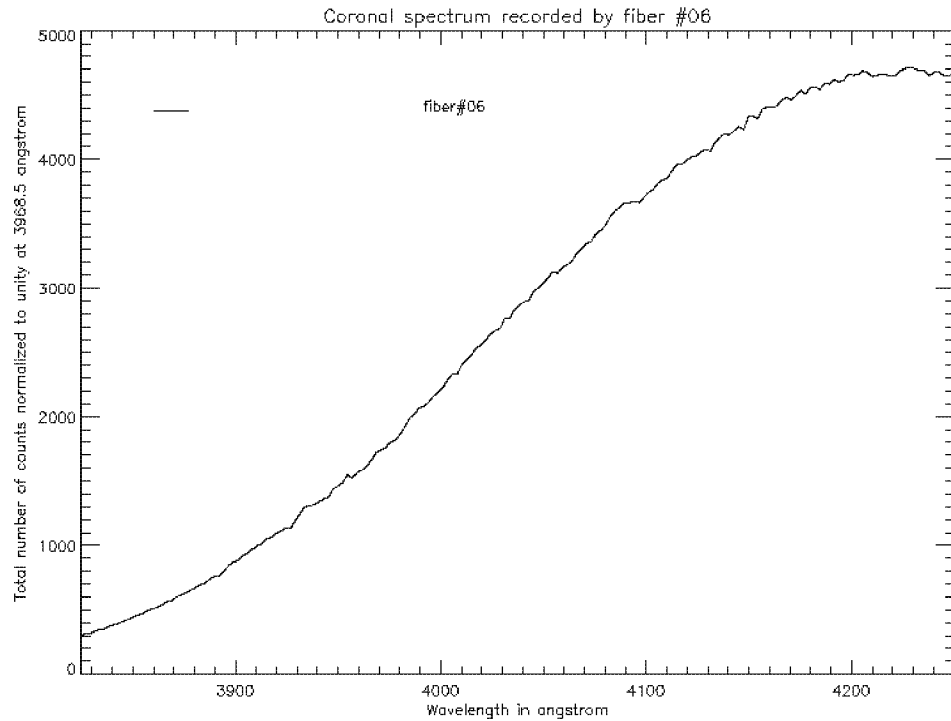


Figure (4.23). The coronal spectrum recorded by fiber #06.

2. A third order polynomial fit was made to the difference between the coronal spectrum subtracted by the F-coronal spectrum. This was possible in the above case since the coronal spectrum of fiber #06 is devoid of any significant emission lines. In the cases with strong emission lines gaussian fits would be made and subtracted with the background added to the continuum. In order to account for the stray light a constant value was subtracted from the coronal spectrum in order to make the overall variation

with wavelength (the ratio of the average intensity in 3700-3800 angstrom and the intensity around 4250 angstrom) to be identical with that of the brightest spectrum recorded by a fiber. For fiber #06 this correction amounted to 55 digital units in a 16-bit dynamic range. Figure (4.24) shows the reduced K-coronal spectrum from fiber #06.

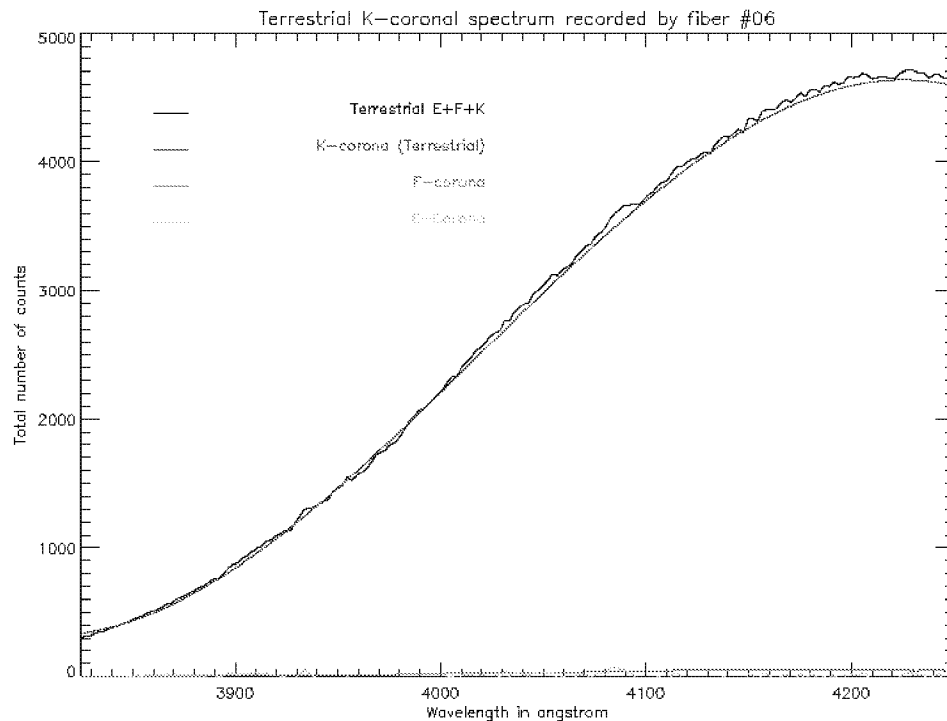


Figure (4.24). The terrestrial K-coronal spectrum reduced from the coronal spectrum recorded by fiber #06.

3. The terrestrial K-coronal spectrum was adjusted by the wavelength sensitivity curve in figure (4.20). This would transform the terrestrial K-coronal spectrum to the extraterrestrial K-coronal spectrum. This curve was used to determine the wind and the temperature sensitive ratios using equation (4.2). Figure (4.25)

shows the extraterrestrial K-coronal intensity derived for fiber #06 together with the wind and the temperature sensitive intensity ratios.

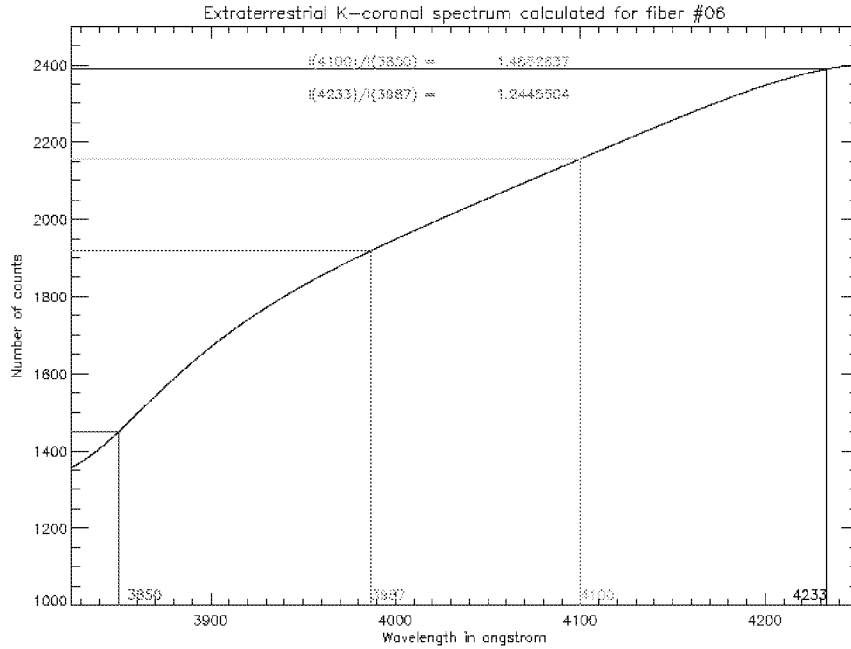


Figure (4.25). This plot shows the extraterrestrial K-coronal spectrum derived for fiber #06. The wind and the temperature sensitive intensity ratios are 1.245 and 1.488, respectively.

4. The theoretical temperature and the wind sensitive plots for the desired line of sight were then used to predict the thermal electron temperature and the solar wind velocity. The figure (4.26) and figure (4.27) show the locations of the temperature and the wind sensitive intensity ratios, derived from figure (4.25), on the theoretical thermal electron temperature and the solar wind velocity plots at 1.1 solar radii, respectively. These plots associate a thermal electron temperature of ~1.73 MK and a solar wind velocity of ~467.0 km/sec for fiber #06's location on the solar corona. The error bars will be discussed in section (4.7).

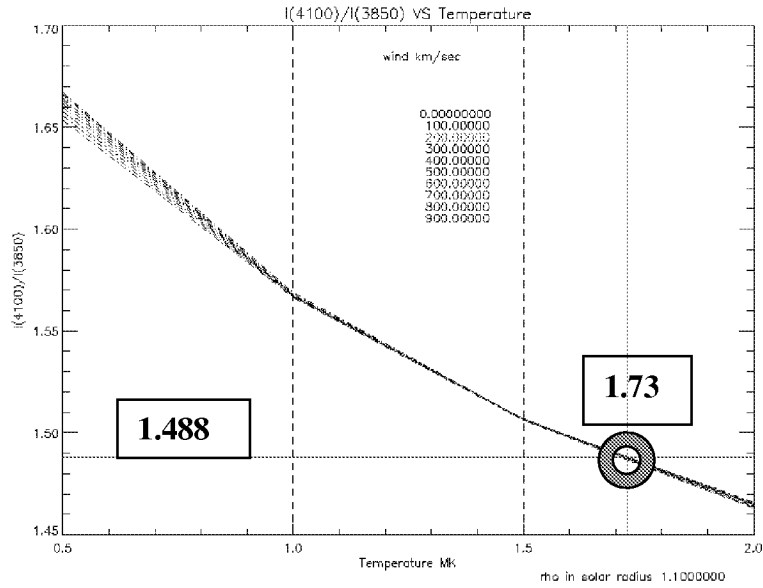


Figure (4.26). The temperature sensitive plot. This assigns a thermal electron temperature of ~1.73 MK for fiber #06.

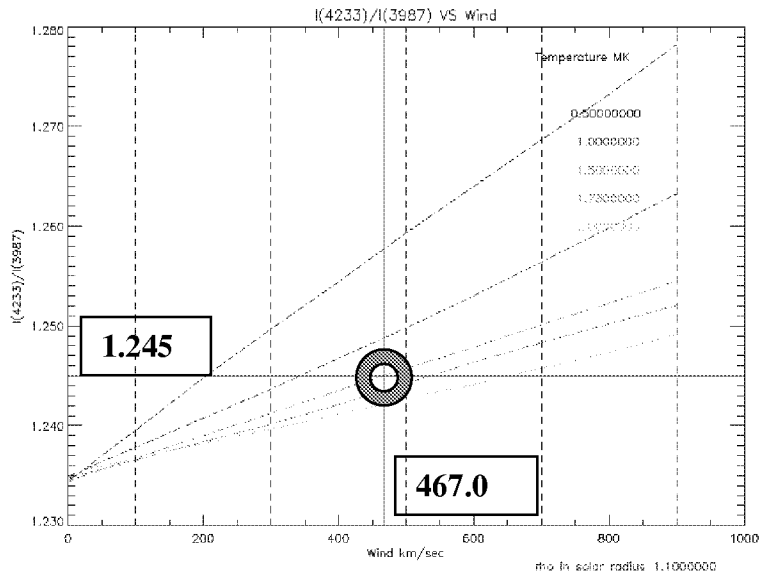


Figure (4.27). The wind sensitive plot. This assigns a solar wind velocity of ~467.0 km/sec for fiber #06.

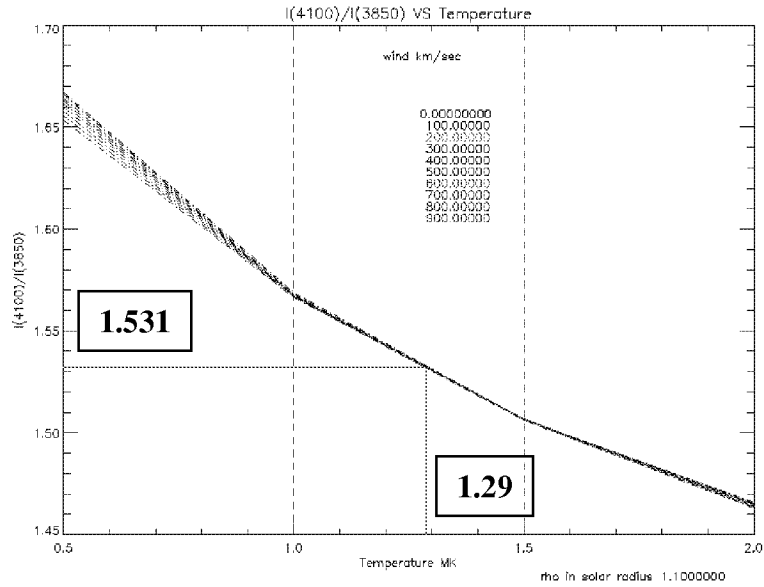


Figure (4.28). The temperature sensitive plot. This assigns a thermal electron temperature of ~1.29 MK for fiber #04.

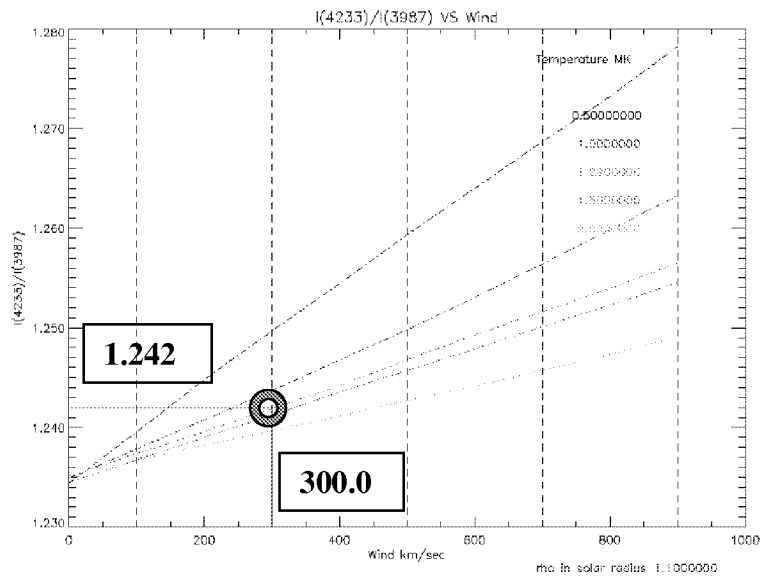


Figure (4.29). The wind sensitive plot. This assigns a solar wind velocity of ~300.0 km/sec for fiber #04.

Similarly figure (4.28) and figure (4.29) show the locations of the temperature and the wind sensitive intensity ratios on the theoretical thermal electron temperature and the solar wind velocity plots at 1.1 solar radii, respectively. These plots associate a thermal electron temperature of ~1.29 MK and a solar wind velocity of ~300.0 km/sec for fiber #06's location on the solar corona. Figure (4.30) shows the extraterrestrial K-coronal spectrum derived for fiber #10. Figure (4.31) and figure (4.32) give a thermal electron temperature of ~1.34 MK and a solar wind velocity of ~571.0 km/sec for fiber #10's location on the solar corona.

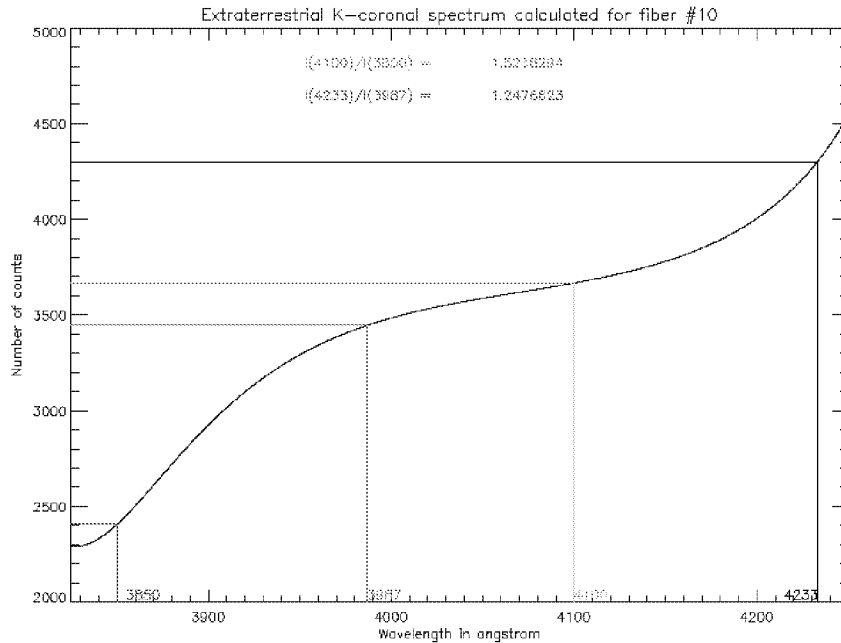


Figure (4.30). This plot shows the extraterrestrial K-coronal spectrum for fiber #10. The wind and the temperature sensitive intensity ratios are 1.248 and 1.524, respectively.

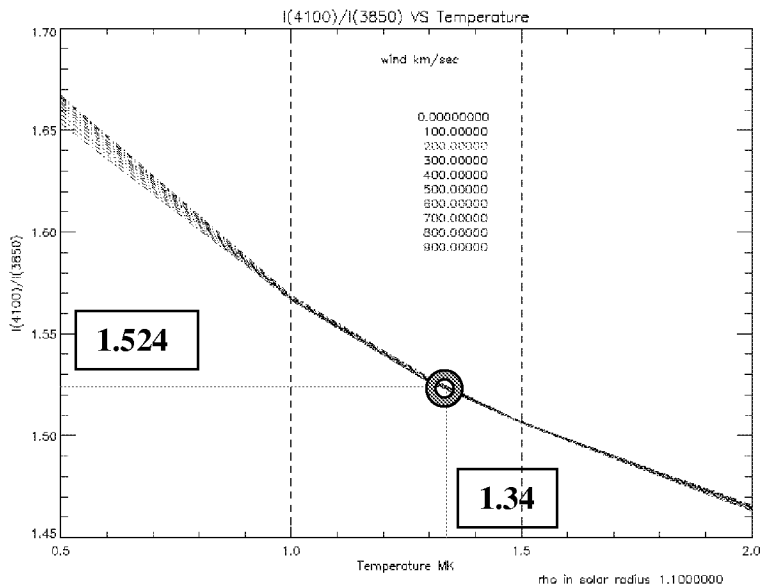


Figure (4.31). The temperature sensitive plot. This assigns a thermal electron temperature of ~1.34 MK for fiber #10.

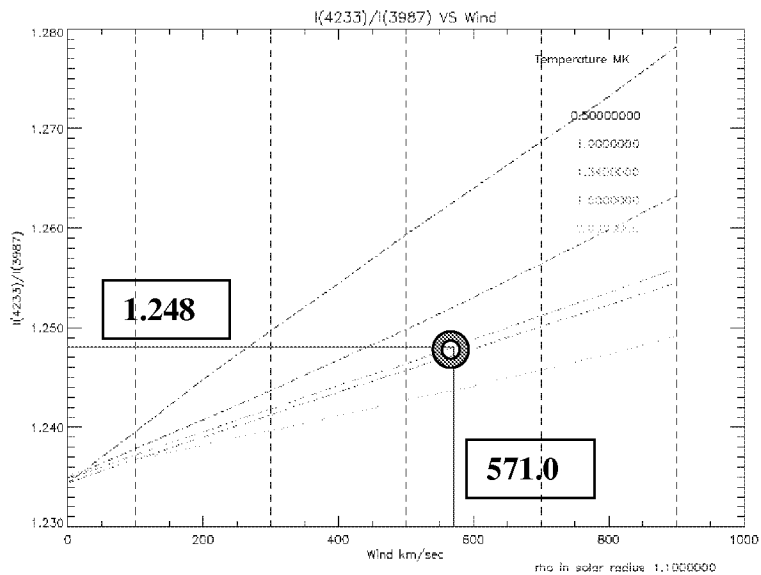


Figure (4.32). The wind sensitive plot. This assigns a solar wind velocity of ~571.0 km/sec for fiber #10.

Figure (4.33) shows the coronal spectrum recorded by fiber #14 that includes prominent emission lines in calcium and hydrogen. The continuum was obtained by fitting a gaussian function of the form given by equation (4.4) to the emission lines and fitting equation (4.5) to the continuum.

$$f(\lambda) = A_0 e^{-\frac{z^2}{2}} + A_3 + A_4 \lambda + A_5 \lambda^2 \quad \text{where } Z = \left(\frac{x - A_1}{A_2} \right) \quad (4.4)$$

$$A_3 + A_4 \lambda + A_5 \lambda^2 \quad (4.5)$$

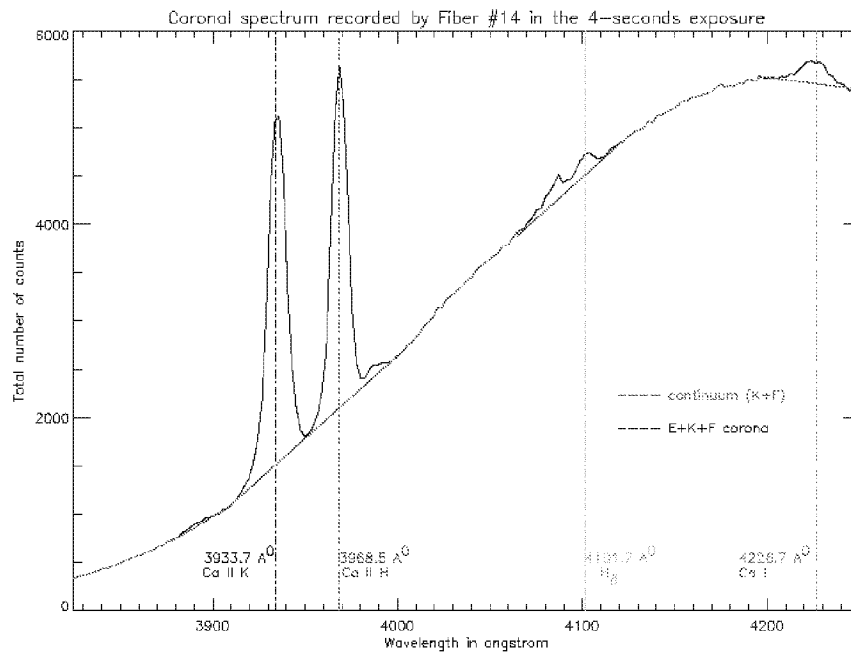


Figure (4.33). This plot shows the terrestrial coronal spectrum recorded by fiber #14. The continuum is a measure of the terrestrial F+K corona. The E-corona is removed by making Gaussian fits of the form given in equation (4.1) to the individual emission lines and fitting the background given by equation (4.2) to the continuum.

Following the steps described above figure (4.34) shows the extraterrestrial K-coronal spectrum reduced for fiber #14.

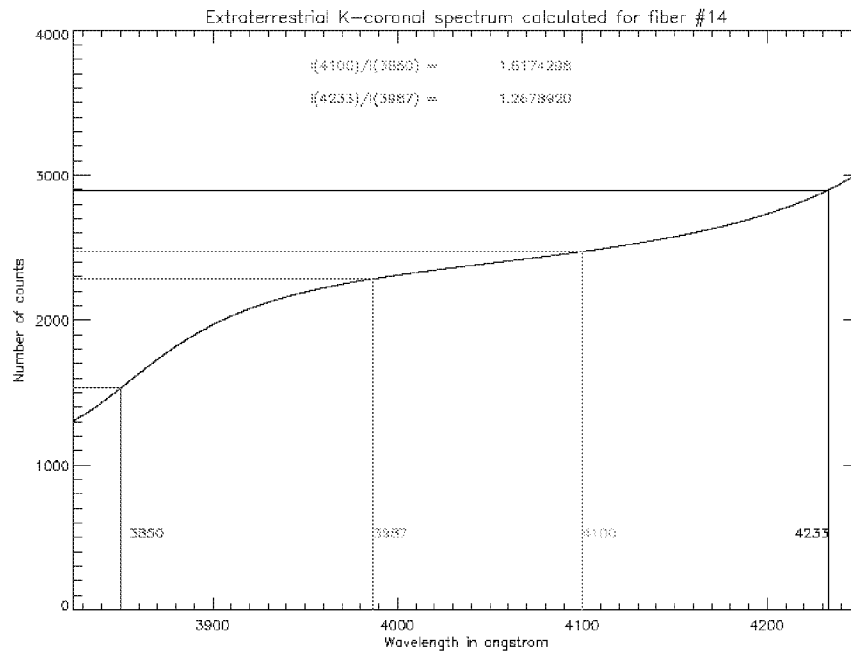


Figure (4.34). This plot shows the extraterrestrial K-coronal spectrum for fiber #14. This is following the elimination of the E-corona from figure (4.33).

From figure (4.35) and figure (4.36) the thermal electron temperature and the solar wind velocity derived for fiber #14 are ~ 0.73 MK and ~ 819.0 km/sec, respectively. However from figure (4.12) and figure (4.13) it is evident of a streamer and some bright structures in the field of view of fiber #14. This fairly low temperature could result from one of two possibilities. Firstly the fiber may have seen the corona very close to the limb based on the possibilities of errors arising from improper alignment of the fiber optic plate in the focal plane of the telescope or improper tracking.

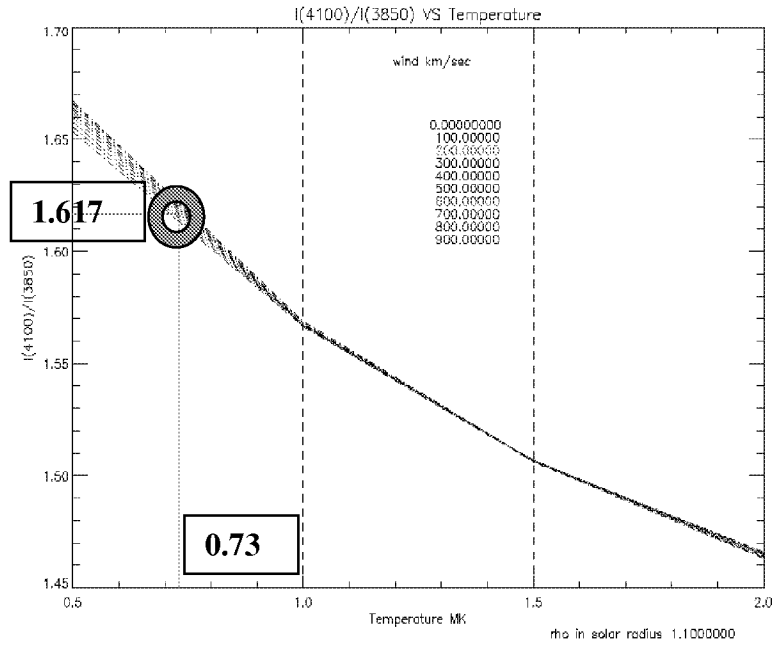


Figure (4.35) The temperature sensitive plot. This assigns a thermal electron temperature of ~0.73 MK for fiber #14.

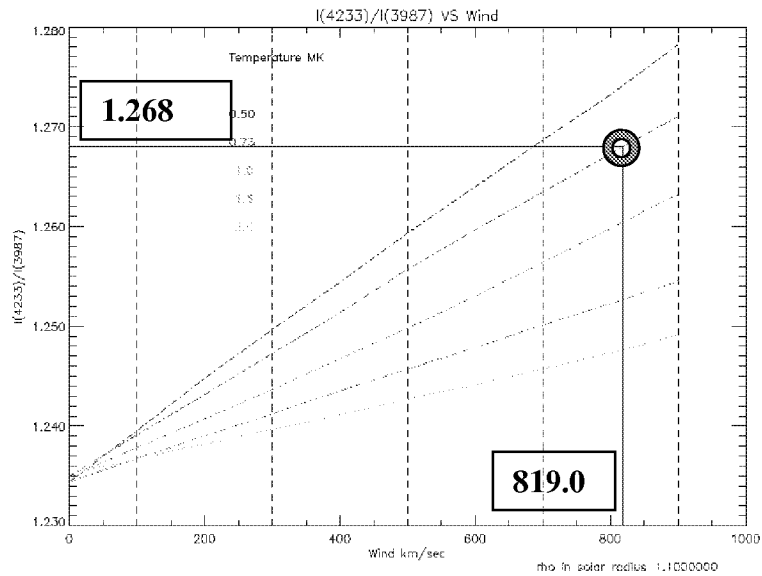


Figure (4.36). The wind sensitive plot. This assigns a solar wind velocity of ~819.0 km/sec for fiber #14.

Secondly, it is apparent that local density enhancement may have resulted at points of intersection of the streamer with the line of sight of fiber #14. Although the actual geometry nor the magnitude of the density enhancement are known, nevertheless, using a trial geometry and an assumed magnitude for density enhancement it can be shown that the temperature determined for fiber #14 may differ widely from the true value. This phenomenon is described in Appendix-C. In the following example the geometry described in Appendix-C was used along with an assumed density enhancement by a factor of 50.0.

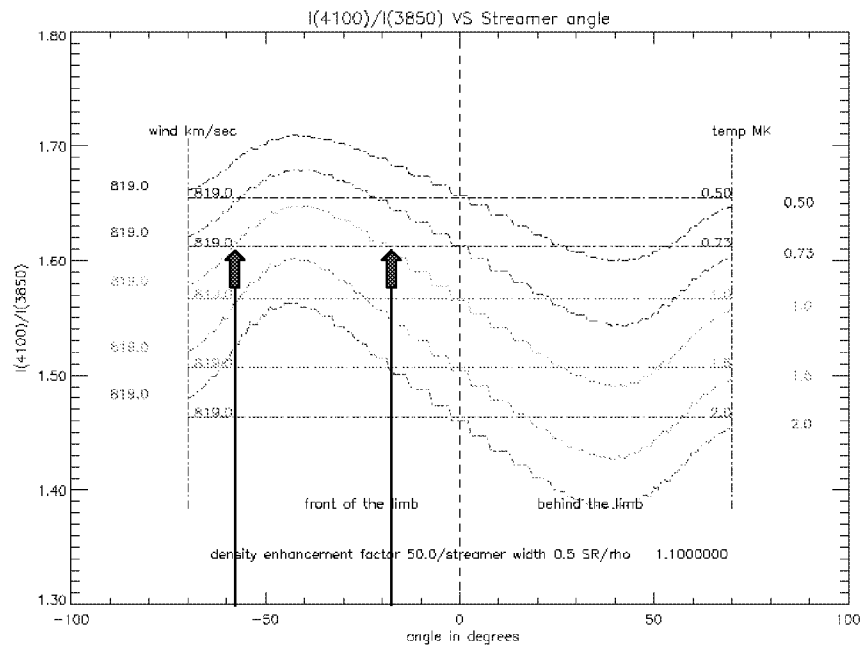


Figure (4.37). Plot showing the variation in the temperature-sensitive intensity ratio, from the theoretical models without streamers, for a streamer of geometry described in Appendix-C and density enhanced by a factor of 50.0 together with various streamer inclinations in front and behind the solar limb.

In figure (4.37) the horizontal lines show the temperature-sensitive intensity ratio for models without streamers. The curves with the matching colors show the variation of this ratio with streamers of the above geometry and density enhancement located at various angles in front and behind the limb. The two arrows indicate that a corona with temperature 1.0 MK and wind velocity 819.0 km/sec along with a streamer enhanced in density by a factor 50.0 and inclined at $\sim 18.0^\circ$ or $\sim 58.0^\circ$ degrees in front of the limb could have given the same temperature-sensitive intensity ratio as the theoretical model without streamers for an isothermal corona of temperature 0.73 MK and solar wind velocity 819.0 km/sec. This example shows the sensitivity of the streamers crossing the lines of sight of the fibers in determining the temperature and the wind velocity. However this cannot be considered a detrimental factor in the broader science of determining the density enhancement associated with streamers, their temperatures and velocities.

My belief for the low temperature recorded by fiber #14 has the following interpretation. From figure (4.1) and (4.14) it is apparent that the fiber #14 was closely placed to the extended prominence. It is very likely in this scenario that the line of sight integration for fiber #14 contained cool material associated with a prominence and is a signature of its likely temperature.

From similar analyses the schematic diagram in figure (4.38) shows the values determined for the thermal electron temperature and the solar wind velocity for fibers #04, 06, 08, 10, 12, 14 & 22 located at 1.1 solar radii and fiber #15 & 17 located at 1.5

solar radii. Unfortunately it has not been successful in determining the wind velocities for fibers # 15 and 22. The spectrum recorded by these fibers show a gradual decline in counts above 4200.0 angstrom for reasons, which are not obvious. All the temperature and wind values determined for the above fibers are based on the theoretical models without consideration for streamers.

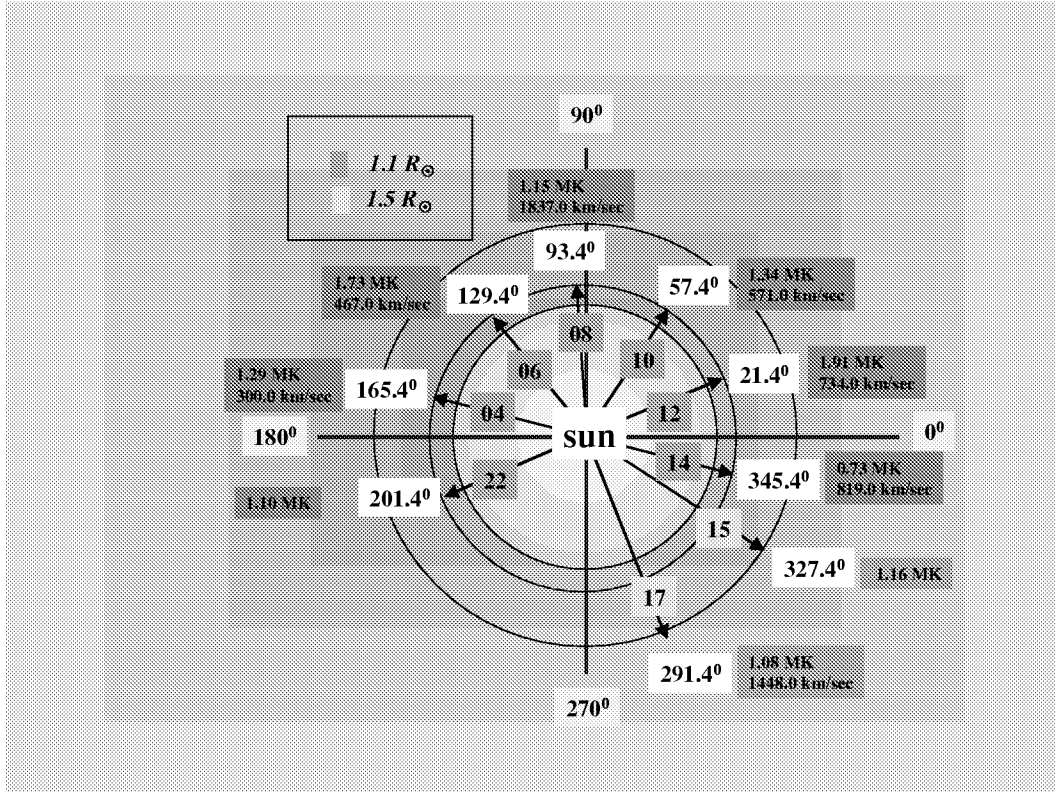


Figure (4.38). The thermal electron temperature and the solar wind velocity determined for solar coronal locations observed by fibers #04, 06, 08, 10, 12, 14 & 22 that are located at 1.1 solar radii and fiber #15 & 17 located at 1.5 solar radii. These values are based on the theoretical models. The temperature and the wind velocity are measured in MK and km/sec, respectively. However the wind measurements seem too far high. In this regard it is acknowledged that the experiment was not successful in measuring the wind velocities and the absolute values should be disregarded.

4.7 Sources of error and error bars

The sources of systematic errors could have resulted from improper alignment of the fiber optic plate in the focal plane of the telescope and tracking inadequacies. These practical reasons for these problems in the present status of MACS are highlighted in chapter-7 with suggested remedial measures.

Another disappointment in this experiment reflects from the spectrum recorded by fiber #23, which was centered in the center of the lunar shadow to record the background counts. The spectrum recorded by fiber #23, which was intended to measure the background counts, is shown in figure (4.39).

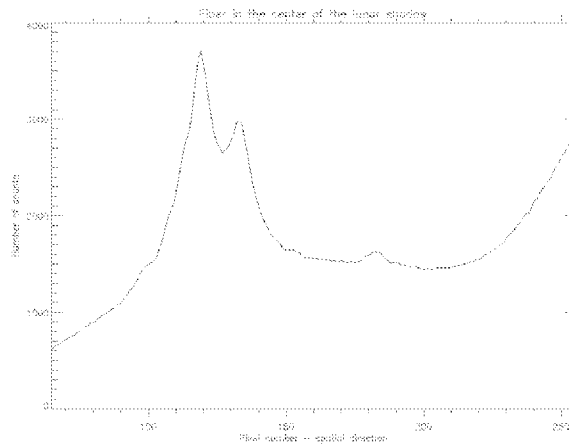


Figure (4.39). The spectrum recorded by fiber #23, which was centered on the lunar shadow during the eclipse. Its purpose was to measure the background counts.

Figure (4.39) highlights the scale of the instrumental scattering specially in the high end of the wavelength region that is sensitive to the wind-sensitive intensity ratio giving a higher count at 4233.0 angstrom. An attempt to quantify its influence on the spectra recorded by the other fibers is given in chapter-6. This may be the reason for obtaining very large measurements for the wind velocities. The wind velocities expected at 1.1 solar radii are of the order of ~100.0 km/sec. In this regard the absolute values determined for the wind velocities should be disregarded. However the ratios of the wind velocities in the equatorial regions to the coronal hole regions do make sense where the wind velocities at the poles are of the order ~3.0 times the wind velocities in the equatorial regions. Instrumental scattering could also be responsible for causing the coronal light recorded by a number of fibers unusable for analyses.

However scattering is an inevitable consequence arising from the financial constraints associated with obtaining superior optics. Also in respect to the time constraint associated with the eclipse duration it was not possible to do repeat measurements for random statistics. However this effort will be feasible with MACS attached to a coronagraph.

As for the temperature-sensitive intensity ratio one of the concern was the association of the wavelength positions to be in close proximity to strong emission lines. For example the proximity of the 4100 angstrom wavelength position to the emission line of H_{δ} at 4101.7 angstrom.

In addition there is also an error associated with the derivation of the instrumental wavelength sensitivity curve. Figure (4.21) shows the application of the wavelength sensitivity curve to the Rayleigh corrected sky spectrum to obtain the extraterrestrial photospheric spectrum (red curve). Matching this extraterrestrial photospheric spectrum (red curve) with what is considered as the true extraterrestrial photospheric spectrum (green curve), as depicted in figure (4.21), the overall deficiency is 0.44%. This is the difference between the area under these two curves. However this does not mean that point to point differences are as low as 0.44%. At the temperature-sensitive wavelength locations at 3850.0 and 4100.0 angstroms, these errors are -4.1% and $+1.9\%$, respectively. This can cause the temperature to be underestimated by 5.7% , which translates to 1.14 MK. The ideal remedy to this problem is an absolute wavelength calibration of MACS with sources of known strengths. However this does not still account for the instrumental scattering.

Although no clouds were reported during observation, yet the haze due to convection that is associated with the very dry terrain in Elazig, Turkey is another hidden consequence on the accurate coronal brightness measurements.

The influence of the numerical procedure and other physical parameters, such as the electron number density profile, used in creating the shape of the K-coronal intensity spectrum is discussed in chapter-5.

4.8 Summary

It has been demonstrated that the concept of MACS could be used as an instrument for global and simultaneous measurements of the thermal electron temperature and the solar wind velocity in the solar corona. The inaugural mission of MACS was beset with problems associated with instrumental scattering, lacking an imaging device to image the eclipse to ascertain tracking reliability and the possible atmospheric dust pollution due to the experimental location in a dry terrain devoid of vegetation. However the remedial measures are very simple in nature and tied to adequate financial resources. Using MACS with a coronagraph will also eliminate the time and terrain constraints associated with eclipses. Using MACS in a space platform that could take it very close to the solar surface and look into the corona will also eliminate the need for a coronagraph and the problems associated with the F-corona. This would be very promising in light of the scattering and the F-corona concerns associated with terrestrial observations. The remedial measures and the uses of other platforms for MACS are detailed in chapter-7.

Chapter 5

MODIFIED CRAM'S THEORY AND ITS DEPENDENCE ON VARIOUS PARAMETERS

5.1 Modified Cram's theory

Lawrence Cram (1976) formulated the theory for the formation of the K-corona. The modified Cram's theory includes the influence of the solar wind velocity in the formation of the K-corona, which is a continuous spectrum. The reasons for the formation of this continuous spectrum and the influence of the solar wind velocity are discussed in chapter-2. Figure (5.1) is a schematic diagram showing the mathematical description of the scattering phenomenon where the photospheric radiation from the sun is scattered by the free electrons lying along the line of sight of an observer. This scattering phenomenon is popularly known as Thomson scattering while the scattered radiation contributes to the formation of the K-corona. A detailed treatment of the scattered intensity, which includes the influence of the solar wind velocity, is provided in Appendix-A. Equation (5.1) gives the intensity of the radiation scattered at an observed wavelength (λ) by the free electron density distribution along the line of sight at height (ρ) above the solar limb.

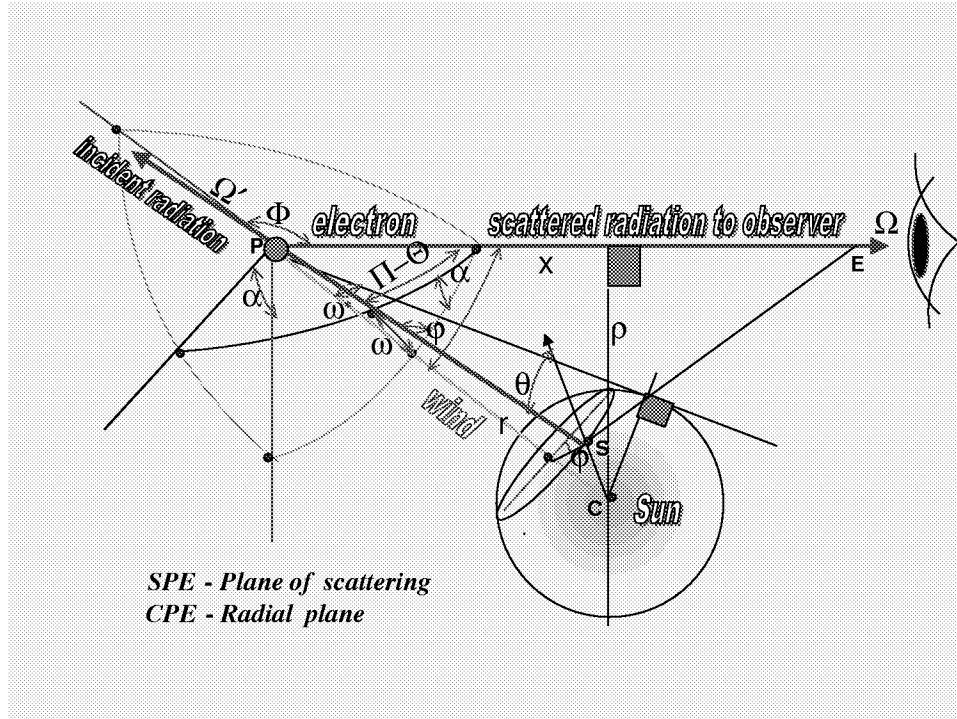


Figure (5.1). This is a schematic diagram showing the mathematical description of the scattering phenomenon where the photospheric radiation from the sun is scattered by the free electrons lying along the line of sight of an observer. The line of sight is at a distance (ρ) from the center of the sun.

$$\begin{aligned}
 I_O^{Ra}(\lambda, \rho R_{\text{solar}}) &= \int_{-\infty}^{+\infty} \int_0^{2\pi} \int_0^1 \int_0^\infty d\lambda' d\phi d\cos\omega d(xR_{\text{solar}}) \times \\
 N_e(\mathbf{r}R_{\text{solar}}) \times Q_O^{Ra}(\alpha, \Theta) \times \\
 \frac{1}{2\sqrt{\pi}\Delta b} I(\lambda', \omega, x) \exp &\left[- \left(\frac{\lambda - \lambda' \left(1 + \frac{2b^2 \cos\omega w(\mathbf{r}R_{\text{solar}})_{\text{radial}}}{c} \right)}{2\Delta b} \right)^2 \right]
 \end{aligned} \tag{5.1}$$

where $O \equiv (//, \perp)$
 $//$ parallel to the radial plane
 \perp perpendicular to the radial plane

$$\begin{aligned}
Q_{//}^{\text{Ra}} &= \frac{3}{16\pi} \sigma_{\text{T}} (\sin^2 \alpha + \cos^2 \alpha \cos^2 \Theta) \\
Q_{\perp}^{\text{Ra}} &= \frac{3}{16\pi} \sigma_{\text{T}} (\cos^2 \alpha + \sin^2 \alpha \cos^2 \Theta) \\
b &= \cos \gamma = \cos \left(\frac{\pi - \Theta}{2} \right) \\
\Delta &= \frac{q\lambda'}{c} \\
q &= \sqrt{\frac{2kT}{m}} \\
I(\lambda', \omega, \mathbf{x}) &= \frac{1}{\pi} \left(\frac{\text{AU}}{\mathbf{R}_{\text{solar}}} \right)^2 \left(\frac{1 - \mathbf{u}_1 + \mathbf{u}_1 \cos \theta}{1 - \frac{1}{3} \mathbf{u}_1} \right) f \\
\Theta &= \pi - \cos^{-1} (\sin \omega \sin \varphi \sin \chi + \cos \omega \cos \chi) \\
\alpha &= \sin^{-1} \left(\frac{\sin \omega \sin \varphi}{\sin(\pi - \Theta)} \right) \\
\chi &= \cos^{-1} \left(\frac{\mathbf{x}}{\mathbf{r}} \right) \\
\omega^* &= \sin^{-1} \left(\frac{1}{\mathbf{r}} \right) \\
\theta &= \sin^{-1} (\mathbf{r} \sin \omega) \\
\mathbf{r}^2 &= \mathbf{x}^2 + \rho^2
\end{aligned} \tag{5.2}$$

The distances \mathbf{r} , ρ and \mathbf{x} are expressed in solar radii as follows.

$$\begin{array}{l}
 \mathbf{r} \rightarrow \mathbf{rR}_{\text{solar}} \\
 \rho \rightarrow \rho R_{\text{solar}} \\
 \mathbf{x} \rightarrow \mathbf{xR}_{\text{solar}}
 \end{array}
 \tag{5.3}$$

The physical parameters that are inherent in equation (5.1) are given in equation (5.4).

$$\begin{array}{l}
 \mathbf{u}_1(\lambda') = \text{limb darkening coefficient} \\
 f(\lambda') = \text{extraterrestrial solar irradiance} \\
 N_e(\mathbf{rR}_{\text{solar}}) = \text{electron density model} \\
 T(\mathbf{rR}_{\text{solar}}) = \text{coronal temperature model} \\
 W(\mathbf{rR}_{\text{solar}}) = \text{solar wind model}
 \end{array}
 \tag{5.4}$$

The detailed derivation of equation (5.1) (=Appendix-A.98) is shown in Appendix-A. The computer code written in IDL to solve equation (5.1) is given in Appendix-B. From the physical parameters that are inherent in equation (5.1), as shown in equation (5.4), it is evident that the shape of the theoretical K-coronal intensity spectrum is dependent upon the models used for the coronal temperature, the solar wind velocity and the electron density distribution structures. In addition the numerical outcome of equation (5.1) can also be affected by the numerical methods employed in solving the various integrals. However the extraterrestrial solar irradiance spectrum and the limb darkening coefficients could be considered as well-established quantities. As such, it is prudent to analyze the dependence of the shape of the theoretical K-coronal intensity spectrum on the coronal temperature, the solar wind velocity and the electron density distribution structures and the numerical methods used in solving the integrals.

5.2 Dependence on the electron density distribution function

The bright corona seen during a solar eclipse is due to the scattering of the photospheric light by the free coronal electrons (F-corona), by dust (F-corona) and the emission lines (E-corona). The F-corona can be easily eliminated with the use of polarizers while the E-corona could be identified with the prominent peaks in an otherwise continuous spectrum. These peaks could be easily removed, as demonstrated in figure (4.33), to isolate the K-corona. The point that needs to be made here is that the most straightforward way of measuring the coronal electron density distribution is by measuring the K-coronal intensity distribution during a solar eclipse that is filtered through polarizers orientated at three different angles to eliminate the K-corona. This information can then be used to determine the electron density distribution that would have yielded the measured intensity distribution due to the scattering of the photospheric spectrum by the free coronal electrons. This method is most suitable for electron density distribution during the maximum phase of the sun, which allows for the corona to assume azimuth symmetry.

One of the pioneering efforts in this regard was due to Baumbach (1937). Baumbach, from an analysis of the photometric material of ten eclipses from 1905 to 1929, deduced the expression given in equation (5.5) for the distribution of brightness in the solar corona. This calculation was based upon averaging for all the observations and for all values of the position angle with the brightness of the center of the solar disk taken as 10^6 .

$$I(\mathbf{r}) = \frac{0.0532}{\mathbf{r}^{2.5}} + \frac{1.425}{\mathbf{r}^{7.0}} + \frac{2.565}{\mathbf{r}^{17.0}} \quad (5.5)$$

From equation (5.5) it is apparent from the last term that the brightness falls off most rapidly in the innermost region of the corona while at large distances the brightness is proportional to the first term, which decreases fairly slowly. This formula gives only a smoothed, average value for the distribution of the brightness. On a brighter note November and Koutchmy (1996) report of a best ever achieved white-light coronal observations. This unique opportunity was afforded by the path of total solar eclipse of 11 July 1991 passing above the 3.6 m Canada-France-Hawaii Telescope (CFHT) on Mauna Kea, Hawaii, which allowed for high spatial resolution white-light coronal observations with the most modern detectors that was denied to Baumbach (1937). The sun was at its maximum phase during this eclipse. Like Baumbach (1937), November and Koutchmy (1996) use the sum of three power –law terms to best approximate three regions of the curve, namely, $\mathbf{r} < 1.1$ SR, $1.1 \text{ SR} < \mathbf{r} < 1.5$ SR, and $\mathbf{r} > 1.5$ SR (SR = solar radii), to obtain the brightness distribution given by equation (5.6). Here again $I(\mathbf{r})$ is in units of 10^6 of the solar disk center and (\mathbf{r}) in units of solar radii.

$$I(\mathbf{r}) = \frac{0.0551}{\mathbf{r}^{2.5}} + \frac{1.939}{\mathbf{r}^{7.8}} + \frac{3.670}{\mathbf{r}^{18.0}} \quad (5.6)$$

Figure (5.2) shows the comparison between the brightness distributions given by equation (5.5) and equation (5.6). November and Koutchmy (1996) conclude that the small difference in the slope to be smaller than the uncertainties in the measurements.

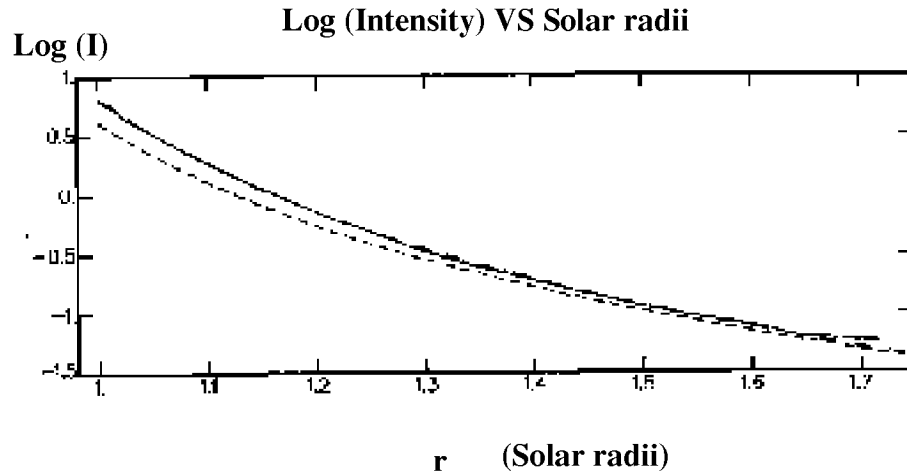


Figure (5.2). A plot showing the solar radial log-intensity variation as a function of solar radii (r) from the center of the sun. The solid curve represents the measurements by November and Koutchmy (1996) while the dashed curve represents the measurements by Baumbach (1937) based on several eclipses observations.

The coronal medium is optically thin. For Thomson scattering in optically thin plasma, the measured K-coronal intensity is proportional to the integral through the line of sight of the electron density times a local dilution factor, which is the solar intensity illuminating the scattering region of the corona. One consequence of this property is that the average radial intensity variation determines the mean radial variation of the electron density. Figure (5.3) shows the electron density distribution derived by Baumbach (1937) and November and Koutchmy (1996). Here an isotropic scattering function is assumed. This is not a bad choice for the inner corona since the illumination dilution

factor becomes equivalent to the nearly isotropic scattering form because it represents a superposition of intensity contributions from a wide range of solar disk angles.

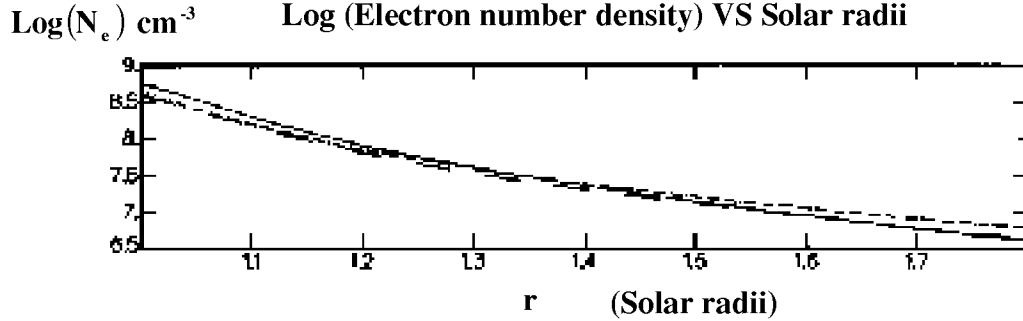


Figure (5.3). A plot showing the log of the electron density variation as a function of the solar radii (r) from the center of the sun. The solid curve represents the calculations by November and Koutchmy (1996) while the dashed curve represents the calculations by Baumbach (1937) based on several eclipses observations.

The electron number density derived by Baumbach (1937) is given by equation (5.7). A detailed derivation of equation (5.7) is also shown in Shklovskii (1965).

$$N_e(r) = 10^8 \times \left(\frac{0.036}{r^{1.5}} + \frac{1.55}{r^{6.0}} + \frac{2.99}{r^{16.0}} \right) \text{ cm}^{-3} \quad (5.7)$$

It is true that the total brightness of the corona changes from one eclipse to another. Generally speaking the coefficients of equation (5.7) too should change from eclipse to eclipse. At sunspot maximum, that is when the sun is at its maximum phase, the corona has approximately a circular form and uniformly bright as shown in figure (5.4). At sunspot minimum, that is when the sun is at its minimum phase, the corona is elongated in the equatorial regions and brighter than the polar regions as shown in figure (5.5).

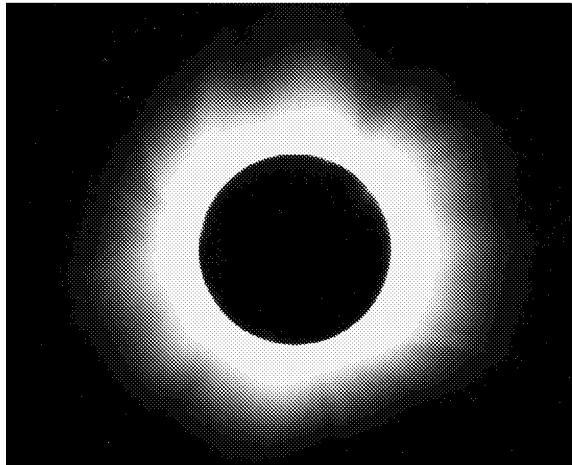


Figure (5.4). A photograph of the solar corona during the total solar eclipse of 11 August 1999 where the sun was approaching the maximum phase. Here the corona is uniformly bright and circular in shape.

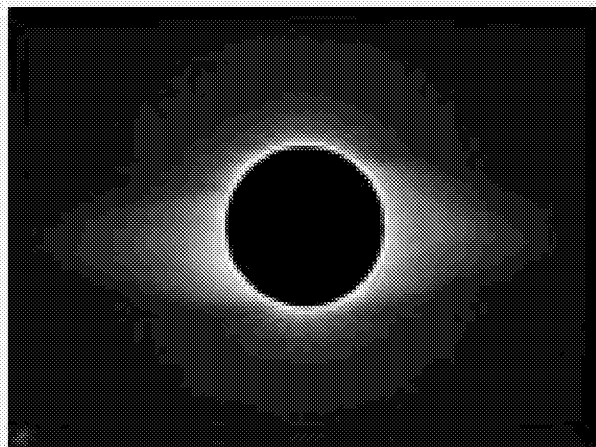


Figure (5.5). A photograph of the solar corona during the total solar eclipse of 4 November 1994 where the sun was approaching the minimum phase. Here the corona is elongated in the equatorial regions and brighter than the polar regions.

For several reasons as listed below, the electron number density distribution given in equation (5.7) was selected as input parameter in equation (5.1) for the computation of the theoretical K-coronal intensity.

(a) This derivation of the electron number density given in equation (5.7) was based upon ten eclipse observations. Although the observations were performed almost 60-80 years ago the shape of the density distribution was reconfirmed by November and Koutchmy (1996) using the most modern telescope for the same purpose. Since the reconfirmation was in conjunction with the sun in maximum phase in July 1991, this density distribution could be considered suitable for the total solar eclipse of August 1999, which again coincided with the maximum phase of the sun. The comparison between the electron number densities determined by Baumbach (1937) and November and Koutchmy (1996) is shown in figure (5.3).

(b) During the maximum phase of the sun the coronal brightness is approximately uniform all around the sun, which is not true for the sun at the minimum phase where the coronal brightness is concentrated in the equatorial regions. For a sun at the minimum phase a single density distribution function may not hold for all latitudes. Most of the other density models are specific regions and in particular hold for the minimum phase of the sun, which are detailed below. Therefore in conjunction with the maximum phase of the sun where the coronal brightness is uniform all around the sun the density model given by equation (5.7) seem to be most appropriate.

- (c) The method employed in determining the electron density given by equation (5.7) is an average over so many other coronal features. In determining the theoretical K-coronal intensity from equation (5.1) it is difficult to integrate over the different coronal features that may cross the line of sight. For such a calculation to be possible individual coronal features have to be identified along with their electron density contrast. In light of the difficulties in such a process it is again most appropriate to use an electron density model averaged over all such coronal features that may occur in conjunction with the maximum phase of the sun.
- (d) The very definition of the white-light corona is the brightness produced by the scattering of the photospheric light by the free coronal electrons, which is identified as the K-corona. Although this may be contaminated by the scattering by dust particles, which is identified as F-corona, this contamination can easily be quantified by the use of polarizers and eliminated. Also in the region of interest of the experiment described in this dissertation, which is from the limb to 1.5 solar radii, the contribution by F-corona is negligible. Therefore it is prudent to use an electron number density calculation determined by the measurement of the brightness of the white-light corona, which is the case for the electron number density determined by Baumbach (1937) and Novemir and Koutchmy (1996).

The electron density model used Cram (1976), in formulating the properties of the K-coronal intensity spectrum for the determination of the thermal electron temperature in the corona, is given in equation (5.8).

$$N_e(\mathbf{r}) = 1.67 \times 10^{(4.0+4.04/r)} \text{ cm}^{-3} \quad (5.8)$$

Ichimoto et al. (1996) used the same electron density model given in equation (5.8) in determining the coronal temperatures. Their eclipse observation of February 1994 coincided with the sun at its minimum phase where the coronal brightness is prominently displayed in an elongated shape in the equatorial regions of the sun.

According to Cram (1976) the model given in equation (5.8) agrees with the Van de Hulst (1950) minimum equator model within 2% for line of sight between 1.5 and 2.0 solar radii. This model is appropriate for the temperature determination by Ichimoto et al. (1996) because their observations were confined to regions between 1.5 and 2.0 solar radii and also their observations on the total solar eclipse of February 1994 coincided with the minimum phase of the sun.

Another model for the electron number density was due to Newkirk (1961). This model was based on radio and optical observations. Here the effects of refraction were considered while neglecting the effects of magnetic fields. The optical depth effects inherent in any radio observations are discussed in section (1.2). Separate values for the electron number densities were obtained for the average corona, the polar caps and the

active regions. The approximate formula for the electron number density presented by Newkirk (1961) is shown in equation (5.9).

$$N_e(r) = 4.2 \times 10^{(4.0+4.32/r)} \text{ cm}^{-3} \quad (5.9)$$

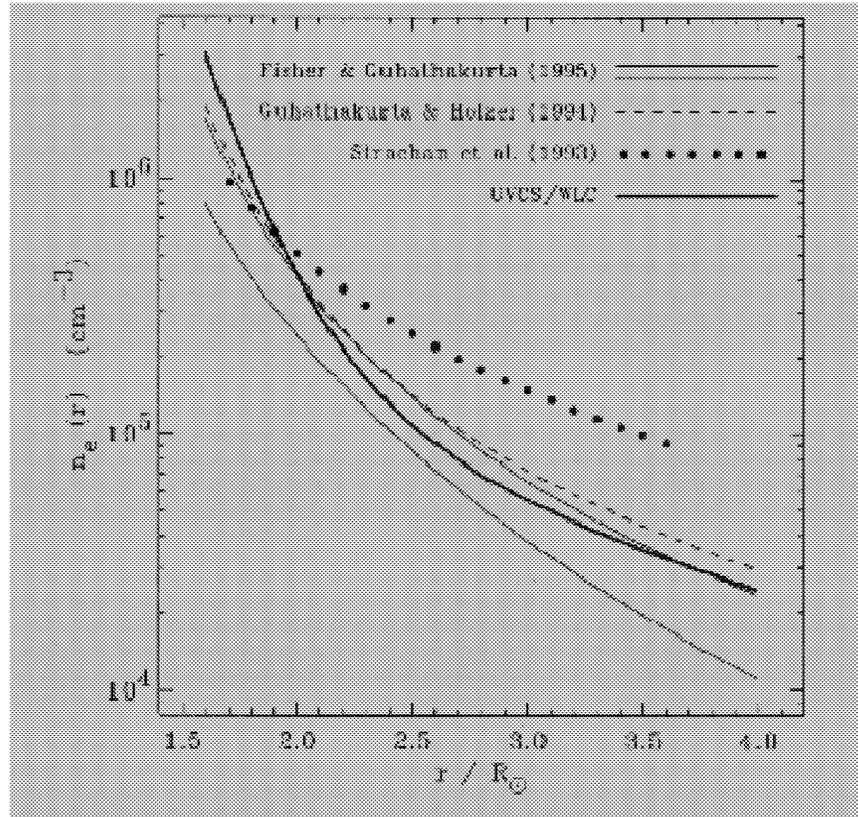


Figure (5.6). A series of plots showing the radial dependence of the mean electron density in coronal holes computed from various sets of polarization brightness data. This plot was obtained from Cranmer et al. (1999).

Various other research groups have computed radial dependence of the mean electron density specific to coronal holes. These calculations were based on various sets K-coronal polarization brightness. Figure (5.6) is a plot from Cranmer et al. (1999) showing the electron number density profiles calculated by various research groups.

In figure (5.6) the heavy solid line is due to Cranmer et al. (1999) using the UVCS/WLC aboard the SOHO satellite. And the electron number density profile obtained by Cranmer et al. (1999) is given by equation (5.10). The observed data in this case is restricted to regions greater than 1.5 solar radii where (r) is in solar radii.

$$N_e(r) = 10^8 \times (3.890 \times r^{-10.5} + 0.00869 \times r^{-2.57}) \text{ cm}^{-3} \quad (5.10)$$

The filled circles in figure (5.6) is due to Strachen et al. (1993) using rocket based coronagraph data. Here they considered the corona to be unstructured and spherically symmetric. However this assumption is reasonable for considerations restricted to the coronal hole. Here again electron density profile is restricted to the coronal hole region at heights above 1.5 solar radii. The electron number density profile obtained by Strachen et al. (1993) is given by equation (5.11) where (r) is in solar radii.

$$N_e(r) = 10^8 \times (0.152 \times r^{-6.71} + 0.0193 \times r^{-2.40}) \text{ cm}^{-3} \quad (5.11)$$

Using data obtained by Spartan 201-01, Guhathakurta and Holzer (1994) have presented an electron density profile for the polar coronal hole region specific to the minimum phase of the solar cycle. This again is valid for heights above 2.0 solar radii from the center of the sun. The electron density model by Guhathakurta and Holzer (1994) is given by equation (5.12) where (r) is in solar radii.

$$N_e(r) = 10^8 \times (0.81 \times r^{-16.87} + 0.80 \times r^{-8.45} + 0.014 \times r^{-2.8}) \text{ cm}^{-3} \quad (5.12)$$

The electron density measurements by Fisher and Guhathakurta (1995) were based on the use of both the Mk-III K-coronameter from Mauna Loa and White Light Coronagraph of the space-borne Spartan 201. This study coincided with the maximum phase of the sun in 1990. However the observations were restricted to the northern and southern coronal holes. Their measurements extended from 1.16 solar radii to 5.5 solar radii. The uncertainties reported for the electron density measurements at 1.16 - 1.3 and 1.4 - 1.8 solar radii are ~15% and (30 % - 35 %), respectively. This latter region coincided with data set where Mk-III and Spartan 201 data were cross calibrated. Figure (5.7) is a plot of the electron density measurements by Fisher and Guhathakurta (1995).

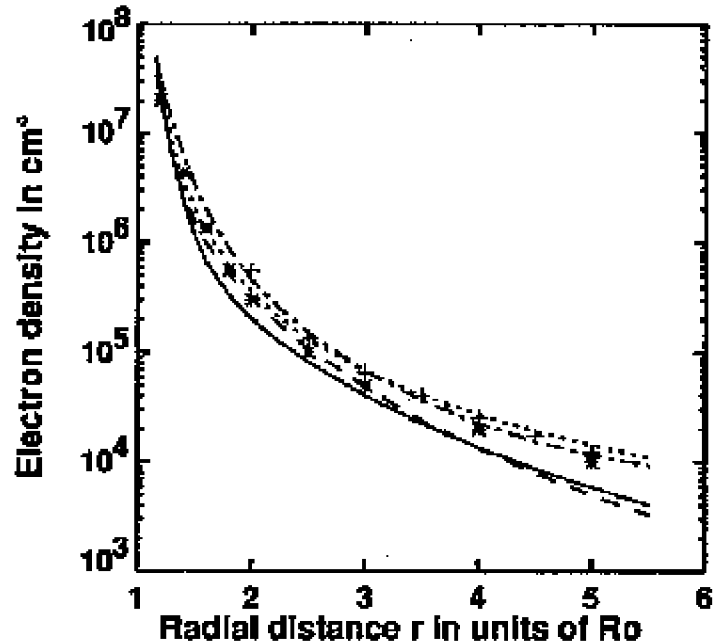


Figure (5.7). A plot showing the electron densities for the north (solid line) and south polar coronal holes (dashed line) and the north (dotted line) and south (dot-dashed line) polar coronal rays as a function of height. Reproduced from Fisher and Guhathakurta (1995).

Figure (5.8) is a comparison of the electron number density functions based on the models by Baumbach (1937, equation (5.7)), Ichimoto et al. (1996, equation (5.8)), Newkirk (1961, equation (5.9)), Cranmer et al. (1999, equation (5.10)) and Guhathakurta and Holzer (1994, equation (5.12)). Figure (5.9) is a comparison of the shapes of the K-coronal intensity spectra based on the Baumbach (1937, equation (5.7)), Ichimoto et al. (1996, equation (5.8)), Newkirk (1961, equation (5.9)), Cranmer et al. (1999, equation (5.10)) and Guhathakurta and Holzer (1994, equation (5.12)) models for the electron number density. These plots are normalized to intensity at 4000.0 angstrom and modeled

for line of sight at 2.0 solar radii above the center of the sun. This plot is simply for the comparison of the shapes of the theoretical K-coronal intensity spectra based on different electron density models. The theory by Cram (1976) for the determination of the thermal electron temperature of the solar corona is based upon the shape of the K-coronal intensity spectrum and not its absolute values. It is evident from figure (5.9) that no discernible differences could be seen in the shapes of the theoretical K-coronal spectra for five different electron density models.

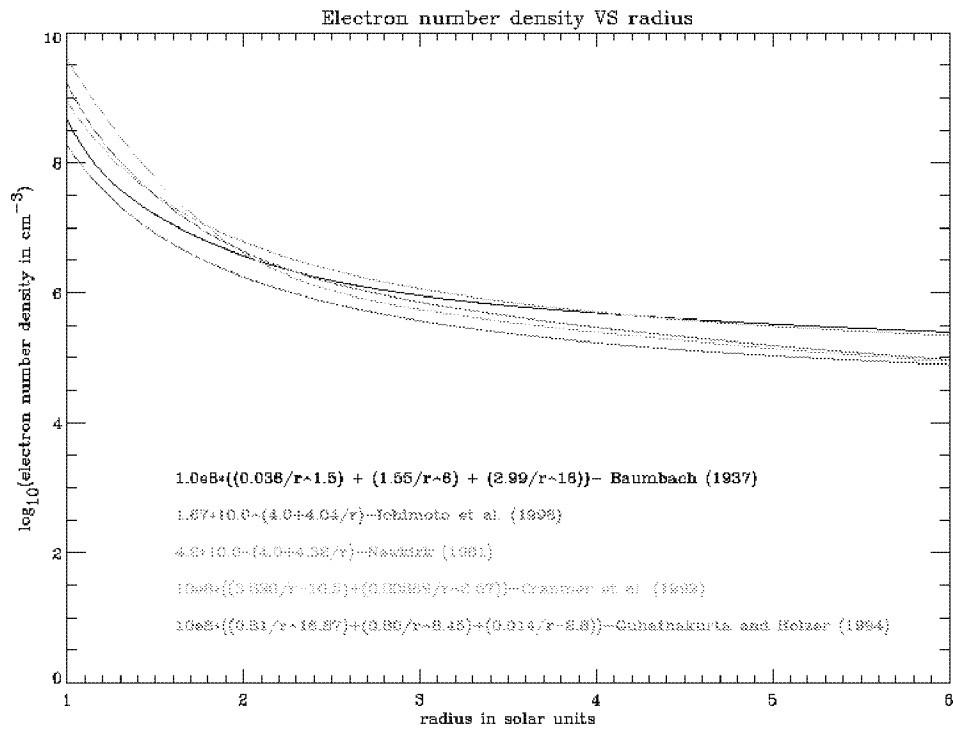


Figure (5.8). A comparison of the electron number density functions based on the models by Baumbach (1937, equation (5.7)), Ichimoto et al. (1996, equation (5.8)), Newkirk (1961, equation (5.9)), Cranmer et al. (1999, equation (5.10)) and Guhathakurta and Holzer (1994, equation (5.12)).

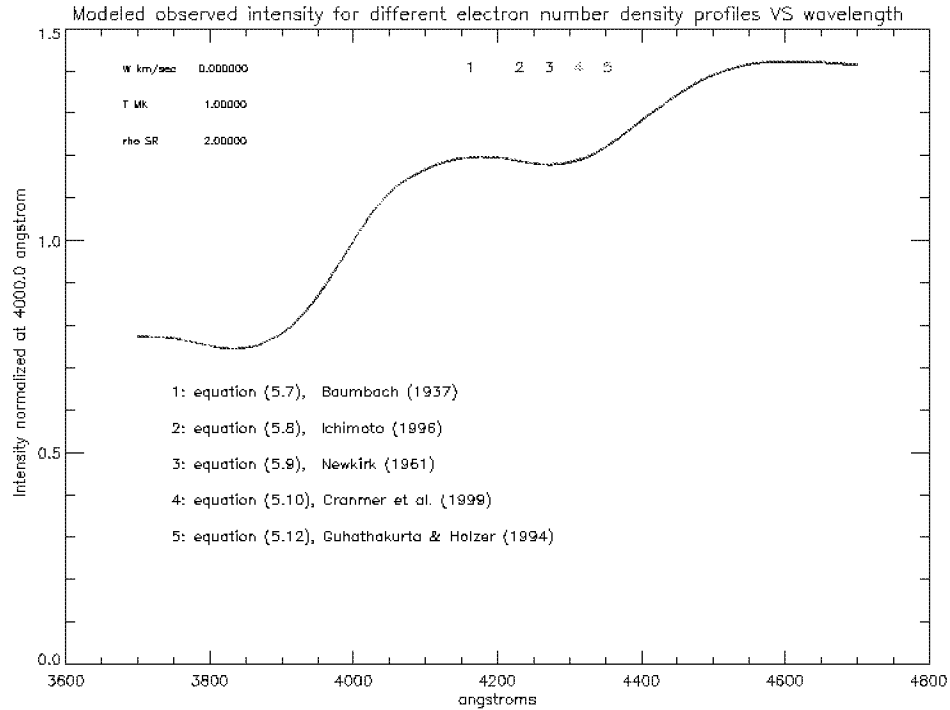


Figure (5.9). Plots of the theoretical K-coronal intensity spectra based on the electron number density functions given by Baumbach (1937, equation (5.7)), Ichimoto et al. (1996, equation (5.8)), Newkirk (1961, equation (5.9)), Cranmer et al. (1999, equation (5.10)) and Guhathakurta and Holzer (1994, equation (5.12)) and the line of sight at 2.0 solar radii from the center of the sun. The curves have been normalized at 4000.0 angstrom.

Figure (5.10) is another plot the theoretical K-coronal intensity based on different density models for the line of sight at 1.1 solar radii. Here again no discerning differences could be observed in the shapes of the K-coronal intensity distribution based on the different electron density models. However the absolute values would differ for the different electron density models although it is irrelevant to this experiment.

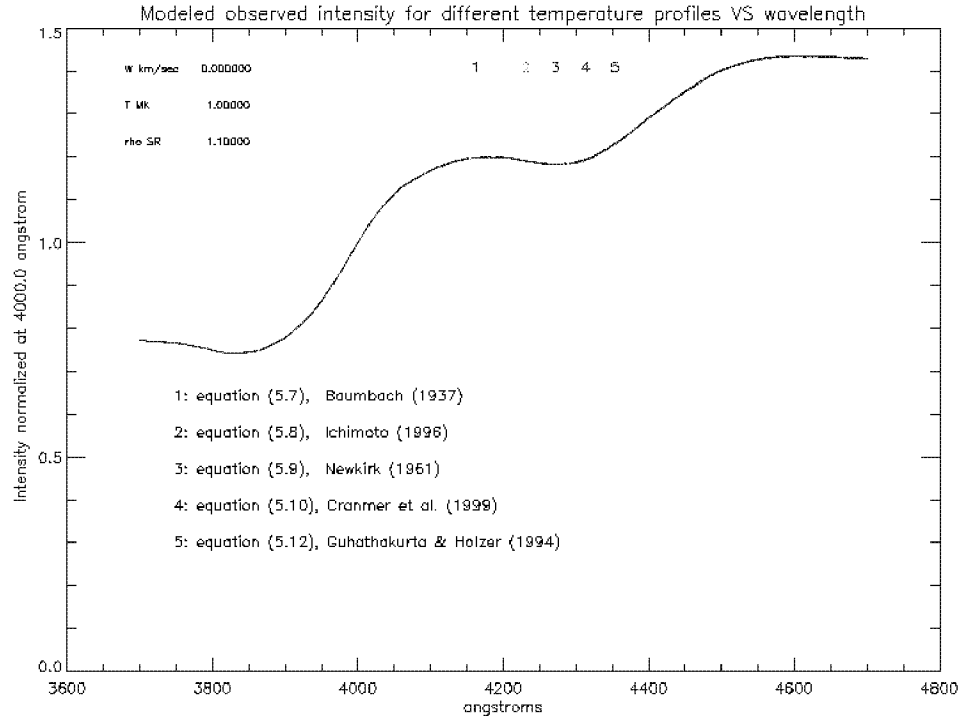


Figure (5.10). Plots of the theoretical K-coronal intensity spectra based on the electron number density functions given by Baumbach (1937, equation (5.7)), Ichimoto et al. (1996, equation (5.8)), Newkirk (1961, equation (5.9)), Cranmer et al. (1999, equation (5.10)) and Guhathakurta and Holzer (1994, equation (5.12)) and the line of sight at 1.1 solar radii from the center of the sun. The curves have been normalized at 4000.0 angstrom.

In summary the electron density measurements given by equations (5.8) to (5.12) are specific to minimum phase of the sun, or specific to the coronal holes or specific to heights above the region of interest of MACS. The region of interest of MACS extends from 1.1 solar radii to 1.5 solar radii and the experiment coincided with the maximum phase of the sun. In this regard it was decided to select the electron number density given by Baumbach (1937), as given by equation (5.7), as input parameter for the theoretical calculation of the K-coronal intensity spectrum. Here the calculations were based on ten

eclipse observations, which avoids the scattering inherent with coronagraphs, and the region of interest extended from 1.0 solar radius to ~3.0 solar radii. Although these measurements were conducted about 60 – 80 years ago, this distribution function was reconfirmed by November and Koutchmy (1996). They had a unique opportunity of performing the same experiment using the most modern 3.6-m CFHT telescope in Hawaii in conjunction with the total solar eclipse of July 1991, where the sun was at its maximum phase.

5.3 Dependence on the temperature profile

Here what need to be investigated are the differences in the theoretical K-coronal intensity profiles based on the assumption of an isothermal corona and temperature profiles with a radial dependence. Usually the radial dependence of the coronal temperature profiles is based on other experimental results. Since the purpose of this dissertation is to determine the temperature and the wind profiles at several coronal heights and latitudes, it will not be helpful in substituting radial temperature profiles determined experimentally. However an important theoretical consideration for the temperature profile of the solar corona is due to Chapman (1957). He assumed that above a certain height in the corona losses by emission to be insignificant compared to conductive losses and derived the following radial dependence for the temperature profile as given by equation (5.13) where (\mathbf{r}) is in solar radii.

$$\mathbf{T}(\mathbf{r}) = \mathbf{T}_0 \times \mathbf{r}^{-2/7} \tag{5.13}$$

For comparison between an isothermal corona and a temperature profile given by equation (5.13) assume the line of sight at 1.3 solar radii with the electron number density profile given by equation (5.7). Also assume that for the case of the temperature profile given by equation (5.13) that the temperature at the intersection between the line of sight at 1.3 solar radii and the plane of the solar limb to be 1.0 MK and then to fall off as $r^{-2/7}$. For such a case the temperature profile is given by equation (5.14) and its variation along the line of sight is given by figure (5.11). Here (r) is the distance to points along the line of sight from the center of the sun. The isothermal corona assumes a temperature of 1.0 MK all along the line of sight.

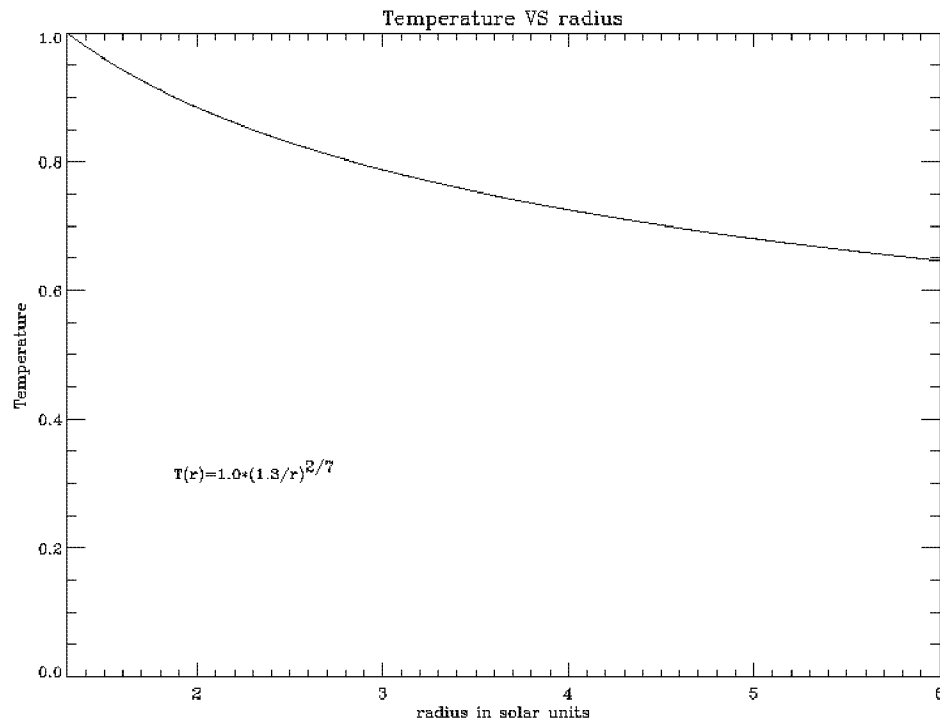


Figure (5.11). This is a plot of the temperature profile along the line of sight at 1.3 solar radii based on the assumption of a conductive corona Chapman (1957). The temperature at the point of intersection of the line of sight and the plane of the solar limb is 1.0 MK.

Figure (5.12) is a plot of the theoretical K-coronal intensity spectra due to an isothermal corona of temperature 1.0 MK and due to temperature profiles given by $T(r) = 1.0 \times (1.3/r)^{2/7}$ and $T(r) = 1.0 + (1.0 + 9.0 * (r - 1.75)^2)^{-1}$. The latter is a hypothetical temperature profile assumed by Cram (1976). From figure (5.12) no discernible differences could be seen between the spectra due to an isothermal corona and the model with a temperature profile given by $T(r) = 1.0 \times (1.3/r)^{2/7}$.

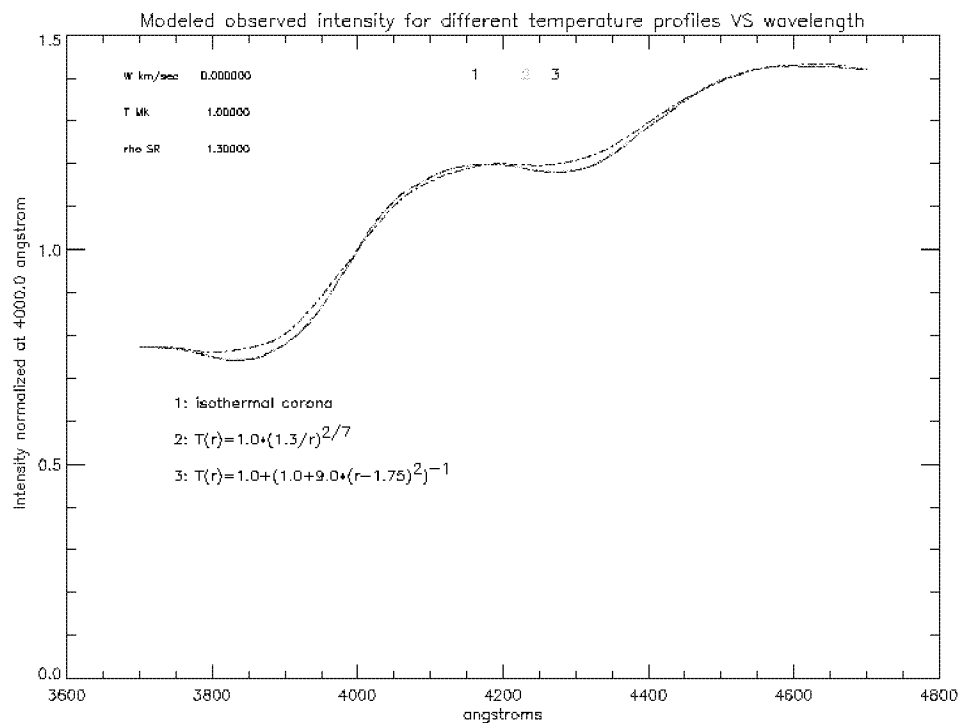


Figure (5.12). This is a plot of the modeled K-coronal intensity spectra for an isothermal corona of 1.0 MK and a model with the temperature profiles given by $T(r) = 1.0 \times (1.3/r)^{2/7}$ and $T(r) = 1.0 + (1.0 + 9.0 * (r - 1.75)^2)^{-1}$. Here (r) is the distance between the center and points along the line of sight 1.3 solar radii. The temperature at the point of intersection of the line of sight and the plane of the solar limb is 1.0 MK.

5.4 Dependence on the wind profile

Here again what need to be investigated are the differences in the theoretical K-coronal intensity profiles based on the assumption of an isothermal corona and wind profiles with a radial dependence. Usually the radial dependence of the coronal wind profiles is based on other experimental results. However one important wind profile based purely on theoretical consideration is due to Parker (1958). The wind structures due to isothermal and non-isothermal coronal conditions, driven by sound waves, driven by dust, driven by lines, driven by the combined effect of the magnetic fields and rotation and driven by Alfvén waves are detailed in Lamers & Cassinelli (1999).

Consider an isothermal wind in which the gas is subject to two forces: the inward directed gravity and the outward directed gradient of the gas pressure. It has been shown that the momentum equation has many solutions, depending on the boundary conditions but only one of them, the critical solution starts subsonic at the lower boundary of the wind and reaches supersonic velocities at large distances. The solution to the wind structure in such a case is given by equation (5.14).

$$\boxed{v \times \exp\left(\frac{-v^2}{a^2}\right) = a \left(\frac{r_c}{r}\right)^2 \times \exp\left(\frac{-2r_c}{r} + \frac{3}{2}\right) \text{ where}} \quad (5.14)$$

$$r_c = \frac{GM_{\text{solar}}}{2a^2}, \quad a = \sqrt{\left(\frac{RT}{\mu}\right)}$$

This phenomenon reveals that a wind is generated as a natural consequence of an isothermal corona. In equation (5.14), G , T , μ , R , a and r_c are the universal gravitational constant, isothermal temperature, mean atomic weight of the particles expressed in units of the mass of the proton, universal gas constant, isothermal sound speed and the critical radius, respectively. For solar composition μ is 0.602. For an isothermal temperature of 1.0 MK the isothermal sound speed (a) and the critical radius (r_c) are 117.5 km/sec and 6.9 solar radii, respectively. Figure (5.13) shows the profile of the wind for the above case.

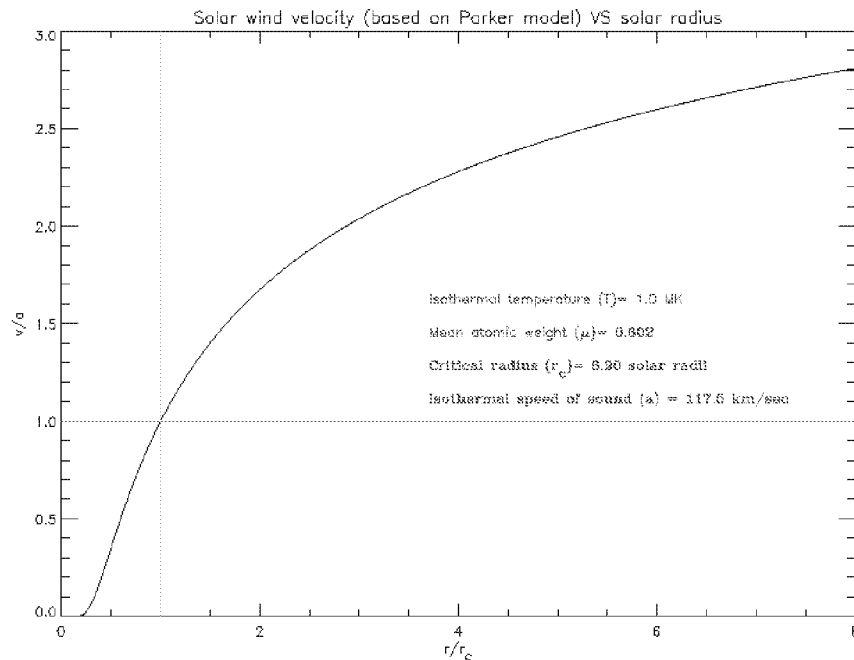


Figure (5.13). Coronal wind profile based on the Parker model for an isothermal corona. In the ideal solution the velocity is equal to the isothermal sound speed at the critical radius and starts with subsonic velocities at the lower boundary and reaches supersonic velocities at large distances.

The Parker wind model shown in figure (5.13) is a natural consequence of an isothermal corona. Therefore, even if the solar wind is neglected in the determination for the theoretical K-coronal intensity spectrum for an isothermal corona, it is worthwhile to investigate the effect on this spectrum by the bulk flow velocity introduced by the Parker model naturally. In figure (5.14) the comparison is made between a theoretical K-coronal spectrum for an isothermal corona of 1.0 MK, zero wind velocity and line of sight at 1.5 solar radii with the spectrum due to the bulk flow velocity that naturally arises with the introduction of the Parker wind model given in equation (5.14).

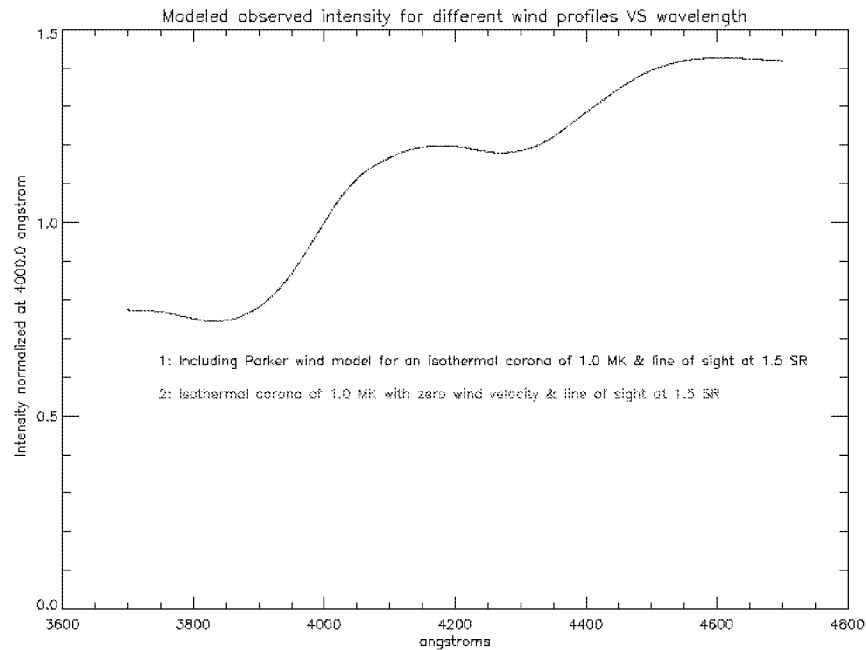


Figure (5.14). Comparison of the theoretical K-coronal intensity spectrum for an isothermal corona at 1.0 MK, zero wind velocity and line of sight at 1.5 solar radii with the intensity spectrum due to the bulk flow velocity that naturally arises with the Parker wind model for an isothermal corona as given in equation (5.14).

In figure (5.14) no discernible differences could be observed between the two K-coronal intensity spectra. The reasons for this are twofold. First, from the Parker wind profile shown in figure (5.13) it is evident that the solar wind velocity at 1.5 solar radii is very small. Second, although the wind profile shown in figure (5.13) indicates that the wind values are significant at large distances, nevertheless, this effect is negligible due to the drop in the electron number density at large distances. Figure (5.15) shows the theoretical K-coronal intensity spectra due to isothermal coronal temperatures of 1.0 and 1.5 MK with the inclusion of the Parker wind model for an isothermal corona given in equation (5.14). As expected the nodes begin to appear mainly due to the temperature differences.

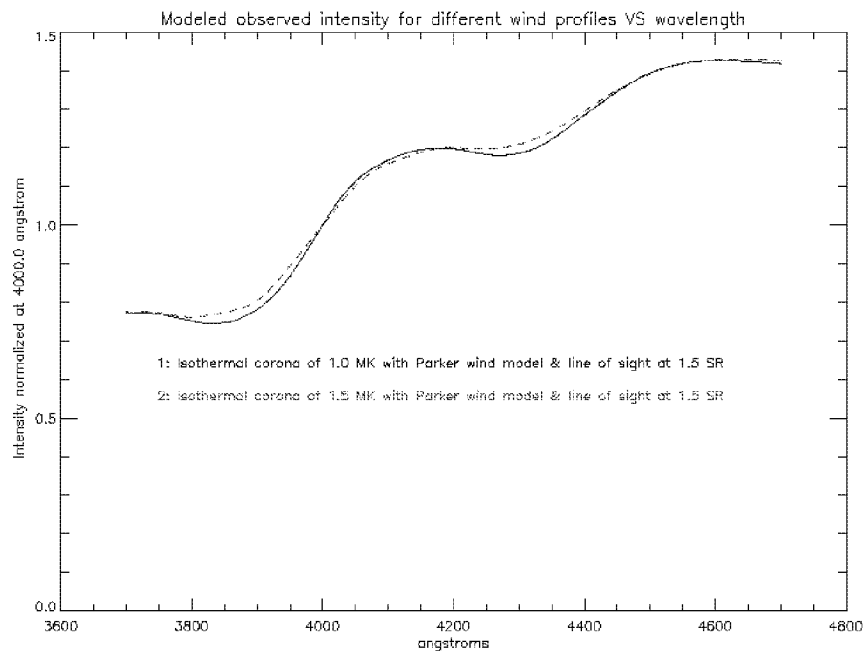


Figure (5.15). Comparison between two theoretical K-coronal intensity spectra due to isothermal coronal temperatures of 1.0 and 1.5 MK and with the inclusion of the Parker wind model for an isothermal corona.

5.5 Dependence on the numerical method

The theoretical model for the K-corona, as shown in equation (5.1), consists of four coupled integrations. In the absence of an analytical solution this equation could be solved only through a four-dimensional numerical quadrature. While acknowledging the existence of multitude of numerical methods, the numerical methods used in solving equation (5.1) were based on procedures presented in the Handbook of Mathematical Functions (Ed. M. Abramowitz and L.A. Stegun). Two of the integrals were calculated using the Trapezoidal Composite Rule while the other two were solved using a Gaussian Quadrature. There is reason to believe in the results since they can reproduce the theoretical results obtained by Cram (1976) and Ichimoto et al. (1996). This numerical procedure was also sufficient to determine the polarization components to confirm that the degree of polarization is almost wavelength independent and that it increases with heights above the solar limb. The degree of polarization (\mathbf{p}) is defined by equation (5.15).

$$\mathbf{p}(\lambda, \rho) = \frac{\mathbf{I}_{//}^{\text{Ra}}(\lambda, \rho) - \mathbf{I}_{\perp}^{\text{Ra}}(\lambda, \rho)}{\mathbf{I}_{//}^{\text{Ra}}(\lambda, \rho) + \mathbf{I}_{\perp}^{\text{Ra}}(\lambda, \rho)} \quad \text{where} \quad (5.15)$$

$\mathbf{I}_{//}^{\text{Ra}}(\lambda, \rho) = \text{Intensity parallel to the radial plane}$
 $\mathbf{I}_{\perp}^{\text{Ra}}(\lambda, \rho) = \text{Intensity perpendicular to the radial plane}$

Figure (5.16) shows a plot of the degree of polarization, for a given isothermal coronal temperature of 1.0 MK, for lines of sight at 1.1, 1.3 and 1.5 solar radii. It is evident from figure (5.16) that the polarization components were calculated with sufficient accuracy to confirm the behavior expected of the polarization. That is, they are wavelength independent and increase with heights above the solar limb.

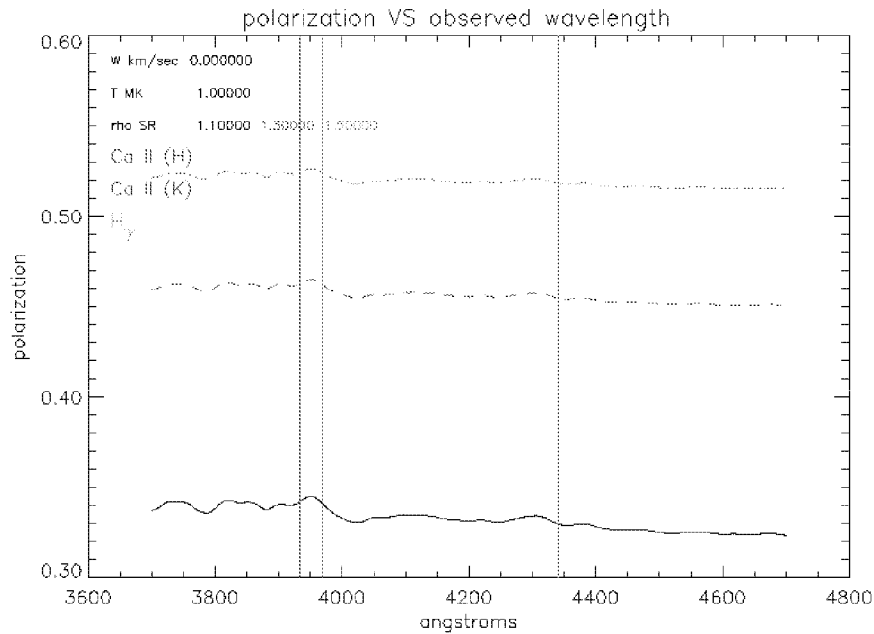


Figure (5.16). Plot of the polarization from theoretical modeling for the formation of the K-corona, at a given isothermal coronal temperature of 1.0 MK, for lines of sight at 1.1, 1.3 and 1.5 solar radii. The behavior of the polarization conforms to the observations. That is, the polarization is almost wavelength independent and increases with coronal heights.

The numerical code to solve equation (5.1) was written in IDL (Interactive Data Language) and took ~100 minutes to calculate the intensity spectrum from 3700 – 4700 angstroms in a Pentium-II 233 MHz PC. Of the four integrals two were solved using the Trapezoidal Composite Rule while the other two were solved using Gaussian Quadrature. In the situation where the Trapezoidal Composite Rule was used, the quadrature points were divided into higher and higher number of points to check for differences in the results. The final number of quadrature points was selected based on the point where the overall results for the intensity converges to within five decimal places. As for the other

two integrals, these were solved using Gaussian quadratures. Their integration limits allowed for the use of Hermite polynomials and its associated weights. That is, these integrals had the form given by equation (5.16).

$$\int_{-\infty}^{+\infty} f(x)e^{-x^2} dx \approx \sum_{i=0}^n f(h_i)w_i \quad \text{where} \quad (5.16)$$

h_i = zeros of Hermite polynomials
 w_i = weights

However the line of sight integration was of the form given by equation (5.17), which was converted to the form given by equation (5.16), which follows the procedure given in the Handbook of Mathematical Functions (Ed. M. Abramowitz and L.A. Stegun, pg. 924).

$$\int_{-\infty}^{+\infty} f(x)dx = \int_{-\infty}^{+\infty} \{f(x)e^{+x^2}\}e^{-x^2} dx \approx \sum_{i=0}^n \{f(h_i)e^{h_i^2}\}w_i \quad \text{where} \quad (5.17)$$

h_i = zeros of Hermite polynomials
 w_i = weights

In equation (5.17) the function $f(x)$ is of the following form given by equation (5.18), which is a convergent function without any singularities in the region of interest.

$$f(x) \equiv \left(\frac{0.036}{(\sqrt{x^2 + \rho^2})^{1.5}} + \frac{1.55}{(\sqrt{x^2 + \rho^2})^6} + \frac{2.99}{(\sqrt{x^2 + \rho^2})^{16}} \right) \times \frac{1}{\sqrt{x^2 + \rho^2} \sqrt{x^2 + \rho^2 + \mu^2 - 1}} \quad (5.18)$$

For example assume $\mu = 1.0$ and $\rho = 1.1$ in equation (5.18). Then the equation (5.18) reduces to equation (5.19).

$$\int_{-\infty}^{+\infty} \left(\frac{0.036}{(\sqrt{x^2 + \rho^2})^{4.5}} + \frac{1.55}{(\sqrt{x^2 + \rho^2})^6} + \frac{2.99}{(\sqrt{x^2 + \rho^2})^{16}} \right) \times \frac{1}{x^2 + \rho^2} dx \quad (5.19)$$

Solving equation (5.19) by using the trapezoidal composite rule, where the integration limit is restricted to $x = \pm 5000$ and dividing this region into 100000 intervals of width 0.1, the result yields a value of 1.1954237. The restriction in the x-range is perfectly valid because the integrand rapidly falls to zero about $x=0$. Performing this operation over a range of values for μ is very time consuming. However by using the Gaussian quadrature over a Hermite polynomial roots of just twenty points, as specified in equation (5.17), the result yields a value of 1.1900812. This value is accurate to within 1.0 % of the result yielded by the trapezoidal composite rule and is also computed very much faster. This is also acceptable in light of the limits imposed by the instrument. An analytical solution also exists for equation (5.19) as shown in equation (5.20) (Standard Mathematical Tables and Formulae).

$$\int_0^{\infty} \frac{x^a}{(m + x^b)^c} dx = \frac{m^{\frac{a+1-bc}{b}}}{b} \left[\frac{\Gamma\left(\frac{a+1}{b}\right) \Gamma\left(c - \frac{a+1}{b}\right)}{\Gamma(c)} \right] \quad (5.20)$$

where $a > -1, b > 0, m > 0, c > \frac{a+1}{b}$, $\Gamma \equiv$ Gamma function

Writing equation (5.19), as shown in equation (5.21), and using equation (5.20) yields a value of 1.1954237, which matches with the value obtained by using the trapezoidal composite rule.

$$\int_{-\infty}^{+\infty} \left(\frac{0.036}{(\sqrt{x^2 + \rho^2})^{1.5}} + \frac{1.55}{(\sqrt{x^2 + \rho^2})^6} + \frac{2.99}{(\sqrt{x^2 + \rho^2})^{16}} \right) \times \frac{1}{x^2 + \rho^2} dx$$

$$= 2 \times \left(0.036 \times \int_0^{\infty} \frac{dx}{(\rho^2 + x^2)^{7/4}} + 1.55 \times \int_0^{\infty} \frac{dx}{(\rho^2 + x^2)^4} + 2.99 \times \int_0^{\infty} \frac{dx}{(\rho^2 + x^2)^9} \right) \tag{5.21}$$

The detailed derivation of the theory and the code written in IDL is provided in Appendix – A and B, respectively. Throughout the code the accuracy of the calculations were checked using the built in CHECK_MATH function, which returns the accumulated math error status, and manually. There were no errors reported.

Chapter 6

COMPARISON BETWEEN OBSERVATION AND THEORY

6.1 An unexpected phenomenon noticed in the observations

As shown in figure (3.4) the fiber optic plate in the focal plane of the telescope contained a single fiber in the center of the frame. During the observations this fiber was positioned at the center of the lunar shadow. The purpose of this fiber was to measure the background signal and was to be subtracted from the signals measured by the other fibers that were exposed to the coronal light.

However the shape of the signal measured by the fiber located in the center of the lunar shadow only provided a clue that the observations were affected by scattering. Figure (6.1) shows the signal recorded by the fiber at the center of the lunar shadow. This prominently shows the peaks of the Calcium H and K lines. The counts recorded by this fiber are not negligible compared to the counts recorded by fibers exposed to the coronal light. This indicates that we have a problem with scattering light. The extent of scattering could not be envisaged in advance for the simple reason that the true observational condition could not be replicated in the laboratory. However Cram (1976)

pointed out that the bright sources of scattered light at the time of a solar eclipse are prominences and the chromosphere, and these have a spectrum quite unlike that of either the F or K corona. The only remedial measure that was taken in order to minimize scattering was to maintain clean optical surfaces of the optical components in MACS. Although the extent of scattering in the different wavelength regions is very difficult to quantify, nevertheless, it is a hard lesson to be learnt for any future observations. In this regard some of the remedial measures for any future observations are highlighted in section (6.3).

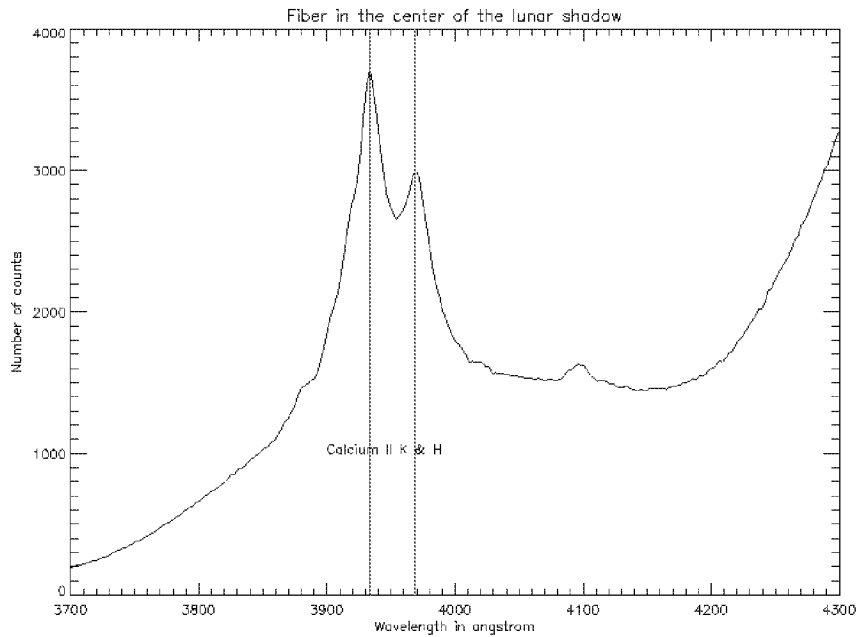


Figure (6.1). The spectrum recorded by the fiber located in the center of the lunar shadow during the eclipse. The x-coordinate corresponds to wavelength scale. The two prominent peaks are associated with the Calcium K & H lines corresponding to 3933.7 and 3968.5 angstroms, respectively.

6.2 Comparison between theory and observation

In chapter-2 temperature and wind sensitive intensity ratios were identified at particular wavelengths. These intensity ratios were at wavelength positions 4100.0/3850.0 and 4233.0/3987.0, respectively, for temperature and wind measurements. In chapter-2, we also showed how to determine the temperature and the wind velocity using the above intensity ratios calculated from the K-coronal intensity spectrum. In contrast to our ratio technique, Ichimoto et al. (1996) chose to determine the coronal temperature by fitting theoretical isothermal K-coronal models to the observed K-coronal spectrum, as shown in figure (6.2).

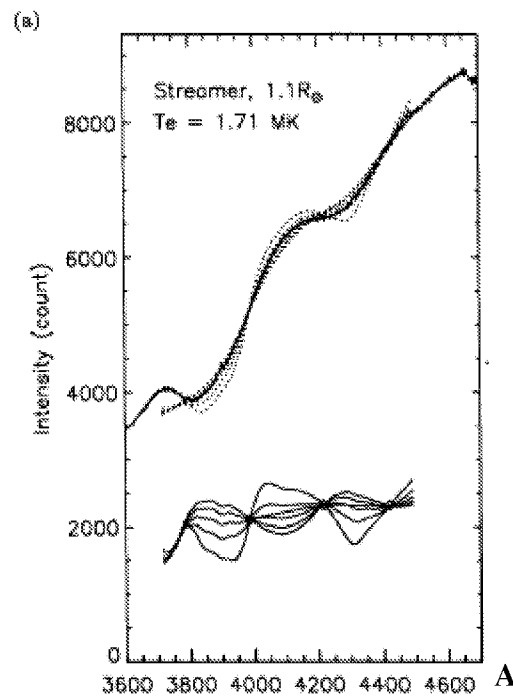


Figure (6.2). Theoretical isothermal K-coronal models fitted to the observed K-coronal intensity spectrum to determine the temperature by Ichimoto et al. (1996). The lower curves show the differences between the observational spectrum and the theoretical models. The model that showed the least difference determined the temperature.

The same temperature measurement, as shown in figure (6.2), could also be determined from the measurement of the temperature sensitive intensity ratio. Such ratio calculations were performed using filters centered at the temperature sensitive wavelength positions by J.M. Pasachoff and his team from Williams College, Massachusetts during the total solar eclipse of 11 August 1999 in Romania. N.L. Reginald and J.M. Davila performed the theoretical calculations for predictions of the temperature for the intensity ratios for J.M. Pasachoff and his team. No results have yet been published by Pasachoff et al.

In chapter-4 the intensity ratio technique was employed to determine the temperature and the wind velocity for several fiber locations. The wind measurements were considered a total failure in this very first attempt to simultaneously and globally determine both temperature and wind velocity at twenty different locations on the solar corona. The reason for this is that the wind measurement is very sensitive to the intensity at 4233.0 angstrom, which is at the high end of the wavelength measurement by MACS. As revealed in figure (6.1) the instrumental scattering was high at the high end of the wavelength region thus predicting very high values for the wind velocity measurements. As for the temperature it too suffered from the instrumental scattering. The reason for this is that the temperature is sensitive to the intensity measurement at 3850.0 angstrom and 4100.0 angstrom. As revealed in figure (6.1) the strong Calcium Hand K lines in the region of 3900-4000 angstrom seem to have contributed strongly to instrumental scattering. Predicting the contribution due to scattering on the coronal intensity measured

by individual fibers is further compounded by its dependency on wavelength. At this juncture the knowledge of instrumental scattering only provides awareness of the problem of instrumental scattering and remedial measures that need to be considered before any future observations. The sole handicap in such observations is the inability to replicate the experiment in the laboratory in the absence of a coronagraph.

Figure (6.3) shows the comparison between experimentally obtained K-coronal spectrum for fiber # 04 with theoretical models for various isothermal temperatures. From the intensity ratio method the wind velocity and the temperature deduced for fiber # 04 are 300.0 km/sec and 1.29 MK, respectively. The theoretical K-coronal models plotted in figure (6.3) correspond to a wind velocity of 300.0 km/sec and isothermal coronal temperatures of 0.5MK, 1.0 MK, 1.5 MK and 2.0 MK. In such a scenario the experimentally obtained K-coronal spectrum may be expected to lie between the theoretical models for 1.0 MK and 1.5 MK. However it is obvious that the experimental K-coronal spectrum deviates from the predictions. This deviation can be divided into four distinct regions on the wavelength scale.

1. 3800 – below: In this region the experimental curve falls below the predictions.
2. 3800 – 4000: In this region the experimental curve rises above the predictions.
3. 4000 – 4200: In this region the experimental curve falls below the predictions.
4. 4200 – above: In this region the experimental curve rises above the predictions.

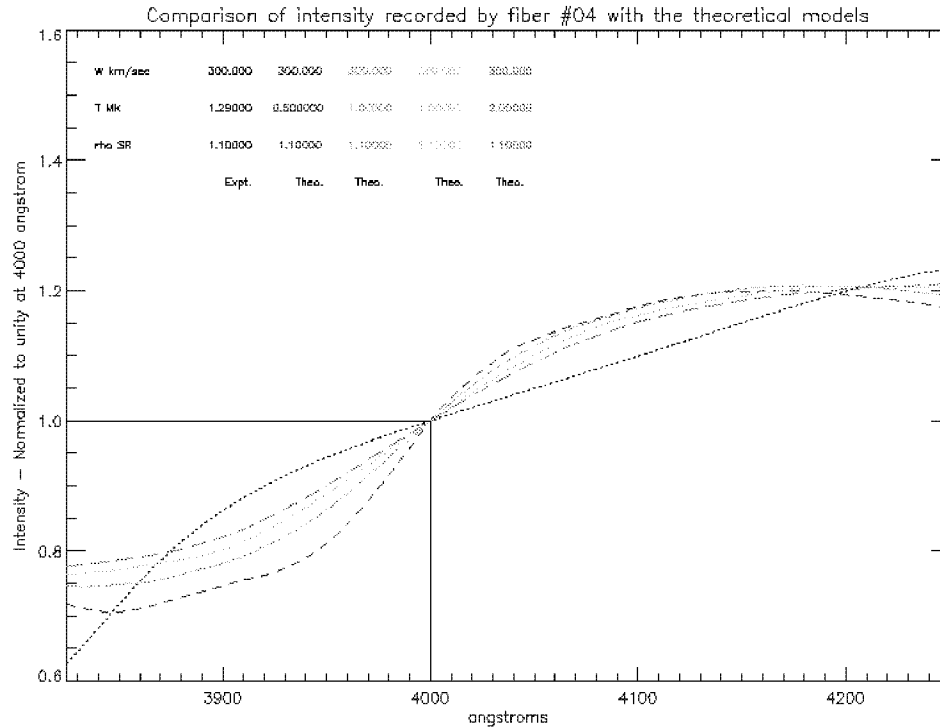


Figure (6.3). This plot shows the comparison between experimentally obtained K-coronal spectrum for fiber # 04 with theoretical models for various isothermal temperatures. From the intensity ratio method the wind velocity and the temperature deduced for fiber # 04 are, 300.0 km/sec and 1.29 MK, respectively. The theoretical K-coronal models plotted in figure (6.3) correspond to a wind velocity of 300.0 km/sec and isothermal coronal temperatures of 0.5MK, 1.0 MK, 1.5 MK and 2.0 MK. In such a scenario the experimentally obtained K-coronal spectrum may be expected to take a position between the theoretical models for 1.0 MK and 1.5 MK. (Expt: = Experimental, Theo: Theoretical)

The comparison between observation and theory for the K-coronal spectrum recorded by fiber # 04, as shown in figure (6.3), needs to be considered in conjunction with the extent of instrumental scattering that is depicted in figure (6.1). Figure (6.1) too can be divided into four distinct regions. Assuming that the signal expected of this fiber located in the center of the lunar shadow to produce a straight line with a positive gradient

signaling a higher background count at higher wavelengths. Based on this assertion, and assuming the signal recorded in the 4000 – 4200 angstrom to represent the correct true background signal, figure (6.2) can be divided into four distinct regions.

1. 3800 – below: Some optical component in MACS seems to possess a very low sensitivity to the blue region of the spectrum.
2. 3800 – 4000: The Calcium II K & H lines contribute a large signal in this region.
3. 4000 – 4200: Assumed to represent the true background count.
4. 4200 - above: Scattering is again significant in the high end of the spectrum.

The above properties pertaining to the four distinct regions in the scattered spectrum is similar to the pattern of deviation of the observed K-coronal spectrum of fiber # 04 from the theoretical models, as shown in figure (6.3). That is, the very low blue sensitivity in the wavelength region 3800 - below and the higher counts from the scattering of the Calcium II K & H lines in the region 3800 – 4000 angstrom may have caused the observed K-coronal spectrum to dip and rise, respectively, in these regions. The scattering associated with the high end of the wavelength region, i.e. 4200 - above, may have caused the observed K-coronal spectrum to again rise above the predicted level. Figure (6.4) is a plot of the superposition of figure (6.1) and figure (6.3). This shows that there is a certain amount of similarity between, on the one hand, the shape of the scattered spectrum, and on the other hand, the deviation between the predicted and observed K-coronal spectra. In figure (6.4), all spectra are normalized to unity at 4000.0

angstrom. It is reasonable to infer from figure (6.4) that some proportion of the scattered light spectrum recorded by the fiber located in the center of the lunar shadow has contaminated spectrum recorded by fiber #04. This could explain the deviations between the observed spectrum and the predictions.

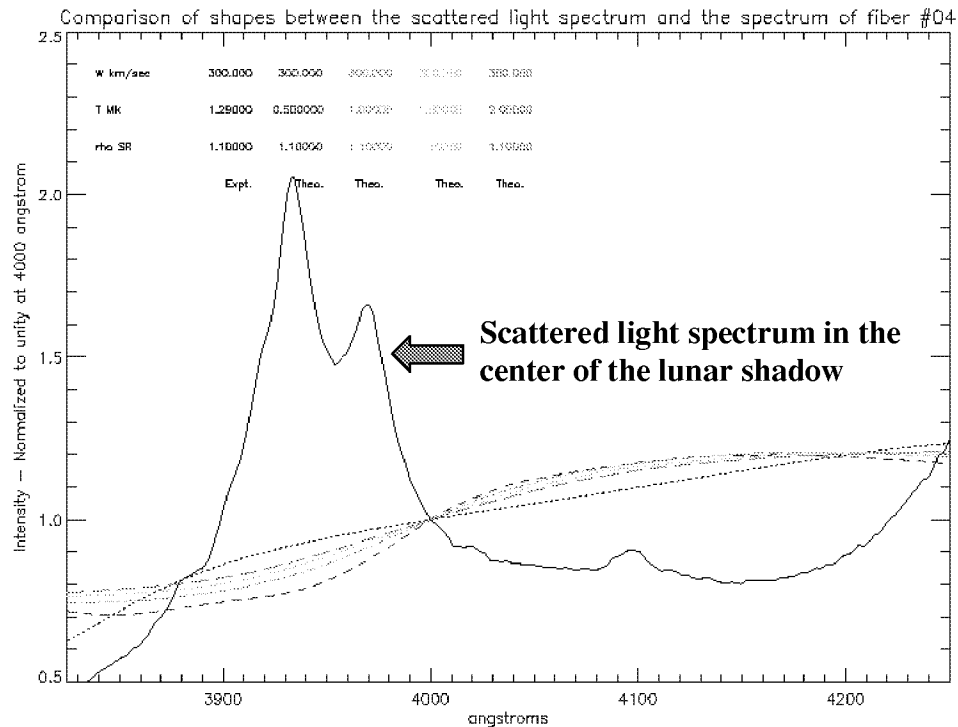


Figure (6.4). A plot of the superposition of figure (6.1) and figure (6.3). The shape of the spectrum recorded by the fiber located in the center of the lunar shadow corresponds with the shape of the observed K-coronal spectrum by fiber #04. The expected location of the observed spectrum is between the theoretical isothermal K-coronal spectra for 1.0 MK and 1.5 MK.

Figure (6.5) shows the superposition of the observed K-coronal spectrum for fiber #04 and the theoretical K-coronal spectrum for a wind velocity and isothermal temperature of 300.0 km/sec and 1.29 MK, respectively, and the difference between the two. The wind velocity and isothermal temperature of 300.0 km/sec and 1.29 MK,

respectively, for fiber #04 were determined from the intensity ratio method. From figure (6.5) it is apparent that the deviations between the observational and the theoretical spectra are larger at wavelengths of 3900 – 3950 angstroms (where the scattered light spectrum peaks), and are smaller at wavelengths around 4100 angstrom. In this regard, the deviations between observed and predicted spectra exhibit certain gross similarities to the shape of the scattered light spectrum. Even a small percentage of the scattered light spectrum being contaminated with fiber #04 could have caused its spectrum to deviate from the theoretical prediction.

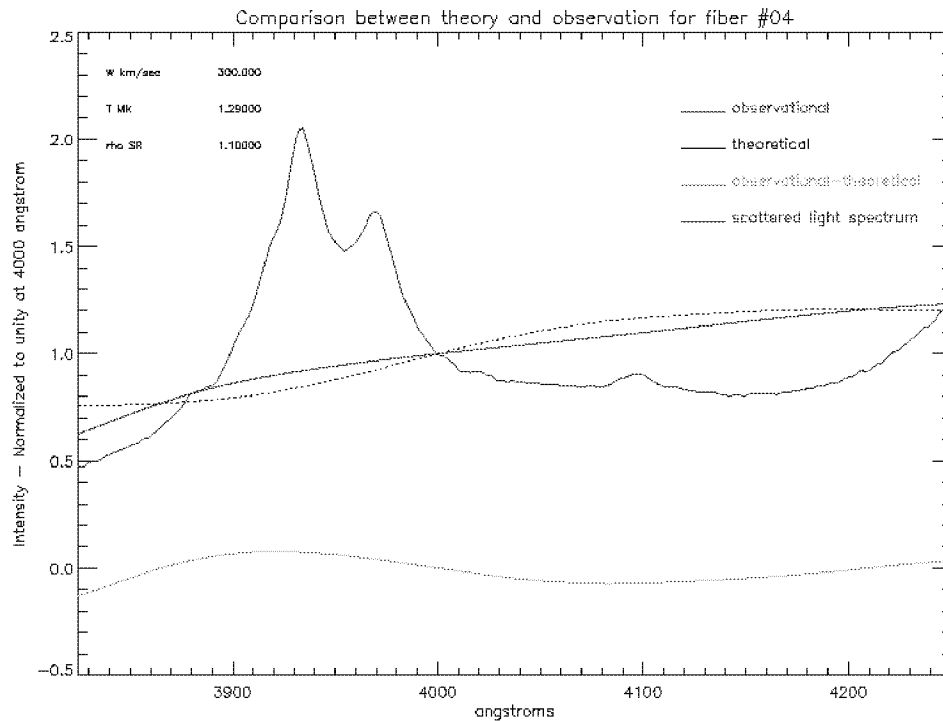


Figure (6.5). A plot showing the observed K-coronal spectrum for fiber #04 along with the theoretical K-coronal spectrum for the wind velocity and temperature derived from fiber #04. The plot also includes the difference between the observational and the theoretical plots along with the scattered light spectrum observed by the fiber in the center of the lunar shadow.

In figure (6.5) the areas under the observational and the theoretical spectra are 0.22168834 and 0.22163162, respectively. That is, the difference between the areas is almost negligible. Nevertheless, since the brightest sources of scattered light (chromospheric or prominence material) have spectra which are quite different from those of F- or K-corona, we can now see that even a slight contamination of our coronal data by such scattered light can have a serious effect on the quantitative interpretation of our results. This was pointed out by Cram (1976) who suggested that any observations should avoid such bright sources. However in MACS twenty fibers were exposed to all around the sun and at different heights above the solar limb. As a result, it is almost inevitable that some of our fibers were unfortunately exposed to bright prominence material. The effects due to exposure to these bright sources could be avoided only through a scatter free instrument. In this regard every effort was made to keep instrumental scattering to a minimum. The present experiment, the very first of its kind, reveals the extent and effects of instrumental scattering and the need for more remedial measures in this regard. The same is true of other fibers that were exposed to the coronal light: each was contaminated by scattered light to a greater or lesser extent.

Table (6.1) gives the wind and the temperature sensitive intensity ratios for fiber #04 from figure (6.5). From table (6.1) it is apparent that the wind and temperature sensitive intensity ratios are well matched in spite of the fact that the observational spectrum deviates from the prediction. This may be somewhat fortuitous, since if the amount of scattered light had been different, the observed spectrum might have matched a totally

different theoretical spectrum. This matter is further compounded by the non-existence of any mechanisms to quantify the degree of contamination of instrumental stray light on the individual fiber. In this regard it appears that in spite of the problems caused by the instrumental scattering the temperatures ratios were somehow maintained. Thus the accuracy of the temperature is to within the error estimates made in chapter- (4.7). That is to within $\sim \pm 6\%$ (± 1.2 MK). As for the wind measurements, as discussed in chapter- (4.7), its measurement was deemed to have been a failure in the current experimental effort. However the high wind values are in line with the uncertainty of ± 200 km/sec for a measurement uncertainty of $\pm 1\%$.

Table (6.1). Comparison of the wind and the temperature sensitive intensity ratios between the observational and the theoretical K-coronal spectrum, for fiber #04. These values are based on figure (6.5).

Fiber #04	Temp: I(4100)/I(3850)	Wind: I(4233)/I(3987)
Observational	1.531	1.242
Theoretical	1.529	1.242

Figure (6.6) shows plots of the observed K-coronal spectrum of fiber #04, as shown in figure (6.5), corrected for the scattered light in a crude manner. Here various fractions of the scattered light recorded by the fiber located in the center of the lunar shadow were subtracted from the spectrum recorded by fiber #04. It is evident from figure (6.6) that the observed K-coronal spectrum then begins to follow closely the shape of the theoretical K-coronal spectrum implying the influence of the scattered light.

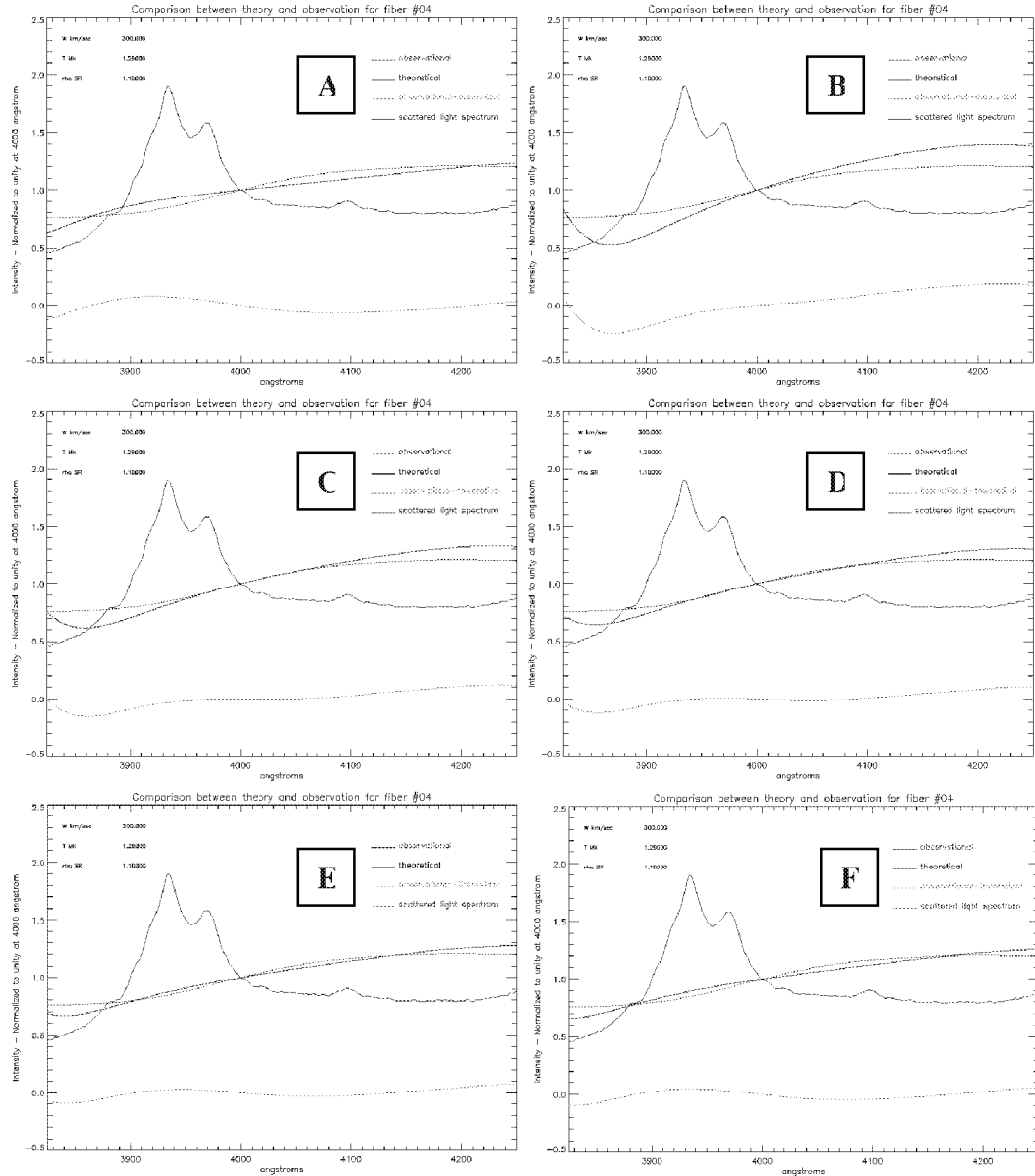


Figure (6.6). Plots showing the effect on the shape of the observed K-coronal spectrum of fiber # 04, as shown in figure (6.5), in comparison with the shape of the theoretical K-coronal spectrum by subtracting various fractions of the scattered spectrum from the observed K-coronal spectrum. A, B, C, D, E and F correspond to a subtraction of 0.0%, 15.0%, 10.0%, 8.0 %, 5.0% and 3.0%, respectively, of the scattered light spectrum recorded by the fiber that was located in the center of the lunar shadow from the spectrum recorded by fiber #04. These plots show that the observed spectrum closely follows the shape of the theoretical spectrum with various fractional subtraction of the scattered spectrum.

A similar pattern as above follows for all the other fibers for which temperatures were determined in chapter- 4. Instrumental scattering can be minimized only by paying careful attention to the optical quality of the components of the instrument. The stricter the demands on optical quality, the higher the cost will be. The very first operation of MACS in conjunction with the total solar eclipse of 11 August 1999 has shed much light and understanding on the effects of instrumental scattering associated with such observations. Apart from better optics, other remedial measures envisaged for future operation of MACS are listed in section (6.3).

6.3 Remedial measures

The principle and the method described in this thesis is unique in its character that allows for the simultaneous and global measurements of the thermal electron temperatures and the solar wind velocities on the solar corona using the shape of the K-coronal spectrum. However the steps described in section (4.6) in isolating the K-coronal spectrum from a terrestrial observation in conjunction with an eclipse are beset with problems. The main problems that arise from terrestrial observation during an eclipse are time constraints and state of the sky. Apart from these, there are other difficulties that arise in connection with the data analysis. We summarize these here.

1. In order to determine the wavelength sensitivity of our instrument, we have assumed that the sky spectrum recorded by MACS (corrected for Rayleigh scattering) should match the photospheric spectrum depicted in figure (2.1). The comparison between the two spectra shown in figure (4.21) demonstrates clearly the nature of the

difficulties we face in this regard, especially close to the Ca line at 3933.7 angstrom and regions at 4000.0 angstrom. Since this method depends on the shape of the K-coronal spectrum these inadequacies, although seem to be irrelevant, do affect the shape of the K-coronal spectrum in a significant manner. However a near perfect wavelength sensitivity curve could be obtained with the use of absolute wavelength calibration using sources of known strengths as commonly done for all advanced instruments with optical elements. This suggests that in this particular experiment the derivation of the wavelength sensitivity curve for MACS was limited in its accuracy by choice.

2. Another problem arises from our assumption that the F-corona must be allowed for in our Rayleigh-corrected MACS sky spectrum. The intensity of the F-corona (which depends on the properties of interplanetary dust between the sun and the earth) has some wavelength dependence, perhaps proportional to $\sqrt{\lambda}$. However on the assumption that the F-corona is unpolarized while the K-corona is polarized (although only orthogonal scattering gives complete polarization as per equations (A.48) and (A.49) there exists an easy practical means to determine the contribution from F-corona. This is done by observing the corona through a polarized filter with the polarization axis at minimum of three known angular positions. A detailed explanation could be found in Golub and Pasachoff (1997). The only concern that hinders this easy maneuver in conjunction with an eclipse is the time constraints. This suggests that the ideal platform to use MACS be in tandem with a coronagraph.

3. The instrumental stray light could be reduced to a great extent only through superior optics. A fair estimate of the distribution of the instrumental stray light could also be estimated by placing many more fibers in the shadow of the moon and outside the field of view in the focal plane of the telescope as depicted in figure (6.7).

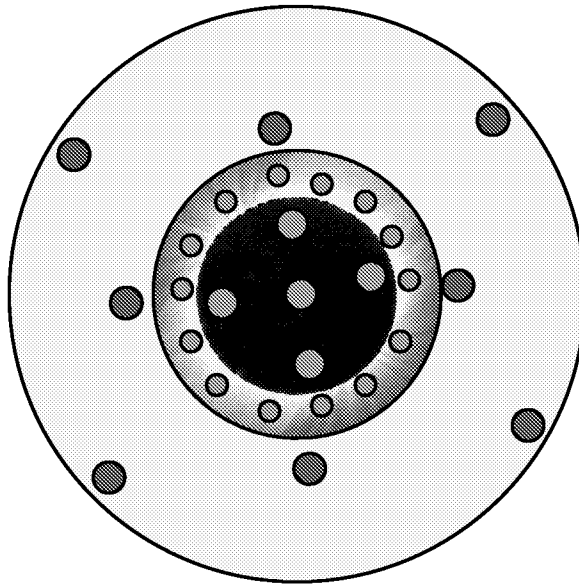


Figure (6.7). The extra fibers placed in the shadow of the moon and outside the field of view in order to record the instrumental stray light distribution.

4. Another important deficiency in MACS in its present state is in its inability to simultaneously visually image the focal plane during the observations. This prevented us from knowing whether the fibers stayed in focus at their intended locations. Deviations from the intended positions can arise from slight movements of the telescope due to wind, and also due to deficiencies in the tracking mechanism. This understanding could be easily satisfied by attaching a CCD-based video camera to the viewfinder of the telescope that in turn is co-aligned with the telescope. The live

video image of the sun through a sun filter projected on a TV screen, at least from one hour prior to the first contact, can be placed on a suitable 2_D grid and its course followed for tracking purposes. The bright pixels prior to the first contact should appear as dark between the second and the third contacts with the sun filter removed. In order to achieve this goal, the viewfinder and the telescope should be perfectly aligned. Although this enables us to monitor the tracking efficiency it does not prove the centering of the sun on the image plane of the telescope. To accomplish this the following maneuver could be followed.

- (a).** First center the sun's image through the sun filter on a reticle eyepiece. The reticle pattern in the Meade brand is a double cross line with two concentric circles. At this stage if the viewfinder is perfectly aligned with the telescope then the sun's image seen through a video recorder attached to the viewfinder should display the sun's image at the center of the detector. Centering on the reticle eyepiece and making adjustments to the telescope's orientations can be carried out alternatively until the image remains centered on the viewfinder and should satisfy the tracking efficiency.
- (b).** Then attach a camera with the lenses demounted for prime focus photography of the sun through a sun filter at the focal plane of the telescope. For the Meade brand of 12-inch Schmidt_Cassegrain telescopes one end of the #62-T adapter connects to the F/6.3 focal reducer and the other end threads into a universal T-adapter with bayonet-mount unique to the brand of 35mm camera and focus the image. This should facilitate the focusing for the experiment since the fiber optic plate too will be located

at the prime focus of the telescope during observations. If step (a) was successfully performed then the image should be centered too.

However the above features do not yet allow for the simultaneous imaging of the coronal image formed on the front surface of the fiber optic plate. The following optical feature as shown in figure (6.8) may be contemplated for MACS in order to obtain simultaneous imaging of the image formed on the focal plane. In figure (6.8) the fibers are embedded on an optical flat (well polished reflecting surface facing the telescope) along with a very thin high transmission glass surface (AB) inclined at 45° to the optical axis and with a semi-reflecting coating on the side facing the fiber optic plate. The reflected image from (AB) is a copy of the image formed on the fiber optic plate with dark dots marking the light transmitted through the fibers. Such an image will identify the actual location observed by each of the individual fibers on the corona. This is ideal to be used in attachment to a coronagraph. This is because any additional photons lost in the transmission through the additional optical component could be compensated by a longer integration time.

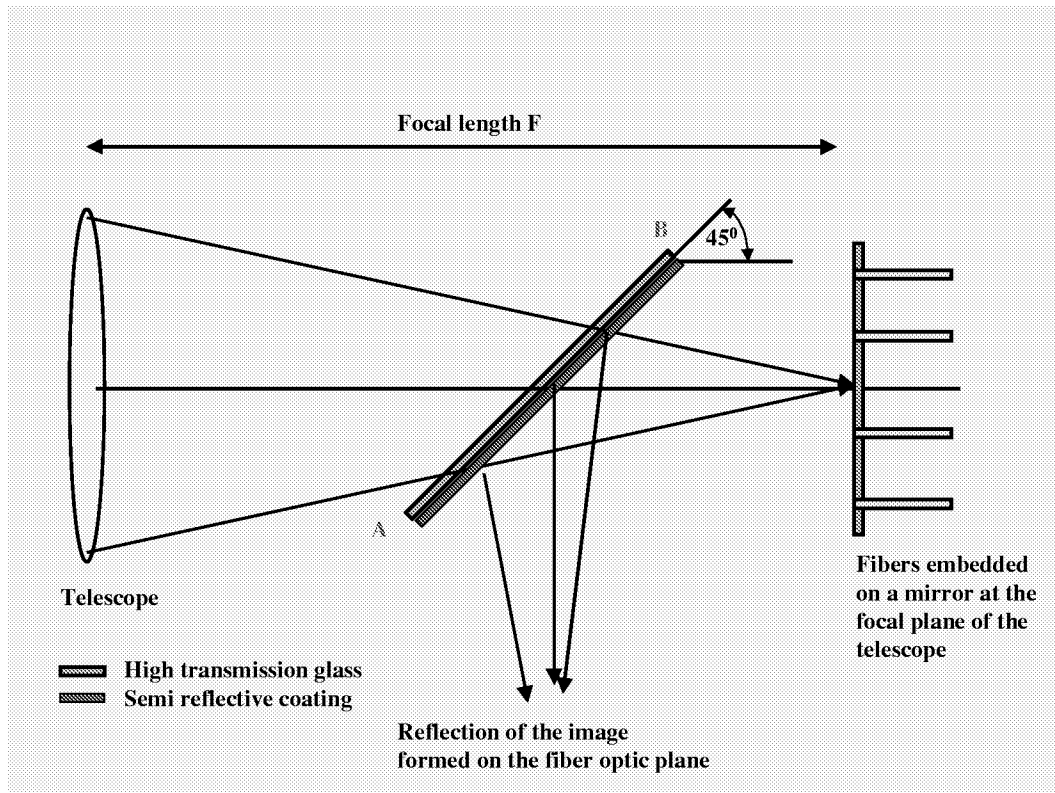


Figure (6.8). A schematic diagram showing the introduction of a very thin high transmission glass surface (AB) inclined at 45° to the optical axis with a semi-reflecting coating on the side facing the fiber optic plate along with the fibers embedded on an optical flat. This alteration will enable the simultaneous imaging of the image formed on the fiber optic plate.

The proposal (NRA:99-OSS-01) to build a coronagraph to accommodate MACS at a cost of ~\$ 500,000.0 has been approved by the NASA's Office of Space Science. NASA's Goddard Space Flight Center and The Catholic University of America will jointly build this instrument over the next three years. Possibilities for observing sites include Sacramento Peak, Hawaii and the Canaries.

Chapter 7

CONCLUSION

7.1 Summary of this thesis

The methodology presented in this thesis is unique in its character: it allows for the simultaneous and global measurement of the temperature and the solar wind velocity in the solar corona. This line of thinking originated from Cram's (1976) theoretical formulation for the formation of the K-corona and its properties. The physical properties that were taken into consideration in the formulation of the theory included the effects due to thermal Doppler broadening, limb darkening effects, angular dependence of the Thomson scattering and the cumulative contribution from different positions along the line of sight. The properties that were derived were the existence of temperature sensitive anti-nodes in the K-coronal spectrum and the remarkable independence of the temperature insensitive nodes with height above the solar limb. It was suggested that these properties could be exploited to measure the coronal temperature from the K-coronal intensity profile. Ichimoto et al. (1996) demonstrated the feasibility of Cram's method by analyzing the K-coronal spectrum obtained using a slit spectrograph during the total solar eclipse of 3 November 1994 in Putre, Chile.

In this thesis Cram's theory was extended by including the effects of coronal expansion in the formation of the K-corona. While confirming the properties derived by Cram, an additional property was discovered with the introduction of the solar wind. This allows for the **simultaneous** determination of both the **temperature** and the **wind velocity** from the same K-coronal spectral measurement. An overview of the theory and of the method can be found in chapters-**1** and **2**. The dependence of the theoretical model on the selection of the electron number density model, different temperature and wind profiles and the numerical procedures are discussed in chapter-**5**.

In this thesis, instead of a slit spectrograph a fiber optic spectrograph was designed whose features allowed for **global** determination of the K-coronal spectra all around the solar limb and at different heights. The instrument is discussed in chapter-**3**. Combining the theoretical prediction on the feasibility to determine both the temperature and the wind velocity from a single K-coronal spectrum and the instruments ability to globally measure the K-coronal spectra, the instrument was named **MACS** for Multi Aperture Coronal Spectrometer. The very first effort of its kind was tested in conjunction with the total solar eclipse of 11 August 1999 in Elazig, Turkey. The observational results are discussed in chapter-**4**. We were successful in determining the electron temperature at various points in the inner corona.

However, an important (and unwelcome) aspect of our observations concerns the degradation of the data due to instrumental scattering. Because of unexpectadly high

levels of scattering, we were not successful in obtaining reliable estimates of wind velocity. Although remedial measures were taken in expectation of possible instrumental scattering, the actual magnitude of the scattered light was not realized. Our efforts to reduce scattering were compounded by the inability to replicate the observing conditions in a laboratory and the lack of funds to obtain high quality optical components. One of the vital ingredient required to minimize instrumental scattering is careful selection of high quality optical components. Another important feature for the success of MACS would be to perform an absolute wavelength calibration in the laboratory. The extent of the instrumental scattering and some of the remedial measures are discussed in chapter-6.

Despite the lack of success in determining the wind velocity, our success in determining the coronal temperature using MACS has already been recognized as a successful proof-of-concept by a funding agency. A proposal to mate MACS concept with a coronagraph was submitted to NASA and it received favourable review. As a result, funds have been awarded for an upgraded version of our experiment in which the scattered light problem should be much reduced. It is hoped that the upgraded version of MACS will be ready for the solar eclipse of 21 June 2001 in Africa. At this eclipse MACS is to be complimented with a filter based system, where filters would be centered at the temperature and wind sensitive wavelength positions. The concept of MACS has also been recommended as an instrument in the proposal for the instrumental package that would fly aboard the Solar Probe. A brief review of the Solar Probe is given in section (7.2).

7.2 Using a spacecraft platform

A space platform envisaged for implementing the theoretical concept of MACS is the unmanned Solar Probe Spacecraft that will approach the sun at four solar radii at its perihelion. In this proposal a series of filters centered on the temperature and the wind sensitive wavelength positions is proposed. This would allow for both temperature and wind velocity measurements. Figure (7.1) shows the parabolic path of Solar Probe.

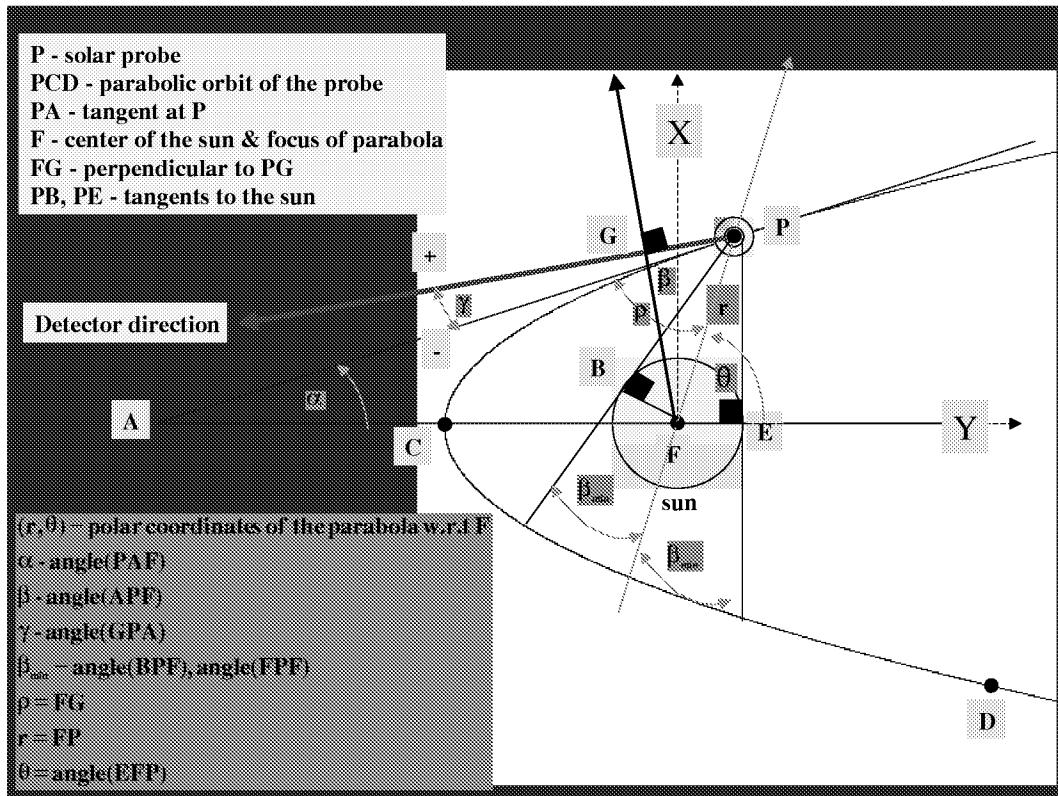


Figure (7.1). The path envisaged for the unmanned Solar Probe Spacecraft. At the perihelion (C) and the poles the spacecraft will be four and eight solar radii, respectively, from the center of the sun. The position of the spacecraft (P) is given by (r, θ) with respect to the center of the sun. In this picture the parabolic path, the detector plane and the center of the sun are in the same plane.

The equation of the parabolic orbit of the Solar Probe as depicted in figure (7.1) in polar coordinates is given by equation (7.1).

$$\begin{aligned}
 r(\theta) &= \frac{2.0 \times FC}{1 - \cos(\theta)} \\
 &= \frac{8.0R}{1 - \cos(\theta)}
 \end{aligned}
 \tag{7.1}$$

where **R** is the solar radius & **FC = 4R**

The angle α made by the tangent at P with the x-axis is given by equation (7.2).

$$\alpha = \tan^{-1} \left(\frac{1 - \cos(\theta)}{\sin(\theta)} \right)
 \tag{7.2}$$

The derivation of equation (7.2) is as follows.

$$y = r \sin(\theta) \rightarrow dy = r \cos(\theta)d\theta + \sin(\theta)dr$$

$$x = r \cos(\theta) \rightarrow dx = -r \sin(\theta)d\theta + \cos(\theta)dr$$

$$\frac{dy}{dx} = \frac{r \cos(\theta)d\theta + \sin(\theta)dr}{-r \sin(\theta)d\theta + \cos(\theta)dr} = \frac{r \cos(\theta) + \sin(\theta)(dr/d\theta)}{-r \sin(\theta) + \cos(\theta)(dr/d\theta)}$$

$$\text{from equation (1)} \frac{dr}{d\theta} = \frac{-2 \times FC \times \sin(\theta)}{(1 - \cos(\theta))^2} \text{ \& using } r = \frac{2 \times FC}{1 - \cos(\theta)}$$

$$\tan(\alpha) = \frac{dy}{dx} = \frac{1 - \cos(\theta)}{\sin(\theta)}$$

From the triangle APE the relationship between α , β and θ is given by equation (7.3).

$$\theta = \alpha + \beta \rightarrow \beta = \theta - \alpha
 \tag{7.3}$$

Supposing the detector direction is γ degrees from the tangent to the orbit at position (**P**) then the perpendicular distance ρ from the center of the sun to the line of sight of the detector is given by equation (7.4).

$$\rho = r \sin(\beta + \gamma) \quad (7.4)$$

At this instance the distance between the spacecraft and the intersection between the line of sight and the normal from the center of the sun is given by equation (7.5).

$$PG = r \cos(\beta + \gamma) \quad (7.5)$$

In order to prevent the detector being pointed directly at the sun the angle γ will have to satisfy the following condition given by equation (7.6).

$\gamma_- > -(\beta - \beta_{\min})$ measured in the (-) direction $\gamma_+ < 2\pi - (\beta + \beta_{\min})$ measured in the (+) direction where $\beta_{\min} = \sin^{-1}\left(\frac{R}{r}\right)$	(7.6)
-------------------------------------------------------------------------------------------------------------------------------------------------------------------------------------------------------------------	-------

In determining the theoretical K-coronal spectrum observed by the Solar Probe the only change occurs in the x-integration (along the line of sight) as shown in equation (7.7).

$$\int_{-\infty}^{+\infty} dx \rightarrow \int_{-PG}^{+\infty} dx \quad (7.7)$$

The above integration may be performed the following way as shown in equation (7.8). The first and the second integrations are performed using trapezoidal composite rule and Laguerre integration, respectively.

$$\begin{aligned}
 \int_{-PG}^{+\infty} f(x) dx &= \int_{-PG}^0 f(x) dx + \int_0^{+\infty} f(x) dx \\
 &= \int_{-PG}^0 f(x) dx + \int_0^{+\infty} e^{-x} (f(x)e^{+x}) dx \\
 &= \frac{h}{2} \left(2 \times \sum_{i=0}^{20} f(z_i) - f(z_0) - f(z_{20}) \right) + \sum_{i=0}^{20} w_i e^{+x_i} f(x_i)
 \end{aligned} \tag{7.8}$$

where $h = \frac{0 - (-PG)}{20}$ & $z_i = -PG + i \times h$

Figure (7.2) and figure (7.3) show for solar wind velocities 0.0 and 400.0 km/sec, respectively, the theoretical K-coronal intensity variation for various detector elevations with respect to the tangent when the spacecraft is positioned at the pole (P). Figure (7.4) shows the variation of the wind-sensitive intensity ratio against the detector tilt γ for various wind velocities at a constant temperature of 1.0 MK and the spacecraft positioned at the pole. Figure (7.5) shows the variation of the temperature-sensitive intensity ratio against the detector tilt γ for various temperatures at a constant wind velocity of 400.0 km/sec and the spacecraft positioned at the pole. Figures (7.6) and (7.7) show the variation of the temperature-sensitive intensity ratio against temperature for various wind velocities and the variation of the wind-sensitive intensity ratio against wind velocity for various temperatures, respectively, for a given detector tilt angle γ and the spacecraft positioned at the pole.

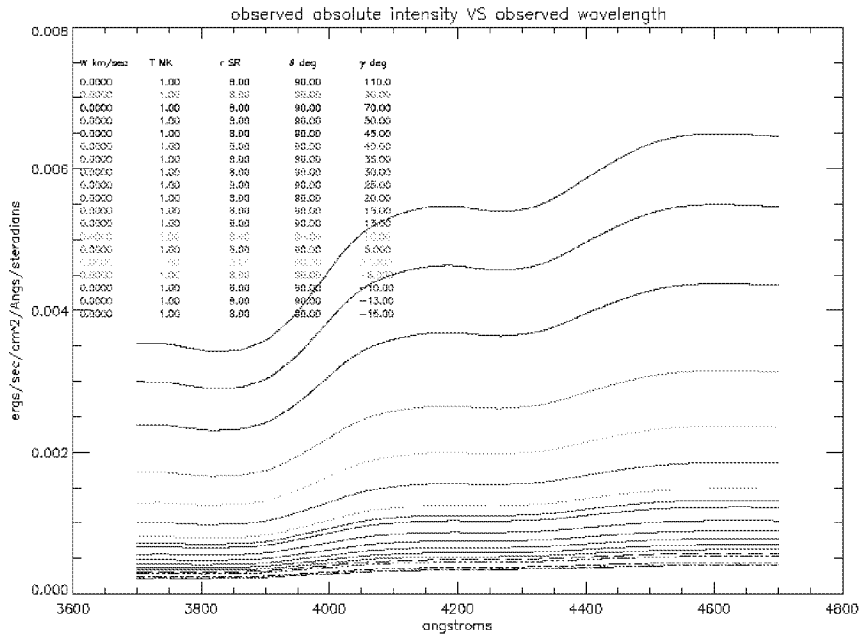


Figure (7.2) The theoretical K-coronal intensity variation for various detector elevations for 0.0 km/sec wind velocity and the spacecraft positioned at the pole (P).

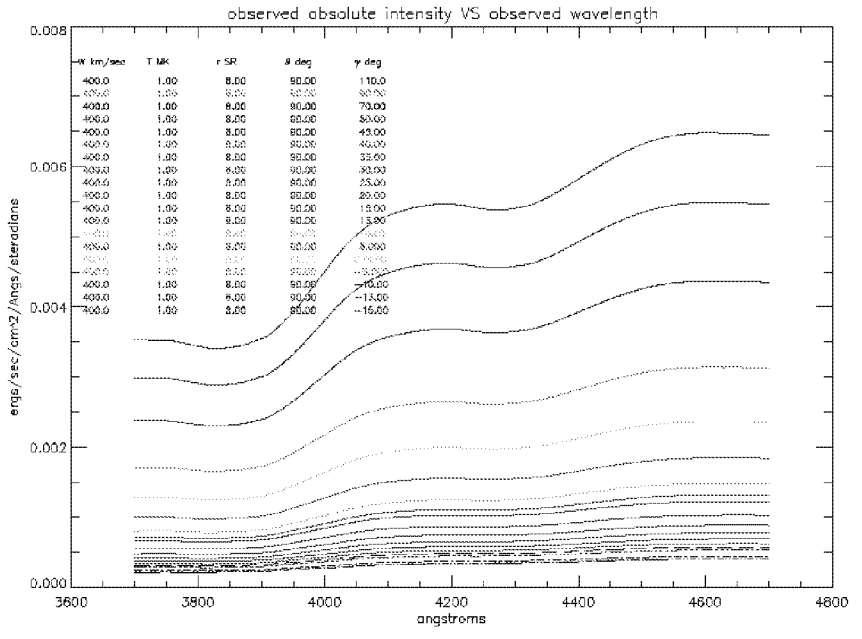


Figure (7.3). The theoretical K-coronal intensity variation for various detector elevations for 400.0 km/sec wind velocity and the spacecraft positioned at the pole (P).

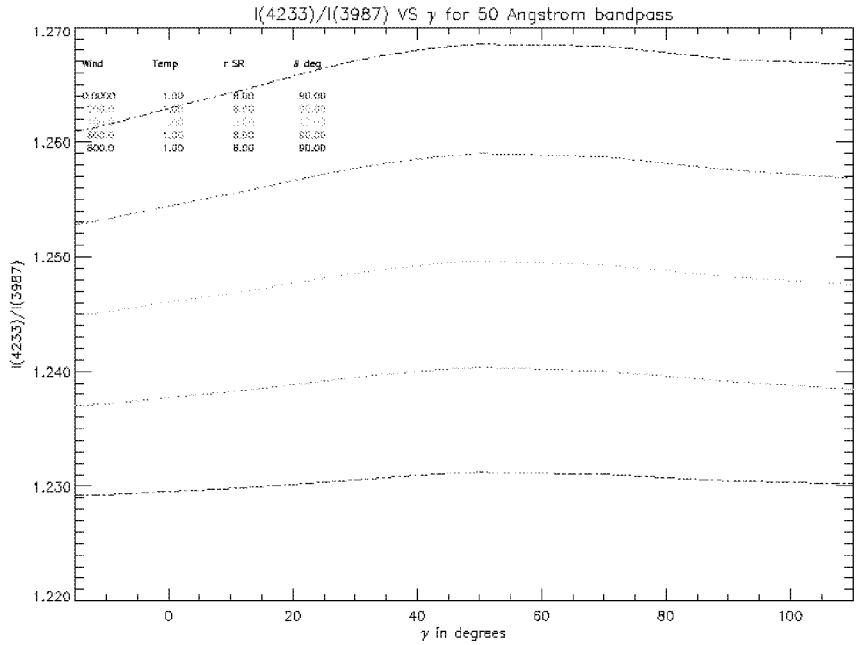


Figure (7.4). The variation of the wind-sensitive intensity ratio against γ for various wind velocities at $T=1.0$ MK and the spacecraft positioned at the pole.

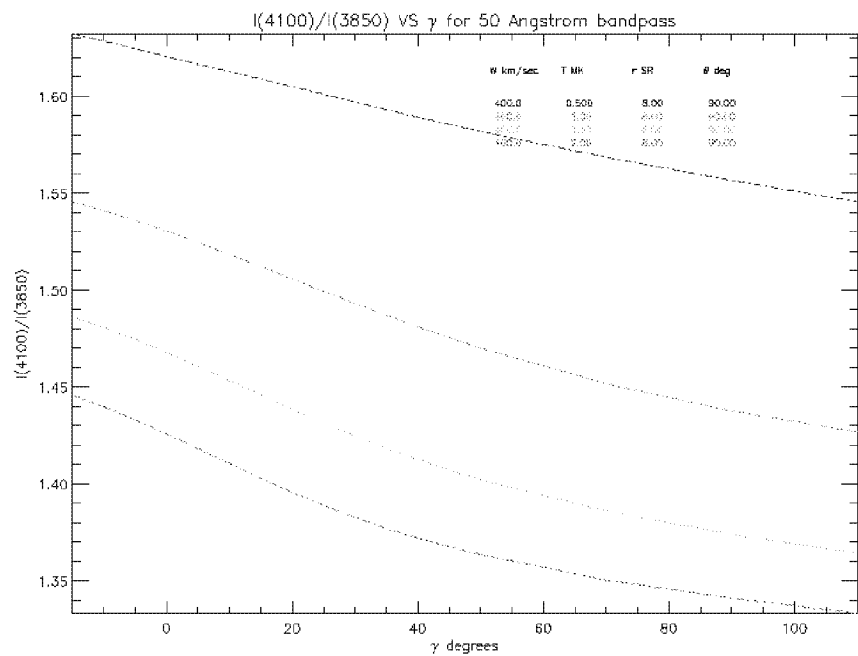


Figure (7.5). The variation of the temperature-sensitive intensity ratio against γ for various temperatures at $W=400.0$ km/sec and the spacecraft positioned at the pole.

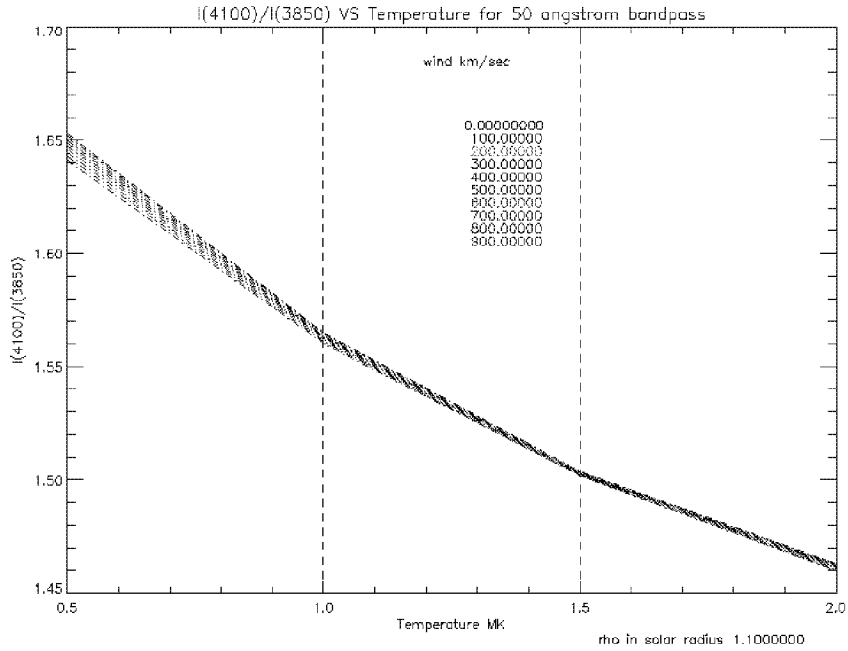


Figure (7.6). Temperature-sensitive intensity ratio VS Temperature for various wind velocities at $\gamma = 0.0$ degrees and the spacecraft positioned at the pole.

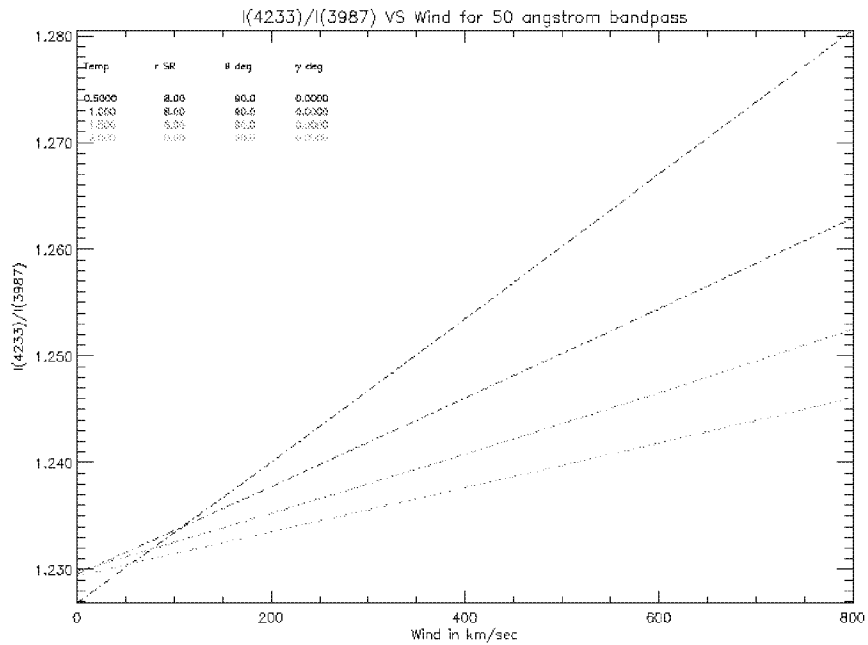


Figure (7.7). Wind-sensitive intensity ratio VS Wind velocity for various temperatures at $\gamma = 0.0$ degrees and the spacecraft positioned at the pole.

These plots show the promise behind the theoretical concept of MACS being employed from a space platform deep inside the solar corona for the measurement of the coronal temperature and the solar wind velocity thus avoiding the F-corona and the use of a coronagraph. Even the spectrograph could be avoided with the use of optical filters centered at the temperature and wind sensitive wavelengths. The temperature and wind sensitive intensity ratios remain almost the same even at fifty angstrom bandpass. Figures (7.8) and (7.9) show the temperature and wind sensitive intensity ratios, respectively, for the use of filters centered at those wavelengths with a fifty angstrom bandpass for line of sight integration from $\pm \infty$ at 1.1 solar radii. This could be verified by the comparison of figures (7.8) and (7.9) with figures (2.3) and (2.20), respectively.

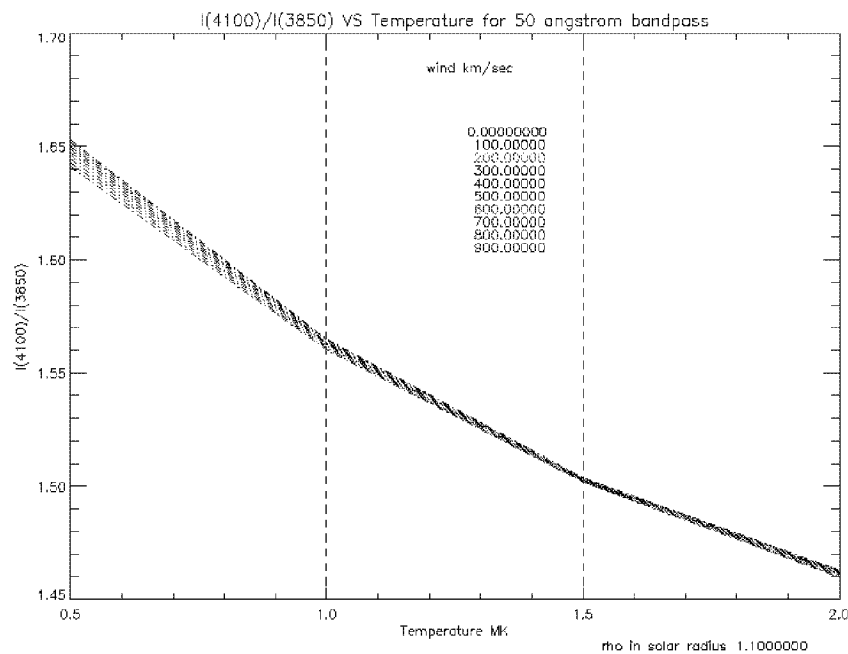


Figure (7.8). Temperature-sensitive intensity ratio VS Temperature for various wind velocities with intensities measured through filters of fifty angstrom bandpass centered at those wavelengths for line of sight at 1.1 solar radii.

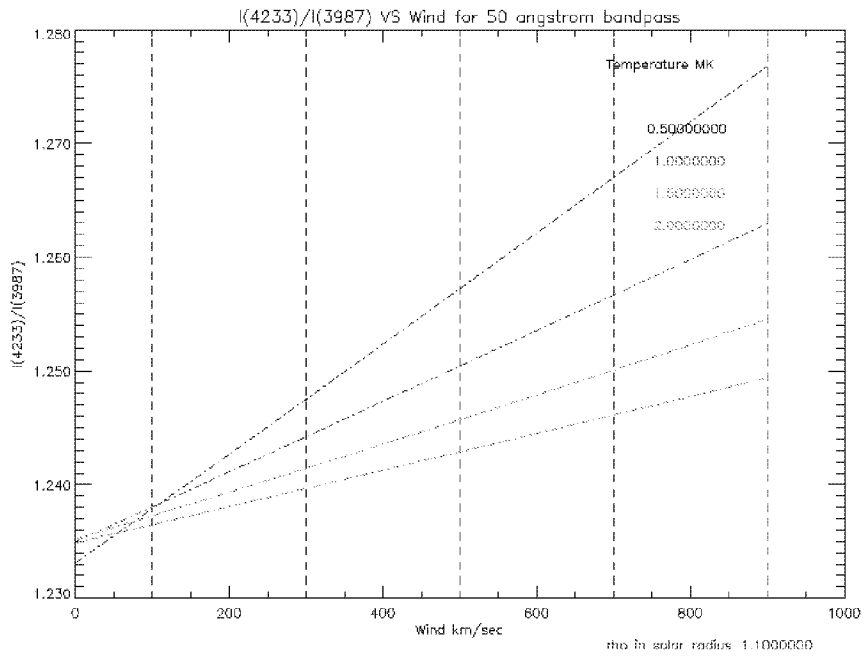


Figure (7.9). Wind-sensitive intensity ratio VS Wind velocities for various temperatures with intensities measured through filters of fifty angstrom bandpass centered at those wavelengths for line of sight at 1.1 solar radii.

In conclusion, with the approval of funding for a coronagraph for MACS the future is very optimistic as a tool for simultaneous and global coronal temperature and wind measurements. There is also good reason to hope that the concept can be applied as an instrument on a space-based platform.

Appendix A

THE THEORY OF FORMATION OF THE K-CORONA

A.1 The general theory on scattering of radiation by free electrons

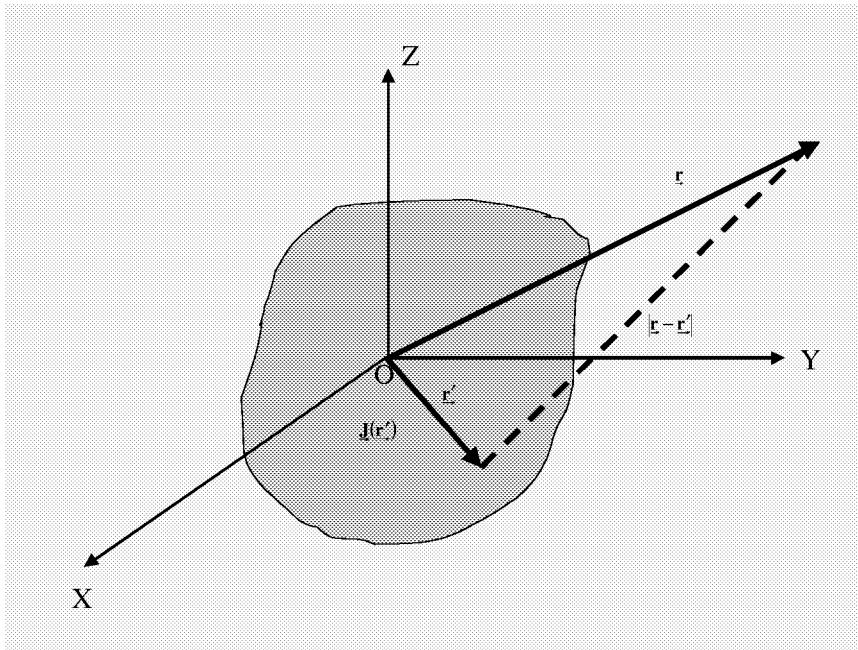


Figure (A.1). The general coordinates where \underline{r} is a field point and \underline{r}' is a source point.

Consider a system whose charges and currents are varying in time. There is no loss in generality by restricting our considerations to potentials, field and radiation from localized systems that vary sinusoidally in time.

The time dependent charge and current densities could be written, respectively, as given by equation (A.1) and equation (A.2), based on coordinates shown in figure (A.1).

$$\rho(\underline{\mathbf{r}}', t) = \rho(\underline{\mathbf{r}}) e^{-i\omega t} \quad (\text{A.1})$$

$$\underline{\mathbf{J}}(\underline{\mathbf{r}}', t) = \underline{\mathbf{J}}(\underline{\mathbf{r}}) e^{-i\omega t} \quad (\text{A.2})$$

And the continuity equation is given by equation (A.3).

$$\nabla \cdot \underline{\mathbf{J}} + \frac{\partial \rho}{\partial t} = \nabla \cdot \underline{\mathbf{J}} + (-i\omega \rho) = 0 \quad (\text{A.3})$$

The scalar and vector potentials for the charge distributions are given, respectively, by equation (A.4) and equation (A.5).

$$\underline{\mathbf{V}}(\underline{\mathbf{r}}) = \frac{1}{4\pi\epsilon_0} \int \frac{\rho(\underline{\mathbf{r}}') e^{i\mathbf{k} \cdot |\underline{\mathbf{r}} - \underline{\mathbf{r}}'|}}{|\underline{\mathbf{r}} - \underline{\mathbf{r}}'|} d^3 \underline{\mathbf{r}}' \quad (\text{A.4})$$

$$\underline{\mathbf{A}}(\underline{\mathbf{r}}) = \frac{\mu_0}{4\pi} \int \frac{\underline{\mathbf{J}}(\underline{\mathbf{r}}') e^{i\mathbf{k} \cdot |\underline{\mathbf{r}} - \underline{\mathbf{r}}'|}}{|\underline{\mathbf{r}} - \underline{\mathbf{r}}'|} d^3 \underline{\mathbf{r}}' \quad (\text{A.5})$$

In the far radiation zone, where $r \gg \lambda$ and $r \gg r'$, the denominator $|\underline{r} - \underline{r}'|$ can be considered to be independent of \underline{r}' although the argument of the complex exponential is not. Thus, equation (A.5) could be written as equation (A.6).

$$\underline{A}(\underline{r}) = \frac{\mu_0}{4\pi r} e^{i\mathbf{k}\cdot\underline{r}} \int \underline{J}(\underline{r}') e^{-i\mathbf{k}\cdot(\underline{r}-\underline{r}')/r} d^3\underline{r}' \quad (\text{A.6})$$

Also if the source dimension r' is small compared to the wavelength, then $kr' \ll 1$ which justifies writing equation (A.6) as equation (A.7).

$$\underline{A}(\underline{r}) = \frac{\mu_0}{4\pi r} e^{i\mathbf{k}\cdot\underline{r}} \sum_l \frac{(-i\mathbf{k})^l}{l!} \int \underline{J}(\underline{r}') \left(\frac{\underline{r}\cdot\underline{r}'}{r} \right)^l d^3\underline{r}' \quad (\text{A.7})$$

The above is true since the electron diameter of 5×10^{-15} m is very small compared to the wavelength of visible light of 5×10^{-7} m. Therefore the expansion of the exponential term in the integrand of equation (A.6) is justified by the summation given equation (A.8).

$$e^{-i\mathbf{k}\cdot(\underline{r}-\underline{r}')/r} = \sum_l \frac{(-i\mathbf{k})^l}{l!} (\underline{r}\cdot\underline{r}')^l \quad (\text{A.8})$$

The scattering of electromagnetic radiation by systems whose physical dimensions are small compared with the wavelength of the wave being scattered, it is reasonable to assume that the incident radiation is inducing electric and magnetic multipoles and these to oscillate in definite phase relationship with the incident wave and

also radiate energy in directions different from the direction of the incident wave. For the case where the wavelength of the incident radiation is very long compared to the size of the scatterer, only the lowest multipoles, usually the electric and magnetic dipoles ($l=0$) are important. Therefore for electric dipole radiation ($l=0$) equation (A.7) reduces to equation (A.9).

$$\underline{A}(\underline{r}) = \frac{\mu_0 e^{i\mathbf{k}\cdot\mathbf{r}}}{4\pi r} \int \underline{J}(\underline{r}') d^3 \underline{r}' \quad (\text{A.9})$$

Consider the following mathematical operation

$$\begin{aligned} \nabla' \cdot (\underline{x}' \underline{J}) &= (\nabla' \cdot \underline{x}') \underline{J} + \underline{x}' \cdot (\nabla' \underline{J}) \\ &= \underline{J} \cdot \underline{x}' + \underline{x}' \cdot (\nabla' \underline{J}) \\ \therefore \underline{J} \cdot \underline{x}' &= \nabla' \cdot (\underline{x}' \underline{J}) - \underline{x}' \cdot (\nabla' \underline{J}) \\ \int \underline{J} \cdot \underline{x}' d^3 \underline{r}' &= \int \nabla' \cdot (\underline{x}' \underline{J}) d^3 \underline{r}' - \int \underline{x}' \cdot (\nabla' \underline{J}) d^3 \underline{r}' \\ &= \oint \underline{x}' \underline{J} \cdot d\underline{s} - \int \underline{x}' \cdot (\nabla' \underline{J}) d^3 \underline{r}' \end{aligned}$$

Using equation(1.3)

$$= \oint \underline{x}' \underline{J} \cdot d\underline{s} + \int \underline{x}' \cdot \frac{\partial \underline{J}}{\partial t} d^3 \underline{r}'$$

Using equation(1.1) and integrating over a large enough volume

$$\cong -i\omega \int \underline{x}' \rho d^3 \underline{r}'$$

and for all components of \underline{J}

$$\int \underline{J}(\underline{r}') d^3 \underline{r}' = -i\omega \int \underline{r}' \rho(\underline{r}') d^3 \underline{r}' = -i\omega \underline{p}$$

where dipole moment $\underline{p} = \int \underline{r}' \rho(\underline{r}') d^3 \underline{r}'$

(A.10)

Equation (A.11) can be written from equation (A.9) and equation (A.10).

$$\underline{\mathbf{A}}(\underline{\mathbf{r}}) = \frac{-i\omega\mu_0 \mathbf{e}^{i\mathbf{k}\mathbf{r}}}{4\pi r} \underline{\mathbf{p}} \quad (\text{A.11})$$

Then, using equation (A.11) the magnetic field is given by equation (A.12).

$$\underline{\mathbf{B}} = \nabla \times \underline{\mathbf{A}}(\underline{\mathbf{r}}) = -\frac{i\omega\mu_0}{4\pi} \nabla \left(\frac{\mathbf{e}^{i\mathbf{k}\mathbf{r}}}{r} \times \underline{\mathbf{p}} \right)$$

and using polar coordinates

$$\nabla(\mathbf{r}, \theta, \phi) = \hat{\mathbf{r}} \frac{\partial}{\partial r} + \frac{\hat{\theta}}{r} \frac{\partial}{\partial \theta} + \frac{\hat{\phi}}{r \sin(\theta)} \frac{\partial}{\partial \phi}$$

$$\underline{\mathbf{B}} = \frac{\omega\mathbf{k}\mu_0}{4\pi} \left(1 - \frac{1}{i\mathbf{k}\mathbf{r}} \right) \frac{\mathbf{e}^{i\mathbf{k}\mathbf{r}}}{r} \hat{\mathbf{r}} \times \underline{\mathbf{p}} \quad (\text{A.12})$$

From Maxwell's equations for outside the source ($\underline{\mathbf{J}}=0$) the magnetic and the electric fields are related by equation (A.13).

$$\nabla \times \underline{\mathbf{B}} = \mu_0 \epsilon_0 \frac{\partial \underline{\mathbf{E}}}{\partial t} + \mu_0 \underline{\mathbf{J}} = -\frac{i\omega}{c^2} \underline{\mathbf{E}}$$

where $c^2 = \frac{1}{\mu_0 \epsilon_0}$ and $\mathbf{k} = \frac{\omega}{c}$

$$\quad (\text{A.13})$$

From equation (A.13) the electric field is given by equation (A.14).

$$\underline{\mathbf{E}}(\underline{\mathbf{r}}) = \frac{ic^2}{\omega} \nabla \times \underline{\mathbf{B}}(\underline{\mathbf{r}}) \quad (\text{A.14})$$

And using the following vector identities

$$\underline{\mathbf{A}} \times (\underline{\mathbf{B}} \times \underline{\mathbf{C}}) = (\underline{\mathbf{A}} \cdot \underline{\mathbf{C}})\underline{\mathbf{B}} - (\underline{\mathbf{A}} \cdot \underline{\mathbf{B}})\underline{\mathbf{C}}$$

$$\nabla \times (\underline{\mathbf{A}} \times \underline{\mathbf{B}}) = \underline{\mathbf{A}}(\nabla \cdot \underline{\mathbf{B}}) - \underline{\mathbf{B}}(\nabla \cdot \underline{\mathbf{A}}) + (\underline{\mathbf{B}} \cdot \nabla)\underline{\mathbf{A}} - (\underline{\mathbf{A}} \cdot \nabla)\underline{\mathbf{B}}$$

and the relations

$$\nabla \cdot \hat{\underline{\mathbf{r}}} = \frac{2}{r}, \quad \nabla \cdot \underline{\mathbf{r}} = 3 \text{ and } \underline{\mathbf{p}} \neq \underline{\mathbf{p}}(\underline{\mathbf{r}})$$

on equation (A.14) the expression for the electric field is given by equation (A.15).

$$\underline{\mathbf{E}}(\underline{\mathbf{r}}) = \frac{ck\omega\mu_0}{4\pi} \frac{e^{ikr}}{r} \hat{\underline{\mathbf{r}}} \times (\underline{\mathbf{p}} \times \hat{\underline{\mathbf{r}}}) + \frac{1}{4\pi\epsilon_0} \frac{(1-ikr)}{r^3} e^{ikr} (3(\hat{\underline{\mathbf{r}}}, \underline{\mathbf{p}}) - \underline{\mathbf{p}}) \quad (\text{A.15})$$

In the radiation zone $kr \gg 1$ where $\mathbf{k} = \omega/c$ the equations (A.15) and (A.12) reduce to equation (A.16).

$$\underline{\mathbf{E}}(\underline{\mathbf{r}}) \cong \frac{ck\omega\mu_0}{4\pi} \frac{e^{ikr}}{r} \hat{\underline{\mathbf{r}}} \times (\underline{\mathbf{p}} \times \hat{\underline{\mathbf{r}}})$$

$$\underline{\mathbf{B}}(\underline{\mathbf{r}}) \cong \frac{k\omega\mu_0}{4\pi} \frac{e^{ikr}}{r} \hat{\underline{\mathbf{r}}} \times \underline{\mathbf{p}}$$

$$\underline{\mathbf{E}}(\underline{\mathbf{r}}) = c\underline{\mathbf{B}}(\underline{\mathbf{r}}) \times \hat{\underline{\mathbf{r}}}$$

(A.16)

The Poynting vector (average power radiated per unit area) is given by equation (A.17).

$$\langle \underline{S} \rangle = \frac{\underline{E} \times \underline{B}^*}{2\mu_0} \text{ Watts/m}^2 \quad (\text{A.17})$$

Using equation (A.16) and the vector identity

$(\underline{A} \times \underline{B}) \times \underline{C} = (\underline{A} \cdot \underline{C})\underline{B} - (\underline{B} \cdot \underline{C})\underline{A}$ and $\underline{D} \cdot (\underline{D} \times \underline{E}) = 0$ and $\mathbf{k} = \omega/c$ the Poynting vector given by equation (A.17) reduces to equation (A.18).

$$\langle \underline{S} \rangle = \frac{\omega^4 \mu_0}{32\pi^2 r^2 c} (\hat{\underline{r}} \times \underline{p})^2 \hat{\underline{r}} \text{ Watts/m}^2 \quad (\text{A.18})$$

Then the total power radiated through an area $d\underline{a}$ is given by equation (A.19).

$$dL = \langle \underline{S} \rangle \cdot d\underline{a} = \langle \underline{S} \rangle \cdot \hat{\underline{r}} r^2 d\Omega \text{ Watts} \quad (\text{A.19})$$

Substituting equation (A.18) in (A.19) gives equation (A.20).

$$dL = \frac{\omega^4 \mu_0}{32\pi^2 r^2 c} (\hat{\underline{r}} \times \underline{p})^2 \hat{\underline{r}} \cdot \hat{\underline{r}} r^2 d\Omega = \frac{\omega^4 \mu_0}{32\pi^2 c} (\hat{\underline{r}} \times \underline{p})^2 d\Omega \text{ Watts} \quad (\text{A.20})$$

Now for an oscillating electric dipole the induced moment \underline{p} is given by equation (A.21).

$$\underline{p} = \underline{p}_0 e^{-i\omega t} \quad (\text{A.21})$$

Differentiating equation (A.21) twice with respect to time gives equation (A.22).

$$\ddot{\underline{\mathbf{p}}} = \omega^2 \underline{\mathbf{p}} \quad (\text{A.22})$$

Substituting equation (A.22) in (A.20) gives equation (A.23).

$$d\mathbf{L} = \frac{\mu_0}{32\pi^2 c} (\hat{\mathbf{r}} \times \ddot{\underline{\mathbf{p}}})^2 d\Omega \quad \text{Watts} \quad (\text{A.23})$$

For a single electron the induced moment $\underline{\mathbf{p}}$ is given by

$$\underline{\mathbf{p}}(t) = e \underline{\mathbf{r}}'(t) \quad (\text{A.24})$$

where $\underline{\mathbf{r}}'$ is a source point with respect to its origin.

From the equation of motion in the non-relativistic case

$$\mathbf{m} \underline{\mathbf{r}}' = e(\underline{\mathbf{E}} + \underline{\mathbf{v}} \times \underline{\mathbf{B}}) \cong e \underline{\mathbf{E}} \quad (\text{A.25})$$

where \mathbf{m} is the mass of the electron.

Substituting equation (A.25) in (A.24) gives equation (A.26).

$$\ddot{\underline{\mathbf{p}}} = \frac{e^2 \underline{\mathbf{E}}}{m} \quad (\text{A.26})$$

Again substituting equation (2.26) in (2.23) gives equation (A.27).

$$d\mathbf{L} = \left(\frac{e^2}{mc^2} \right)^2 \frac{\mu_0 c^3}{32\pi^2} (\hat{\mathbf{r}} \times \underline{\mathbf{E}})^2 d\Omega \quad (\text{A.27})$$

Diving and multiplying equation (A.27) by $6\pi\epsilon_0$ gives equation (A.28).

$$d\mathbf{L} = \frac{3}{16\pi} \sigma_{\text{T}} \epsilon_0 c (\hat{\mathbf{r}} \times \underline{\mathbf{E}})^2 d\Omega \quad (\text{A.28})$$

where σ_{T} is the Thomson scattering cross section given by equation (A.29).

$$\sigma_{\text{T}} = \frac{1}{6\pi\epsilon_0} \left(\frac{e^2}{mc^2} \right)^2 \quad (\text{A.29})$$

Therefore from equation (A.28) the power radiated per unit solid angle is given by equation (A.30).

$$\boxed{\frac{d\mathbf{L}}{d\Omega} = \frac{3}{16\pi} \sigma_{\text{T}} (\hat{\mathbf{r}} \times \underline{\mathbf{E}})^2 \text{ Watts/solid angle}} \quad (\text{A.30})$$

A.2 Total power radiated per solid angle for the cases where the electric vector is aligned parallel and perpendicular to the scattering plane

Consider the case where the electric vector is parallel to the scattering plane. In figure (A.2) $\underline{\hat{n}}_{in}$ and $\underline{\hat{n}}_{out}$ are unit vectors in the directions of the incident and the scattered radiation and they both lie on the scattering plane and Θ is the scattering angle. $\underline{\hat{E}}_{//}^{Sc}$ is the unit vector of the component of the electric vector parallel to the scattering plane and $\underline{\hat{E}}_{\perp}^{Sc}$ is the unit vector of the component of the electric vector perpendicular to the scattering plane.

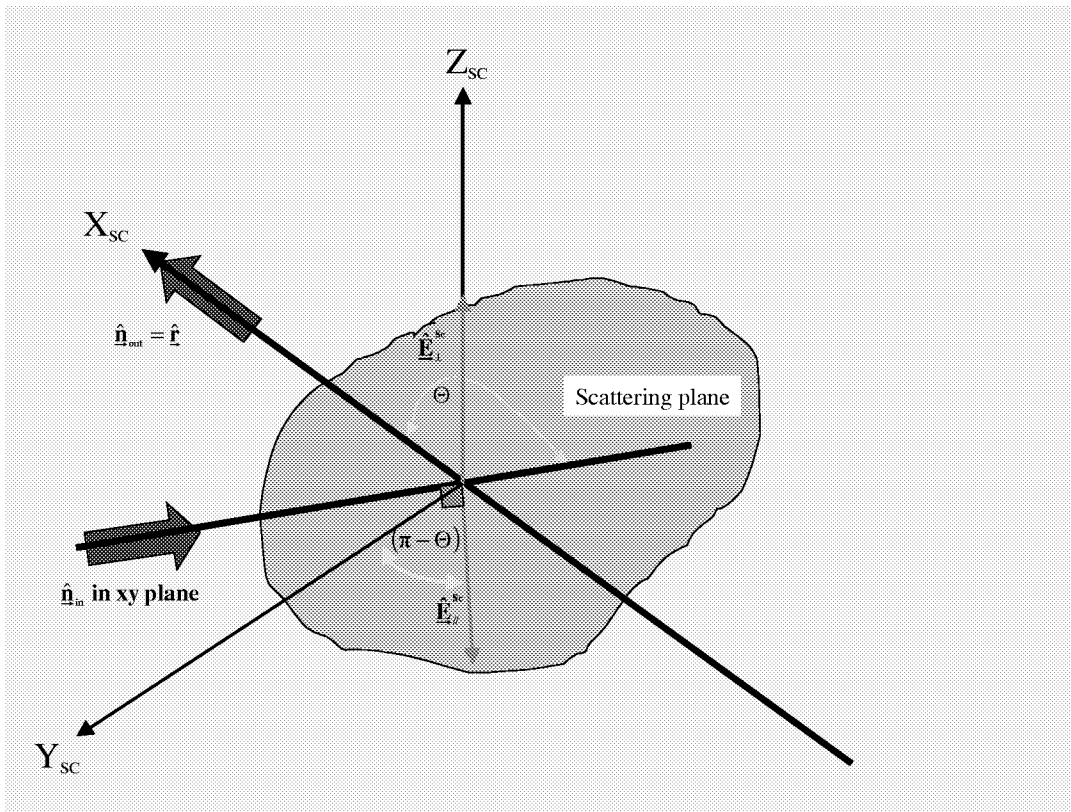


Figure (A.2). The general coordinates of the incident and scattered radiation and the orientations of the parallel and the perpendicular components of the electric vectors with respect to the scattering plane.

The direction cosines of $\hat{\mathbf{n}}_{\text{in}}$ and $\hat{\mathbf{n}}_{\text{out}}$ are given by equation (A.31) and equation (A.32), respectively.

$$\hat{\mathbf{n}}_{\text{in}} = \left(-\sin\left(\Theta - \frac{\pi}{2}\right), -\cos\left(\Theta - \frac{\pi}{2}\right), 0 \right) = (\cos \Theta, -\sin \Theta, 0) \quad (\text{A.31})$$

$$\hat{\mathbf{n}}_{\text{out}} = (1, 0, 0) \quad (\text{A.32})$$

From figure (A.2) the dot product of $\hat{\mathbf{n}}_{\text{in}}$ and $\hat{\mathbf{n}}_{\text{out}}$ gives equation (A.33)

$$\hat{\mathbf{n}}_{\text{in}} \cdot \hat{\mathbf{n}}_{\text{out}} = |\hat{\mathbf{n}}_{\text{in}}| |\hat{\mathbf{n}}_{\text{out}}| \cos(\Theta) \quad (\text{A.33})$$

and the square of its cross product gives equation (A.34).

$$(\hat{\mathbf{n}}_{\text{in}} \times \hat{\mathbf{n}}_{\text{out}})^2 = |\hat{\mathbf{n}}_{\text{in}}|^2 |\hat{\mathbf{n}}_{\text{out}}|^2 \sin^2(\Theta) \quad (\text{A.34})$$

The direction cosines for the electric vectors $\hat{\mathbf{E}}_{\parallel}^{\text{Sc}}$ and $\hat{\mathbf{E}}_{\perp}^{\text{Sc}}$ are, respectively, given by equation (A.35) and equation (A.36).

$$\hat{\mathbf{E}}_{\parallel}^{\text{Sc}} = (-\sin(\pi - \Theta), \cos(\pi - \Theta), 0) = (-\sin \Theta, -\cos \Theta, 0) \quad (\text{A.35})$$

$$\hat{\mathbf{E}}_{\perp}^{\text{Sc}} = (0, 0, 1) \quad (\text{A.36})$$

The sum of the cross products of equation (A.32) with (A.34) and (A.35) is gives equation (A.37).

$$\begin{aligned} \hat{\mathbf{n}}_{\text{out}} \times \hat{\mathbf{E}}_{//}^{\text{Sc}} + \hat{\mathbf{n}}_{\text{out}} \times \hat{\mathbf{E}}_{\perp}^{\text{Sc}} &= \begin{vmatrix} \hat{\mathbf{i}} & \hat{\mathbf{j}} & \hat{\mathbf{k}} \\ \mathbf{1} & \mathbf{0} & \mathbf{0} \\ -\sin \Theta & -\cos \Theta & \mathbf{0} \end{vmatrix} + \begin{vmatrix} \hat{\mathbf{i}} & \hat{\mathbf{j}} & \hat{\mathbf{k}} \\ \mathbf{1} & \mathbf{0} & \mathbf{0} \\ \mathbf{0} & \mathbf{0} & \mathbf{1} \end{vmatrix} \\ &= -\cos \Theta \hat{\mathbf{k}} + \hat{\mathbf{j}} \end{aligned} \quad (\text{A.37})$$

From figure (A.2) using the relation $\hat{\mathbf{r}} = \hat{\mathbf{n}}_{\text{out}}$ and equation (A.37) the following relations are obtained as given by equation (A.38) and equation (A.39).

$$\left(\hat{\mathbf{r}} \times \hat{\mathbf{E}}_{//}^{\text{Sc}} \mathbf{E}_{//}^{\text{Sc}} \right)^2 = (\mathbf{E}_{//}^{\text{Sc}})^2 \sin^2(90 - \Theta) = (\mathbf{E}_{//}^{\text{Sc}})^2 \cos^2 \Theta \quad (\text{A.38})$$

$$\left(\hat{\mathbf{r}} \times \hat{\mathbf{E}}_{\perp}^{\text{Sc}} \mathbf{E}_{\perp}^{\text{Sc}} \right)^2 = (\mathbf{E}_{\perp}^{\text{Sc}})^2 \quad (\text{A.39})$$

Now substituting the equation (A.38) and equation (A.39) in equation (A.30) give equation (A.40) and equation (A.41), respectively.

$$\left(\frac{d\mathbf{L}}{d\Omega} \right)_{//}^{\text{Sc}} = \frac{3}{16\pi} \sigma_{\text{T}} (\epsilon_0 \mathbf{c} (\mathbf{E}_{//}^{\text{Sc}})^2) \cos^2 \Theta \quad (\text{A.40})$$

$$\left(\frac{d\mathbf{L}}{d\Omega} \right)_{\perp}^{\text{Sc}} = \frac{3}{16\pi} \sigma_{\text{T}} (\epsilon_0 \mathbf{c} (\mathbf{E}_{\perp}^{\text{Sc}})^2) \quad (\text{A.41})$$

But for isotropic radiation equation (A.42) is true.

$$\left| \vec{E}_{//}^{\text{Sc}} \right| = \left| \vec{E}_{\perp}^{\text{Sc}} \right| = \frac{1}{2} |\vec{E}| \quad (\text{A.42})$$

Substituting equation (A.42) in (A.40) and (A.41) give equation (A.43) and (A.44), respectively.

$$\left(\frac{dL}{d\Omega} \right)_{//}^{\text{Sc}} = \frac{3}{16\pi} \sigma_{\text{T}} \left(\frac{1}{2} c \epsilon_0 \mathbf{E}^2 \right) \cos^2 \Theta \quad (\text{A.43})$$

$$\left(\frac{dL}{d\Omega} \right)_{\perp}^{\text{Sc}} = \frac{3}{16\pi} \sigma_{\text{T}} \left(\frac{1}{2} c \epsilon_0 \mathbf{E}^2 \right) \quad (\text{A.44})$$

Consider a plane monochromatic wave as shown in figure (A.3).

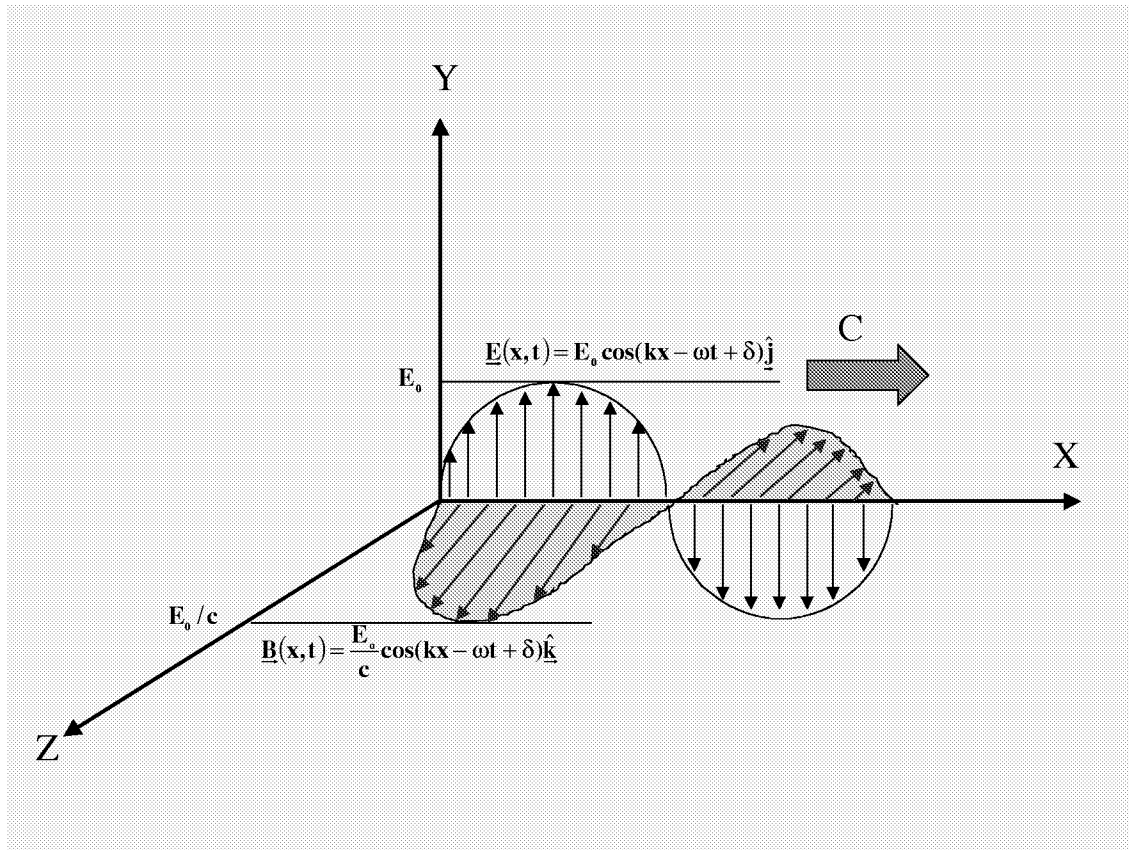


Figure (A.3). Propagation of a monochromatic plane EM waves.

Using the Poynting vector $\underline{S} = \frac{1}{\mu_0} \underline{E} \times \underline{B}$ the energy flux density transported by the plane monochromatic electromagnetic wave depicted in figure (A.3) is given by equation (A.45).

$$\underline{S} = c\epsilon_0 E_0^2 \cos^2(kx - \omega t + \delta) \hat{i} \quad (\text{A.45})$$

and averaging equation (A.45) over a cycle gives equation (A.46).

$$\begin{aligned}
 \langle \underline{S} \rangle &= c\epsilon_0 E_0^2 \left\langle \cos^2 \left(\mathbf{kx} - \frac{2\pi}{T} t + \delta \right) \right\rangle \hat{\mathbf{i}} \\
 &= c\epsilon_0 E_0^2 \frac{1}{T} \int_0^T \cos^2 \left(\mathbf{kx} - \frac{2\pi}{T} t + \delta \right) dt \hat{\mathbf{i}} \\
 &= \frac{1}{2} c\epsilon_0 E_0^2 \hat{\mathbf{i}}
 \end{aligned} \tag{A.46}$$

From equation (A.46) the average power per unit area transported by an electromagnetic wave is called the intensity and is given by equation (A.47).

$$\mathbf{I}_o = \langle \underline{S} \rangle = \frac{1}{2} c\epsilon_0 E_0^2 \tag{A.47}$$

Substituting equation (A.47) in equation (A.43) and equation (A.44) give equation (A.48) and equation (A.49), respectively.

$$\mathbf{I}_{//}^{Sc} \equiv \left(\frac{d\mathbf{L}}{d\Omega} \right)_{//}^{Sc} = \frac{3}{16\pi} \sigma_T \mathbf{I}_o \cos^2 \Theta \text{ Joules/sec.steradian. } \overset{0}{\text{A.electron}} \tag{A.48}$$

$$\mathbf{I}_{\perp}^{Sc} \equiv \left(\frac{d\mathbf{L}}{d\Omega} \right)_{\perp}^{Sc} = \frac{3}{16\pi} \sigma_T \mathbf{I}_o \text{ Joules/sec.steradian. } \overset{0}{\text{A.electron}} \tag{A.49}$$

where \mathbf{I}_o is the incident radiation.

Consider a radial plane inclined at an angle α to the scattering plane, as shown in figure (A.4). The variation of intensity through an angle β is given by equation (A.50).

$$I = I_M \cos^2 \beta \quad (\text{A.50})$$

where I_M is the maximum intensity.

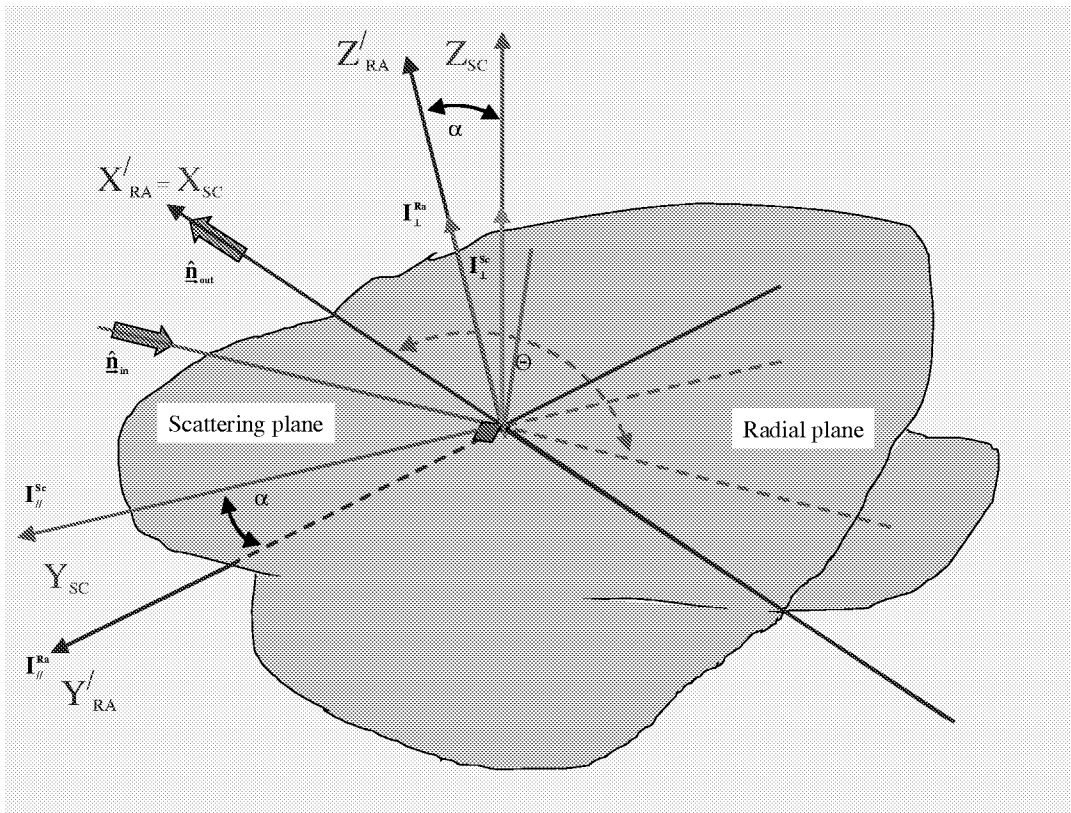


Figure (A.4). Coordinates for the rotational transformation of the scattering plane through an angle α about the line of sight.

From figure (A.4) and using equation (A.50) equation (A.51) and equation (A.52) are obtained for the intensity parallel and perpendicular to the radial plane, respectively.

$$\begin{aligned} \mathbf{I}_{//}^{\text{Ra}} &= \mathbf{I}_{//}^{\text{Sc}} \cos^2 \alpha + \mathbf{I}_{\perp}^{\text{Sc}} \cos^2 \left(\frac{\pi}{2} - \alpha \right) \\ &= \mathbf{I}_{//}^{\text{Sc}} \cos^2 \alpha + \mathbf{I}_{\perp}^{\text{Sc}} \sin^2 \alpha \end{aligned} \quad (\text{A.51})$$

$$\begin{aligned} \mathbf{I}_{\perp}^{\text{Ra}} &= \mathbf{I}_{\perp}^{\text{Sc}} \cos^2 \alpha + \mathbf{I}_{//}^{\text{Sc}} \cos^2 \left(\frac{\pi}{2} - \alpha \right) \\ &= \mathbf{I}_{//}^{\text{Sc}} \sin^2 \alpha + \mathbf{I}_{\perp}^{\text{Sc}} \cos^2 \alpha \end{aligned} \quad (\text{A.52})$$

Substituting equation (A.48) and equation (A.49) in equation (A.51) and equation (A.52) give equation (A.53) and equation (A.54), respectively.

$$\begin{aligned} \mathbf{I}_{//}^{\text{Ra}} &\equiv \left(\frac{d\mathbf{L}}{d\Omega} \right)_{//}^{\text{Ra}} = \frac{3}{16\pi} \sigma_{\text{T}} \mathbf{I}_0 (\sin^2 \alpha + \cos^2 \Theta \cos^2 \alpha) \\ &= \mathbf{I}_{\perp}^{\text{Sc}} \sin^2 \alpha + \mathbf{I}_{//}^{\text{Sc}} \cos^2 \alpha \\ &\equiv \mathbf{Q}_{//}^{\text{Ra}}(\alpha, \Theta) \mathbf{I}_0 \text{ Joules/sec.steradian.A}^\circ \text{.electron} \end{aligned} \quad (\text{A.53})$$

$$\begin{aligned} \mathbf{I}_{\perp}^{\text{Ra}} &\equiv \left(\frac{d\mathbf{L}}{d\Omega} \right)_{\perp}^{\text{Ra}} = \frac{3}{16\pi} \sigma_{\text{T}} \mathbf{I}_0 (\cos^2 \alpha + \cos^2 \Theta \sin^2 \alpha) \\ &= \mathbf{I}_{\perp}^{\text{Sc}} \cos^2 \alpha + \mathbf{I}_{//}^{\text{Sc}} \sin^2 \alpha \\ &\equiv \mathbf{Q}_{\perp}^{\text{Ra}}(\alpha, \Theta) \mathbf{I}_0 \text{ Joules/sec.steradian.A}^\circ \text{.electron} \end{aligned} \quad (\text{A.54})$$

Using the scattering theories derived above the same could be applied for the scattering of photospheric radiation by the coronal electrons. Figure (A.5) shows the corresponding geometrical configurations depicted by figures (A.2) and (A.4) for the case of photospheric radiation being scattered by the coronal electrons to an observer on earth.

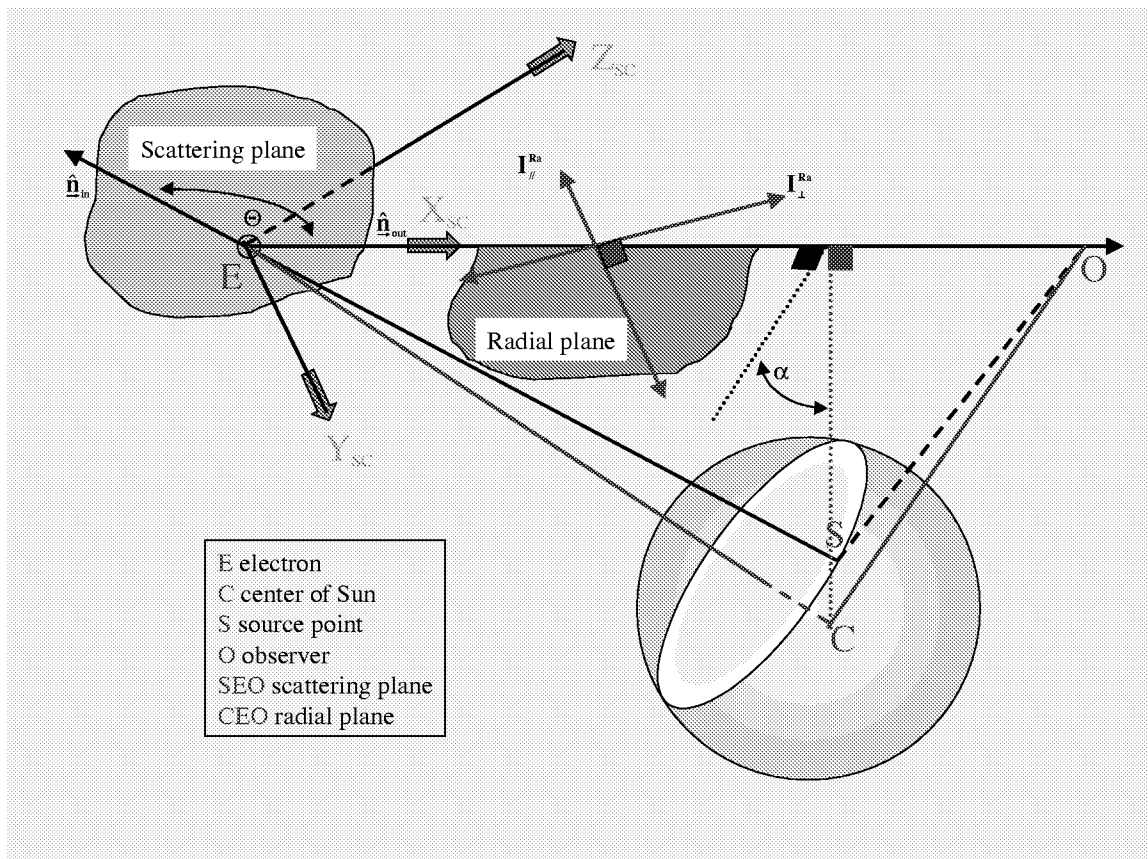


Figure (A.5). Geometrical configuration for the scattering of photospheric radiation by coronal electrons.

The following figure (A.6) shows the geometrical configuration for the formation of the K-Corona, which also incorporates the effect due to the radial solar wind.

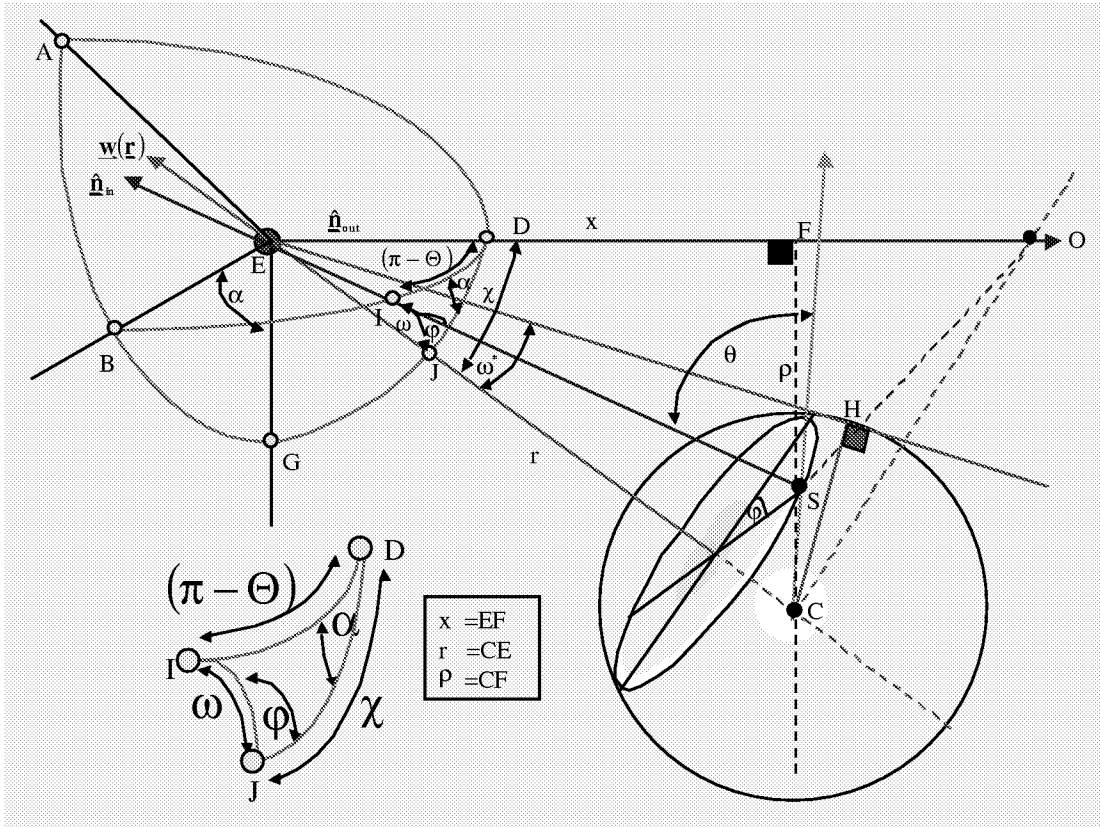


Figure (A.6). Geometrical configuration for the formation of the K- Corona. Photospheric radiation emitted from a point S on the Sun is scattered from an electron E towards an observer O. The solar wind on the electron is radial and blows in the direction CE.

A.3 Contribution due to Compton scattering

In the rest frame of the electron the scattering of the photospheric light incident on the electron is coherent. The red shift due to the Compton effect is very negligible. To quantify the contribution due to Compton effect, consider radiation of wavelength λ incident on a stationary electron, as shown in figure (A.7). Let the radiation scattered off the electron be of wavelength λ' and the velocity of the electron now be \underline{v} . The scattering angles for the radiation and the electron are, θ and ϕ , respectively.

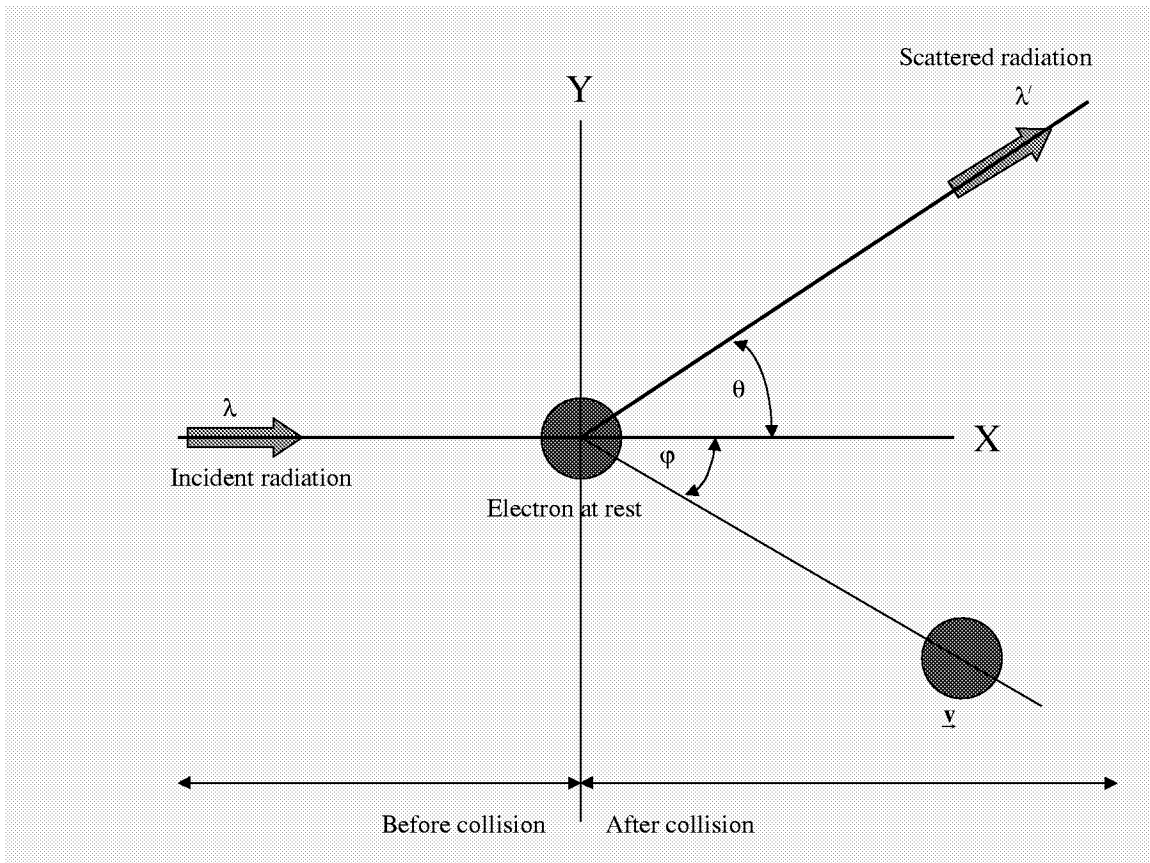


Figure (A.7). Scattering of radiation off an electron also known as Compton scattering.

From conservation of energy in figure (A.7) equation (A.55) is obtained.

$$\frac{hc}{\lambda} = \frac{hc}{\lambda'} + mc^2 \left(\frac{1}{\sqrt{1 - \left(\frac{v}{c}\right)^2}} - 1 \right) \quad (\text{A.55})$$

From figure (A.7) using conservation of momentum in the X the Y directions, respectively, equation (A.56) and equation (A.57) are obtained.

$$\frac{h}{\lambda} = \frac{h}{\lambda'} \cos \theta + \frac{mv}{\sqrt{1 - \left(\frac{v}{c}\right)^2}} \cos \phi \quad (\text{A.56})$$

$$0 = \frac{h}{\lambda'} \sin \theta + \frac{mv}{\sqrt{1 - \left(\frac{v}{c}\right)^2}} \sin \phi \quad (\text{A.57})$$

where

h = Planck constant = 6.63×10^{-34} J.s

m = electron mass = 9.11×10^{-31} Kg

c = speed of light = 3×10^8 ms⁻¹

Eliminating ϕ and v from equation (A.55), (A.56) and (A.57), the wavelength shift is given by equation (A.58).

$$\begin{aligned} \Delta\lambda = \lambda' - \lambda &= \frac{h}{mc} (1 - \cos \theta) \\ &= 0.0243 \text{Å} (1 - \cos \theta) \leq 0.0486 \text{Å} \end{aligned} \quad (\text{A.58})$$

A.4 Expression for the total K-Coronal scattered intensity

From figure (A.6) for the calculation of the total K-Coronal scattered intensity in the rest frame of the electron, first, it is necessary to consider an electron velocity distribution over a volume element at P in order to determine the number density. Consider a Maxwellian velocity distribution for the coronal electrons. Then the number density at the point P in the velocity interval $(\underline{u}, \underline{u} + d\underline{u})$ is given by equation (A.59).

$$f_e(\underline{u}) = N_e(P) \frac{1}{(\sqrt{\pi}q)^3} e^{\left(\frac{-u^2}{q^2}\right)} \quad \text{where}$$

$$q(P) = \text{mean electron thermal velocity} = \sqrt{\frac{2kT_e}{m_e}} = 5508\sqrt{T_e} \text{ kms}^{-1}$$

$$k = \text{Boltzmann constant} = 1.38 \times 10^{-23} \text{ JK}^{-1}$$

$$m_e = \text{electron mass} = 9.11 \times 10^{-31} \text{ kg}$$

$$T_e \text{ in } 10^6 \text{ Kelvins}$$
(A.59)

However, in the rest frame of the observer, the scattered radiation off a moving electron will be altered in wavelength from the monochromatic radiation incident on that electron. Consider a coronal electron with velocity \underline{u} subjected to radial solar wind velocity \underline{w} in a coordinate system where the x-axis bisects the supplement of the scattering angle, as shown in figure (A.8).

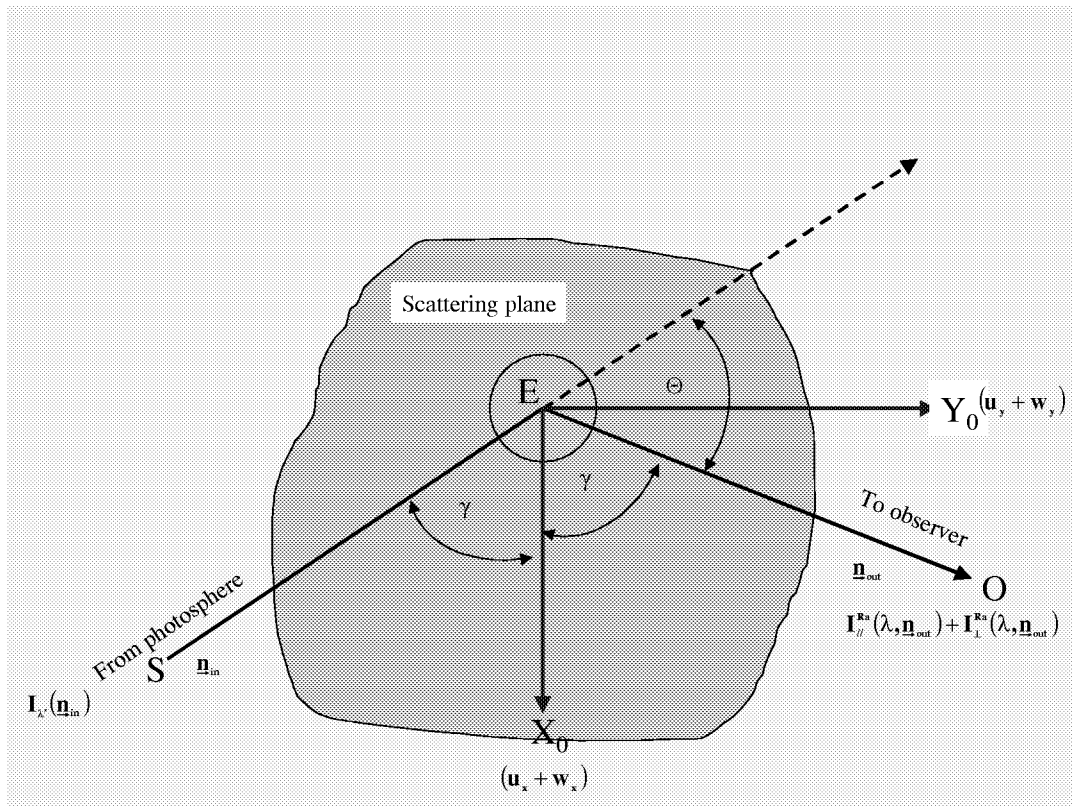


Figure (A.8). Construction to obtain an expression for the scattered intensity in the rest frame of the observer. Consider a coronal electron with velocity \underline{u} subjected to radial solar wind velocity \underline{w} in a coordinate system where the x-axis bisects the supplement of the scattering angle.

From figure (A.8) the direction cosines of the unit vectors $\underline{\mathbf{n}}_{\text{in}}$ and $\underline{\mathbf{n}}_{\text{out}}$ are then given by equation (A.60) and equation (A.61).

$$\underline{\mathbf{n}}_{\text{in}} = (-\cos \gamma, \sin \gamma, 0) \quad (\text{A.60})$$

$$\underline{\mathbf{n}}_{\text{out}} = (\cos \gamma, \sin \gamma, 0) \quad (\text{A.61})$$

And the net velocity vector $\underline{\mathbf{V}}$ is given by equation (A.62).

$$\underline{\mathbf{V}} = (\mathbf{u}_x + \mathbf{w}_x, \mathbf{u}_y + \mathbf{w}_y, \mathbf{u}_z + \mathbf{w}_z) \quad (\text{A.62})$$

From Doppler effect, in the rest frame of the observer, the observed radiation has wavelength given by equation (A.63).

$$\lambda_{\text{observed}} = \lambda_{\text{scattered}} \left(\frac{\mathbf{1} - \frac{\underline{\mathbf{n}}_{\text{out}} \cdot \underline{\mathbf{V}}}{c}}{\mathbf{1} + \frac{\underline{\mathbf{n}}_{\text{out}} \cdot \underline{\mathbf{V}}}{c}} \right)^{\frac{1}{2}} \quad (\text{A.63})$$

The relationship between $\lambda_{\text{observed}}$ and $\lambda_{\text{photosphere}}$ is given by equation (A.64).

$$\lambda_{\text{scattered}} = \lambda_{\text{photosphere}} \left(\frac{\mathbf{1} + \frac{\underline{\mathbf{n}}_{\text{in}} \cdot \underline{\mathbf{V}}}{c}}{\mathbf{1} - \frac{\underline{\mathbf{n}}_{\text{in}} \cdot \underline{\mathbf{V}}}{c}} \right)^{\frac{1}{2}} \quad (\text{A.64})$$

From equation (A.63) and equation (A.64) eliminating $\lambda_{\text{scattered}}$ gives equation (A.65).

$$\lambda_{\text{observed}} = \lambda_{\text{photosphere}} \left(\frac{1 - \frac{\mathbf{n}_{\text{out}} \cdot \mathbf{V}}{c}}{1 + \frac{\mathbf{n}_{\text{out}} \cdot \mathbf{V}}{c}} \right)^{\frac{1}{2}} \left(\frac{1 + \frac{\mathbf{n}_{\text{in}} \cdot \mathbf{V}}{c}}{1 - \frac{\mathbf{n}_{\text{in}} \cdot \mathbf{V}}{c}} \right)^{\frac{1}{2}} \quad (\text{A.65})$$

Since the speed of light $c \gg V$ equation (A.65) can be reduced to equation (A.66).

$$\lambda_{\text{observed}} \cong \lambda_{\text{photosphere}} \left(\frac{1 + \frac{(\mathbf{n}_{\text{in}} - \mathbf{n}_{\text{out}}) \cdot \mathbf{V}}{c}}{1 - \frac{(\mathbf{n}_{\text{in}} - \mathbf{n}_{\text{out}}) \cdot \mathbf{V}}{c}} \right)^{\frac{1}{2}} \quad (\text{A.66})$$

By Taylor expansion of equation (A.66) it could be reduced to equation (A.67).

$$\lambda_{\text{observed}} \cong \lambda_{\text{photosphere}} \left(\frac{1 + \frac{(\mathbf{n}_{\text{in}} - \mathbf{n}_{\text{out}}) \cdot \mathbf{V}}{c}}{1 - \frac{(\mathbf{n}_{\text{in}} - \mathbf{n}_{\text{out}}) \cdot \mathbf{V}}{c}} \right)^{\frac{1}{2}} \quad (\text{A.67})$$

$$\cong \lambda_{\text{photosphere}} \left(1 + \frac{(\mathbf{n}_{\text{in}} - \mathbf{n}_{\text{out}}) \cdot \mathbf{V}}{c} \right)$$

From equation (A.60), (A.61) and (A.62) equation (A.68) could be obtained.

$$(\vec{n}_{in} - \vec{n}_{out}) \cdot \frac{\mathbf{v}}{c} = \left[-2 \cos \gamma \left(\frac{\mathbf{u}_x + \mathbf{w}_x}{c} \right) \right] \quad (\text{A.68})$$

From equation (A.67) and equation (A.68) and using the notations used in figure (A.8) equation (A.69) could be obtained, which relates between $\lambda_{\text{observed}}$ and $\lambda_{\text{photosphere}}$.

$$\lambda = \lambda' \left(1 - 2 \cos \gamma \left(\frac{\mathbf{u}_x + \mathbf{w}_x}{c} \right) \right) \text{ where} \quad (\text{A.69})$$

$$\lambda = \lambda_{\text{observed}}$$

$$\lambda' = \lambda_{\text{photosphere}}$$

Equation (A.79) is obtained by rearranging equation (A.69).

$$\left[\left(\frac{2 \cos \gamma \lambda'}{c} \right) \mathbf{u}_x - \left[\lambda' \left(1 - \frac{2 \cos \gamma}{c} \mathbf{w}_x \right) - \lambda \right] \right] = 0 \quad (\text{A.70})$$

Equation (A.70) satisfies the condition that scattering is coherent in the rest frame of the electron.

Now, from figure (A.8) and equation (A.53), (A.54), (A.59), (A.70) the intensity scattered from an electron at point P is given by equation (A.71).

$$\mathbf{I}_{//}^{\text{Ra}}(\lambda, \underline{\mathbf{n}}_{\text{out}}) + \mathbf{I}_{\perp}^{\text{Ra}}(\lambda, \underline{\mathbf{n}}_{\text{out}}) = \mathbf{I}(\lambda', \underline{\mathbf{n}}_{\text{out}}) \times (\mathbf{Q}_{//}^{\text{Ra}}(\alpha, \Theta) + \mathbf{Q}_{\perp}^{\text{Ra}}(\alpha, \Theta)) \times \mathbf{ND} \quad (\text{A.71})$$

where

$$\mathbf{ND} = \frac{N_e(\mathbf{P})}{(\sqrt{\pi q})^3} \int_{-\infty}^{+\infty} e^{-\frac{u^2}{q^2}} \delta \left[\left(\frac{2 \cos \gamma \lambda'}{c} \right) \mathbf{u}_x - \left(\lambda' \left(\mathbf{1} - \frac{2 \cos \gamma}{c} \mathbf{w}_x \right) - \lambda \right) \right] d\mathbf{u}_x d\mathbf{u}_y d\mathbf{u}_z$$

The expression for \mathbf{ND} in equation (A.71) reduces to equation (A.72).

$$\begin{aligned} \mathbf{ND} &= \frac{N_e(\mathbf{P})}{(\sqrt{\pi q})^3} \int_{-\infty}^{+\infty} e^{-\frac{u_y^2}{q^2}} d\mathbf{u}_y \int_{-\infty}^{+\infty} e^{-\frac{u_z^2}{q^2}} d\mathbf{u}_z \times \\ &\quad \int_{-\infty}^{+\infty} e^{-\frac{\left(\frac{2b\lambda' \mathbf{u}_x}{c}\right)^2}{\left(\frac{2bq\lambda'}{c}\right)^2}} \delta \left[\left(\frac{2b\lambda' \mathbf{u}_x}{c} \right) - \left(\lambda' \left(\mathbf{1} - \frac{2b\mathbf{w}_x}{c} \right) - \lambda \right) \right] \frac{d\left(\frac{2b\lambda' \mathbf{u}_x}{c}\right)}{\left(\frac{2b\lambda'}{c}\right)} \\ &= \frac{N_e(\mathbf{P})}{(\sqrt{\pi q})^3} \times (\sqrt{\pi q}) \times (\sqrt{\pi q}) \times \exp \left[-\frac{\left(\lambda' \left(\mathbf{1} - \frac{2b\mathbf{w}_x}{c} \right) - \lambda \right)^2}{\left(\frac{2bq\lambda'}{c}\right)^2} \right] \frac{1}{\left(\frac{2b\lambda'}{c}\right)} \\ &= \frac{N_e(\mathbf{P})}{(2\sqrt{\pi \Delta b})} \exp \left[-\frac{\left(\lambda - \lambda' \left(\mathbf{1} - \frac{2b\mathbf{w}_x}{c} \right) \right)^2}{(2\Delta b)} \right] \end{aligned} \quad (\text{A.72})$$

where $\Delta = \frac{q\lambda'}{c}$ and $b = \cos \gamma = \cos \left(\frac{\pi - \Theta}{2} \right)$

From equation (A.71) and (A.72) the scattered intensity from point P is given by equation (A.73).

$$\mathbf{I}_O^{\text{Ra}}(\lambda, \underline{\mathbf{n}}_{\text{out}}) = \mathbf{I}(\lambda', \underline{\mathbf{n}}_{\text{in}}) \times \mathbf{Q}_O^{\text{Ra}}(\alpha, \Theta) \times \frac{\mathbf{N}_c(\mathbf{P})}{2\sqrt{\pi}\Delta\mathbf{b}} \exp \left[- \left(\frac{\lambda - \lambda' \left(1 - \frac{2\mathbf{b}w_x}{c} \right)}{2\Delta\mathbf{b}} \right)^2 \right] \quad (\text{A.73})$$

where $\mathbf{O} \equiv (//, \perp)$

To obtain an expression for the total observed scattered intensity, from figure (A.6), the equation (A.73) needs to be integrated over the following parameters.

1. All wavelengths from each point on the photosphere

$$\int_0^{\infty} d\lambda' \quad (\text{A.74})$$

2. From all points on the photosphere

$$\int_0^{2\pi} d\phi \int_0^{\omega^*} \sin \omega d\omega \equiv \int_0^{2\pi} d\phi \int_{\cos \omega^*}^1 d \cos \omega \quad (\text{A.75})$$

3. From all points along the line of sight

$$\int_{-\infty}^{+\infty} d\mathbf{x} \quad (\text{A.76})$$

From figure (A.6) and figure (A.8) the radial solar wind velocity has components given by equation (A.77).

$$\underline{w} = (-\cos \omega \cos \gamma, \cos \omega \sin \gamma, \sin \omega) \equiv (w_x, w_y, w_z) \quad (\text{A.77})$$

Using equation (A.74), (A.76), (A.76) and (A.77) in (A.73) gives the expression for the total observed intensity for a given observed wavelength λ at a given line of sight distance ρ from the center of the Sun (see figure (A.6)), as given by equation (A.78).

$$\mathbf{I}_O^{\text{Ra}}(\lambda, \rho) = \int_{-\infty}^{+\infty} \int_0^{\cos \omega} \int_0^{2\pi} \int_0^{\infty} d\lambda' d \cos \omega d\phi dx \times$$

$$\mathbf{N}_e(\mathbf{r}) \times \mathbf{Q}_O^{\text{Ra}}(\alpha, \Theta) \times$$

$$\frac{1}{2\sqrt{\pi}\Delta b} \mathbf{I}(\lambda', \underline{\mathbf{n}}_{\text{in}}) \exp \left[- \left(\frac{\lambda - \lambda' \left(1 + \frac{2b^2 \cos \omega w(\mathbf{r})_{\text{radial}}}{c} \right)}{2\Delta b} \right)^2 \right] \quad (\text{A.78})$$

where $\mathbf{O} \equiv (//, \perp)$
// parallel to the radial plane
 \perp perpendicular to the radial plane

A.5 Expressions for the dependent variables in equation (A.78) in terms of the independent variables

Figure (A.9) is a highlight from figure (A.6) of the triangles formed by SEW (scattering plane), CEF (radial plane) and CSE.

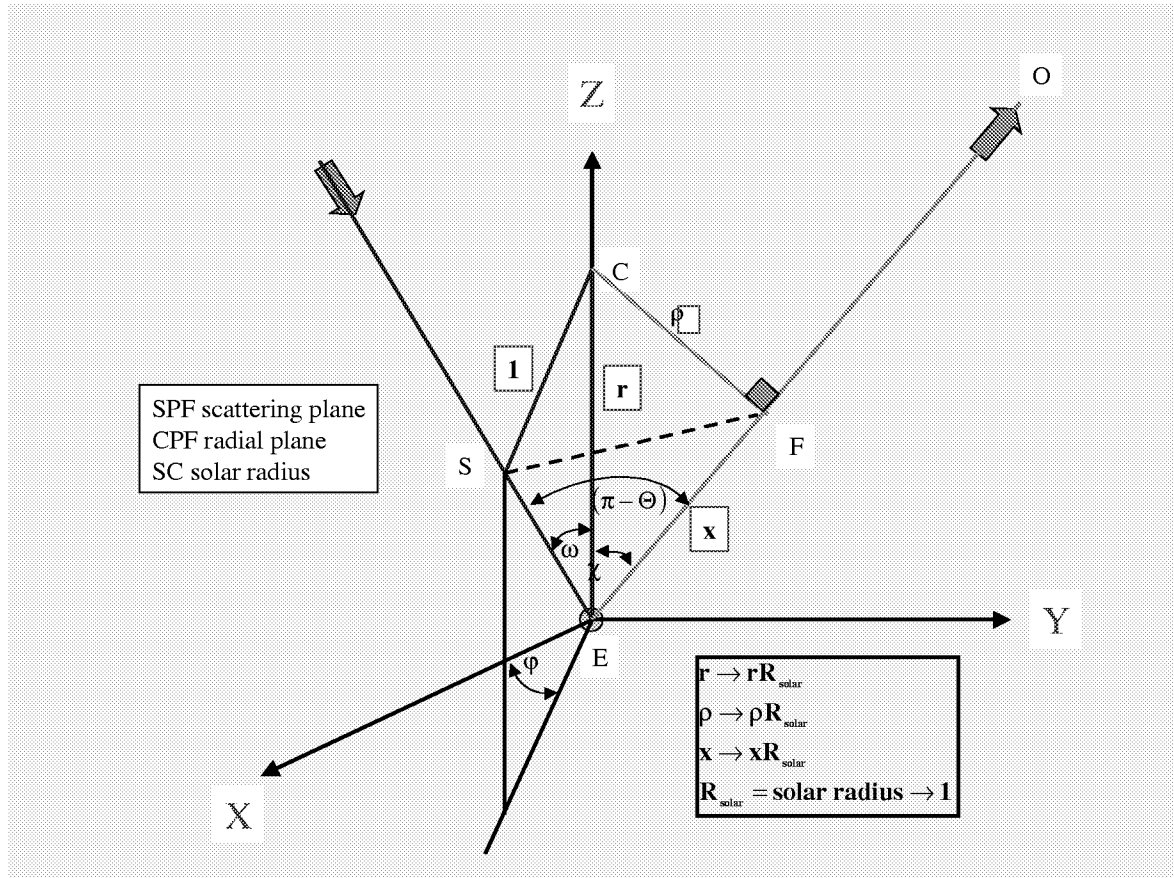


Figure (A.9). Highlighted map of the radial and the scattering planes of figure (A.6).

From figure (A.9) equation (A.79) and equation (A.80) can be obtained.

$$\underline{ES} = |\underline{ES}|(\sin \omega \cos \varphi, \sin \omega \sin \varphi, \cos \omega) \tag{A.79}$$

$$\underline{EF} = |\underline{EF}|(0, \sin \chi, \cos \chi) \tag{A.80}$$

And the dot product of equation (A.79) and equation (A.80) gives equation (A.81).

$$\begin{aligned}\underline{\mathbf{ES}} \cdot \underline{\mathbf{EF}} &= |\underline{\mathbf{ES}}| |\underline{\mathbf{EF}}| (\sin \omega \sin \phi \sin \chi + \cos \omega \cos \chi) \\ &= |\underline{\mathbf{ES}}| |\underline{\mathbf{EF}}| \cos(\pi - \Theta)\end{aligned}\tag{A.81}$$

From equation (A.81) the expression for Θ is given by equation (A.82).

$$\Theta = \pi - \cos^{-1}(\sin \omega \sin \phi \sin \chi + \cos \omega \cos \chi)\tag{A.82}$$

Also from figure (A.9) the expression for angle χ is given by equation (A.83).

$$\cos \chi = \frac{x}{r}\tag{A.83}$$

From figure (A.6) and measuring distances in solar radius the expression for angle ω^* is given by equation (A.84).

$$\sin \omega^* = \frac{HC}{EC} = \frac{1}{r}\tag{A.84}$$

From figure (A.6) consider the spherical triangle formed by EDJI, as shown in figure (A.10).

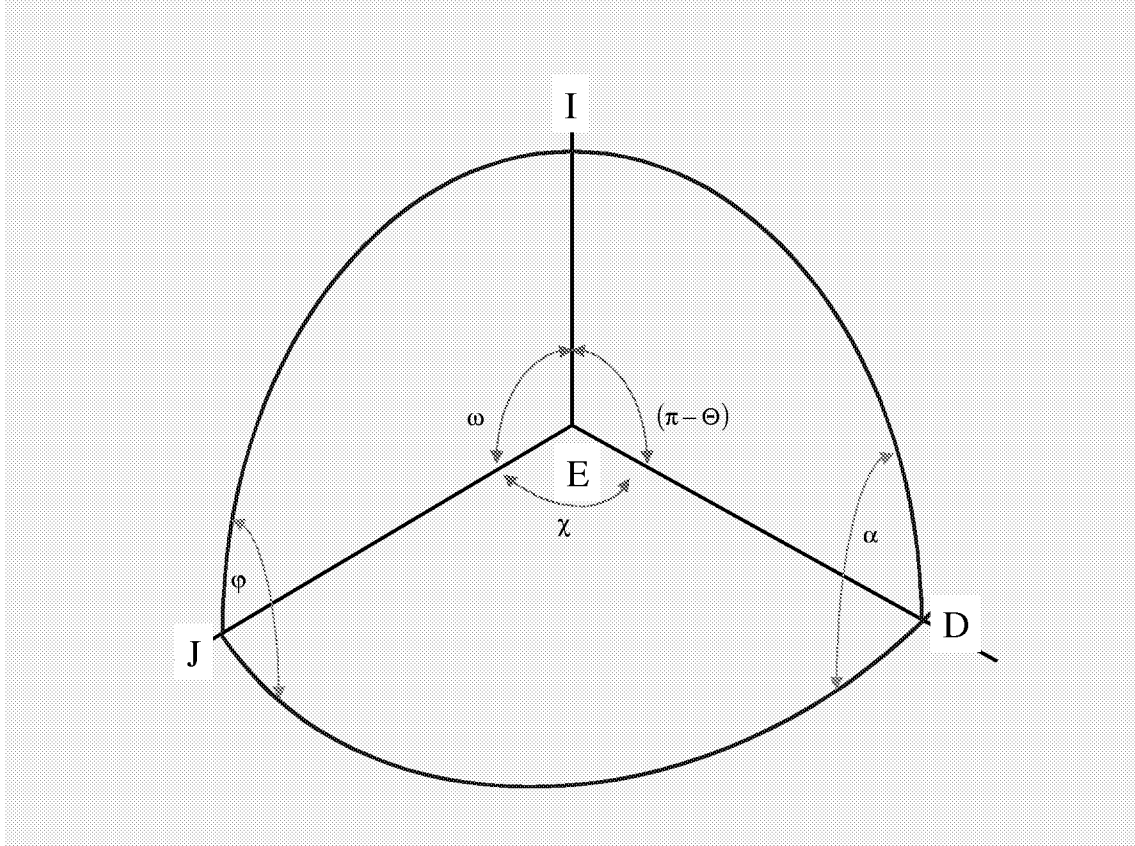


Figure (A.10). Highlight of the spherical triangle formed by EDJI in figure (A.6).

From figure (A.10) the relationship between the angles is given by equation (A.85).

$$\frac{\sin \alpha}{\sin \omega} = \frac{\sin \varphi}{\sin(\pi - \Theta)} \tag{A.85}$$

From equation (A.85) the expression for angle α is given by equation (A.86).

$$\alpha = \sin^{-1} \left(\frac{\sin \omega \sin \varphi}{\sin(\pi - \Theta)} \right) \quad (\text{A.86})$$

Figure (A.11) shows the triangle ECS from figure (A.6).

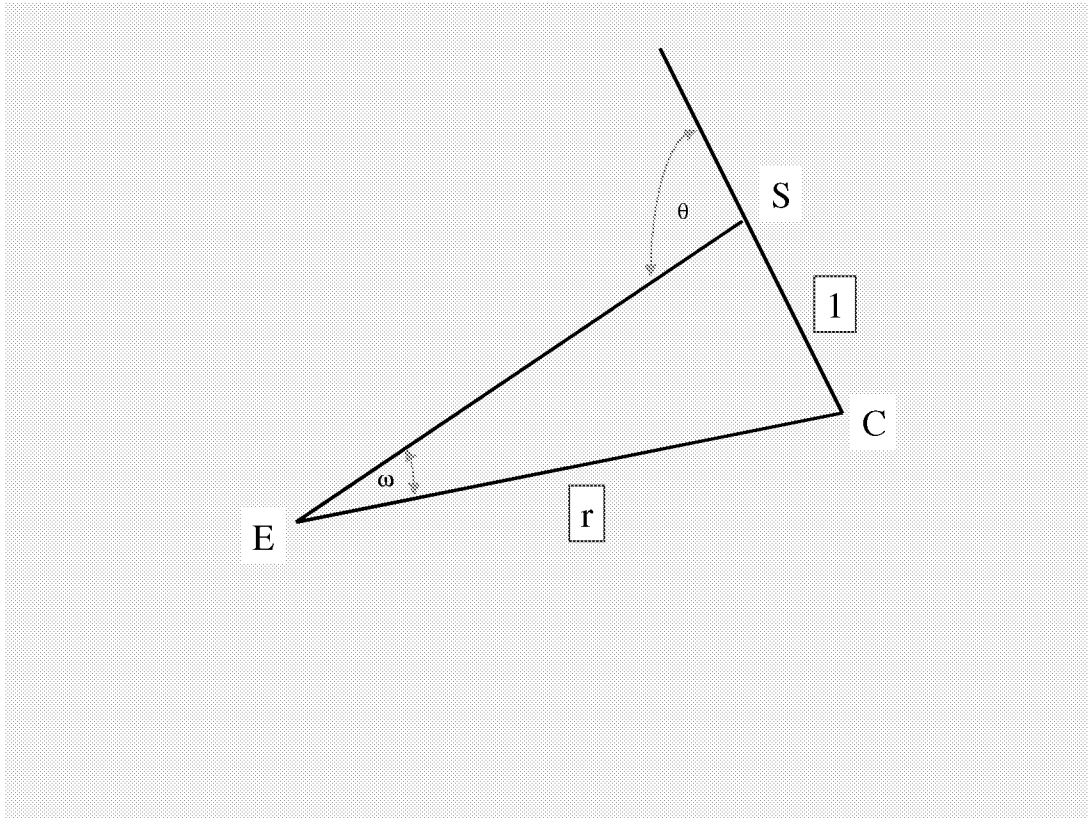


Figure (A.11). Highlight of the triangle ECS of figure (A.6).

From figure (A.11) the relationship between the angles θ and ω is given by equation (A.87).

$$\frac{1}{\sin \omega} = \frac{r}{\sin(\pi - \theta)} \quad (\text{A.87})$$

$$\therefore \sin \theta = r \sin \omega$$

A.6 Expression for the incident solar intensity on the coronal electrons

In order to evaluate equation (A.78) the incident solar intensity $I(\lambda', \mathbf{n}_{in})$ need to be known. The following expressions are from *Astrophysical Quantities* by *Allen*. Let $I(\lambda', \theta)$ be the intensity of the solar continuum at an angle θ from the center of the disk and $I(\lambda', \mathbf{0})$ the continuum intensity at the center of the disk. The results may be fitted by the expression given by equation (A.88).

$$\frac{I(\lambda', \theta)}{I(\lambda', \mathbf{0})} = 1 - u_2 - v_2 + u_2 \cos \theta + v_2 \cos^2 \theta \quad (\text{A.88})$$

where u_2 and v_2 are limb darkening constants

Or less accurately equation (A.88) can be written as equation (A.89).

$$\frac{I(\lambda', \theta)}{I(\lambda', \mathbf{0})} = 1 - u_1 + u_1 \cos \theta \quad (\text{A.89})$$

where $\cos \theta$ is the heliocentric angle shown in figure (A.6).

And for determining the value of \mathbf{u}_1 it is preferable to make a fit at $\cos\theta = 0.5$, which gives the expression given by equation (A.90).

$$\begin{aligned}
 \cos^2 \theta &= \frac{1}{2}(3 \cos \theta - 1) \text{ at } \cos \theta = 0.5 \text{ and} \\
 \frac{\mathbf{I}(\lambda', \theta)}{\mathbf{I}(\lambda', 0)} &= 1 - \mathbf{u}_2 - \mathbf{v}_2 + \mathbf{u}_2 \cos \theta + \mathbf{v}_2 \frac{1}{2}(3 \cos \theta - 1) \\
 &= 1 - \left(\mathbf{u}_2 + \frac{3}{2} \mathbf{v}_2 \right) + \left(\mathbf{u}_2 + \frac{3}{2} \mathbf{v}_2 \right) \cos \theta \\
 &\equiv 1 - \mathbf{u}_1 + \mathbf{u}_1 \cos \theta \quad \text{where} \\
 \mathbf{u}_1 &= \left(\mathbf{u}_2 + \frac{3}{2} \mathbf{v}_2 \right)
 \end{aligned}
 \tag{A.90}$$

The ratio of mean to central intensity is given by equation (A.91).

$$\begin{aligned}
 \frac{\mathbf{F}(\lambda')}{\mathbf{I}(\lambda', 0)} &= 1 - \frac{1}{3} \mathbf{u}_2 - \frac{1}{2} \mathbf{v}_2 \\
 &= 1 - \frac{1}{3} \left(\mathbf{u}_2 + \frac{3}{2} \mathbf{v}_2 \right) \\
 &= 1 - \frac{1}{3} \mathbf{u}_1
 \end{aligned}
 \tag{A.91}$$

From equation (A.90) and (A.91) the ratio of $\mathbf{I}(\lambda', \theta)/\mathbf{F}(\lambda')$ is given by equation (A.92).

$$\frac{\mathbf{I}(\lambda', \theta)}{\mathbf{F}(\lambda')} = \frac{1 - \mathbf{u}_1 + \mathbf{u}_1 \cos \theta}{1 - \frac{1}{3} \mathbf{u}_1}
 \tag{A.92}$$

The emittance of solar surface per unit wavelength range is given by equation (A.93).

$$E(\lambda') = \pi F(\lambda') \quad (\text{A.93})$$

And the solar flux outside the Earth atmosphere per unit area and wavelength range is given by equation (A.94).

$$\boxed{\begin{aligned} f(\lambda') &= E(\lambda') \left(\frac{R_{\text{solar}}}{\text{AU}} \right)^2 \\ &= \pi \left(\frac{R_{\text{solar}}}{\text{AU}} \right)^2 F(\lambda') \end{aligned}} \quad (\text{A.94})$$

From equation (A.90) and equation (A.92) the incident intensity on the coronal electrons is given by equation (A.95).

$$\boxed{I(\lambda', \theta) = \left(\frac{1}{\pi} \right) \frac{1 - u_1 + u_1 \cos \theta}{1 - \frac{1}{3} u_1} \left(\frac{\text{AU}}{R_{\text{solar}}} \right)^2 f(\lambda')} \quad (\text{A.95})$$

In equation (A.94) and equation (A.95) AU is the Sun-Earth distance. The wavelength dependent limb-darkening coefficient u_1 can be obtained from *Astrophysical Quantities* by *Allen*

A.7 Final expression for the observed intensity

From figure (A.6) and equation (A.78) all the following expressions are given in terms of solar radii, as shown in equation (A.96).

$$\boxed{\begin{array}{l} \mathbf{r} \rightarrow \mathbf{rR}_{\text{solar}} \\ \rho \rightarrow \rho\mathbf{R}_{\text{solar}} \\ \mathbf{x} \rightarrow \mathbf{xR}_{\text{solar}} \end{array}} \quad (\text{A.96})$$

And the observed intensity is given by equation (A.97).

$$\boxed{\begin{array}{l} \mathbf{I}_{\mathbf{O}}^{\text{Ra}}(\lambda, \rho\mathbf{R}_{\text{solar}}) = \int_{-\infty}^{+\infty} \int_{\cos \omega^*}^1 \int_0^{\infty} \mathbf{d}\lambda' \mathbf{d}\phi \mathbf{d}\cos \omega \mathbf{d}(\mathbf{xR}_{\text{solar}}) \times \\ \mathbf{N}_{\mathbf{e}}(\mathbf{rR}_{\text{solar}}) \times \mathbf{Q}_{\mathbf{O}}^{\text{Ra}}(\alpha, \Theta) \times \\ \frac{1}{2\sqrt{\pi}\Delta\mathbf{b}} \mathbf{I}(\lambda', \omega, \mathbf{x}) \exp \left[- \frac{\left(\lambda - \lambda' \left(1 + \frac{2\mathbf{b}^2 \cos \omega \mathbf{w}(\mathbf{rR}_{\text{solar}})_{\text{radial}}}{\mathbf{c}} \right) \right)^2}{2\Delta\mathbf{b}} \right] \end{array}} \quad (\text{A.97})$$

where $\mathbf{O} \equiv (//, \perp)$
// parallel to the radial plane
 \perp perpendicular to the radial plane

The expressions for physical parameters in equation (A.97) in terms of independent variables are given in equation (A.98). Equation (A.99) gives the parameters in equation (A.97) for which suitable models or actual measurements need to be used.

$$\begin{aligned}
Q_{//}^{\text{Ra}} &= \frac{3}{16\pi} \sigma_T (\sin^2 \alpha + \cos^2 \alpha \cos^2 \Theta) \\
Q_{\perp}^{\text{Ra}} &= \frac{3}{16\pi} \sigma_T (\cos^2 \alpha + \sin^2 \alpha \cos^2 \Theta) \\
b &= \cos \gamma = \cos \left(\frac{\pi - \Theta}{2} \right) \\
\Delta &= \frac{q\lambda'}{c} \\
q &= \sqrt{\frac{2kT}{m}} \\
I(\lambda', \omega, x) &= \frac{1}{\pi} \left(\frac{\text{AU}}{R_{\text{solar}}} \right)^2 \left(\frac{1 - u_1 + u_1 \cos \theta}{1 - \frac{1}{3} u_1} \right) f \\
\Theta &= \pi - \cos^{-1} (\sin \omega \sin \phi \sin \chi + \cos \omega \cos \chi) \\
\alpha &= \sin^{-1} \left(\frac{\sin \omega \sin \phi}{\sin(\pi - \Theta)} \right) \\
\chi &= \cos^{-1} \left(\frac{x}{r} \right) \\
\omega^* &= \sin^{-1} \left(\frac{1}{r} \right) \\
\theta &= \sin^{-1} (r \sin \omega) \\
r^2 &= x^2 + \rho^2
\end{aligned}$$

(A.98)

$$\begin{aligned}
u_1(\lambda') &= \text{limb darkening coefficient} \\
f(\lambda') &= \text{extraterrestrial solar irradiance} \\
N_e(rR_{\text{solar}}) &= \text{electron density model} \\
T(rR_{\text{solar}}) &= \text{coronal temperature model} \\
W(rR_{\text{solar}}) &= \text{solar wind model}
\end{aligned}$$

(A.99)

Appendix B

CODE

B.1 The basic equation to be solved

The basic equation to be solved is equation (A.97) as developed in Appendix A and reproduced below. The observed K-Coronal intensity is given by equation (B.1). The expressions for physical parameters in equation (B.1) in terms of independent variables are given in equation (B.2). Equation (B.3) gives the parameters in equation (B.1) for which suitable models or actual measurements need to be used.

$$\begin{aligned}
 \mathbf{I}_O^{\text{Ra}}(\lambda, \rho \mathbf{R}_{\text{solar}}) = & \int_{-\infty}^{+\infty} \int_0^{2\pi} \int_{\cos \omega^*}^1 \int_0^{\infty} d\lambda' d \cos \omega d\phi d(\mathbf{xR}_{\text{solar}}) \times \\
 & \mathbf{N}_e(\mathbf{rR}_{\text{solar}}) \times \mathbf{Q}_O^{\text{Ra}}(\alpha, \Theta) \times \\
 & \frac{1}{2\sqrt{\pi}\Delta b} \mathbf{I}(\lambda', \omega, \mathbf{x}) \exp \left[- \left(\frac{\lambda - \lambda' \left(1 + \frac{2b^2 \cos \omega \mathbf{w}(\mathbf{rR}_{\text{solar}})_{\text{radial}}}{c} \right)}{2\Delta b} \right)^2 \right]
 \end{aligned} \tag{B.1}$$

where $\mathbf{O} \equiv (//, \perp)$
// parallel to the radial plane
 \perp perpendicular to the radial plane

$$\begin{aligned}
Q_{//}^{\text{Ra}} &= \frac{3}{16\pi} \sigma_{\text{T}} (\sin^2 \alpha + \cos^2 \alpha \cos^2 \Theta) \\
Q_{\perp}^{\text{Ra}} &= \frac{3}{16\pi} \sigma_{\text{T}} (\cos^2 \alpha + \sin^2 \alpha \cos^2 \Theta) \\
b &= \cos \gamma = \cos \left(\frac{\pi - \Theta}{2} \right) \\
\Delta &= \frac{q\lambda'}{c} \\
q &= \sqrt{\frac{2k\Gamma}{m}} \\
I(\lambda', \omega, \mathbf{x}) &= \frac{1}{\pi} \left(\frac{\text{AU}}{\mathbf{R}_{\text{solar}}} \right)^2 \left(\frac{1 - u_1 + u_1 \cos \theta}{1 - \frac{1}{3} u_1} \right) f \\
\Theta &= \pi - \cos^{-1} (\sin \omega \sin \varphi \sin \chi + \cos \omega \cos \chi) \\
\alpha &= \sin^{-1} \left(\frac{\sin \omega \sin \varphi}{\sin(\pi - \Theta)} \right) \\
\chi &= \cos^{-1} \left(\frac{\mathbf{x}}{\mathbf{r}} \right) \\
\omega^* &= \sin^{-1} \left(\frac{1}{\mathbf{r}} \right) \\
\theta &= \sin^{-1} (\mathbf{r} \sin \omega) \\
\mathbf{r}^2 &= \mathbf{x}^2 + \rho^2
\end{aligned} \tag{B.2}$$

$$\begin{aligned}
u_1(\lambda') &= \text{limb darkening coefficient} \\
f(\lambda') &= \text{extraterrestrial solar irradiance} \\
N_e(\mathbf{rR}_{\text{solar}}) &= \text{electron density model} \\
T(\mathbf{rR}_{\text{solar}}) &= \text{coronal temperature model} \\
W(\mathbf{rR}_{\text{solar}}) &= \text{solar wind model}
\end{aligned} \tag{B.3}$$

B.2 Approximations to the $\int d\lambda'$ integral

Consider the exponent in equation (B.1) be represented by y as shown in equation (B.4).

$$y = \frac{\lambda - \lambda' \left(1 + 2b^2 \cos \omega \frac{w}{c} \right)}{2\Delta b} \quad \text{where } \Delta = \frac{q\lambda'}{c} \quad (\text{B.4})$$

The first approximation to be made on equation (B.4) is given in equation (B.5).

$$\Delta = \frac{q\lambda'}{c} \rightarrow \frac{q\lambda}{c} \quad (\text{B.5})$$

This approximation is justified on the grounds that the speed of light c (3×10^5) **km/sec** is much larger than the thermal electron velocity q (**5500 km/sec**) so that a difference of about 10 Angstroms between λ and λ' would hardly have any effect on the value of Δ .

Then differentiating equation (B.4) with respect to λ' together with the approximation given by equation (B.5) gives equation (B.6).

$$\frac{dy}{d\lambda'} = - \frac{1 + 2b^2 \cos \omega \frac{w}{c}}{2\Delta b} \quad (\text{B.6})$$

The second approximation to be made on the integration limits in equation (B.4) is given by equation (B.7).

<p>When $\lambda' \rightarrow 0$ then $y \rightarrow \frac{\lambda}{2\Delta b} = \frac{\lambda}{2\frac{q}{c}\lambda b} = \frac{c}{2qb}$</p> <p>where $c = 3 \times 10^5$ km/sec</p> <p>$q \cong 5500$ km/sec</p> <p>$b \leq 1$</p> <p>$\therefore y \rightarrow \infty$</p>	(B.7)
----------------------------------------------------------------------------------------------------------------------------------------------------------------------------------------------------------------------------------------------------------------------------------------------------------------------------------------------------------------------------------	--------------

When $\lambda' \rightarrow \infty$ then $y \rightarrow -\infty \left(\frac{1 + 2b^2 \cos \omega \frac{w}{c}}{2\Delta b} \right) \rightarrow -\infty$

Using the limits derived in equation (B.7), the exponent in equation (B.1) together with all other λ' dependent parameters reduces the integral over $\int d\lambda'$ to equation (B.8).

$\int_0^{\infty} e^{-\left(\frac{\lambda - \lambda' \left(1 + 2b^2 \cos \omega \frac{w}{c} \right)}{2\Delta b} \right)^2} \frac{f(\lambda')}{2\Delta b} d\lambda' = \frac{1}{1 + 2b^2 \cos \omega \frac{w}{c}} \int_{-\infty}^{+\infty} f \left(\frac{\lambda + y(2\Delta b)}{1 + 2b^2 \cos \omega \frac{w}{c}} \right) e^{-y^2} dy$ <p>and $\lambda' = \frac{\lambda + y(2\Delta b)}{1 + 2b^2 \cos \omega \frac{w}{c}}$</p> $= \frac{\lambda \left(1 + 2\frac{q}{c} by \right)}{1 + 2b^2 \cos \omega \frac{w}{c}}$	(B.8)
-------------------------------------------------------------------------------------------------------------------------------------------------------------------------------------------------------------------------------------------------------------------------------------------------------------------------------------------------------------------------------------------------------------------------------------------------------------------------------------------------------------------------------------------	--------------

B.3 \mathbf{b} , $Q_{//}^{Ra}$ and Q_{\perp}^{Ra} in terms of the independent variables ω , φ and \mathbf{x}

From equation (B.2) the expression for \mathbf{b} is given by equation (B.9).

$$\begin{aligned}
 \mathbf{b} &= \cos \gamma \quad \text{and} \quad 2\gamma = \pi - \Theta \\
 &= \cos\left(\frac{\pi - \Theta}{2}\right) \\
 &= \sin\left(\frac{\Theta}{2}\right)
 \end{aligned}
 \tag{B.9}$$

Using the trigonometric identity $\cos(2\gamma) = 2\cos^2(\gamma) - 1$ on equation (B.9) together with expressions for $\cos(\pi - \Theta)$, $\sin\chi$, $\cos\chi$ and \mathbf{r} from equation (B.2) gives the following expression for \mathbf{b} , as shown in equation (B.10).

$$\begin{aligned}
 \mathbf{b} &= \frac{1}{\sqrt{2}} (1 + \cos(2\gamma))^{\frac{1}{2}} \\
 &= \frac{1}{\sqrt{2}} (1 + \cos(\pi - \Theta))^{\frac{1}{2}} \\
 &= \frac{1}{\sqrt{2}} (1 + \sin \omega \sin \chi \sin \varphi + \cos \omega \cos \chi)^{\frac{1}{2}} \\
 &= \frac{1}{\sqrt{2}} \left(1 + \sin \omega \frac{\rho}{\sqrt{\mathbf{x}^2 + \rho^2}} \sin \varphi + \cos \omega \frac{\mathbf{x}}{\sqrt{\mathbf{x}^2 + \rho^2}} \right)^{\frac{1}{2}} \\
 &= \frac{1}{\sqrt{2}} \left(1 + \sqrt{1 - \cos^2 \omega} \frac{\rho}{\sqrt{\mathbf{x}^2 + \rho^2}} \sin \varphi + \cos \omega \frac{\mathbf{x}}{\sqrt{\mathbf{x}^2 + \rho^2}} \right)^{\frac{1}{2}}
 \end{aligned}
 \tag{B.10}$$

From equation (B.2) the expression for $Q_{//}^{\text{Ra}}$ is given by equation (B.11).

$$\begin{aligned}
 Q_{//}^{\text{Ra}} &= \frac{3}{16\pi} \sigma_{\text{T}} (\sin^2 \alpha + \cos^2 \alpha \cos^2 \Theta) \\
 &= \frac{3}{16\pi} \sigma_{\text{T}} (\sin^2 \alpha + (1 - \sin^2 \alpha) \cos^2 \Theta) \\
 &= \frac{3}{16\pi} \sigma_{\text{T}} (\cos^2 \Theta + \sin^2 \alpha (1 - \cos^2 \Theta)) \\
 &= \frac{3}{16\pi} \sigma_{\text{T}} (1 - \sin^2 \Theta + \sin^2 \alpha (1 - \cos^2 \Theta)) \\
 &= \frac{3}{16\pi} \sigma_{\text{T}} (1 + \sin^2 \alpha \sin^2 \Theta - \sin^2 \Theta)
 \end{aligned}
 \tag{B.11}$$

Now, using the relationships $\sin(2\gamma) = \sin \Theta$ and $\sin \alpha = \frac{\sin \omega \sin \varphi}{\sin \Theta}$ from equation (B.2)

and the trigonometric identities $\sin(2\gamma) = 2\sin \gamma \cos \gamma$ and $\sin^2 \gamma + \cos^2 \gamma = 1$ on equation

(B.11) reduces equation (B.11) to equation (B.12).

$$Q_{//}^{\text{Ra}} = \frac{3}{16\pi} \sigma_{\text{T}} (1 + \sin^2 \omega \sin^2 \varphi - 4(1 - \cos^2 \gamma) \cos^2 \gamma)
 \tag{B.12}$$

The expression for $\cos \gamma$ as a function of $(\omega, \varphi, \mathbf{x})$ is given by equation (B.10).

Again, from equation (B.2) the expression for Q_{\perp}^{Ra} is given by equation (B.13).

$$\begin{aligned}
 Q_{\perp}^{\text{Ra}} &= \frac{3}{16\pi} \sigma_{\text{T}} (\cos^2 \alpha + \sin^2 \alpha \cos^2 \Theta) \\
 &= \frac{3}{16\pi} \sigma_{\text{T}} (1 - \sin^2 \alpha + \sin^2 \alpha \cos^2 \Theta) \\
 &= \frac{3}{16\pi} \sigma_{\text{T}} (1 - \sin^2 \alpha (1 - \cos^2 \Theta)) \\
 &= \frac{3}{16\pi} \sigma_{\text{T}} (1 - \sin^2 \alpha \sin^2 \Theta) \\
 &= \frac{3}{16\pi} \sigma_{\text{T}} \left(1 - \frac{\sin^2 \omega \sin^2 \varphi}{\sin^2 \Theta} \sin^2 \Theta \right) \\
 &= \frac{3}{16\pi} \sigma_{\text{T}} (1 - \sin^2 \omega \sin^2 \varphi)
 \end{aligned} \tag{B.13}$$

And using the relation $\sin \alpha = \frac{\sin \omega \sin \varphi}{\sin \Theta}$ from equation (B.2) in equation (B.13) gives

equation (B.14).

$$Q_{\perp}^{\text{Ra}} = \frac{3}{16\pi} \sigma_{\text{T}} (1 - \sin^2 \omega \sin^2 \varphi) \tag{B.14}$$

B.4 Rewriting the basic equation with all parameters expressed in terms of the independent variables (ω, φ, x, y)

With change of variables introduced in section B.2 and the relationships developed in section B.3 the expression for the observed K-Coronal intensity is given by equation (B.15). The expressions for the physical parameters in equation (B.15) in terms of the independent variables are given in equation (B.16). Equation (B.17) gives the

parameters in equation (B.15) for which suitable models or actual measurements need to be used in terms of the given distance ρ and observed wavelength λ .

$$\mathbf{I}_O^{\text{Ra}}(\lambda, \rho \mathbf{R}_{\text{solar}}) = \int_{-\infty}^{+\infty} \int_0^{2\pi} \int_{\cos \omega^*}^1 \int_{-\infty}^{+\infty} \mathbf{d}y \mathbf{d}\varphi \mathbf{d} \cos \omega \mathbf{d}(\mathbf{x} \mathbf{R}_{\text{solar}}) \times$$

$$\mathbf{N}_e \left(\sqrt{\mathbf{x}^2 + \rho^2} \mathbf{R}_{\text{solar}} \right) \times \mathbf{Q}_O^{\text{Ra}}(\omega, \varphi, \mathbf{x}) \times$$

$$\frac{1}{\sqrt{\pi}} \mathbf{I}(y, \omega, \varphi, \mathbf{x}) \frac{\exp[-y^2]}{1 + 2\mathbf{b}^2 \cos \omega \frac{\mathbf{w}}{\mathbf{c}}}$$

where $\mathbf{O} \equiv (//, \perp)$
// parallel to the radial plane
\perp perpendicular to the radial plane

$$\mathbf{b} = \frac{1}{\sqrt{2}} \left(1 + \sqrt{1 - \cos^2 \omega} \frac{\rho}{\sqrt{\mathbf{x}^2 + \rho^2}} \sin \varphi + \cos \omega \frac{\rho}{\sqrt{\mathbf{x}^2 + \rho^2}} \right)^{1/2}$$

$$\mathbf{Q}_{//}^{\text{Ra}} = \frac{3}{16\pi} \sigma_{\text{T}} (1 + \sin^2 \omega \sin^2 \varphi - 4(1 - \mathbf{b}^2) \mathbf{b}^2)$$

$$\mathbf{Q}_{\perp}^{\text{Ra}} = \frac{3}{16\pi} \sigma_{\text{T}} (1 - \sin^2 \omega \sin^2 \varphi)$$

$$\Delta = \frac{q\lambda}{\mathbf{c}}$$

$$q = \sqrt{\frac{2k\text{T}}{\mathbf{m}}}$$

$$\mathbf{I}(y, \omega, \varphi, \mathbf{x}) = \frac{1}{\pi} \left(\frac{\text{AU}}{\mathbf{R}_{\text{solar}}} \right)^2 \left(\frac{1 - \mathbf{u}_1 + \mathbf{u}_1 \cos \theta}{1 - \frac{1}{3} \mathbf{u}_1} \right) \mathbf{f}$$

$$\cos \omega^* = \cos \left(\sin^{-1} \left(\frac{1}{\sqrt{\mathbf{x}^2 + \rho^2}} \right) \right)$$

$$\cos \theta = \cos \left(\sin^{-1} \left(\sqrt{\mathbf{x}^2 + \rho^2} \sin \omega \right) \right)$$

$\mathbf{u}_1(\xi) = \text{limb darkening coefficient}$ $\mathbf{f}(\xi) = \text{extraterrestrial solar irradiance}$ $\xi = \frac{\lambda \left(1 + 2 \frac{q}{c} by \right)}{1 + 2b^2 \cos \omega \frac{w}{c}}$ $\mathbf{N}_e \left(\sqrt{x^2 + \rho^2} R_{\text{solar}} \right) = \text{electron density model}$ $\mathbf{T} \left(\sqrt{x^2 + \rho^2} R_{\text{solar}} \right) = \text{coronal temperature model}$ $\mathbf{W} \left(\sqrt{x^2 + \rho^2} R_{\text{solar}} \right) = \text{solar wind model}$	(B.17)
------------------------------------------------------------------------------------------------------------------------------------------------------------------------------------------------------------------------------------------------------------------------------------------------------------------------------------------------------------------------------------------------------------------------------------------------------------------------------------------------------------------------------------	--------

B.5 Changing the independent variable $\cos \omega$ to $\cos \theta$

Consider the integral in equation (B.15) as shown in equation (B.18).

$$\int_{\cos \omega^*}^1 d \cos \omega \tag{B.18}$$

From equation (B.2) the expression for $\cos \omega^*$ and θ are given by equation (B.19) and equation (B.20), respectively.

$\cos \omega^* = \sqrt{1 - \sin^2 \omega^*}$ $= \sqrt{1 - \frac{1}{x^2 + \rho^2}}$	(B.19)
------------------------------------------------------------------------------------	--------

$\theta = \sin^{-1} \left(\sqrt{x^2 + \rho^2} \sin \omega \right)$ $\therefore \sin \omega = \frac{\sin \theta}{\sqrt{x^2 + \rho^2}}$ $= \sqrt{\frac{1 - \cos^2 \theta}{x^2 + \rho^2}}$ $\therefore \cos \omega = \cos \left(\sin^{-1} \left(\sqrt{\frac{1 - \cos^2 \theta}{x^2 + \rho^2}} \right) \right)$	(B.20)
----------------------------------------------------------------------------------------------------------------------------------------------------------------------------------------------------------------------------------------------------------------------------------------------------------------	--------

Substituting $\cos \theta = \mu$ equation (B.20) can be written as shown in equation (B.21).

$$\cos \omega = \cos \left(\sin^{-1} \left(\sqrt{\frac{1 - \mu^2}{x^2 + \rho^2}} \right) \right) \quad (\text{B.21})$$

Differentiating equation (B.21) with respect to μ gives equation (B.22).

$$\begin{aligned} \frac{d \cos \omega}{d\mu} &= -\sin \left(\sin^{-1} \left(\sqrt{\frac{1 - \mu^2}{x^2 + \rho^2}} \right) \right) \frac{1}{\sqrt{1 - \frac{1 - \mu^2}{x^2 + \rho^2}}} \times \\ &\quad \frac{1}{\sqrt{x^2 + \rho^2}} \left(\frac{1}{2} \right) (1 - \mu^2)^{-\frac{1}{2}} (-2\mu) \\ &= \frac{\mu}{\sqrt{x^2 + \rho^2} \sqrt{x^2 + \rho^2 + \mu^2 - 1}} \end{aligned} \quad (\text{B.22})$$

And the limits on the integration $\int_{\cos \omega^*}^1 d \cos \omega$ will change to the following form.

From equation (B.16) the expression for μ can be written as equation (B.23).

$$\begin{aligned} \mu &= \cos \theta \\ &= \sqrt{1 - \sin^2 \theta} \\ &= \sqrt{1 - r^2 \sin^2 \omega} \\ &= \sqrt{1 - (x^2 + \rho^2)(1 - \cos^2 \omega)} \end{aligned} \quad (\text{B.23})$$

when $\cos \omega = 1$ then $\mu = 1$ and

when $\cos \omega = \cos \omega^* = \sqrt{1 - \frac{1}{x^2 + \rho^2}}$ then $\mu = 0$

Incorporating the change of variable from ω to θ the basic equation (B.15) changes to equation (B.24). The expressions for physical parameters in equation (B.24) in terms of independent variables are given in equation (B.25). Equation (B.26) gives the parameters in equation (B.24) for which suitable models or actual measurements need to be used in terms of distance ρ and observed wavelength λ .

$$\begin{aligned}
 \mathbf{I}_O^{\text{Ra}}(\lambda, \rho \mathbf{R}_{\text{solar}}) = & \int_{-\infty}^{+\infty} \int_0^{2\pi} \int_0^1 \int_{-\infty}^{+\infty} dy \, d\varphi \, d\mu \, d(x\mathbf{R}_{\text{solar}}) \times \\
 & N_e \left(\sqrt{x^2 + \rho^2} \mathbf{R}_{\text{solar}} \right) \times Q_O^{\text{Ra}}(\mu, \varphi, \mathbf{x}) \times \\
 & \frac{\mu}{\sqrt{x^2 + \rho^2} \sqrt{x^2 + \rho^2 + \mu^2 - 1}} \times \\
 & \frac{1}{\sqrt{\pi}} \mathbf{I}(y, \mu, \varphi, \mathbf{x}) \frac{\exp[-y^2]}{1 + 2b^2\beta \frac{w}{c}}
 \end{aligned} \tag{B.24}$$

where $\mathbf{O} \equiv (//, \perp)$
// parallel to the radial plane
 \perp perpendicular to the radial plane

$$\begin{aligned}
b &= \frac{1}{\sqrt{2}} \left(1 + \sqrt{1 - \beta^2} \frac{\rho}{\sqrt{x^2 + \rho^2}} \sin \varphi + \beta \frac{\rho}{\sqrt{x^2 + \rho^2}} \right)^{1/2} \\
Q_{//}^{\text{Ra}} &= \frac{3}{16\pi} \sigma_{\text{T}} (1 + (1 - \beta^2) \sin^2 \varphi - 4(1 - b^2) b^2) \\
Q_{\perp}^{\text{Ra}} &= \frac{3}{16\pi} \sigma_{\text{T}} (1 - (1 - \beta^2) \sin^2 \varphi) \\
\beta &= \cos \left(\sin^{-1} \left(\sqrt{\frac{1 - \mu^2}{x^2 + \rho^2}} \right) \right) \\
\Delta &= \frac{q\lambda}{c} \\
q &= \sqrt{\frac{2kT}{m}} \\
I(y, \mu, \varphi, x) &= \frac{1}{\pi} \left(\frac{\text{AU}}{R_{\text{solar}}} \right)^2 \left(\frac{1 - u_1 + u_1 \mu}{1 - \frac{1}{3} u_1} \right) f
\end{aligned}$$

(B.25)

$$\begin{aligned}
u_1(\xi) &= \text{limb darkening coefficient} \\
f(\xi) &= \text{extraterrestrial solar irradiance} \\
\xi &= \frac{\lambda \left(1 + 2 \frac{q}{c} b y \right)}{1 + 2b^2 \beta \frac{w}{c}} \\
N_e(\sqrt{x^2 + \rho^2} R_{\text{solar}}) &= \text{electron density model} \\
T(\sqrt{x^2 + \rho^2} R_{\text{solar}}) &= \text{coronal temperature model} \\
W(\sqrt{x^2 + \rho^2} R_{\text{solar}}) &= \text{solar wind model}
\end{aligned}$$

(B.26)

B.6 Expression for the extraterrestrial solar irradiance $f(\xi)$

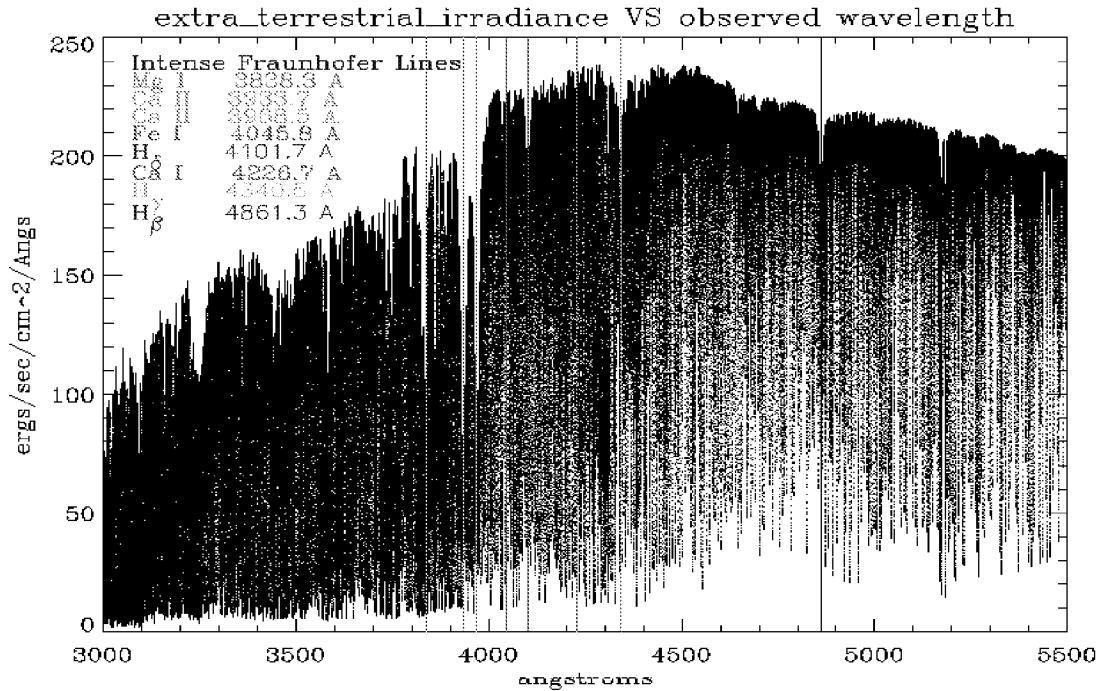


Figure (B.1). The plot of extraterrestrial solar irradiance VS wavelength obtained with a Fourier Transform Spectrometer at the McMath/Pierce Solar Telescope on Kitt Peak, Arizona.

The spectrum of extraterrestrial solar irradiance shown in figure (B.1) was downloaded from <ftp.noao.edu/fts/fluxatl>. The spectrum was then recreated in intervals of 0.0025 Angstroms through linear interpolation. The reasons for this change will be apparent in section (B.10). Here $f(\xi)$ is the wavelength dependent extraterrestrial solar irradiance with wavelength ξ measured in Angstroms.

B.7 Expressions for the limb-darkening coefficient $u_1(\xi)$

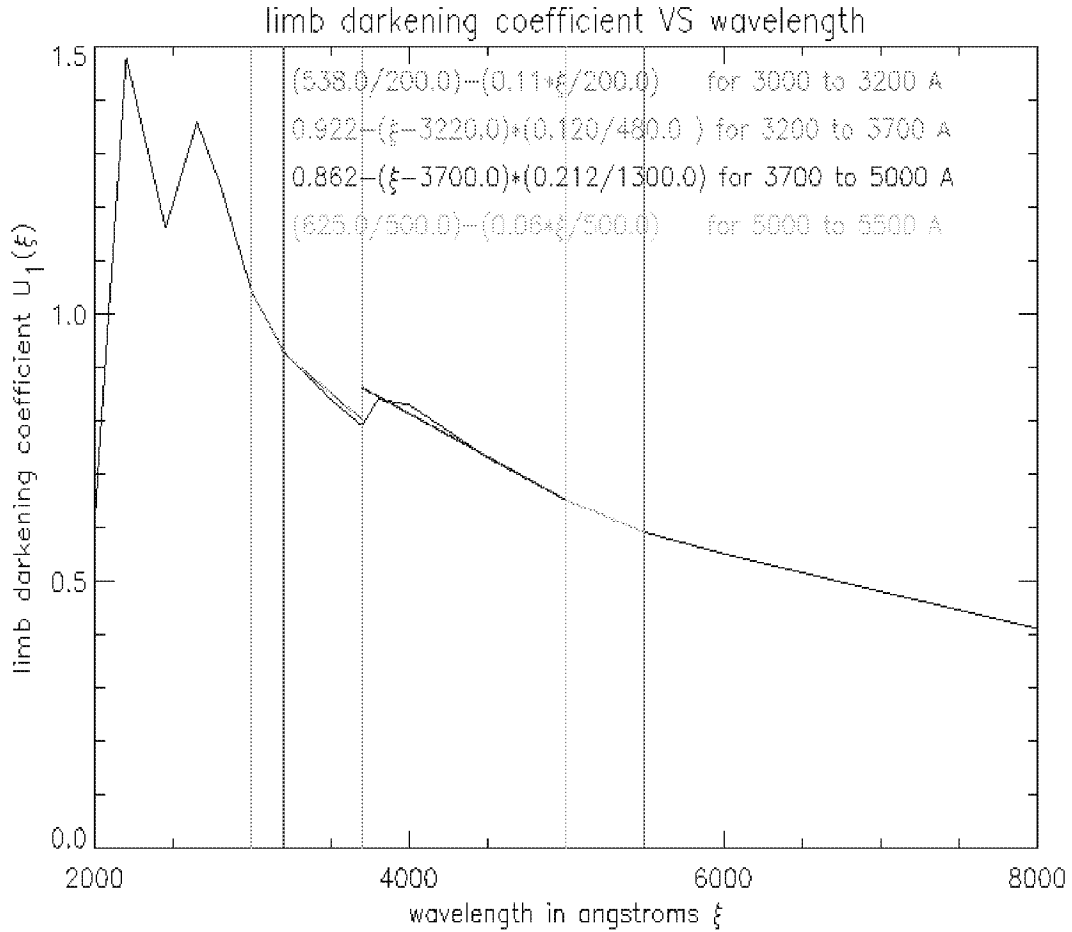


Figure (B.2). The plot of limb-darkening coefficient versus wavelength with linear approximation super imposed.

Using the wavelength dependent limb-darkening coefficient from *Astrophysical Quantities* by *Allen* the following linear fits were made for the different wavelength regions.

(1) 3000 – 3200 Angstroms

$$u_1(\xi) = \frac{538.0}{200.0} - \frac{0.11 \times \xi}{200.0} \quad (\text{B.27})$$

(2) 3200 – 3700 Angstroms

$$u_1(\xi) = 0.922 - \frac{(\xi - 3220.0) \times 0.120}{480.0} \quad (\text{B.28})$$

(3) 3700 – 5000 Angstroms

$$u_1(\xi) = 0.862 - \frac{(\xi - 3700.0) \times 0.212}{1300.0} \quad (\text{B.29})$$

(4) 5000 – 5500 Angstroms

$$u_1(\xi) = \frac{625.0}{500.0} - \frac{0.06 \times \xi}{500.0} \quad (\text{B.30})$$

In the above equations ξ is the wavelength measured in Angstroms.

B.8 Expression for the coronal electron density model $N_e(\sqrt{x^2 + \rho^2} R_{\text{solar}})$

If the eclipse takes place at sunspot maximum, the corona has an approximate circular form. This means that the coronal rays are most probably equally distributed between the polar and the equatorial regions of the Sun. Since the Sun is expected to reach sunspot maximum in the year 2000 the solar corona at the August 11, 1999 total solar eclipse will assumed to be of circular form. This assumption justifies using a radial dependent expression for the electron number density.

From the analysis of the photometric data on ten eclipses from 1905 to 1929 Baumbach (1937) deduced the following expression for the coronal electron density.

$$N_e(r) = 10^8 (0.036r^{-1.5} + 1.55r^{-6} + 2.99r^{-16}) \text{cm}^{-3} \quad (\text{B.31})$$

where $r = \sqrt{x^2 + \rho^2}$

Cram (1976) used the expression given in equation (B.32).

$$N_e(r) = 1.67 \times 10^{(4+4.04/r)} \text{cm}^{-3} \quad (\text{B.32})$$

where $r = \sqrt{x^2 + \rho^2}$

Equation (B.32) agrees within 2% in the region $1.5 < r < 2.0$ to the minimum equator model given by Van de Hulst (1950). In this code the electron density model given by equation (B.31) was used. Figure (B.3) shows the electron density plots given by equation (B.31) and equation (B.32).

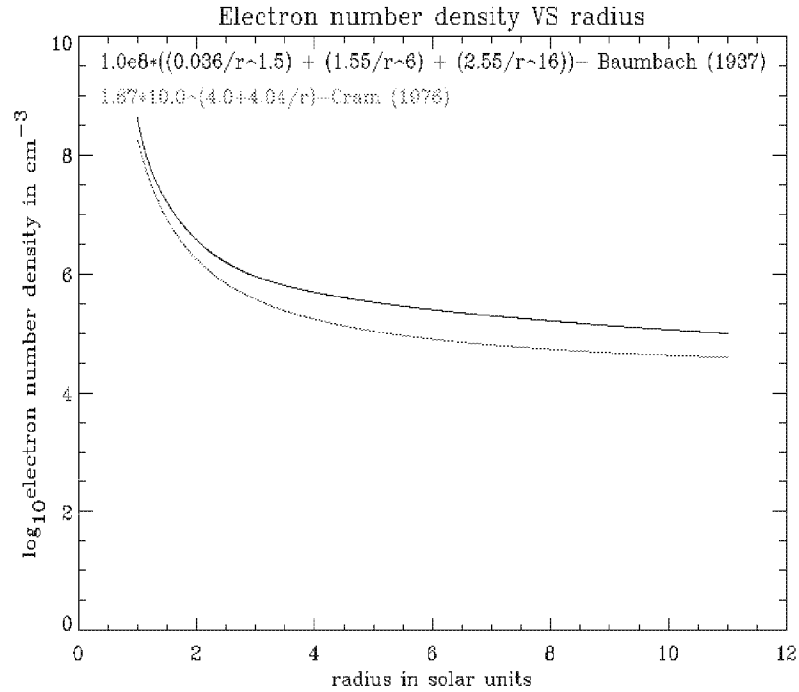


Figure (B.3). The plot of electron number density versus the radial distance from the solar surface for the two models given by equation (B.31) and equation (B.32).

B.9 Expressions for the coronal temperature model $T(\sqrt{x^2 + \rho^2 R_{\text{solar}}})$ and the solar wind model $W(\sqrt{x^2 + \rho^2 R_{\text{solar}}})$

In this code the corona is considered to be isothermal which implies that that the temperature T is a constant. As regards the solar wind W , it is considered to be radial, isotropic and constant. The idea is to construct multiple models for different combinations of temperature T and solar wind velocity W . Nevertheless, the code does not restrict from applying a coordinate dependent temperature and wind profiles that are measured independently.

B.10 Evaluation of the integrals

Rewriting equation (B.24) incorporating all of the parameters introduced in sections B.6 to B.9 give equation (B.33) and (B.24) for $\mathbf{I}_{//}^{\text{Ra}}$ and $\mathbf{I}_{\perp}^{\text{Ra}}$, respectively.

$$\begin{aligned}
 \mathbf{I}_{//}^{\text{Ra}}(\lambda, \rho) &= \text{constant} \times \int_{-\infty}^{+\infty} \int_0^{2\pi} \int_0^{+\infty} \int_0^{+\infty} dy \, d\varphi \, d\mu \, dx \times \\
 & 10^8 \times \left(0.036 \times (\sqrt{x^2 + \rho^2})^{-1.5} + 1.55 \times (\sqrt{x^2 + \rho^2})^{-6} + 2.99 \times (\sqrt{x^2 + \rho^2})^{-16} \right) \times \\
 & \frac{\mu}{\sqrt{x^2 + \rho^2} \sqrt{x^2 + \rho^2 + \mu^2 - 1}} \times \\
 & (1 + (1 - \beta^2) \sin^2 \varphi - 4(1 - b^2) b^2) \times \\
 & \frac{1 - \mathbf{u}_1(\xi) + \mu \mathbf{u}_1(\xi)}{1 - \frac{1}{3} \mathbf{u}_1(\xi)} \mathbf{f}(\xi) \times \\
 & \frac{\exp[-y^2]}{1 + 2b^2 \beta \frac{w}{c}} \quad \text{where} \\
 & \text{constant} = \frac{3 \times \sigma_T (\text{AU})^2}{16\pi^{5/2} \mathbf{R}_{\text{Solar}}} \\
 & b = \frac{1}{\sqrt{2}} \left(1 + \rho \sqrt{\frac{1 - \beta^2}{x^2 + \rho^2}} \sin \varphi + \frac{\beta \rho}{\sqrt{x^2 + \rho^2}} \right)^{1/2} \\
 & \beta = \cos \left(\sin^{-1} \left(\sqrt{\frac{1 - \mu^2}{x^2 + \rho^2}} \right) \right) \\
 & \xi = \frac{\lambda \left(1 + 2 \frac{q}{c} by \right)}{1 + 2b^2 \beta \frac{w}{c}} \quad \text{and} \quad q = \sqrt{\frac{2kT}{m}}
 \end{aligned} \tag{B.33}$$

$$\begin{aligned}
\mathbf{I}_{\perp}^{\text{Ra}}(\lambda, \rho) &= \text{constant} \times \int_{-\infty}^{+\infty} \int_0^1 \int_0^{+\infty} \int_0^{+\infty} dy \, d\varphi \, d\mu \, dx \times \\
&10^8 \times \left(0.036 \times (\sqrt{x^2 + \rho^2})^{-1.5} + 1.55 \times (\sqrt{x^2 + \rho^2})^{-6} + 2.99 \times (\sqrt{x^2 + \rho^2})^{-16} \right) \times \\
&\frac{\mu}{\sqrt{x^2 + \rho^2} \sqrt{x^2 + \rho^2 + \mu^2 - 1}} \times \\
&(1 - (1 - \beta^2) \sin^2 \varphi) \times \\
&\frac{1 - \mathbf{u}_1(\xi) + \mu \mathbf{u}_1(\xi)}{1 - \frac{1}{3} \mathbf{u}_1(\xi)} f(\xi) \times \\
&\frac{\exp[-y^2]}{1 + 2b^2 \beta \frac{w}{c}} \quad \text{where} \\
\text{constant} &= \frac{3 \times \sigma_{\text{T}} (\text{AU})^2}{16\pi^{5/2} \mathbf{R}_{\text{Solar}}} \\
b &= \frac{1}{\sqrt{2}} \left(1 + \rho \sqrt{\frac{1 - \beta^2}{x^2 + \rho^2}} \sin \varphi + \frac{\beta \rho}{\sqrt{x^2 + \rho^2}} \right)^{1/2} \\
\beta &= \cos \left(\sin^{-1} \left(\sqrt{\frac{1 - \mu^2}{x^2 + \rho^2}} \right) \right) \\
\xi &= \frac{\lambda \left(1 + 2 \frac{q}{c} by \right)}{1 + 2b^2 \beta \frac{w}{c}} \\
q &= \sqrt{\frac{2kT}{m}}
\end{aligned} \tag{B.34}$$

$\sigma_T = 6.677 \times 10^{-25} \text{ cm}^2$ $R_{\text{solar}} = 6.96 \times 10^{10} \text{ cm}$ $AU = 1.496 \times 10^{13} \text{ cm}$	(B.35)
--------------------------------------------------------------------------------------------------------------------------------------------------	--------

From equation (B.33) and equation (B.34) the total observed intensity is given by equation (B.36).

$$\mathbf{I}_{\text{Total}}(\lambda, \rho) = \mathbf{I}_{//}^{\text{Ra}}(\lambda, \rho) + \mathbf{I}_{\perp}^{\text{Ra}}(\lambda, \rho) \quad (\text{B.36})$$

1. Evaluation of the $\int_{-\infty}^{+\infty} \mathbf{A}(\mathbf{x}) d\mathbf{x}$ integral

The above integral is evaluated using a 20-point Hermite polynomial expansion as shown in equation (B.37).

$$\int_{-\infty}^{+\infty} \mathbf{A}(\mathbf{x}) d\mathbf{x} = \int_{-\infty}^{+\infty} \left(\mathbf{A}(\mathbf{x}) e^{x^2} \right) e^{-x^2} d\mathbf{x} \quad (\text{B.37})$$

$$\cong \sum_{i=1}^{20} \mathbf{A}(\mathbf{h}_i) e^{(\mathbf{h}_i)^2} \mathbf{w}_i$$

where \mathbf{h}_i and \mathbf{w}_i are the Hermite polynomials and the associated weights, respectively.

2. Evaluation of the $\int_0^{2\pi} \mathbf{B}(\varphi) d\varphi$ integral

This integral is evaluated using 20-point trapezoidal composite rule as shown in equation (B.38).

$$\int_0^{2\pi} \mathbf{B}(\varphi) d\varphi \cong \frac{\mathbf{h}_B}{2} \left(2 \times \sum_{j=0}^{20} \mathbf{B}(\varphi_j) - \mathbf{B}(\varphi_0) - \mathbf{B}(\varphi_{20}) \right) \text{ where} \quad (\text{B.38})$$

$$\mathbf{h}_B = \frac{2\pi - 0}{20}$$

$$\varphi_j = 0 + \mathbf{h}_B \times j$$

3. Evaluation of the $\int_0^1 \mathbf{C}(\mu) d\mu$ integral

This integral is evaluated using 10-point trapezoidal composite rule as shown in equation (B.39).

$$\int_0^1 \mathbf{C}(\mu) d\mu \cong \frac{\mathbf{h}_C}{2} \left(2 \times \sum_{k=0}^{10} \mathbf{C}(\mu_k) - \mathbf{C}(\mu_0) - \mathbf{C}(\mu_{10}) \right) \text{ where} \quad (\text{B.39})$$

$$\mathbf{h}_C = \frac{1 - 0}{10}$$

$$\mu_k = 0 + \mathbf{h}_C \times k$$

4. Evaluation of the $\int_{-\infty}^{+\infty} \mathbf{D}(\mathbf{y}) e^{-y^2} d\mathbf{y}$ integral

This integral is evaluated using a 12-point Hermite polynomial expansion as shown in equation (B.40).

$$\int_{-\infty}^{+\infty} \mathbf{D}(\mathbf{y}) e^{-y^2} d\mathbf{y} \cong \sum_{l=1}^{12} \mathbf{D}(\mathbf{h}_l) \mathbf{w}_l \quad (\text{B.40})$$

where \mathbf{h}_l and \mathbf{w}_l are the Hermite polynomials and the associated weights, respectively.

Consider the integral $\int_{-\infty}^{+\infty} \mathbf{D}(\mathbf{y}) e^{-y^2} d\mathbf{y}$ its \mathbf{y} dependent parameters and the expansion outlines

in equation (B.40) in equation (B.41).

$$\begin{aligned}
 \int_{-\infty}^{+\infty} \mathbf{D}(\mathbf{y}) e^{-y^2} d\mathbf{y} &\equiv \int_{-\infty}^{+\infty} \frac{\mathbf{1} - \mathbf{u}_1(\xi) + \mu \mathbf{u}_1(\xi)}{\mathbf{1} - \frac{1}{3} \mathbf{u}_1(\xi)} f(\xi) e^{-y^2} d\mathbf{y} \\
 \text{where } \xi &= \xi(\mathbf{y}) \\
 &\equiv \sum_{i=1}^{12} \frac{\mathbf{1} - \mathbf{u}_1(\xi_i) + \mu \mathbf{u}_1(\xi_i)}{\mathbf{1} - \frac{1}{3} \mathbf{u}_1(\xi_i)} f(\xi_i) w_i \\
 &= \sum_{i=1}^{12} \frac{\mathbf{1} - \mathbf{u}_1(\xi_i)}{\mathbf{1} - \frac{1}{3} \mathbf{u}_1(\xi_i)} f(\xi_i) w_i + \mu \sum_{i=1}^{12} \frac{\mathbf{u}_1(\xi_i)}{\mathbf{1} - \frac{1}{3} \mathbf{u}_1(\xi_i)} f(\xi_i) w_i
 \end{aligned}
 \tag{B.41}$$

$$\text{where } \xi_i = \frac{\lambda \left(\mathbf{1} + 2 \frac{\mathbf{q}}{\mathbf{c}} \mathbf{b} \mathbf{h}_i \right)}{\mathbf{1} + 2 \mathbf{b}^2 \beta \frac{\mathbf{w}}{\mathbf{c}}}$$

Due to the rapid intensity variations associated with the Fraunhofer lines, as evident in figure (B.1), this effect is included by taking the mean value for $f(\xi_i)$ over each interval in the Hermite polynomial expansion coefficients \mathbf{h}_i . The mean is then given by equation (B.42).

$$\begin{aligned}
& \left\langle \frac{1 - u_1(\xi_l) + \mu u_1(\xi_l)}{1 - \frac{1}{3}u_1(\xi_l)} f(\xi_l) \right\rangle \\
&= \frac{1}{\left(\frac{\xi_l + \xi_{l+1}}{2}\right) - \left(\frac{\xi_l + \xi_{l-1}}{2}\right)} \int_{\left(\frac{\xi_l + \xi_{l-1}}{2}\right)}^{\left(\frac{\xi_l + \xi_{l+1}}{2}\right)} \frac{1 - u_1(\eta) + \mu u_1(\eta)}{1 - \frac{1}{3}u_1(\eta)} f(\eta) d\eta \\
&\equiv \frac{1}{\eta_R} \int_{\eta_{lower}}^{\eta_{upper}} \frac{1 - u_1(\eta) + \mu u_1(\eta)}{1 - \frac{1}{3}u_1(\eta)} f(\eta) d\eta \\
&= \frac{1}{\eta_R} \int_{\eta_{lower}}^{\eta_{upper}} \frac{1 - u_1(\eta)}{1 - \frac{1}{3}u_1(\eta)} f(\eta) d\eta + \frac{\mu}{\eta_R} \int_{\eta_{lower}}^{\eta_{upper}} \frac{u_1(\eta)}{1 - \frac{1}{3}u_1(\eta)} f(\eta) d\eta
\end{aligned}$$

where $\eta_{upper} = \frac{\lambda - \lambda \frac{q}{c} b(h_1 + h_{l+1})}{1 + 2b^2\beta \frac{w}{c}}$

$\eta_{lower} = \frac{\lambda - \lambda \frac{q}{c} b(h_1 + h_{l-1})}{1 + 2b^2\beta \frac{w}{c}}$

$\eta_R = \eta_{upper} - \eta_{lower}$

for $l = 1, h_{l-1} = 0$
for $l = 12, h_{l+1} = 0$

(B.42)

In order to evaluate the integral in equation (B.42) the following procedure was followed in order to expedite the calculation.

1. The extraterrestrial solar irradiance spectrum was recreated in intervals of 0.0025 Angstroms (η').

2. For a given set of values for (\mathbf{x}, ϕ, μ) from the integrals $(\int d\mathbf{x}, \int d\phi, \int d\mu)$ the values $(\eta_{\text{upper}}, \eta_{\text{lower}}, \eta_{\text{R}})$ were calculated.
3. $(\eta_{\text{upper}}, \eta_{\text{lower}})$ were assigned new values $(\eta'_{\text{upper}}, \eta'_{\text{lower}})$ which are divisible by 0.0025 and closest of (η') to $(\eta_{\text{upper}}, \eta_{\text{lower}})$.
4. The values $(\mathbf{f}(\eta_{\text{upper}}), \mathbf{f}(\eta_{\text{lower}}))$ now corresponded to $(\eta'_{\text{upper}}, \eta'_{\text{lower}})$.
5. This procedure allowed the integral to be expanded in intervals of 0.0025 Angstroms.
6. Within the range of 0.0025 Angstroms the limb-darkening coefficient \mathbf{u}_1 extraterrestrial solar irradiance \mathbf{f} could be assumed to be a constant. This allows for writing equation (B.42) as shown in equation (B.43).

$$\begin{aligned}
& \frac{1}{\eta_{\text{R}}} \int_{\eta_{\text{lower}}}^{\eta_{\text{upper}}} \frac{1 - \mathbf{u}_1(\eta)}{1 - \frac{1}{3} \mathbf{u}_1(\eta)} \mathbf{f}(\eta) d\eta + \frac{\mu}{\eta_{\text{R}}} \int_{\eta_{\text{lower}}}^{\eta_{\text{upper}}} \frac{\mathbf{u}_1(\eta)}{1 - \frac{1}{3} \mathbf{u}_1(\eta)} \mathbf{f}(\eta) d\eta \\
& \cong \frac{1}{\eta_{\text{R}}} \left[\int_{\eta_{\text{lower}}}^{\eta'_{\text{lower}} + 0.0025 \text{ \AA}} \frac{1 - \mathbf{u}_1(\eta)}{1 - \frac{1}{3} \mathbf{u}_1(\eta)} \mathbf{f}(\eta) d\eta + \int_{\eta'_{\text{lower}} + 0.0025 \text{ \AA}}^{\eta'_{\text{lower}} + 0.0050 \text{ \AA}} \frac{1 - \mathbf{u}_1(\eta)}{1 - \frac{1}{3} \mathbf{u}_1(\eta)} \mathbf{f}(\eta) d\eta + \right. \\
& \quad \dots + \left. \int_{\eta'_{\text{upper}} - 0.0025 \text{ \AA}}^{\eta'_{\text{upper}}} \frac{1 - \mathbf{u}_1(\eta)}{1 - \frac{1}{3} \mathbf{u}_1(\eta)} \mathbf{f}(\eta) d\eta \right] \\
& + \frac{\mu}{\eta_{\text{R}}} \left[\int_{\eta_{\text{lower}}}^{\eta'_{\text{lower}} + 0.0025 \text{ \AA}} \frac{\mathbf{u}_1(\eta)}{1 - \frac{1}{3} \mathbf{u}_1(\eta)} \mathbf{f}(\eta) d\eta + \int_{\eta'_{\text{lower}} + 0.0025 \text{ \AA}}^{\eta'_{\text{lower}} + 0.0050 \text{ \AA}} \frac{\mathbf{u}_1(\eta)}{1 - \frac{1}{3} \mathbf{u}_1(\eta)} \mathbf{f}(\eta) d\eta + \right. \\
& \quad \dots + \left. \int_{\eta'_{\text{upper}} - 0.0025 \text{ \AA}}^{\eta'_{\text{upper}}} \frac{\mathbf{u}_1(\eta)}{1 - \frac{1}{3} \mathbf{u}_1(\eta)} \mathbf{f}(\eta) d\eta \right]
\end{aligned} \tag{B.43}$$

Now to elaborate on the method, by which the integration is expedited, consider the following table. Columns **1** and **4** are from section **B.6** and columns **2** and **3** are from section **B.7**. Here **T** is divisible by 0.00025.

Table (B.1). The dependence of the extraterrestrial solar irradiance and the limb-darkening functions with the wavelength.. The columns 1 and 4 are from section (B.6) and columns 2 and 3 are from section (B.7).

Wavelength η in Nanometers (nm)	$\frac{1 - u_1(\eta)}{1 - \frac{1}{3}u_1(\eta)}$	$\frac{u_1(\eta)}{1 - \frac{1}{3}u_1(\eta)}$	Extraterrestrial Solar irradiance $f(\eta)$
T	A1	B1	C1
T+0.00025	A2	B2	C2
T+0.00050	A3	B3	C3
T+0.00075	A4	B4	C4
T+0.00100	A5	B5	C5
T+0.00125	A6	B6	C6
T+0.00150	A7	B7	C7
T+0.00175	A8	B8	C8
T+0.00200	A9	B9	C9
continued	continued	continued	continued

In the code T is 300.00025 nm and then increases in intervals of 0.00025 nm to 550.00000 nm.

Now create a new table with each row reflecting the cumulative sum of table (B.1) for the columns 2, 3 and 4.

Table (B.2). Cumulative values of the columns 2,3 and 4 of table (B.1).

T	A1*C1	B1*C1	C1
T+0.00025	A2*C2	B2*C2	C2
T+0.00050	A3*C3	B3*C3	C3
continued	continued	continued	continued

In the code the following format is used, where columns 2 and 3 are multiplied by column 4 of table (B.2).

Table (B.3). Multiplying column 4 of table (B.2) with column 2 and 3 of table (B.2). This is the format of the table used by the code.

T	A1*C1	B1*C1
T+0.00025	(A1*C1)+(A2*C2)	(B1*C1)+(B2*C2)
T+0.00050	(A1*C1)+(A2*C2)+ (A3*C3)	(B1*C1)+(B2*C2)+ (B3*C3)
T+0.00075	(A1*C1)+(A2*C2)+ (A3*C3)+ (A4*C4)	(B1*C1)+(B2*C2)+ (B3*C3)+ (B4*C4)
continued	continued	continued

Going back to equation (B.43) the integrals could be written as a summation, as shown in equation (B.44). Figure (B.4) illustrates the evaluation of the first integral of equation (B.44) where the integration under each interval is approximated as the area under the square. This procedure is justified on ground of the very small interval.

$$\begin{aligned}
 & \frac{1}{\eta_R} \int_{\eta_{\text{lower}}}^{\eta_{\text{upper}}} \frac{1 - u_1(\eta)}{1 - \frac{1}{3}u_1(\eta)} f(\eta) d\eta + \frac{\mu}{\eta_R} \int_{\eta_{\text{lower}}}^{\eta_{\text{upper}}} \frac{u_1(\eta)}{1 - \frac{1}{3}u_1(\eta)} f(\eta) d\eta \\
 & \cong \frac{\Delta\eta}{\eta_R} \sum_{\substack{\eta = \eta'_{\text{lower}} \\ \text{in intervals} \\ \text{of } 0.0025\text{\AA}}}^{\eta'_{\text{upper}}} \frac{1 - u_1(\eta)}{1 - \frac{1}{3}u_1(\eta)} f(\eta) + \frac{\mu\Delta\eta}{\eta_R} \sum_{\substack{\eta = \eta'_{\text{lower}} \\ \text{in intervals} \\ \text{of } 0.0025\text{\AA}}}^{\eta'_{\text{upper}}} \frac{u_1(\eta)}{1 - \frac{1}{3}u_1(\eta)} f(\eta)
 \end{aligned} \tag{B.44}$$

where $\Delta\eta = 0.0025\text{\AA}$
 $\eta_R = \eta'_{\text{upper}} - \eta'_{\text{lower}}$

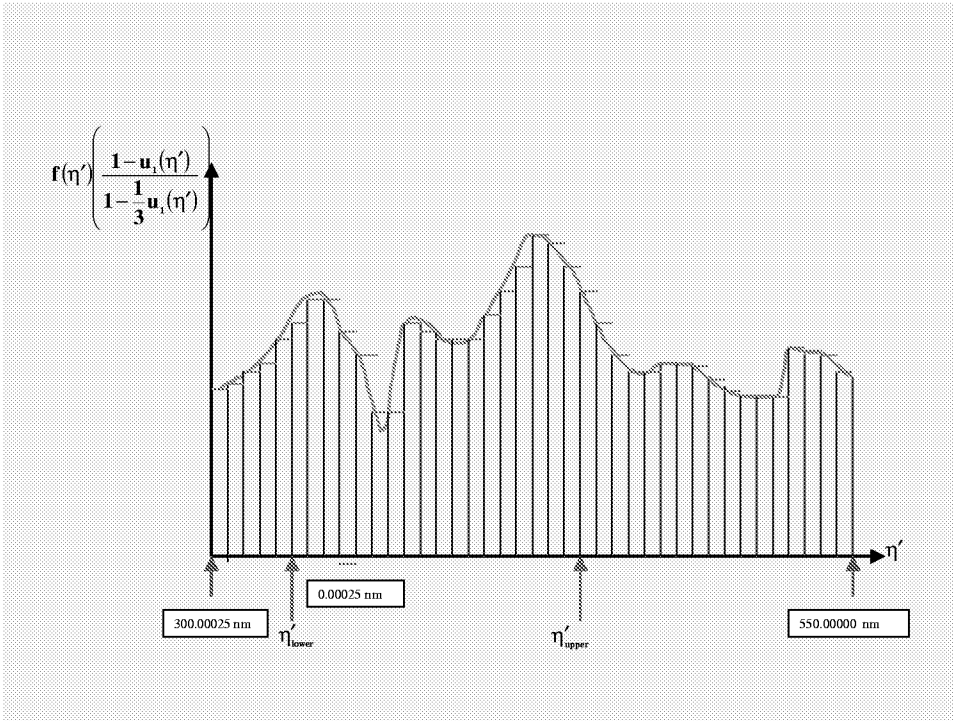


Figure (B.4). Illustrating the integration procedure of the first integral in equation (B.44).

Taking the cumulative value of the parameter reflected on the y-axis of figure (B.4) would give the following, as shown in figure (B.5).

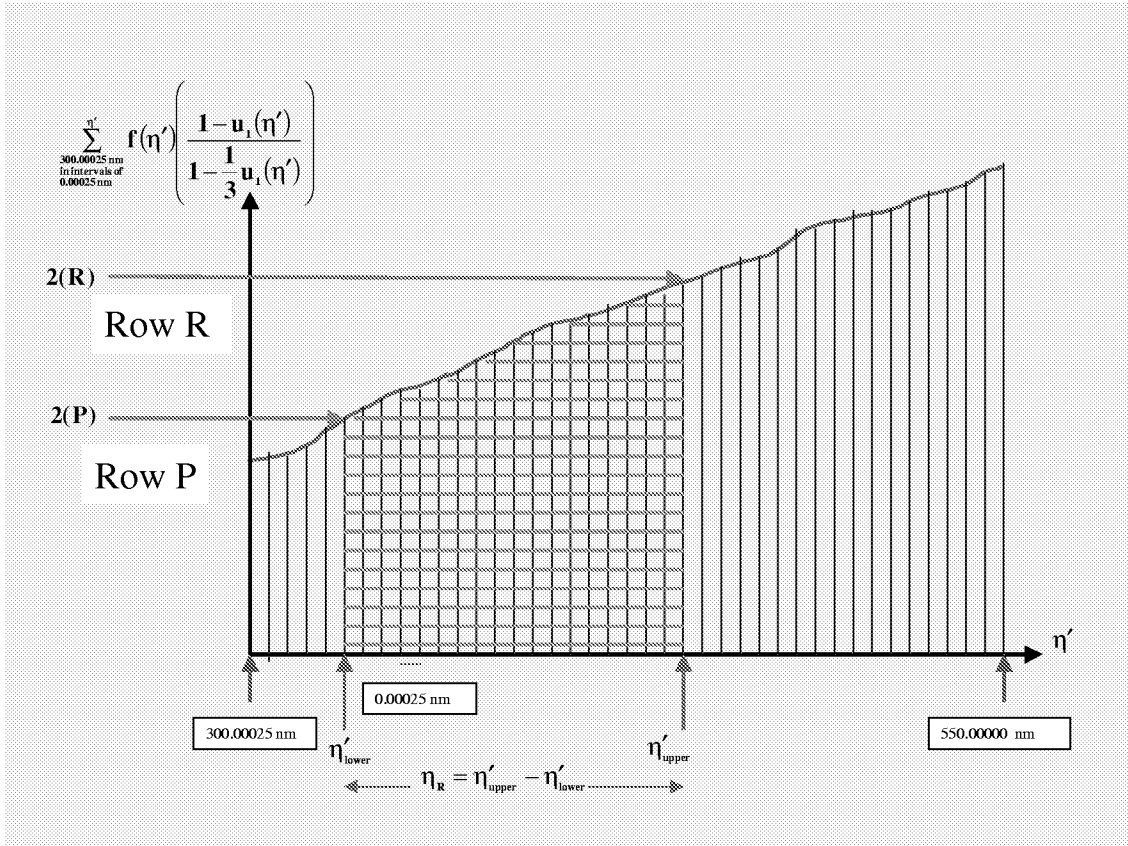


Figure (B.5). Plot of the cumulative y-axis values of figure (B.4) against the wavelength η' .

The same procedure as above could be performed for the second integral in equation (B.44) too.

In terms of expediting the calculation of the integral presented in equation (B.42), equation (B.44) allows the code do the calculation in two easy steps in conjunction with table (B.3) and illustrated by figure (B.5) for the first integral, as follows.

1. Find the corresponding row numbers, say, rows (**R,P**), respectively, which equal the values $(\eta'_{\text{upper}}, \eta'_{\text{lower}})$ in column **1** of table (B.3) and as depicted in figure (B.5).
2. Find the values in columns **2** and **3** corresponding to the rows (**R,P**) in table (B.3) and as shown by the arrows cutting across the y-axis in figure (B.5).
3. Now calculate $[(2(\mathbf{R}) - 2(\mathbf{P})) + \mu(3(\mathbf{R}) - 3(\mathbf{P}))] \times \frac{\Delta\eta}{\eta_{\mathbf{R}}}$ where the numbers correspond to the column numbers. The first part $2(\mathbf{R}) - 2(\mathbf{P})$ corresponds to the first integral in equation (B.44) and the second part $3(\mathbf{R}) - 3(\mathbf{P})$ corresponds to the second integral in equation (B.44). In figure (B.5), $\frac{(2(\mathbf{R}) - 2(\mathbf{P}))}{\eta_{\mathbf{R}}}$ evaluates the first integral in equation (B.44).

B.11 The symbols used in the code

The following symbols have been used in the code.

x	\rightarrow	x
φ	\rightarrow	y
μ	\rightarrow	z
η_{upper}	\rightarrow	cetaU
η_{lower}	\rightarrow	cetaL
η'_{upper}	\rightarrow	a(0,u)
η'_{lower}	\rightarrow	a(0,t)
h_1	\rightarrow	hermite_12(l)
w_1	\rightarrow	weights_12(l)
h_i	\rightarrow	hermite_20(i)
w_i	\rightarrow	weights_20(i)
b	\rightarrow	bb
ρ	\rightarrow	rho
λ	\rightarrow	lambda

(B.45)

In the code table (B.3) is given by **3000_5500_cum_irradiance.dat**

From equation (B.2) the following relationships could be derived.

$$\begin{aligned}
 \text{angle_1} &\equiv \sin(\omega) \\
 &= \frac{\sin(\theta)}{\sqrt{x^2 + \rho^2}} \\
 &= \frac{\sin(\cos^{-1}(\cos\theta))}{\sqrt{x^2 + \rho^2}} \\
 &= \frac{\sin(\cos^{-1}(\mu))}{\sqrt{x^2 + \rho^2}}
 \end{aligned}
 \tag{B.46}$$

$$\begin{aligned}
 \text{angle_2} &\equiv \cos(w) \\
 &= \cos(\sin^{-1}(\text{angle_1}))
 \end{aligned}
 \tag{B.47}$$

$$\begin{aligned}
 \text{angle_3} &\equiv \cos(\chi) \\
 &= \frac{x}{\sqrt{x^2 + \rho^2}}
 \end{aligned}
 \tag{B.48}$$

$$\begin{aligned}
 \text{angle_4} &\equiv \sin(\chi) \\
 &= \sin(\cos^{-1}(\text{angle_3}))
 \end{aligned}
 \tag{B.49}$$

$$\begin{aligned}
 \text{angle_5} &\equiv \cos(\pi - \Theta) \\
 &= \cos(\omega)\cos(\chi) + \sin(\omega)\sin(\chi)\sin(\phi) \\
 &= \text{angle_2} \times \text{angle_3} + \text{angle_1} \times \text{angle_4} \times \sin(y)
 \end{aligned}
 \tag{B.50}$$

$$\begin{aligned}
 \text{angle_6} &\equiv (\pi - \Theta) \\
 &= \cos^{-1}(\text{angle_5})
 \end{aligned}
 \tag{B.51}$$

$$\begin{aligned}
\mathbf{bb} &\equiv \mathbf{b} \\
&= \cos(\gamma) \\
&= \cos\left(\frac{\pi - \Theta}{2}\right) \\
&= \cos\left(\frac{\text{angle_6}}{2}\right)
\end{aligned}
\tag{B.52}$$

From equation (B.16) the following relationships could be derived.

$$\begin{aligned}
\mathbf{cc_t} &\equiv \frac{16\pi}{3\sigma_T} Q_{\perp}^{\text{Ra}} \\
&= 1.0 - \sin^2(\varphi)\sin^2(\omega) \\
&= 1.0 - \sin^2(y)(\text{angle_1})^2
\end{aligned}
\tag{B.53}$$

$$\begin{aligned}
\mathbf{cc_r} &\equiv \frac{16\pi}{3\sigma_T} Q_{\parallel}^{\text{Ra}} \\
&= 1.0 + \sin^2(\varphi)\sin^2(\omega) - 4(1 - \mathbf{b}^2)\mathbf{b}^2 \\
&= 1.0 + \sin^2(y)(\text{angle_1})^2 - 4(1 - (\mathbf{bb})^2)(\mathbf{bb})^2
\end{aligned}
\tag{B.54}$$

B.12 The IDL code

The following is the code written in IDL where (;) is a comment symbol and (\$) a command continuation symbol.

```
;README
;DECIDE ON THE RADIAL WIND VELOCITY IN KM\SEC
;DECIDE ON THE ISOTHERMAL CORONAL TEMPERATURE IN MK
;DECIDE ON THE VALUES FOR RHO IN SOLAR RADIUS
;000.0 0.50 1.10
;400.0 2.00 1.30
;800.0 1.50 1.40
;ENTER THE ABOVE INFORMATION IN BATCH_FILE.PRO

;COMPILE ECLIPSE_SIMULATION.PRO
;RUN ECLIPSE_SIMULATION.PRO

;THE DATA WILL BE STORED AS
;'ES_w000.0_T0.50_r1.10.dat'
;'ES_w400.0_T2.00_r1.30.dat'
;'ES_w800.0_T1.50_r1.40.dat'

;CALULATING AVERAGE INTENSITY IN THE REGION [cetaU,cetaL]
function KURUCZ_TABLE,a,z,cetaU,cetaL

u=long(round(((double(cetaU)-300.00025d0)/0.00025d0)));a(0,0)=300.00025
t=long(round(((double(cetaL)-300.00025d0)/0.00025d0)));a(0,0)=300.00025
interval=a(0,u)-a(0,t)
irradiance=((a(1,u)-a(1,t))+z*(a(2,u)-a(2,t)))*0.00025d0/interva
;microwatts/cm squared/nm
return,irradiance ;microwatts/cm squared/nm
end

;CALCULATE FOURTH_INTEGRAL PARAMETRS AND THE VALUE
function calculate_fourth_integral_value ,a,lambda,rho,hermite_12,weights_12,x,y,z,w,T
q =5508.0*sqrt(T) ;thermal electron velocity in km/sec
c =3.0d5 ;velocity of light in km/sec
final_sum_4=dblarr(2,1)
angle_1=sin(acos(z))/sqrt(x^2+rho^2) ;sin(omega)
angle_2=cos(asin(angle_1)) ;cos(omega)
```

```

angle_3=x/sqrt(x^2+rho^2)           ;cos(chi)
angle_4=sin(acos(angle_3))         ;sin(chi)

angle_5=angle_2*angle_3 + angle_1*angle_4*sin(y)
angle_6=acos(angle_5)

r=sqrt(x^2+rho^2)                   ;radius
aa=1.0d8*(0.036/(r^1.5) + 1.55/(r^6) + 2.55/(r^16)) ;Baumbach model
bb=cos(angle_6/2.0)                 ;cos(gamma)
cc_t=1.0-(sin(y)^2)*(angle_1^2)     ;tangential
cc_r=1.0+(sin(y)^2)*(angle_1^2)-4.0*(1.0-bb^2)*(bb^2);radial
dd=(1.0*z)/(sqrt(x^2+rho^2)*sqrt(x^2+rho^2+z^2-1.0))
;changing d(cos(omega))to d(mu)
ee=1.0+2.0*bb^2*angle_2*(w/c)      ;wind component

N=11; Nth order hermite polynomial expansion is used
sum_i_tangential=0.0
sum_i_radial =0.0

for i=0,N do begin; first_loop

  if (i eq 0 ) then begin
    cetaL=(lambda-lambda*(q/c)*bb*hermite_12(i))/ee
    ;nanometers
  end else if (i ne 0) then begin
    cetaL=(lambda-lambda*(q/c)*bb*(hermite_12(i)+hermite_12(i-1)))/ee
    ;nanometers
  endif

  if (i eq 11) then begin
    cetaU=(lambda-lambda*(q/c)*bb*hermite_12(i))/ee
    ;nanometers
  end else if (i ne 11) then begin
    cetaU=(lambda-lambda*(q/c)*bb*(hermite_12(i)+hermite_12(i+1)))/ee
    ;nanometers
  endif

  if (((cetaU or cetaL) lt 300.00025d0) or ((cetaU or cetaL) gt 550.00000d0)) then begin
    final_sum_4(0,0)=99999999999.9999
    final_sum_4(1,0)=99999999999.9999
    goto,terminate_4
  endif
endif

```

**;CALCULATING THE AVERAGE INTENSITY CORRESPONDING TO
;[cetaU,cetaL]**

```
irradiance=KURUCZ_TABLE(a,z,cetaU,cetaL) ;microwatts/cm squared/nm
FC=irradiance*1.0d-7 ;W/cm squared/Angstroms
```

```
sum_i_tangential=sum_i_tangential+weights_12(i)*(FC)
sum_i_radial =sum_i_radial +weights_12(i)*(FC)
```

```
endfor ;loop_i
```

```
final_sum_4(0,0)=sum_i_tangential*aa*cc_t*dd*(1.0/ee)
final_sum_4(1,0)= sum_i_radial*aa*cc_r*dd*(1.0/ee)
terminate_4:
return,final_sum_4
end
```

;CALCULATE THIRD INTEGRAL PARAMETRS AND THE VALUE

function calculate_third_integral_value ,a,lambda,rho,hermite_12,weights_12,x,y,w,T

;THIRD INTEGRAL BOUNDS

```
a3=0.0
b3=1.0
n3=10.0
h3=(b3-a3)/n3
f3=fix(n3)
sum_z_t=dblarr(f3+1)
sum_z_r=dblarr(f3+1)
total_sum_z_t=0.0
total_sum_z_r=0.0
final_sum_3=dblarr(2,1)
```

```
for r=0,f3 do begin
z=a3+r*h3 ;mu=cos(theta)
final_sum_4=calculate_fourth_integral_value $
(a,lambda,rho,hermite_12,weights_12,x,y,z,w,T)
if ( final_sum_4(0,0) eq 99999999999.9999) then begin
final_sum_3=final_sum_4
goto, terminate_3
endif
sum_z_t(r)=final_sum_4(0,0)
total_sum_z_t=total_sum_z_t+final_sum_4(0,0)
```

```

sum_z_r(r)=final_sum_4(1,0)
total_sum_z_r=total_sum_z_r+final_sum_4(1,0)
endfor

final_sum_3(0,0)=(h3/2.0)*(2.0*total_sum_z_t-sum_z_t(0)-sum_z_t(n3))
final_sum_3(1,0)=(h3/2.0)*(2.0*total_sum_z_r-sum_z_r(0)-sum_z_r(n3))
terminate_3:
return, final_sum_3
end

;CALCULATE SECOND INTEGRAL PARAMETERS AND THE VALUE
function calculate_second_integral_value ,a,lambda,rho,hermite_12,weights_12,x,w,T

;SECOND INTEGRAL BOUNDS
a2=0.0
b2=2.0*pi
n2=20.0
h2=(b2-a2)/n2
f2=fix(n2)
sum_y_t=dblarr(f2+1)
sum_y_r=dblarr(f2+1)
total_sum_y_t=0.0
total_sum_y_r=0.0
final_sum_2=dblarr(2,1)

for v=0,f2 do begin
y=a2+v*h2 ; in radians
final_sum_3=calculate_third_integral_value $
(a,lambda,rho,hermite_12,weights_12,x,y,w,T)
if ( final_sum_3(0,0) eq 999999999999.9999) then begin
final_sum_2=final_sum_3
goto, terminate_2
endif
sum_y_t(v)=final_sum_3(0,0)
total_sum_y_t=total_sum_y_t+final_sum_3(0,0)
sum_y_r(v)=final_sum_3(1,0)
total_sum_y_r=total_sum_y_r+final_sum_3(1,0)

endfor

final_sum_2(0,0)=(h2/2.0)*(2.0*total_sum_y_t-sum_y_t(0)-sum_y_t(n2))
final_sum_2(1,0)=(h2/2.0)*(2.0*total_sum_y_r-sum_y_r(0)-sum_y_r(n2))
terminate_2:

```

```

return, final_sum_2
end

```

;CALCULATE FIRST INTEGRAL PARAMETERS AND THE VALUE

```

functioncalculate_first_integral_value $
,a,lambda,rho,hermite_12,weights_12,hermite_20,weights_20,w,T

```

;FIRST INTEGRAL USING HERMITE POLYNOMIALS

```

n1=19
sum_x_t=dblarr(n1+1)
total_sum_x_t=0.0
sum_x_r=dblarr(n1+1)
total_sum_x_r=0.0
intensity=dblarr(2,1)

for h= 0,n1 do begin
x=hermite_20(h)
final_sum_2=calculate_second_integral_value $
(a,lambda,rho,hermite_12,weights_12,x,w,T)
if (final_sum_2(0,0) eq 999999999999.9999) then begin
intensity=final_sum_2
goto, terminate_1
endif
sum_x_t(h)=final_sum_2(0,0)*weights_20(h)*exp(x*x)
total_sum_x_t=total_sum_x_t+sum_x_t(h)
sum_x_r(h)=final_sum_2(1,0)*weights_20(h)*exp(x*x)
total_sum_x_r=total_sum_x_r+sum_x_r(h)
endfor

```

```

sigma=6.677E-25 ;Thomson Scattering Cross Section cm squared
AU=1.49597870E+13 ;cm-symbol D in CRAM
solar_radius=6.96E+10 ;cm-symbol R in CRAM
constant=(3.0*sigma*(AU)^2.0)/(16.0*solar_radius*(!pi)^(2.5))

```

```

intensity(0,0)=constant*total_sum_x_t ;Watts/cm squared/Angstroms/steradians
intensity(1,0)=constant*total_sum_x_r ;Watts/cm squared/Angstroms/steradians

```

```

terminate_1:
return,intensity
end

```

```

print,'starting time ', systime(0)

```

**;FILES TO BE READ
;READING THE KURUCZ EXTRATERRESTRIAL IRRADIANCE AT 0.00025A
;INTERVALS FROM 3000A TO 5500A**

```
a=dblarr(3,10000001)
openr,2,'3000_5500_cum_irradiance.dat'
readf,2,a
close,2
```

**;READING THE ROOTS OF 12TH ORDER HERMITE POLYNOMIALS
;HANDBOOK OF TABLES OF MATHEMATICS:SELBY 3RD EDITION PAGE
;843**

```
hermite_12=dblarr(1,12)
openr,3,'hermite_12_roots.dat'
readf,3,hermite_12
close,3
```

**;READING THE WEIGHTS OF 12TH ORDER HERMITE POLYNOMIALS
;HANDBOOK OF TABLES OF MATHEMATICS:SELBY 3RD EDITION PAGE
;843**

```
weights_12=dblarr(1,12)
openr,4,'hermite_12_weights.dat'
readf,4,weights_12
close,4
```

**;READING THE ROOTS OF 20TH ORDER HERMITE POLYNOMIALS
;HANDBOOK OF MATHEMATIC FUNCTIONS EDITED BY M.ABRAMOWITZ
;AND L.A. STEGUN PAGE 924**

```
hermite_20=dblarr(1,20)
openr,5,'hermite_20_roots.dat'
readf,5,hermite_20
close,5
```

```

;READING THE WEIGHTS OF 20TH ORDER HERMITE POLYNOMIALS
;HANDBOOK OF MATHEMATIC FUNCTIONS EDITED BY M.ABRAMOWITZ
;AND L.A. STEGUN PAGE 924

```

```

weights_20=dblarr(1,20)
openr,6,'hermite_20_weights.dat'
readf,6,weights_20
close,6

```

```

;READING THE BATCH_FILE.PRO
;THIS FILE CONTAINS THE WIND,TEMPERATURE AND RHO VALUES

```

```

data=read_ascii('batch_file.pro',$
comment_symbol='xxx.x',data_start=1)
data_elements=n_elements(data.field1)

counter=(data_elements/3)-1

for j=0,counter do begin

    wind= data.field1(3*j+0);wind in km\sec
    temp= data.field1(3*j+1);Temperature in MK
    rhoo= data.field1(3*j+2);rho in solar radius

    str_w=string(wind)
    parts=str_sep(str_w,',')
    w1=parts[0]
    w2=strmid(parts[1],0,1)

    str_t=string(temp)
    parts=str_sep(str_t,',')
    t1=parts[0]
    t2=strmid(parts[1],0,2)

    str_r=string(rhoo)
    parts=str_sep(str_r,',')
    r1=parts[0]
    r2=strmid(parts[1],0,2)

    w=double(wind)
    T=double(temp)
    rho=double(rhoo)
    print,'wind = ',w,' km\sec temp = ',temp,' MK $

```

```
rho = ',rhoo,' solar radius'
```

;RECORDING THE OUTPUT

```
openw,9,'ES_w'+trim(w1,'(i3.3)')+'. '+trim(w2,'(i1.1)')+ '_T'$  
+trim(t1,'(i1.1)')+'. '+trim(t2,'(i2.2)')+ '_r'+trim(r1,'(i1.1)')+ '$'  
+trim(r2,'(i2.2)')+ '.dat'
```

```
for r=0,1000 do begin ;370.0 nm to 470.0 nm  
lambda=370.0d0 + r*0.1d0 ;nano meters
```

```
intensity=calculate_first_integral_value $  
    (a,lambda,rho,hermite_12,weights_12,hermite_20,weights_20,w,T)  
if (intensity(0,0) eq 999999999999.9999) then begin  
print,'intensity(0,0) = 999999999999.9999 for $  
        lambda = ',lambda  
goto, intensity_out_of_range  
endif
```

```
total_intensity=intensity(0,0)+intensity(1,0);Watts/cm squared/Angstroms/steradians
```

```
print,'lambda= ',lambda*10.0,' Angstroms','$  
intensity = ',total_intensity*1.0E+7,$  
    ' ergs/sec/cm squared/Angs/steradians'  
;print,'time = ',systeme(0)  
printf, 9, format='(4E15.5)',lambda*10.0,total_intensity,intensity(0,0),$  
intensity(1,0)  
flush, 9
```

```
intensity_out_of_range:  
endfor ; the r loop for intensity
```

```
close, 9  
endfor ; the j loop for batch_file  
print,'ending time ',systeme(0)  
end
```

An example of the input data information given in BATCHFILE.PRO

Table (B.4). The format of the input information on the wind velocity in km/sec, isothermal temperature in MK and the distance to the line of sight in SR.

Wind(km/sec)	Temperature(MK)	RHO(SR)
400.0	1.50	1.10
300.0	0.50	1.50
continued	continued	continued
XXX.X	XX.X	XX.X

Appendix C

A STREAMER MODEL

C.1 The effects due to streamers

Due to the structural nature of the solar corona it is important to consider the effects on the K-corona due to coronal inhomogeneities. In this regard consider a streamer imbedded in a spherically symmetric isothermal corona. The model streamer considered has the following structure as depicted in figure (C.1). The streamer is of thickness \mathbf{d} and the extremes of the streamer, namely, \mathbf{RT} and \mathbf{UV} are equidistant from the solar center \mathbf{C} and are inclined at an angle ε to the plane of the solar limb. Within the streamer the electron number density is enhanced by a factor \mathbf{f}_s and the thermal electron temperature is \mathbf{T}_s . From figure (C.1) the expressions for \mathbf{X}_1 (=FV) and \mathbf{X}_2 (=FT) are given by equation (C.1).

$$\boxed{\begin{aligned} \mathbf{x}_1 &= \rho \times \tan(\varepsilon) - \frac{\mathbf{d}/2}{\cos(\varepsilon)} \text{ and} \\ \mathbf{x}_2 &= \rho \times \tan(\varepsilon) + \frac{\mathbf{d}/2}{\cos(\varepsilon)} \end{aligned}} \quad (\text{C.1})$$

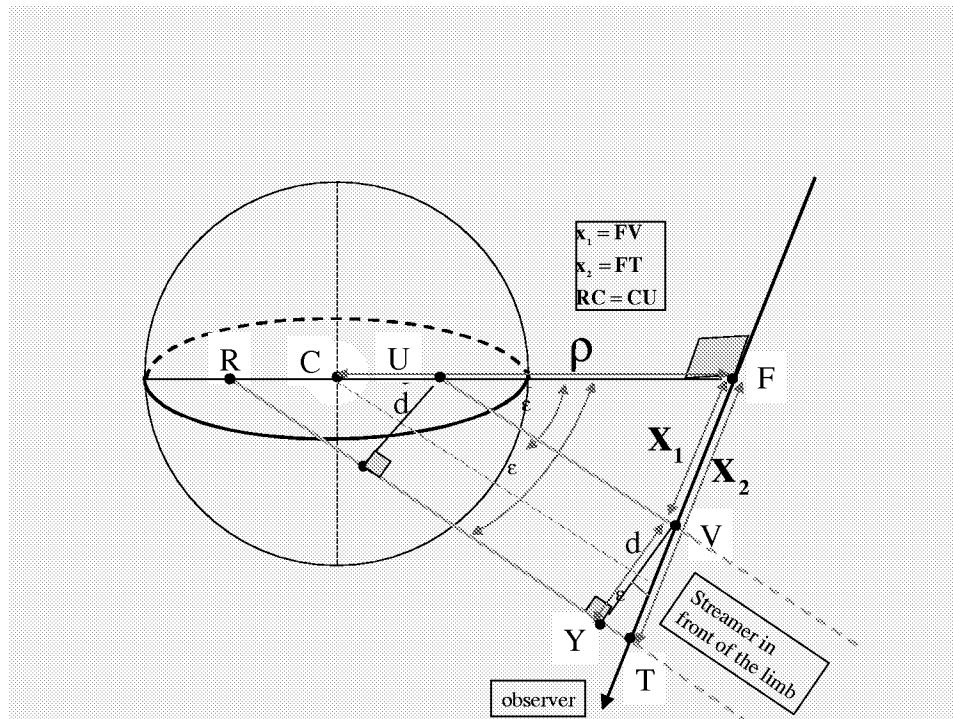


Figure (C.1). Model streamer of thickness d in front of the solar limb with an electron density enhancement by a factor f_s and thermal electron temperature T_s .

And in the streamer model considered the electron density is enhanced by a factor f_s in the region between x_2 and x_1 along the line of sight. The incorporation of the effect due to the streamer in the code, as described in section (B.12), is as follows.

1. For specified values for d, ρ and ϵ calculate x_1 and x_2 .
2. In the x -integration (integration along the line of sight) if x lies between and including x_1 and x_2 then multiply the electron number density by a factor f_s and substitute T_s for T where f_s and T_s are specified.

3. Perform the x -integration by trapezoidal composite rule instead of the Hermite polynomial expansion. This was found to be necessary in order to pick up sufficient x -values in the region $[x_1 \text{ and } x_2]$. Since the Hermite polynomial expansion considered in the code is of twentieth order there may not be sometimes any x -values in the region $[x_1 \text{ and } x_2]$.
4. The x -integration is substituted by the following commands

;CALCULATE FIRST INTEGRAL PARAMETERS AND THE VALUE

```
function calculate_first_integral_value $ ,a,lambda,rho,hermite_12,weights_12,w,T
```

```
;FIRST INTEGRAL BOUNDS
```

```
a1=-6.0 ;lower bound at - 6.0 solar radii
```

```
b1=+6.0 ;upper bound at +6.0 solar radii
```

```
n1=120.0 ;region divided into 120 equal intervals
```

```
h1=(b1-a1)/n1
```

```
f1=fix(n1)
```

```
sum_x_t=dblarr(f1+1)
```

```
sum_x_r=dblarr(f1+1)
```

```
total_sum_x_t=0.0
```

```
total_sum_x_r=0.0
```

```
intensity=dblarr(2,1)
```

```

for h=0,f1 do begin
  x=a1+h*h1
  final_sum_2=calculate_second_integral_value $
    (a,lambda,rho,hermite_12,weights_12,x,w,T)
  if (final_sum_2(0,0) eq 999999999999.9999) then begin
    intensity=final_sum_2
    goto, terminate_1
  endif
  sum_x_t(h)=final_sum_2(0,0)
  total_sum_x_t=total_sum_x_t+sum_x_t(h)
  sum_x_r(h)=final_sum_2(1,0)
  total_sum_x_r=total_sum_x_r+sum_x_r(h)
endfor

```

Although x-integration need to be considered in the interval $[-\infty, +\infty]$ it is sufficient to restrict the integration to $[-6.0, +6.0]$ solar radii due to the rapid falloff in the electron number density.

Consider a streamer model as depicted by figure (C.1) with a streamer width (**d**) of 0.5 solar radii, density enhancement factor (**f_s**) of 4.0 within the streamer and assuming the thermal electron temperature (**T_s**) within the streamer to be equal to isothermal coronal temperature (**T**) for the rest of the corona. Figure (C.2) shows the effect of streamers, at angles (**ε**) **-45.0** degrees (front of the limb) and **+45.0** degrees (behind the limb) to the limb of the solar corona, on the K-coronal spectrum.

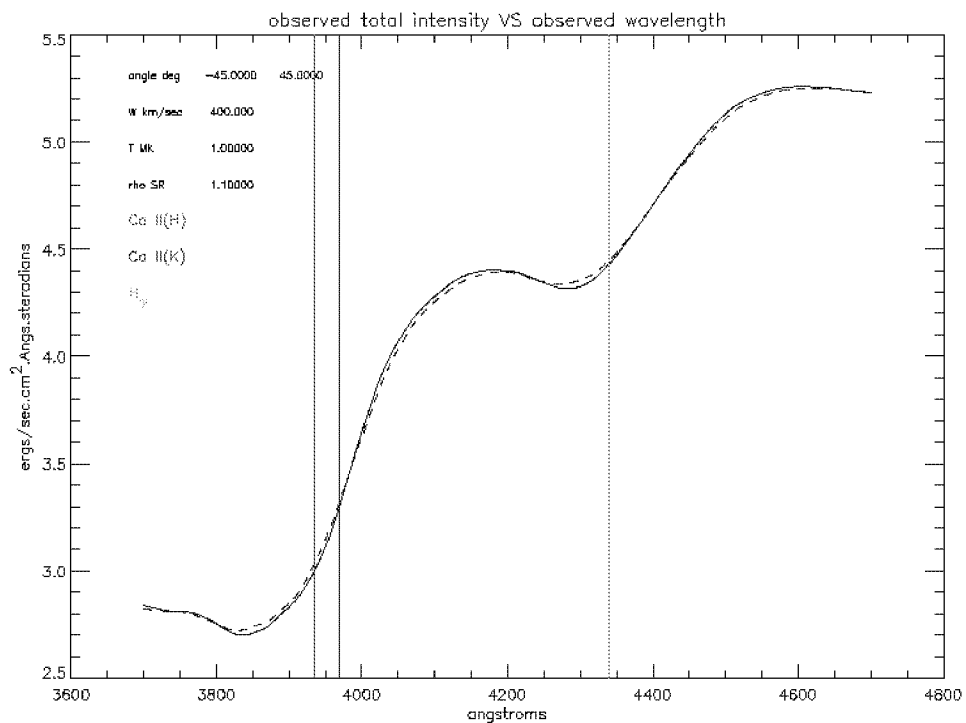


Figure (C.2). Plot to show the effect of streamers on the K-coronal spectrum with $d=0.5$ SR, $f_s=4.0$, $T_s=T=1.0$ MK and at angles $\epsilon = -45.0$ and $+45.0$ degrees.

Although the two streamers considered in figure (C.2) are symmetric about the plane of the solar limb the asymmetry in the two theoretical spectra is due to the fact that the streamers scatter through different angles in reaching the observer. Figure (C.3) illustrates this point.

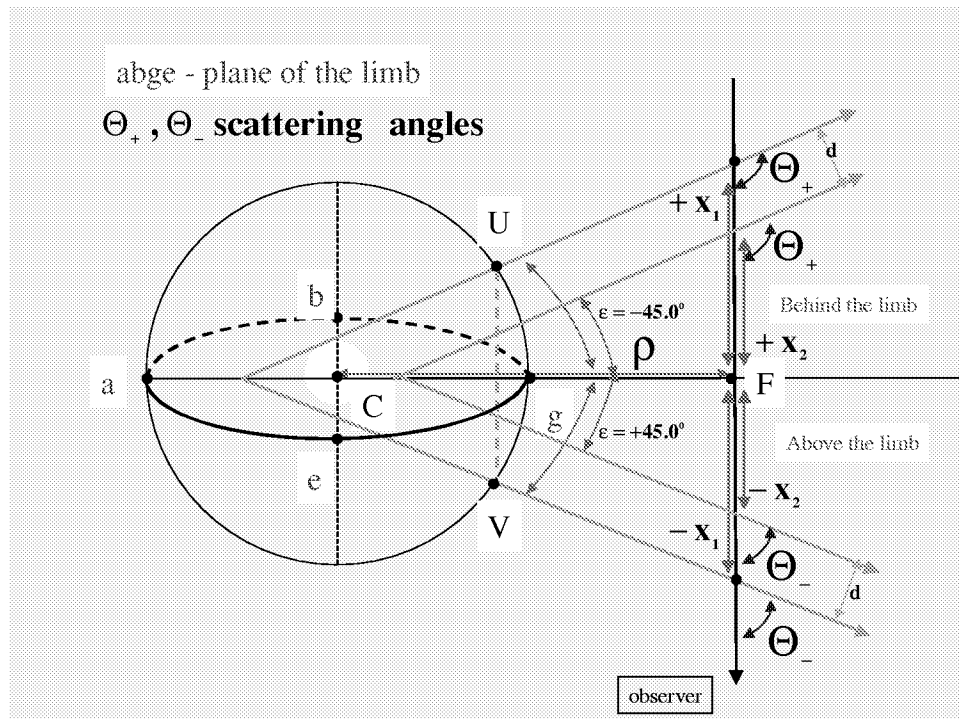


Figure (C.3). Model streamers of similar dimensions at -45.0 and -45.0 degrees above and below the plane of the solar limb, respectively.

Figure (C.4) shows the effect of streamers, at series of angles (ϵ) in front and behind the plane of the solar limb, on the K-coronal spectrum. As per the streamer model considered the intensity of the K-coronal spectrum decreases as the location of the streamer moves away from the plane of the solar limb.

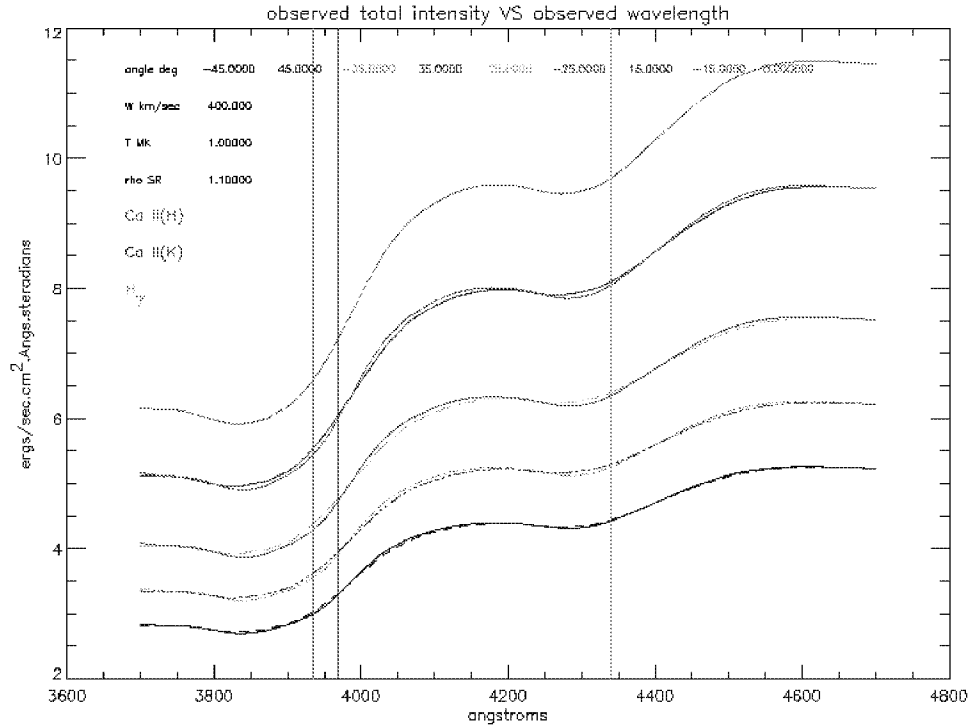


Figure (C.4). Plot to show the effect of streamers on the K-coronal spectrum with $d=0.5$ SR, $f_s=4.0$, $T_s=T=1.0$ MK and spread over various angles ϵ .

The following figures (C.5) to (C.6) show the effect on the wind and temperature sensitive intensity ratios $I(4233)/I(3987)$ and $I(4100)/I(3850)$, respectively, by a streamer of the shape depicted by figure (C.1) and with a streamer width (d) of 2.0 solar radii, density enhancement factor (f_s) of 4.0 within the streamer and assuming the thermal electron temperature (T_s) within the streamer to be equal to isothermal coronal temperature (T). The horizontal lines show the intensity ratio for a given solar wind speed, isothermal coronal temperature and line of sight in the absence of streamers. The curves are the corresponding ratios with a streamer of the shape depicted in figure (C.1)

but at various angles in front and behind the solar limb. This is only one example of a streamer model.

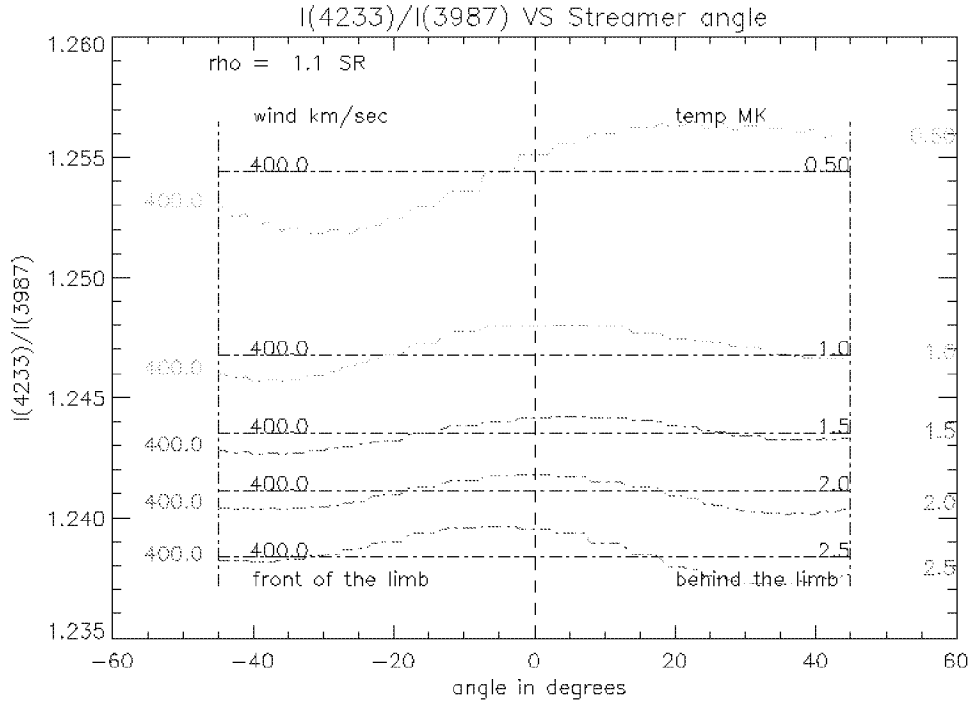


Figure (C.5). Effects by streamers on the ratio $I(4233)/I(3987)$ for $W=400$ km/sec and $\rho=1.1$ SR. The horizontal lines show the intensity ratio for a given solar wind velocity of 400.0 km/sec and line of sight at 1.1 solar radii, and for different isothermal coronal temperature in the absence of streamers.

From figure (C.5) it is apparent that even for a simple streamer structure shown in figure (C.1) the wind sensitive intensity ratio can differ from the ratios predicted by models that do not consider streamer structures. The horizontal lines in figure (C.5) are from models that do not consider any streamer structures. A similar occurrence could also be seen for the temperature sensitive intensity ratio as shown in figure (C.6).

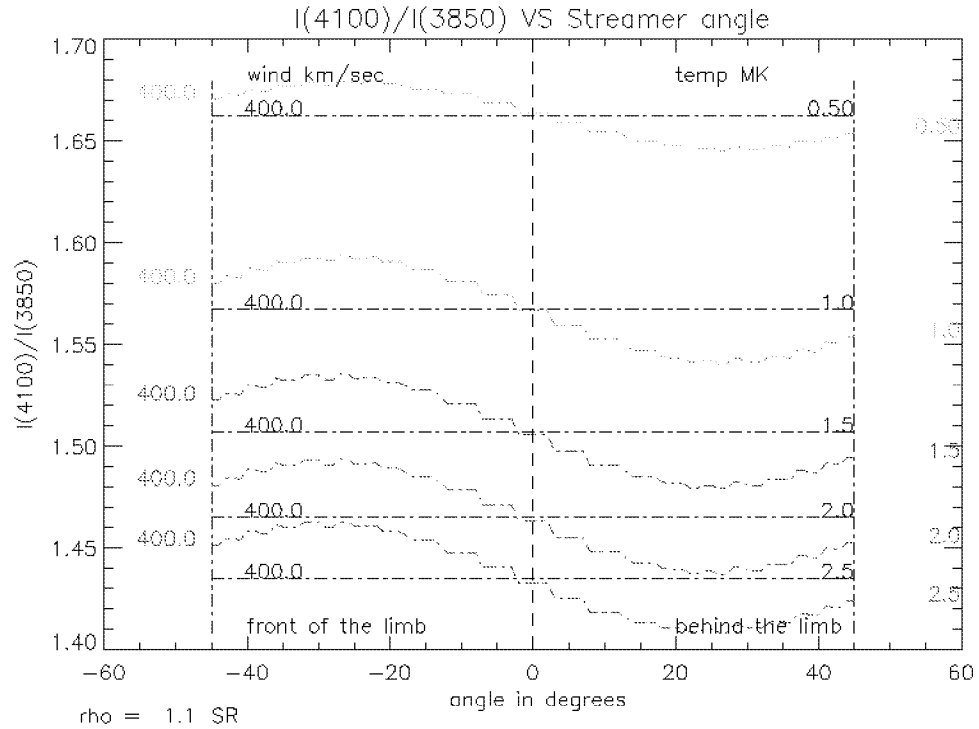


Figure (C.6). Effects by streamers on the ratio $I(4100)/I(3850)$ for $W=400$ km/sec and $\rho=1.1$ SR. The horizontal lines show the intensity ratio for a given solar wind velocity of 400.0 km/sec and line of sight at 1.1 solar radii, and for different isothermal coronal temperature in the absence of streamers.

Unfortunately it is not an easy task to incorporate realistic streamer models simply by observing an eclipse. Nevertheless figure (C.5) and figure (C.6) are examples that show the effect on the wind and the temperature sensitive intensity ratios by streamers.

REFERENCES

1. Athay, R.G., and Orrall, Q., 1957, *ApJ*, **126**, 167
2. Allen, C.P., 1973, *Astrophysical Quantities*, Athlone Press, London
3. Baumbach, S., 1937, *Astr. Nach.*, **263**, 121
4. Bird, M.K., 1982, *Space Sci. Rev.*, **33**, 99
5. Chapman, S., 1957, *Smithsonian Contrib. Astrophys.*, **2**, 1
6. Coles, W.A., Esser, R., Lovhang, U.P., and Markkenan, J., 1991, and *J. Geophys. Res.*, **96**, 13849
7. Cram, L.E., 1976, *Solar Phys.*, **48**, 3
8. Cranmer, S.R., Kohl, J.L., Noci, G., Antonucci, E., Tondello, G., Huber, M.C.E., Strachan, L., Panasyuk, A.V., Gardner, L.D., Romoli, M., Fineschi, S., Dobrzycka, D., Raymond, J.C., Nicolosi, P., Siegmund, O.H.W., Spadaro, D., Benna, C., Ciaravella, A., Giordano, S., O'Neal, R.H., Pernechele, C., Poletto, G., Smith, P.L., and Suleiman, R.M., 1999, *ApJ*, **511**, 481
9. Edlen, B., 1937, *Zs. Ph.*, **104**, 107
10. Efimov, A.I., 1994, *Space Sci. Rev.*, **70**, 397
11. Fisher, R., and Guhathakurta, M., 1995, *ApJ*, **447**, L139
12. Gabriel, A.H., 1971, *Sol. Phys.*, **21**, 392

13. Golub, L., and Pasachoff, J.M., 1997, *The Solar Corona*, Cambridge University Press
14. Guhathakurta, M and Holzer, T.E., 1994, *ApJ.*, **426**, 782
15. Guhathakurta, M., Rottman, G.J., Fisher, R.R., Orrall, F.Q., and Alrock, R.C., 1992, *ApJ*, **388**, 633
16. Handbook of Mathematical Functions With Formulas, Graphs, and Mathematical Tables, U.S. Department of Commerce, National Bureau of Standards, Applied Mathematics Series 55, Ed. Abramowitz, M and Stegun, L.A.
17. Hara, H, Tsuneta, S, lemon, J.R., Acton, L.W., and McTiernon, J.M., 1992, *PASJ*, **44**, 135
18. Hara, H., Tsuneta, S., Acton, L.W., Bruner, M.E., Lemen, J.R., and Ogawara, Y, 1994, *PASJ*, **46**, 493
19. Ichimoto, K., Kumagai, K., Sano, I., Kobiki, T., Sakurai, T., and Munoz, A., 1996, *PASJ*, **48**, 545
20. Jefferies, J.T., Smith, E.V.P., and Smith, H.J, 1959, *ApJ*, **129**, 146
21. Koutchmy, S., 1971, *A&A*, **13**, 79
22. Lamers, H.J.G.L.M., and Cassinelli, J.P., 1999, *Introduction to Stellar Winds*, Cambridge University Press
23. Nakada, M.P., Chapman, R.D., Neupert, W.M., Thomas, R.J., 1975, *Sol. Phys.*, **137**, 87
24. Narain, U., and Ulmsnhneider, P., 1990, *Space Sci. Rev.*, **54**, 377
25. Narain, U., and Ulmsnhneider, P., 1996, *Space Sci. Rev.*, **75**, 453

26. Newkirk, G., 1961, *ApJ.*, **133**, 983
27. November, L., and Koutchmy, S., 1996, *ApJ.*, **466**, 512
28. Parker, E.N., 1958, *ApJ*, **128**, 664
29. Parker, E.N., 1965, *Space Sci. Rev.*, **4**, 666
30. Reginald, N.L and Davila, J.M., 2000, Paper I, *Solar Phys.* (in print), Submitted on 27 September 1999 and accepted on 23 March 2000
31. Reginald, N.L and Davila, J.M., 2000, Paper II, *Solar phys.*, In preparation
32. Saito, K., 1965, *PASJ*, **17**, 1
33. Solar Wind Nine, 1998, *Proceedings of the Ninth International Solar Wind Conference*, AIP Conference Proceedings 471, Nantucket, Massachusetts. Ed. Shadia R. Habbal, Ruth Esser, Joseph V. Hollweg and Philip A. Isenberg
34. Standard Mathematical Tables and Formulae, CRC press, 29th Edition, equation 615, Ed. William H. Beyer
35. Strachan, L., Kohl, J.L., Weiser, H., Withbroe, G.L., and Munro, R.H., 1993, *ApJ*, **412**, 410
36. Tsubaki, T., 1975, *Sol. Phys*, **43**, 147
37. Tsuneta, S., 1996, *Solar and Astrophysical Magnetohydrodynamic Flows*, Ed. K. Tsinganos, Kluwer Academic Publishers, Holland
38. Watanabe, T., and Schwenn, R., 1989, *Space Sci. Rev.*, **51**, 147
39. Withbroe, G.L., 1988, *ApJ*, **325**, 442
40. Withbroe, G.L., Kohl, J.L., Weiser, H., and Munro, R.H., 1985, *ApJ*, **297**, 324
41. Yakovlev, O.I, and Mullan, D.J., 1996, *Irish AJ*, **23**, 7

42. Van de Hulst, H.C., 1950, *Bull. Astron. Inst. Neth.*, **410**, 135
43. Zirin, H., 1966, *The Solar Atmosphere*, (Blaisdell Publishing Company, Waltham)
44. Zirker, J.B., 1993, *Solar Phys.*, **148**, 43

REPORT DOCUMENTATION PAGEForm Approved
OMB No. 0704-0188

Public reporting burden for this collection of information is estimated to average 1 hour per response, including the time for reviewing instructions, searching existing data sources, gathering and maintaining the data needed, and completing and reviewing the collection of information. Send comments regarding this burden estimate or any other aspect of this collection of information, including suggestions for reducing this burden, to Washington Headquarters Services, Directorate for Information Operations and Reports, 1215 Jefferson Davis Highway, Suite 1204, Arlington, VA 22202-4302, and to the Office of Management and Budget, Paperwork Reduction Project (0704-0188), Washington, DC 20503.

1. AGENCY USE ONLY (Leave blank)		2. REPORT DATE December 2000	3. REPORT TYPE AND DATES COVERED Technical Memorandum	
4. TITLE AND SUBTITLE MACS, An Instrument and a Methodology for Simultaneous and Global Measurements of the Coronal Electron Temperature and the Solar Wind Velocity on the Solar Corona			5. FUNDING NUMBERS 682	
6. AUTHOR(S) Nelson L. Reginald				
7. PERFORMING ORGANIZATION NAME(S) AND ADDRESS (ES) Goddard Space Flight Center Greenbelt, Maryland 20771			8. PERFORMING ORGANIZATION REPORT NUMBER 2001-00786-0	
9. SPONSORING / MONITORING AGENCY NAME(S) AND ADDRESS (ES) National Aeronautics and Space Administration Washington, DC 20546-0001			10. SPONSORING / MONITORING AGENCY REPORT NUMBER TM—2000—209973	
11. SUPPLEMENTARY NOTES				
12a. DISTRIBUTION / AVAILABILITY STATEMENT Unclassified—Unlimited Subject Category: 92 Report available from the NASA Center for AeroSpace Information, 7121 Standard Drive, Hanover, MD 21076-1320. (301) 621-0390.			12b. DISTRIBUTION CODE	
13. ABSTRACT (Maximum 200 words) In Cram's (1976) theory for the formation of the K-coronal spectrum he observed the existence of temperature sensitive anti-nodes, which were separated by temperature insensitive nodes, at certain wavelengths in the K-coronal spectrum. Cram also showed these properties were remarkably independent of altitude above the solar limb. In this thesis Cram's theory has been extended to incorporate the role of the solar wind in the formation of the K-corona, and we have identified both temperature and wind sensitive intensity ratios. The instrument, MACS, for Multi Aperture Coronal Spectrometer, a fiber optic based spectrograph, was designed for global and simultaneous measurements of the thermal electron temperature and the solar wind velocity in the solar corona. The first ever experiment of this nature was conducted in conjunction with the total solar eclipse of 11 August 1999 in Elazig, Turkey. Here twenty fiber optic tips were positioned in the focal plane of the telescope to observe simultaneously at many different latitudes and two different radial distances in the solar corona. The other ends were vertically stacked and placed at the primary focus of the spectrograph. By isolating the K-coronal spectrum from each fiber the temperature and the wind sensitive intensity ratios were calculated.				
14. SUBJECT TERMS Solar physics, solar corona, solar wind, MACS.			15. NUMBER OF PAGES 288	
			16. PRICE CODE	
17. SECURITY CLASSIFICATION OF REPORT Unclassified	18. SECURITY CLASSIFICATION OF THIS PAGE Unclassified	19. SECURITY CLASSIFICATION OF ABSTRACT Unclassified	20. LIMITATION OF ABSTRACT UL	